Lappeenranta
University of Technology

Anna-Leena Erkkilä

HYGRO-ELASTO-PLASTIC BEHAVIOR OF PLANAR ORTHOTROPIC MATERIAL

Thesis for the degree of Doctor of Philosophy to be presented with due permission for public examination and criticism in the Auditorium 1382 at Lappeenranta University of Technology, Lappeenranta, Finland on the 6th of May, 2015, at noon.

Acta Universitatis
Lappeenrantaensis 631

Supervisors Professor, PhD Jari Hämäläinen
Vice President for Research
Lappeenranta University of Technology (LUT)
Finland

Postdoctoral Researcher, PhD Teemu Leppänen
LUT School of Engineering Science
LUT Savo Sustainable Technologies, Varkaus unit
Lappeenranta University of Technology (LUT)
Finland

Reviewers Professor, PhD Tetsu Uesaka
Fibre Science and Communication Network
Department of Chemical Engineering
Mid Sweden University
Sweden

Professor, PhD Sören Östlund
KTH Engineering Sciences
Department of Solids Mechanics
KTH Royal Institute of Technology
Sweden

Opponent Professor, DSc (Tech) Mikko Alava
Aalto University School of Science
Department of Applied Physics
Aalto University
Finland

ISBN 978-952-265-768-8
ISBN 978-952-265-769-5 (PDF)
ISSN-L 1456-4491
ISSN 1456-4491
Lappeenrannan teknillinen yliopisto
Yliopistopaino 2015

Abstract

Anna-Leena Erkkilä
HYGRO-ELASTO-PLASTIC BEHAVIOR OF PLANAR ORTHOTROPIC MATERIAL
Lappeenranta, 2015
54 p.
Acta Universitatis Lappeenrantaensis 631
Diss. Lappeenranta University of Technology
ISBN 978-952-265-768-8, ISBN 978-952-265-769-5 (PDF), ISSN-L 1456-4491,
ISSN 1456-4491

The mechanical and hygroscopic properties of paper and board are factors affecting the whole life-cycle of a product, including paper/board quality, production, converting, and material and energy savings. The progress of shrinkage profiles, loose edges of web, baggy web causing wrinkling and misregistration in printing are examples of factors affecting runnability and end product quality in the drying section and converting processes, where paper or board is treated as a moving web. The structural properties and internal stresses or plastic strain differences built up during production also cause the end-product defects related to distortion of the shape of the product such as sheet or box. The objective of this work was to construct a model capable of capturing the characteristic behavior of hygroscopic orthotropic material under moisture change, during different external in-plane stretch or stress conditions. Two independent experimental models were constructed: the elasto-plastic material model and the hygroexpansivity-shrinkage model. Both describe the structural properties of the sheet with a fiber orientation probability distribution, and both are functions of the dry solids content and fiber orientation anisotropy index. The anisotropy index, introduced in this work, simplifies the procedure of determining the constitutive parameters of the material model and the hygroexpansion coefficients in different in-plane directions of the orthotropic sheet. The mathematically consistent elasto-plastic material model and the dry solids content dependent hygroexpansivity have been constructed over the entire range from wet to dry. The presented elasto-plastic and hygroexpansivity-shrinkage models can be used in an analytical approach to estimate the plastic strain and shrinkage in simple one-dimensional cases. For studies of the combined and more complicated effects of hygro-elasto-plastic behavior, both models were implemented in a finite element program for a numerical solution. The finite element approach also offered possibilities for studying different structural variations of orthotropic planar material, as well as local buckling behavior and internal stress situations of the sheet or web generated by local strain differences. A comparison of the simulation examples presented in this work to results published earlier confirms that the hygro-elasto-plastic model provides at least qualitatively reasonable estimates. The application potential of the hygro-elasto-plastic model is versatile, including several phenomena and defects appearing in the drying, converting and end-use conditions of the paper or board webs and products, or in other corresponding complex planar materials.

Keywords: Elasto-plasticity, Hygroexpansivity, Anisotropy, Dry solids content, Shrinkage, Paper, Fiber orientation, Deformations

To Mariel and Mikael

Acknowledgment

I wish to express my profound gratitude to my supervisors Prof. Jari Hämäläinen and Postdoc Teemu Leppänen. Throughout the entire process, they have provided me invaluable guidance, criticism, suggestions, and encouragement.

I am using this opportunity to express my sincere gratitude to all those individuals that have been contributed in any part of this work: Pasi Lipponen, Juha Happonen, Collin Hii, Kari Luostarinen, Tiina Hälikkä, Markku Ora, Seppo Virtanen, Tarja Sinkko, Mikko Oksanen, Pia Vento, Tero Tuovinen, Ismo Mäkinen, Jussi Timonen, Sami Anttilainen, Mike Odell, Jarmo Kouko, Marko Avikainen, Markku Markkanen, Petri Niemi, Matti Luontama, Petri Jetsu, Ari Puurtinen, Merja Selenius, including those I may have inadvertently omitted. My special thanks goes to Pekka Pakarinen and Heimo Ihalainen for their constant support and for valuable co-operation and discussions.

I wish to thank the official reviewers, Prof. Tetsu Uesaka and Prof. Sören Östlund, for their constructive criticism, which greatly improved this manuscript.

I would like to express my appreciation to my parents and my sister for their constant support from the very beginning. I thank Matti Kurki for patience and interesting discussions. Finally, I express my warm thanks and love to my son Mikael and my daughter Mariel, who have taught me the most important things of life.

I greatly appreciate Valmet Corp. and UPM-Kymmene Corp. for the financial support and for providing experimental data for my use, and University of Jyväskylä, Department of Mathematical Information Technology for providing facilities to assist in finalizing this work. The simulations were performed by commercial software ABAQUS which was licensed to CSC (the Finnish IT center for science).

Lappeenranta, February 2015

Anna-Leena Erkkilä

LIST OF THE ORIGINAL ARTICLES AND THE AUTHOR'S CONTRIBUTION

This thesis consists of an introductory part, four original refereed articles in scientific journals and one original refereed article in conference proceedings. The articles and the author's contributions to them are summarized below.

I **A.-L. Erkkilä, P. Pakarinen and M. Odell**, Sheet forming studies using layered orientation analysis, *Pulp & Paper Canada*, 99(1), 81-85, 1998.

II **P. Lipponen, A.-L. Erkkilä, T. Leppänen and J. Hämäläinen**, On the importance of in-plane shrinkage and through-thickness moisture gradient during drying on cockling and curling phenomena, *Transactions of the 14th Fundamental Research Symposium*, 389-436, 2009.

III **A.-L. Erkkilä, T. Leppänen and J. Hämäläinen**, Empirical plasticity models applied for paper sheets having different anisotropy and dry solids content levels, *International Journal of Solids and Structures*, 50(14–15), 2151-2179, 2013.

IV **A.-L. Erkkilä, T. Leppänen, M. Ora, T. Tuovinen and A. Puurtinen**, Hygroexpansivity of anisotropic sheets, *Nordic Pulp and Paper Research Journal*, In Press, 2015.

V **A.-L. Erkkilä, T. Leppänen, J. Hämäläinen and T. Tuovinen**, Hygro-elasto-plastic model for orthotropic sheet, *International Journal of Solids and Structures*, In Press, 2015.

The author of this thesis is the principal author of Publications **I** and **III**-**V**. The author had a central role in interpreting results and the writing in all Publications **I**-**V**. The author also had a major role in processing and analyzing the experiment data in all Publications. However, the art of numerical finite element modeling was mainly constructed by Teemu Leppänen. Erkkilä is also author of the following thesis topics related publications not included in the thesis.

A.-L. Erkkilä, I. Mäkinen, M. Luontama and S. Anttilainen, Introduction to out-of-plane deformations - The challenge of top quality, flat paper, *Assosiation of Chemical Pulp and Paper Chemists and Engineers in Germany (Zellcheming) 104th Annual Meeting*, Wiesbaden, Germany, 2009.

T. Leppänen, A.-L. Erkkilä and J. Hämäläinen, Effect of fiber orientation structure on simulated cockling of paper, *Pulp & Paper Canada*, 109(2), 31-38, 2008.

P. Lipponen, T. Leppänen, A.-L. Erkkilä and J. Hämäläinen, The effect of drying on simulated cockling of paper, *Journal of Pulp and Paper Science*, 34(4), 226-233, 2008.

T. Leppänen, A.-L. Erkkilä, P. Jetsu and J. Hämäläinen, Mathematical modelling of moisture induced cockling of a paper sheet, *PAPTAC 92nd Annual Meeting Preprints - Book A*, Montreal, Canada, 315-320, 2006.

T. Leppänen, J. Sorvari, A.-L. Erkkilä and J. Hämäläinen, Mathematical modelling of moisture induced out-of-plane deformation of a paper sheet, *Modelling and Simulation in Materials Science and Engineering*, 13(6), 841-850, 2005.

A.-L. Erkkilä, P. Pakarinen and M. Odell, The effect of forming mechanisms on layered fiber structure in roll and blade gap forming, *Tappi99 - preparing for the next millennium*, Atlanta, USA, 389-400, 1999.

H. Kiiskinen, P. Pakarinen, M. Luontama and A.-L. Laitinen, Using infrared thermography as a tool to analyze curling and cockling of paper, *Aerospace Sensing, International Society for Optics and Photonics*, Orlando, USA, 134-141, 1992.

PART I: OVERVIEW OF THE THESIS

CHAPTER I

Introduction

1.1 Background

The mechanical properties of paper and board are factors affecting the whole life-cycle of a product, including paper/board quality, production, converting, and material and energy savings. Paper or board can be described as an elasto-visco-plastic continuum material including such rheological behaviors as delayed strain recovery, stress relaxation, and creep (Skowronski and Robertson (1986); Rance (1956); Steenberg (1947); Gates and Kenworthy (1963); Lyne and Gallay (1954)). The hygroscopic nature of fibers results in dimensional changes caused by humidity changes or treatments which involve water intake or drying (Rance (1954); Page and Tydeman (1962); Uesaka (1994); Nanko and Wu (1995)). Shrinkage during drying (Wahlström and Lif (2003); Hoole et al. (1999); Nanri and Uesaka (1993); Kiyoaki (1987)) and hygro- and hydroexpansivity (Uesaka (1991); Salmen et al. (1987); Larson and Wågberg (2008); Lif et al. (1995); Mendes et al. (2011)) are widely studied components of the sorption based dimensional instabilities of paper and board. Natural fibers and their treatments, bonds between fibers, their orientation in the fiber network, additives, and manufacturing conditions all affect dimensional instability and the mechanical properties of paper or board (Silvy (1971); Wahlström and Fellers (2000); Alava and Niskanen (2006); Kouko et al. (2007); Nordman (1958); Fahey and Chilson (1963); Salmen et al. (1987); Uesaka et al. (1992); Uesaka and Qi (1994); Mäkelä (2009); Lyne et al. (1996); de Ruvo et al. (1976); Manninen et al. (2011); Setterholm and Kuenzi (1970); Glynn et al. (1961); Leppänen et al. (2008)).

In paper manufacturing or the web-fed printing process, the continuous, moving paper web has to be transported from one paper/printing machine component to another. Tension is needed in the web velocity direction (machine direction, MD) when the paper web is moved from one roll surface to another. Within transportation from the press section to the drying section the dry solids content of the paper web may be as low as 35%, while in other production stages it may increase up to 98%. The required web tension is generated by straining the web in MD and controlled by velocity difference between supporting surfaces. When the generation and maintenance of suitable tension is considered, the time-dependent stress-strain behavior of both the wet and dry web is an essential parameter. This transport of the strain-controlled web also generates plastic deformations in the paper. Plastic deformations may vary locally and in different directions, because of irregularity in the paper structure and the processing conditions.

The structural anisotropy arises from the paper making process, which usually orients fibers to align

more along the MD than the transverse direction (cross direction, CD), so that fiber orientation distribution is virtually always anisotropic. During drainage, orientated shear occurs between the unformed suspension and the wire/fiber mat, which produces paper with an orientated structure. If drainage has been proceed by filtration, each individual fiber layer is formed separately. The orientated shear can be described by a simple theory of inclined filtration (Radvan et al. (1965); Parker (1972); Meyer (1971)). By means of this theory the degree of fiber orientation anisotropy as well as misalignment angle for each individual layer of paper, can be calculated by varying both the shear and dewatering velocity of the suspension. In addition to fiber orientation anisotropy, the level of mechanical anisotropy is affected by the paper making process in such a way that in the velocity direction of the web (MD) the tension needed for stable transfer increases the elastic modulus and decreases the breaking strain in that direction. In the transverse direction (CD), no external tension is applied and the web can deform more freely at the edges, although in the middle of the web the most shrinkage is prevented by internal forces.

Depending on changes in the temperature and on the relative humidity of the air, cellulosic fibers absorb, adsorb or desorb water. Most of the hygroexpansivity of fibers takes place diametrically; the changes in the length and cross sections are in the order of 1% to 2% and 20% to 50%, respectively, over the range of relative humidity (RH%) (Page and Tydeman (1962)). The lateral hygroexpansivity of the fibers is transferred to the macroscopic dimensional changes of the paper sheet via inter-fiber bonding (Rance (1954); Page and Tydeman (1962); Uesaka (1994); Nanko and Wu (1995)). The fiber composition, degree of refining, chemical modifications and restraints during drying influence the dimensional stability of paper, while anisotropic fiber orientation generates the anisotropic in-plane hygroexpansivity of the sheet together with the drying conditions (Stamm and Beasley (1961); Page and Tydeman (1962); Fahey and Chilson (1963); Uesaka (1994); Lyne et al. (1996); Li et al. (2009)).

Several models to predict in-plane mechanical and rheological properties, and shrinkage and hygroexpansivity have been introduced. Johnson and Urbanik (1984, 1987) provided a nonlinear elastic model to study material behavior in stretching, bending and buckling of axially loaded paperboard plates. The nonlinear elastic biaxial failure criteria were studied by Suhling et al. (1985) and Fellers et al. (1983). The in-plane orthotropic elasto-plastic approaches have been presented in order to estimate the tensile response and deformation of paper by Castro and Ostoja-Starzewski (2003), Mäkelä and Östlund (2003) and Xia et al. (2002). The viscoelastic models have been used extensively in studying the creep or relaxation behavior (Brezinski (1956); Lif et al. (1999); Lu and Carlsson (2001); Pecht et al. (1984); Pecht and Johnson (1985); Rand (1995); Uesaka et al. (1980)).

The formula for the hygroexpansion of paper has been derived from the hygroexpansion of a single fiber and the efficiency of the stress transfer between fibers by Uesaka (1994). In the study of Lavrykov et al. (2004) the traditional theory for linear thermoelasticity was applied to estimate hygroexpansion strains. Hygro-viscoelastic models have been used by Uesaka et al. (1989), Lif et al. (2005) and Lif (2006) to estimate the history-dependent dimensional stability and hygroexpansivity. Mechano-sorptive creep has been modeled, for example, by Urbanik (1995), Strömbro and Gudmundson (2008), Alftan (2004) and Haslach (1994). Wahlström et al. (1999) have proposed an orthotropic hypoelastic constitutive model for studies of phenomena behind the shrinkage profile. In the model, the total strain including a hygroscopic strain component and the elastic modulus dependent on the moisture ratio are described by an exponential relation. The relation between strain history and tensile stiffness was assumed to be linear, and the model and isotropic inputs were calibrated by laboratory scale experiments. Constantino et al. (2005) have presented an empirical model to predict the change of shape of shrinkage profiles resulting from changes in raw material,

running conditions or machine design. The measured moisture dependency of material constants was utilized by Yeh et al. (1991) in the nonlinear elastic model to investigate the effect of moisture on mechanical behavior. Carlsson et al. (1980) have derived an analytical equation for sheet curl (curvature) resulting from the hygroexpansion coefficients and elastic properties of the plies using elastic lamination theory. Subsequently, Bloom and Coffin (2000), Leppänen et al. (2005) and Kulachenko et al. (2005) have studied the hygroscopic out-of-plane deformations using the elastic constitutive model, while the elasto-plastic model has been applied by Lipponen et al. (2008). Hygroexpansion coefficients are independent of the moisture content in these models.

1.2 Objective

The ultimate purpose of this work is to contribute to the solution of several undesired phenomena that can be considered to be connected to the hygroscopic and stress-strain behavior of paper or similar material during production processes and in end-use. Examples of such phenomena are the development of shrinkage profiles, loose edges of a web, a baggy paper web causing possible wrinkling and misregistration in printing, or distortion in the shape of a product such as a sheet or box. These defective events have been studied widely by different experimental and modeling approaches, but there are still elements that remain unidentified.

The objective of this work is to construct a model to estimate the behavior of orthotropic planar material under different moisture contents subjected to external stress, strain and moisture changes. The contribution of this work to solving the ultimate purpose described above is to provide estimates of plastic strain, internal stresses and deformations on a sheet or web due to these changes. Two independent empirical models were constructed: the elasto-plastic material model and the hygroexpansivity-shrinkage model. Both models are functions of the dry solids content and fiber orientation anisotropy index and can be used in an analytical approach to estimate plastic strain and in-plane deformations in simple one-dimensional cases. For studies of the combined and more complicated effects of hygro-elasto-plastic behavior, these two models were implemented in a finite element program for numerical solution of the sheet or web. The finite element approach also allowed the possibility of studying different structural variations of an orthotropic sheet as well as the buckling behavior and internal stress situations of sheets or webs caused by local or layered strain differences. The time- or history-dependent phenomena were omitted from the analytical models at this stage. Thus, the applicability of the model to studies of storage and multi-chained processes is limited.

CHAPTER II

Layered fiber orientation

A large number of different indirect measuring methods have been developed to determine the fiber orientation or anisotropy of sheet. Several of them are based on measuring the anisotropy of mechanical properties, i.e. the angular variation of tensile strength, elastic modulus, zero-span tensile strength (Kallmes (1969); Cowan and Cowdrey (1974); Fleischman et al. (1982)) or sonic modulus (Craver and Taylor (1965); Mann et al. (1980)). The deformation of a sheet in heat shrinkage is also an indicator of anisotropy and a misalignment angle (Koskimies (1986)). Generally, the mechanical and deformation properties of sheet strongly depends on both drying restraint and fiber orientation. Different applications using visible light or other radiation to determine structural orientation have also been introduced, for example, laser light diffraction, diffusion and scattering (Rudström and Sjölin (1970); Bauer and Stark (1988); Sadowsky (1979); Abe and Sakamoto (1991); Fiadeiro et al. (2002)), polarized far infrared (Boulay et al. (1986); Drouin and Gagnon (1993)), X-ray diffraction (Ruck and Krässig (1958); Prud'homme et al. (1975); Yuhara et al. (1991)) or transmitted microwave intensity (Habeger and Baum (1987); Osaki (1987)). In the first direct methods, the distribution of the fiber orientation was measured from a sheet formed from a furnish containing a small fraction of stained fibers. Both manual and digitized microscopic counting techniques have been developed (Danielson and Steenberg (1947); Forgacs and Strelis (1963); Crosby et al. (1981)). These methods measure the orientation of stained fibers only on the outer surfaces. The fiber orientation distribution of surfaces is also measured by light diffraction by Fiadeiro et al. (2002) and light reflection by Abe et al. (1995), Niskanen (1993), Enomae et al. (2004) and Takalo et al. (2014).

Usually, a technique to divide a paper sample into a number of distinct layers is needed to enable the measurement of the variation of the fiber orientation structure in thickness direction (z-direction) of the sample. In a Beloit sheet splitter, the wet paper sample is delaminated when both of its surfaces are frozen in the nip onto the surfaces of rotating steel rolls, which are cooled below the freezing point of water. The Beloit sheet splitter was developed by Parker and Mih (1964) and was used by Kallmes (1969) to determine zero-span tensile strength anisotropy throughout the thickness of a sheet. Waterhouse et al. (1987) and Östlund et al. (2004) removed layers by surface grinding to measure the z-directional variation of the internal stress of a sheet. Adhesive or lamination tape splitting was applied by Abe and Sakamoto (1991), Erkkilä (1995), Lloyd and Chalmers (2001), Neagu et al. (2005) and Hirn and Bauer (2007), as well as in Publication **I**, Publication **II**. In sectioning, some damage to the fiber network is inevitable, and thus, Xu et al. (1999) and Enomae et al. (2008) have proposed the non-destructive confocal laser scanning microscopy techniques to visualize the fibers

within the structure. Determination of the three dimensional fiber segment orientation using X-ray microtomography has been demonstrated for paper by Kondo and Aidun (2007) and for nonwovens by Tausif et al. (2014). Images describing the mass density or reflection of a whole sample or an individual layer and captured by soft X-ray, X-ray, radiography, light transmission, light reflection, or optical or scanning electron microscopes are processed with several methods to determine the characteristic parameters of the fiber orientation. The Fourier transform from surface optical micrographs or scanning electron micrographs was used by Yuhara et al. (1991) and Enomae et al. (2004, 2008). The Hough transform was proposed by Xu et al. (1999) and Thorpe (1999). One of the most widely used methods is based on local gradient determination (Erkkilä (1995); Scharcanski and Dodson (1996); Publication **I**; Scharcanski and Dodson (2000); Publication **II**; Lloyd and Chalmers (2001); Neagu et al. (2005)). A variogram based-method and segmentation by skeletonization have been compared with the gradient method by Kärkkäinen et al. (2001) and Hirn and Bauer (2007). A curvelet-based method for orientation estimation is studied by Sampo et al. (2014) and Takalo et al. (2014).

Fibers are usually curled or kinked and may be more curly in the cross direction than those in the machine direction due to the paper making process. Also the length and thickness of fibers varies and the image of fibers may appear discontinuous as they overlap each others. The fiber orientation distribution is defined in different ways when different image processing techniques or measuring methods of structural properties are used (Niskanen and Sadowski (1989)). There is no common consensus on how the contribution of each fiber to fiber orientation distribution should be weighted.

For this work, the fiber orientation parameters are measured using the layered fiber orientation method developed by Erkkilä (Erkkilä (1995); Publication **I**; Publication **II**). The important features of this method are that laminate tape splitting provides large analyzing areas, fairly low resolutions can be used in digitizing, individual fibers do not needed to be identified in image processing by the gradient method, and it is suitable for both measurements of global values and local variations. In this method, the sample layers are placed against a black background, and an image of a suitable area (for example, 192 mm $\times$ 192 mm) is captured by scanner from the fiber side (in contrast to the tape side) with a 30 μm/pix resolution using reflective illumination. When analyzing the layer images, the aim is to detect the edges of fibers or fiber bundles and to determine their orientations. Fibers are distinguishable against a dark background as high intensity values.

The detection of edges is based on the computation of image gradients in every image element. For a discrete digital image, the derivatives $\frac{\partial f}{\partial x}$ and $\frac{\partial f}{\partial y}$ can be approximated through a discrete differentiation operator. The operator uses two kernels $k_x(i,j)$ and $k_y(i,j)$ that are convolved with the original image $f(x,y)$ to calculate approximations of the horizontal and vertical derivatives:

$$\frac{\partial f(x,y)}{\partial x} \approx D_x(x,y) = (f * k_x)(x,y), \tag{2.1}$$

$$\frac{\partial f(x,y)}{\partial y} \approx D_y(x,y) = (f * k_y)(x,y), \tag{2.2}$$

where $*$ denotes the 2-dimensional convolution operation. The coefficients of the kernels used are based on the principle of binomial filter design (Publication **II**). The magnitude (length) $|\nabla f(x,y)|$

and direction $\theta_f(x, y)$ of gradient vectors at each local image point are calculated by applying Equations 2.3 and 2.4:

$$|\nabla f(x, y)| = \sqrt{D_x^2 + D_y^2}, \tag{2.3}$$

$$\theta_f(x, y) = \tan^{-1} \frac{D_y}{D_x}. \tag{2.4}$$

The magnitude of gradient vector is directly related to the probability that the part of the image examined represents the edge of the fiber. At the fiber edge the direction of gradient corresponds with the direction normal to that segment of fiber edge. The discrete orientation distribution is then formed as a weighted probability density function of the local orientations $P(\theta_P)$, where the weighting factor is the gradient magnitude $|\nabla f(x, y)|$. The direction histogram is

$$P(\theta_P) = \frac{\Sigma_{x,y} \left(|\nabla f(x, y)| \, \delta_{\theta_{f(x,y)}, \theta_P} \right)}{\Sigma_{x,y} |\nabla f(x, y)|} \tag{2.5}$$

where $\delta_{\theta_{f(x,y)}, \theta_P}$ is Kronecker's delta function and $\{\theta_P, \theta_f \in Z : 0 \leq \theta_P, \theta_f < 360\}$. The main direction of the orientation (orientation angle) θ is defined as the deviation of the longer symmetry axis from the machine direction. The anisotropy of the fiber orientation distribution ξ is defined as a ratio of the maximum distribution value $P(\theta)$ and the value in the perpendicular direction to the maximum value $P(\theta + 90)$.

The elasto-plastic, hygroexpansivity and shrinkage parameters were fitted to the experimental values as a function of the anisotropy index in Publications **III** and **IV**; and the final models were constructed from those fittings in Publication **V**. In order to derive the anisotropy index ϕ, two assumptions were made: (1) the shape of the orientation distribution is elliptical and (2) the area of the orientation distributions of different orientation levels and samples can be normalized to the same constant value. For simplicity the area of orientation distribution is defined to be π. By means of these assumptions the lengths of the minor and major semi-axes of the fiber orientation distribution ellipse obtains the values $1/\sqrt{\xi}$ and $\sqrt{\xi}$, respectively. Then the equation for the anisotropy index ϕ, describing the distance of ellipse point from the origin in the direction γ, can be written as

$$\phi_\gamma = \sqrt{\frac{1 - \xi^2}{\xi + \tan^2 \gamma / \xi} + \xi}. \tag{2.6}$$

when γ is the angle from the minor axis of the fiber orientation distribution.

The layered orientation measuring method, described above and presented in Publications **I**, **II** and **III**, has been proved to be a valuable tool both for studying the paper forming conditions at the wet end of the paper machine (Publication **I**; Erkkilä (1995); Erkkilä et al. (1999); Lindström et al. (2009); Kiviranta and Pakarinen (2001)) and for estimating the structural based out-of-plane deformation tendency of the paper sheet (Leppänen et al. (2006); Publication **II**; Kiviranta and

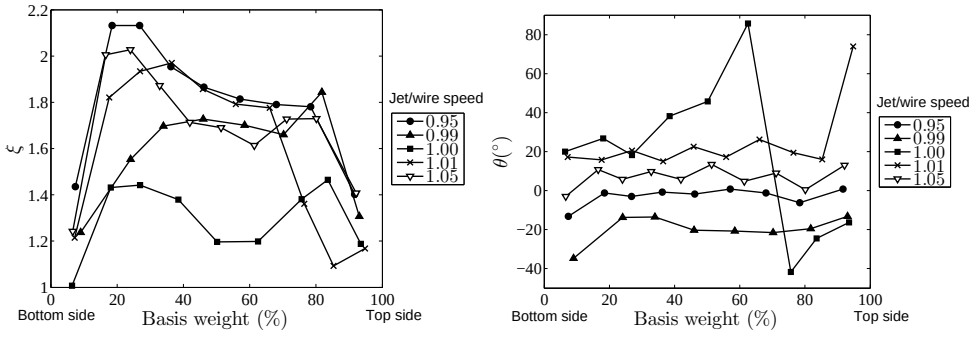

Figure 2.1: Layered fiber orientation anisotropy (left) and angle (right) profiles at different jet-to-wire speed ratio values. (Publication **I**)

Pakarinen (2001)). The velocity difference of the jet and the wire causes orientated shear between the unformed suspension and the wire/fiber mat (Parker (1972)). The large speed difference gives high fiber orientation anisotropy, while turbulence increases randomness and reduces the effect of orientated shear. The misalignment angle (deviation of fiber orientation main axis from machine direction) may occur if the orientated shear has a transverse component difference between the wire and the suspension velocities. The fiber orientation in each layer of paper is governed by the conditions of the flow field that were prevailing as that layer was drained. An example of a layered fiber orientation structures with five different jet-to-wire speed ratio values is presented in Fig. 2.1 for fine paper sheets produced by hybrid forming.

The anisotropy of the fiber orientation is a significant factor for the anisotropic behavior of the mechanical and the hygroexpansion parameters of the paper or board. In some applications these anisotropic properties may be useful if the strength or dimensional stability is required in some specific direction of the product, but several unwanted defects may arise from the two-sidedness or other variations in the fiber orientation. For variation studies the layer images can be sectioned for example to 2 mm $\times$ 2 mm subregions, and orientation distributions and parameters can be calculated separately for all of these small regions. An example of the variation of fiber orientation at the bottom side of a news sample is presented in Fig. 2.2 (below) using line segments to describe the local anisotropy (the length of the line) and orientation angle (the direction of the line). In this case the high correspondence between the fiber orientation variation and out-of-plane deformations (cockling) (Fig. 2.2 (above)) can be detected even by visual comparison.

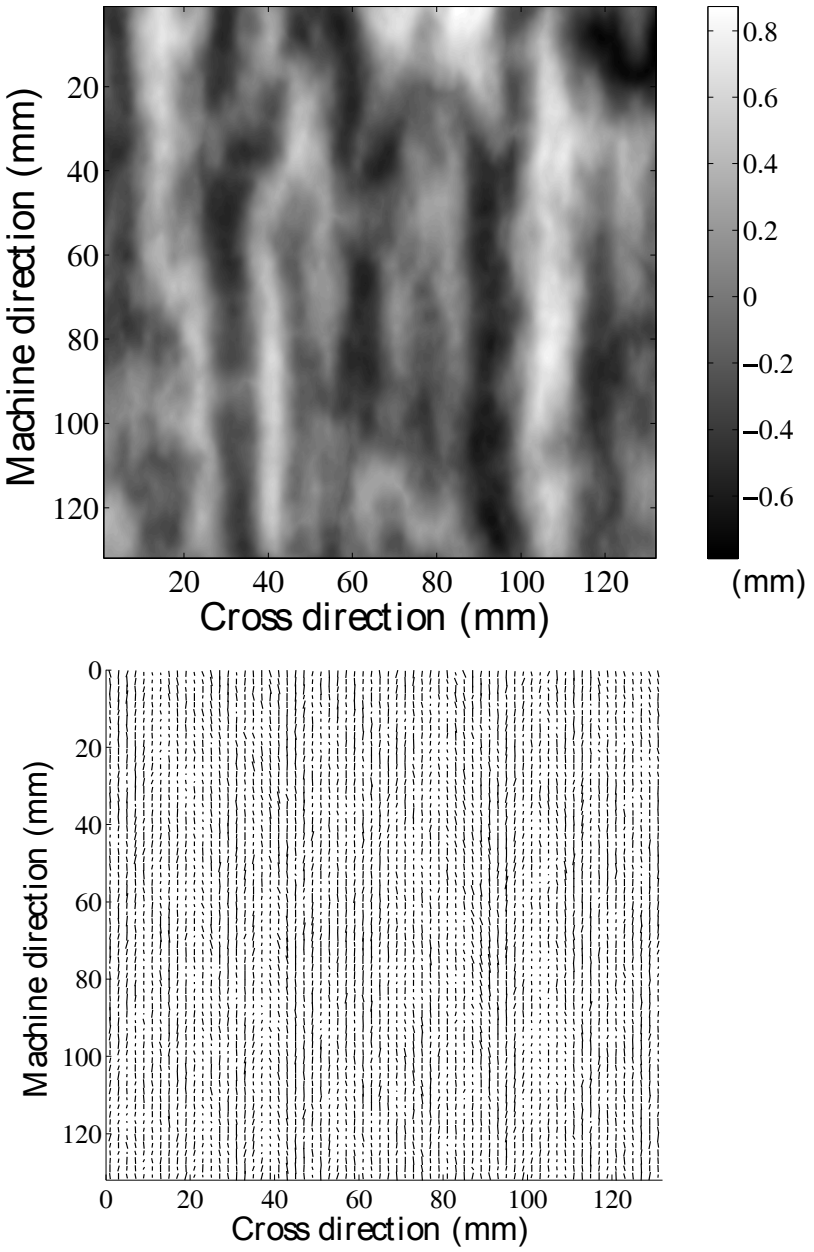

Figure 2.2: News sample showing wavy cockling and fiber orientation structure. Example of region of cockling topography (above) and orientation lines calculated for 2 mm $\times$ 2 mm subareas from the bottom side layers from a corresponding region (below). The length and direction of the orientation lines describes the anisotropy values and orientation angles, respectively. The size of the region is 132 mm $\times$ 132 mm.

CHAPTER III

Elasto-plastic material model

Several different approaches to characterize the mechanical properties of sheet materials from stress-strain curves have been introduced (Hill (1944); Ludwik (1909); Prager (1942); Ramberg and Osgood (1943); Swift (1952); Voce (1948)) and they are applied to paper or cellulosic materials, for example, by Andersson and Berkyto (1951), Castro and Ostoja-Starzewski (2003), Johnson et al. (1979), Mäkelä and Östlund (2003), Stenberg et al. (2001), Suhling et al. (1985) and Urbanik (1982). These methods have been developed to model either the overall curve shape or the material parameters, such as elastic modulus, yield point, yield offset, proportional limit, and tensile strength. If a material is considered as elasto-plastic, special interest is focused on the yield point and hardening behavior. In Publication **III** several different models were studied to describe the uniaxial stress-strain behavior of paper. These methods included commonly used approaches such as bilinear, hyperbolic, exponential, power law and Ramberg-Osgood approximations. In this research, the target was to model a whole stress-strain curve and determine the material parameters: elastic modulus, yield strain, yield stress, and stress and strain at failure. By exploiting information from these approximations a modified approach to describe the whole stress-strain behavior of paper was proposed.

The study of the proportional limit determination was based directly on the definition, that the proportional limit is the point at which the load-elongation curve deviates from linearity. The general idea was to determine the specific point of the stress-strain curve where the nonlinear model starts to have a better fit to the data than the linear function fitted to the beginning of the stress-strain curve. The aim was to fit a parabolic function only to the region where the stress-strain curve starts to deviate from the linear behavior, in order to guarantee a high goodness of fit around the proportional limit. The goodness of fit of the two different functions fitted to the same measuring data has to be equal at that infinitesimal position where those functions intersect. The intersection of the parabolic fit and linear equation with a slope according to the elastic modulus E can be determined by the equation:

$$\varepsilon_y = \begin{cases} \left(-G_2 + 1/E + \sqrt{2G_2 - 2/E - 4G_1G_3}\right)/2G_1 & \text{if} \quad 2G_2 - 2/E - 4G_1G_3 \geq 0 \\ 0.5(1/E - G_2)/G_1 & \text{otherwise} \end{cases} \tag{3.1}$$

where the first equation calculates the intersection point and the second equation the point of the equal tangents, which is used if no intersection occurs. The parameters G_1, G_2 and G_3 are constants of the parabolic dependency $\varepsilon = G_1\sigma^2 + G_2\sigma + G_3$ fit to strain interval from 0.1% to 0.4%, and ε,

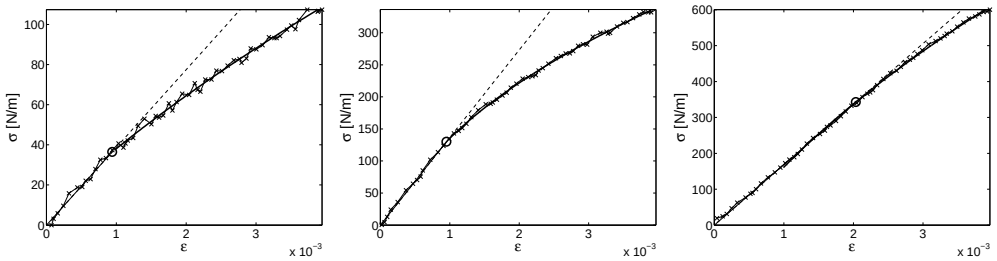

Figure 3.1: The proportional limit (yield point) determination using the parabolic approach. The yield point marked by the circle, measured data by the crosses and the linear fit having a slope of the elastic modulus by the dashed line. Dry solids contents and anisotropy indexes are in left $R_{sc} = 56.8\%$, $\phi = 1.421$, in the middle $R_{sc} = 75.3\%$, $\phi = 1.421$ and on the right $R_{sc} = 95.6\%$, $\phi = 0.704$. (Publication **III**)

σ and ε_y are the strain, stress and the yield strain, respectively. Three examples of the determination of the proportional limit (here considered equal with yield point) is presented in Fig. 3.1.

The following equation was concluded in Publication **III** to be suitable to describe all uniaxial stress-strain relationships measured:

$$\sigma = \begin{cases} E\varepsilon & \text{if} \quad \varepsilon \leq \varepsilon_y \\ E\varepsilon_y - \frac{H}{2E} + \sqrt{H\left(\frac{H}{4E^2} + \varepsilon - \varepsilon_y\right)} & \text{if} \quad \varepsilon > \varepsilon_y \end{cases} \tag{3.2}$$

where the elastic modulus E, yield strain ε_y and hardening constant H are fitting parameters. The fitted material parameters for different dry solids contents (R_{sc}) and anisotropy index (ϕ) levels are presented in Fig. 3.2. Stress-strain measurements used for these fittings were presented in Lipponen et al. (2008) and in Publication **III**. To construct the material model the following equation was presented in Publication **V** for fitting the parameters σ_y, ε_y and H as a function of R_{sc} and ϕ:

$$P = (A_1 + A_2\phi + A_3 R_{sc})^{1/n} \quad P = \{\sigma_y, \varepsilon_y, H\} \tag{3.3}$$

where A_1, A_2, A_3 and n are the fitting constants listed in Table 3.1. Table 3.1 also includes the coefficient of determination r^2 values between the measured parameters from Publication **III** and their estimates according to Eq. (3.3). The elastic modulus is determined by $E = \sigma_y/\epsilon_y$ (r^2 = 0.985).

Table 3.1: The fitting parameters of Eq. (3.3) and the coefficients of determination r^2 for the yield stress σ_y, the yield strain ε_y and the hardening constant H. (Publication **V**)

	A_1	A_2	A_3	n	r^2
σ_y	-5.9030 (Pa^n)	3.1959 (Pa^n)	18.3077 (Pa^n)	0.1760 (-)	0.965
ε_y	380.4181 (-)	14.3408 (-)	-269.8327 (-)	-0.7720 (-)	0.816
H	-0.6021 (Pa^{2n})	4.0423 (Pa^{2n})	11.3795 (Pa^{2n})	0.0715 (-)	0.890

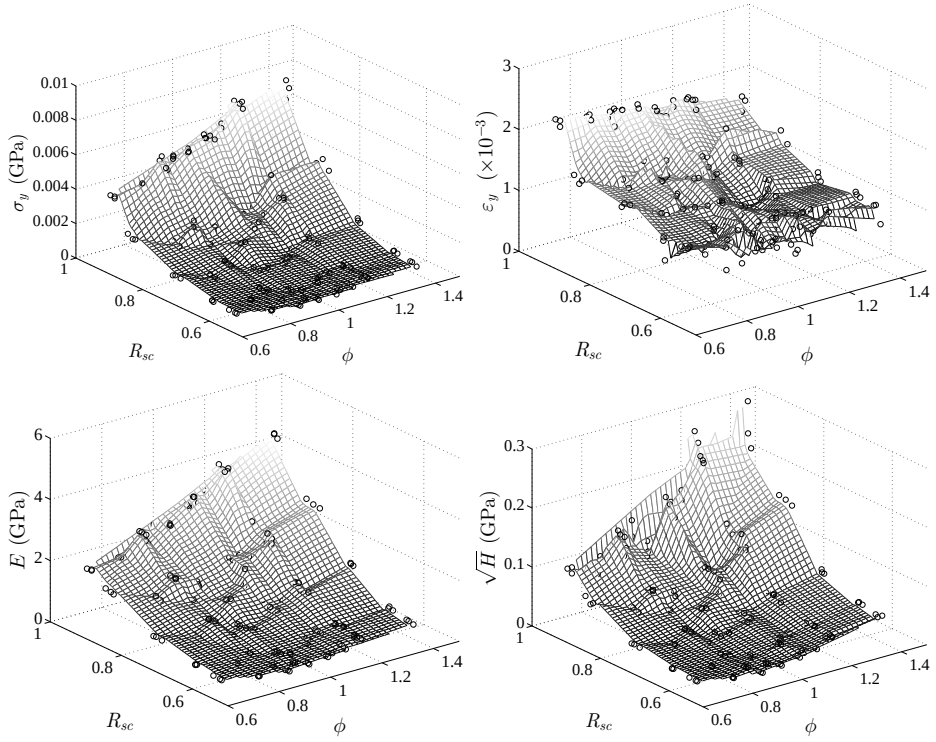

Figure 3.2: Material parameters as a function of the anisotropy index ϕ and dry solids content R_{sc}, determined from measured uniaxial stress-strain curves. The surfaces are interpolant of material parameter data. (Publication **III**)

The material model parameters as a function of ϕ and R_{sc} are presented in Fig. 3.3. The functions fitted according Eq. (3.3) behave monotonically. This allows a reasonable amount of extrapolation, which may be needed, for example, if the local variation of fiber orientation is considered. The model has a lower limit for dry solids content, i.e. the model is valid if $R_{sc} > 0.3$; the parenthetical expression of Eq. (3.3) reach negative values for yield stress σ_y with low dry solids content and if the anisotropy index is also simultaneously low. The material model can be used directly to calculate the in-plane material parameters of an orthotropic sample in any direction or at any dry solids content over 30%. The determined plastic strain dependence on the dry solids content and anisotropy index, as a consequence of 0.3% or 1% strain, is presented in Fig. 3.4.

In the continuum mechanical model plane stress is assumed and dependence between stress $\boldsymbol{\sigma} = (\sigma_1, \sigma_2, \sigma_{12})^\top$ and strain $\boldsymbol{\varepsilon} = (\varepsilon_1, \varepsilon_2, \varepsilon_{12})^\top$ is defined by the generalized Hooke's law as

$$\boldsymbol{\sigma} = \boldsymbol{C}\boldsymbol{\varepsilon} \tag{3.4}$$

where $\boldsymbol{C}$ is the constitutive matrix. Hill's yield function (Hill (1948)) was used to describe the yield surface. Hill's yield function is commonly used for paper and paperboard although there are known

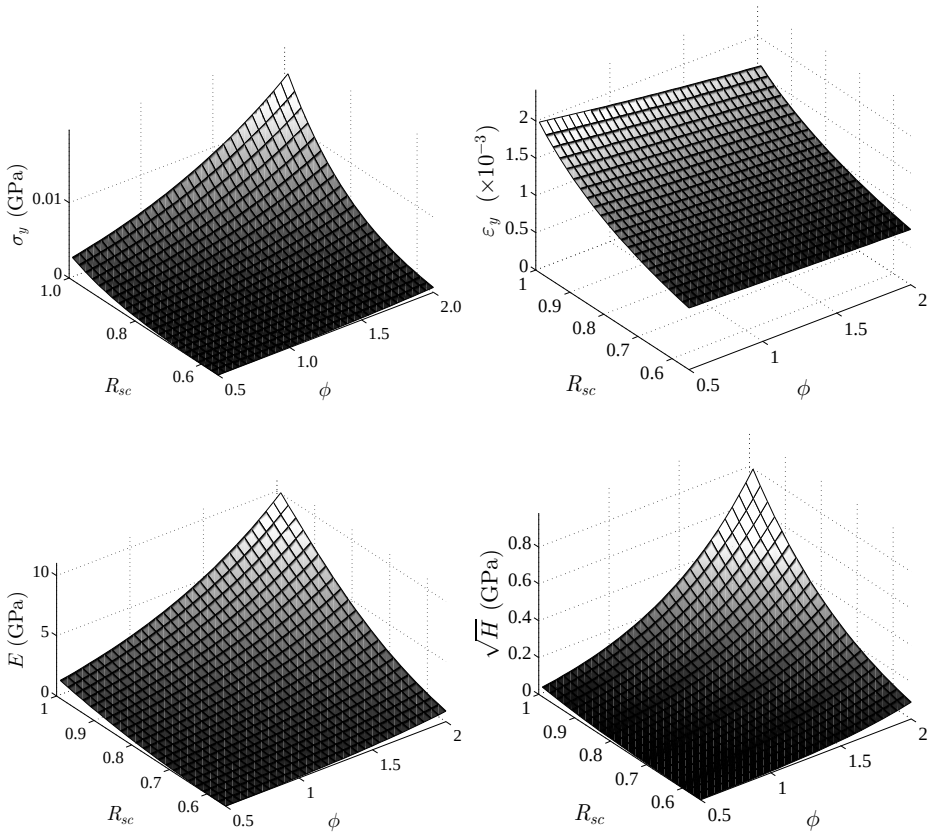

Figure 3.3: Material parameters as a function of anisotropy index ϕ and dry solids content R_{sc} according to Eq. (3.3) and Table 3.1. (Publication **V**)

limitations related to it, for example, the origin symmetry of the Hill's yield surface does not generally hold for paper or paperboard. An essential factor supporting the usage of Hill's yield function is the relatively simplicity of the parameter definition; in the case of paper the measurements needed for the determination of more exact yield surface are very complicated. According to Hoffman's approximation as found in Lipponen et al. (2008) the yield function has the form

$$f(\boldsymbol{\sigma}) = \sqrt{\sigma_1^2 - \sigma_1\sigma_2 + \left(\frac{\sigma_{y,1}}{\sigma_{y,2}}\right)^2 (\sigma_2^2 - \sigma_{12}^2) + \left(\frac{2\sigma_{y,1}}{\sigma_{y,45^\circ}}\right)^2 \sigma_{12}^2} \tag{3.5}$$

where σ_1, σ_2 and σ_{12} are the components of the stress tensor and $\sigma_{y,1}$, $\sigma_{y,2}$ and $\sigma_{y,45^\circ}$ are the yield stresses in the main direction, the cross direction, and in the direction deviating 45 degrees from the main direction, respectively. Elastic moduli are defined for directions 1, 2 and 45° as:

$$E_i = \frac{\sigma_{y,i}}{\varepsilon_{y,i}} \tag{3.6}$$

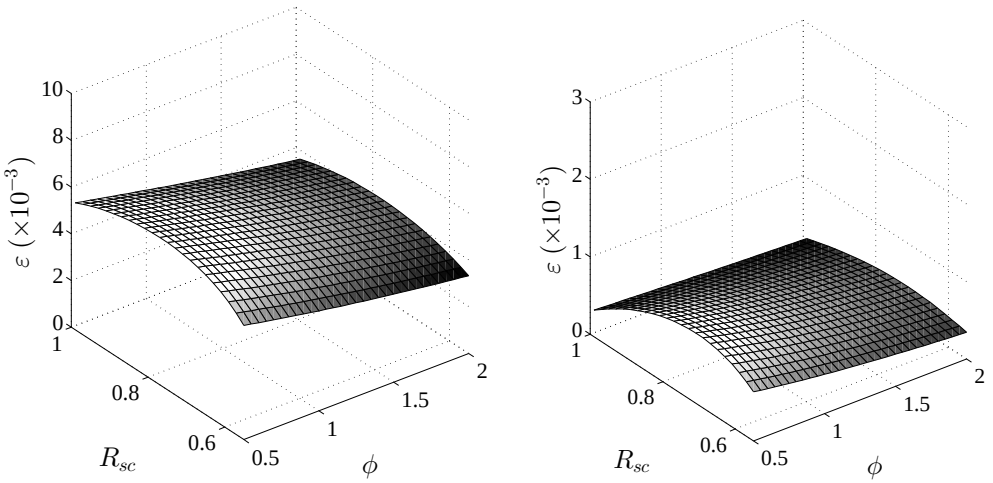

Figure 3.4: Plastic strains induced by 0.01 strain (left) and 0.003 strain (right) as a function of orientation index ϕ and dry solids content R_{sc}. (Publication **V**)

where $\varepsilon_{y,i}$ is the yield strain in the direction specified by the subscript i. All in-plane stress and strain parameters are defined by Eq. (3.3). Other details of numerical simulations are described in Publication **V**.

Following example is presented to demonstrate the elasto-plastic model in a stretching situation without dry solids content changes. For the finite element numerical study, anisotropic sheet having two 100 mm wide anisotropy streaks, but otherwise homogeneous structure, was set up, see Fig. 3.5 and Publication **V**. The sheet thickness used in the simulations was 0.1 mm. The 1% MD strain

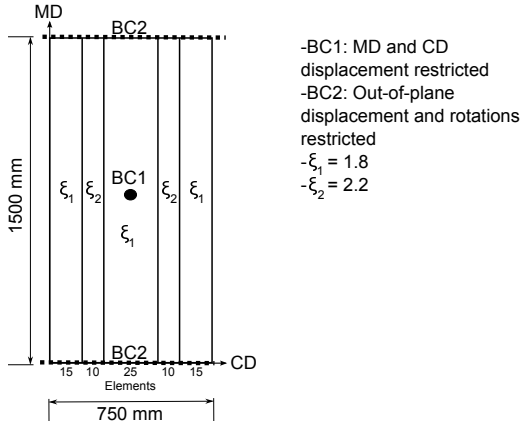

Figure 3.5: The anisotropy streaks setup for the numerical simulations.

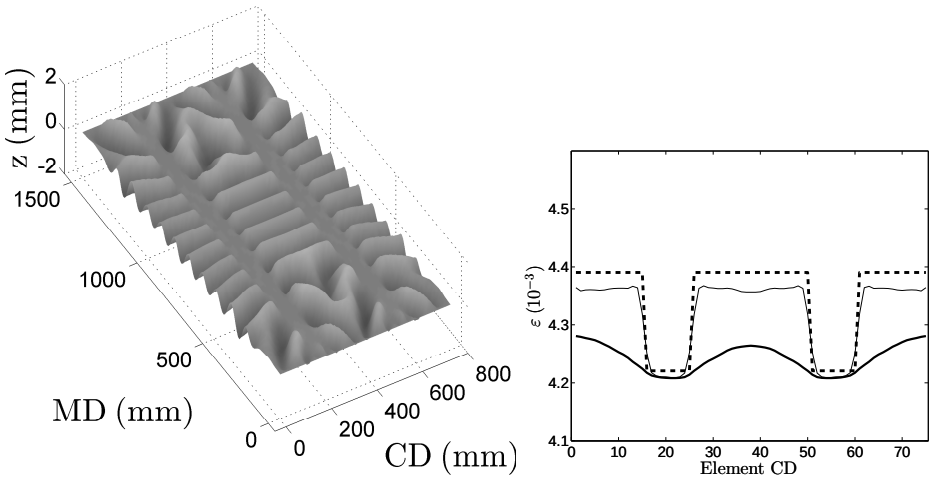

Figure 3.6: Simulated out-of-plane deformations (left) and CD profile of MD strains (right) after the sample is stretched to 0.01 strain in the MD and released. Dry solids content R_{sc} = 0.60. In the streaks the fiber orientation anisotropy $\xi = 2.2$, in the surrounding ξ = 1.8. The right-hand figure shows: the in-plane deformation of the simulated sample in MD (solid thick line), the MD strain determined using integrated MD length of the simulated sample (solid narrow line), and the plastic strain determined using the analytical one-dimensional model (dashed line). (Publication **V**)

was applied to the sheet having dry solids content R_{sc} = 60%, while the CD was unconstrained. The simulated MD stress in the streaks and in other positions were equal to the MD stress determined analytically from the one-dimensional material model (Publication **V**). By uniform stretching a higher tension was arisen in the streaks where the anisotropy is higher. After release of the stretching, the stress drops back to zero and only some minor disturbance was detected near the interfaces between regions with different anisotropies (Publication **V**). The out-of-plane deformations, presented in Fig. 3.6 (left), appeared after unloading. The out-of-plane deformations are small compared to the in-plane dimensions of the simulated sample and for examination of topography the z-axis is zoomed. The MD in-plane and strain deformations of the sample in finite element simulations and plastic strain determined analytically using one-dimensional material model (Eq. (3.3)) are presented in Fig. 3.6 (right). The plastic strain differences between streaks and surrounding caused the tight streaks and buckling in the slack surrounding region of the sheet. Buckling is highly dependent on boundary conditions, element size, disturbance etc. and the topography result can only be considered as indicative. For visual appearance the MD gradient image of a similar simulation at R_{sc} = 90% is presented in Fig. 3.7. The gradient image approximates the inclined illuminated situation, but in reality, the visual appearance of out-of-plane deformation depends on illumination and detection angle, the glossiness of the paper surface, and the ratio of wavelength and detection distance.

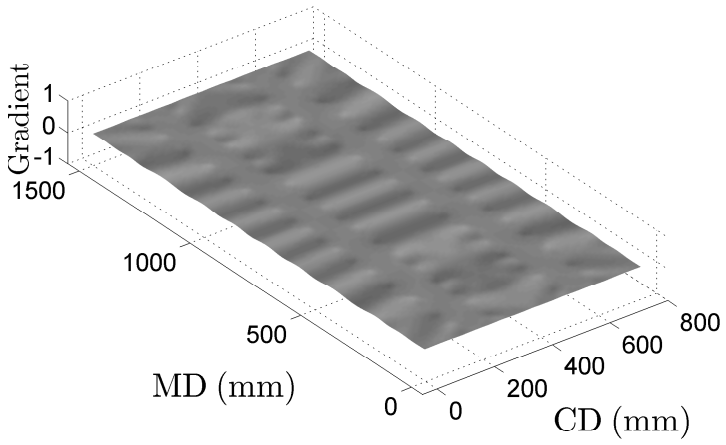

Figure 3.7: Gradient presentation for visualizing the out-of-plane deformation after the sample was stretched to 0.01 strain in the MD and released. Dry solids content R_{sc} = 0.90. In the streaks the fiber orientation anisotropy $\xi = 2.2$, in the surrounding ξ = 1.8. (Publication **V**)

CHAPTER IV

Hygroexpansivity-shrinkage model

This chapter introduces a hygroexpansivity-shrinkage model that is a function of the dry solids content and fiber orientation anisotropy index. The relation of the dry paper hygroexpansion coefficient to the anisotropy index and drying shrinkage was determined empirically from oriented laboratory sheets made from two different pulps and their mixture in Publication **IV**. Usually, the hygroexpansivity, which estimates the change in dimensions of a dry paper subject to the relative humidity change, has been considered to be constant i.e. independent of the moisture content level. However, here the dry solids content dependent hygroexpansivity is introduced over the entire range from wet to dry. The drying shrinkage strain as a function of the dry solids content is constructed with an exponential formula based on the measurements provided by Ivarsson (1954), Kijima and Yamakawa (1978) and Tydeman et al. (1966) and summarized by Wahlström et al. (1999) and Wahlström (2004). The relation between the hygroexpansivity and the solids content is derived from the drying shrinkage strain function in Publication **V**. The hygroexpansivity-shrinkage model is incorporated into the continuum mechanical model as a hygroscopic strain. Numerical simulations are used to estimate the drying strains in moisture and anisotropy streak examples, and the results are compared with analytical one-dimensional solutions.

The derived hygroexpansivity-shrinkage model is based on the measured relationships between dry paper hygroexpansivity β_d and anisotropy index ϕ

$$\beta_d = k\phi^v \tag{4.1}$$

and between the drying strain ε_d and the dry paper hygroexpansivity

$$\varepsilon_d = -\frac{1}{a}\beta_d + \frac{b}{a}\left(1 - \exp\left(-100\frac{\beta_d}{a}\right)\right) \tag{4.2}$$

where k, v, a and b are fitted constants for freely dried (fd) and restraint-dried (rd) samples made of softwood (SW) or thermomechanical pulp (TMP), or a mixture of those (MIX) displayed in Table 4.1. The measured data and relationships are presented in Fig. 4.1 and in Fig. 4.2; the fitting procedures are described in Publications **IV** and **V**.

Based on the exponential drying shrinkage strain relationship presented in Wahlström et al. (1999) and Wahlström (2004), the following equation for hygroexpansion coefficient can be obtained by

Table 4.1: The fitting parameters of Eq. (4.1) and Eq. (4.2) in the case freely dried (fd) and restraint-dried (rd) samples made of SW, TMP and MIX pulp. Values are from Publication **IV**.

	k (-)	v (-)	a (-)	b (-)
SW fd	0.1557	-0.9809	2.6599	0.0244
SW rd	0.0535	-0.4987	2.6599	0.0244
TMP fd	0.1037	-1.3436	2.9596	0.0249
TMP rd	0.0687	-0.9002	2.9596	0.0249
MIX fd	0.1098	-1.3015	2.5054	0.0250
MIX rd	0.0439	-0.9015	2.5054	0.0250

deriving the drying shrinkage strain function with respect to dry solids content R_{sc}:

$$\beta = \frac{\beta_d}{R_{sc}^2} \exp\left(\frac{\beta_d}{\varepsilon_d}\left(\frac{1}{R_{sc}} - 1\right)\right) \tag{4.3}$$

where β_d is defined by Eq. (4.1) and ε_d by Eq. (4.2). The hygroscopic shrinkage strain in the dry solids content interval $[R_{sc1} R_{sc2}]$ can be expressed as an integral

$$\varepsilon_h = -\int_{R_{sc1}}^{R_{sc2}} \beta dR_{sc}. \tag{4.4}$$

In the continuum mechanical model the equilibrium strain is shifted by the hygroscopic strain $\boldsymbol{\varepsilon_h}$ i.e. Eq. (3.4) takes the form

$$\boldsymbol{\sigma} = \boldsymbol{C}\left(\boldsymbol{\varepsilon} - \boldsymbol{\varepsilon_h}\right). \tag{4.5}$$

In the case of the isotropic sheet, β and ε_h for interval $[0, R_{sc}]$ as a function of R_{sc} are presented in Fig. 4.3 for freely and restraint dried SW, TMP and MIX samples. The dependency of β on ϕ and R_{sc} for freely and restraint-dried MIX samples is presented in Fig. 4.4.

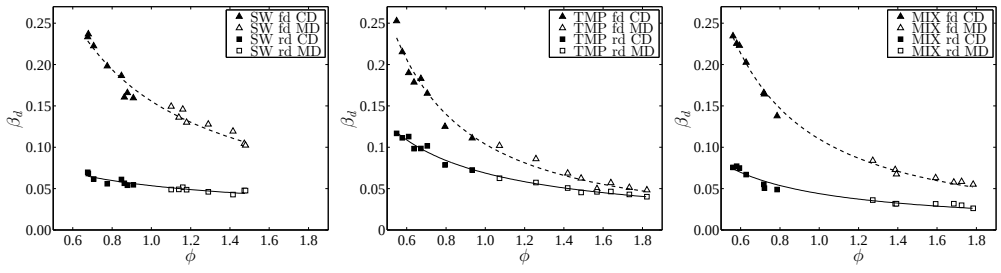

Figure 4.1: Fitted curves for dry paper hygroexpansion coefficient β_d as a function of fiber orientation anisotropy index ϕ. Fittings and measured data from Publication **IV**.

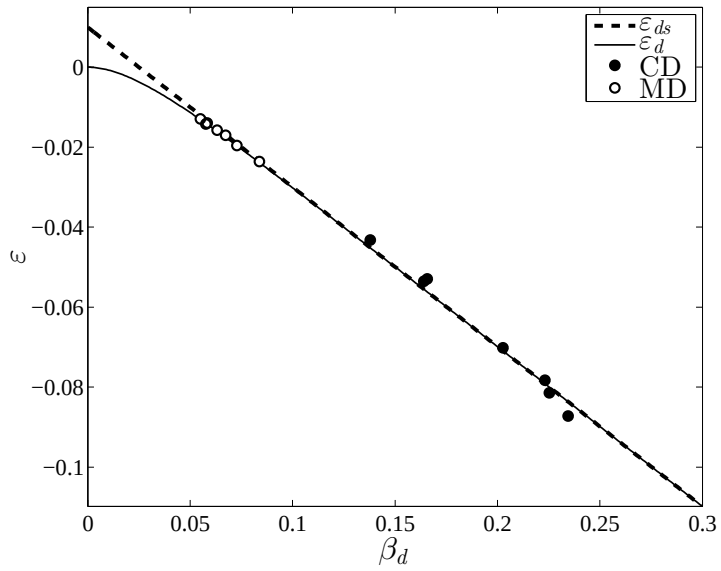

Figure 4.2: The relationship between drying shrinkage strain ε and hygroexpansion coefficient β_d of the dry sample. Measured results of MIX samples are shown for CD (full dots) and for MD (open dots), linear fitting (ε_{ds}) and relationship according to Eq. (4.2) (ε_d). (Publication **V**)

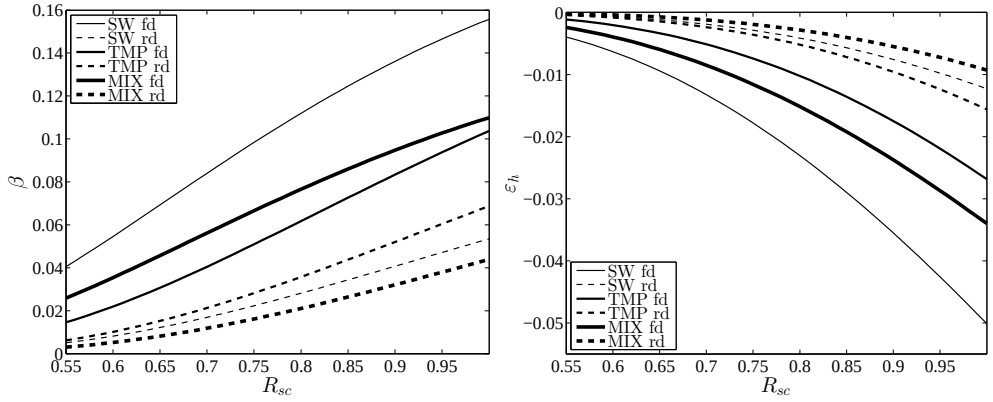

Figure 4.3: Hygroexpansion coefficent β (left) and cumulative drying shrinkage strain ε_h (right) of an isotropic sheet as a function of solids content R_{sc}. (Publication **V**)

Even when the purpose is solely to study the effects of hygroexpansivity through finite element simulations, the results are not independent of the material model. However, the one-dimensional

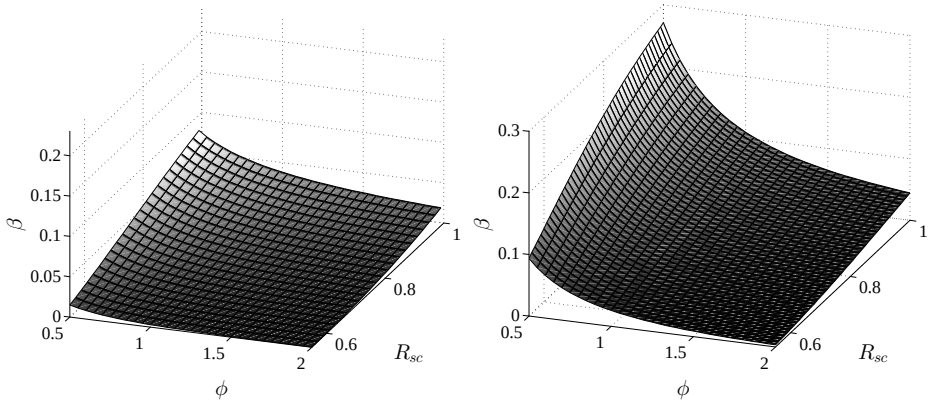

Figure 4.4: The dependence of hygroexpansion coefficient β on the anisotropy index ϕ and dry solids content R_{sc} for restraint dried (left) and freely dried (right) MIX samples. (Publication **V**)

analytical results can be solved directly without any material model using Eq. (4.4). The effect of moisture streaks applied to structurally homogeneous MD orientated sheet were studied using the setup presented in Fig. 4.5. The sample was dried from dry solids content 90% to 91% except in MD streaks, in which no changes were applied i.e. the solids content at those streaks remained at 90%. The drying was performed under MD restraint with unconstrained CD. After drying, the sample was released and left to deform freely. The fitting parameters of the restraint-dried MIX sheet was used in these simulations (see Table 4.1 and Eqs. 4.1 and 4.2). The gradient and topography images, and MD strain profiles are presented in Fig. 4.6. The shrinkage of the dried areas was almost equal between the finite element simulations and the results of the one-dimensionall hygroexpansivity-

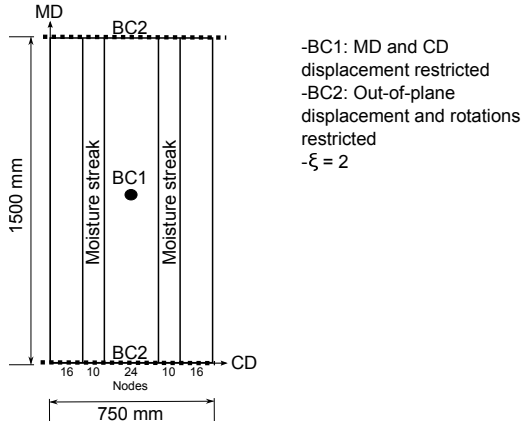

Figure 4.5: The moisture streaks setup for the numerical simulations.

shrinkage model. If in the following step the streak areas are dried equivalently from 90% to 91%, all out-of-plane deformations disappear, the internal stresses are reduced to zero at every position, and the amount of shrinkage is equal everywhere (Fig. 4.6). No plastic deformations arose under such a small stress difference of 808 kPa (tension = 80.8 N/m) in the restraint sample or due to minor shrinkage differences (only 0.022% between the surrounding region and streaks).

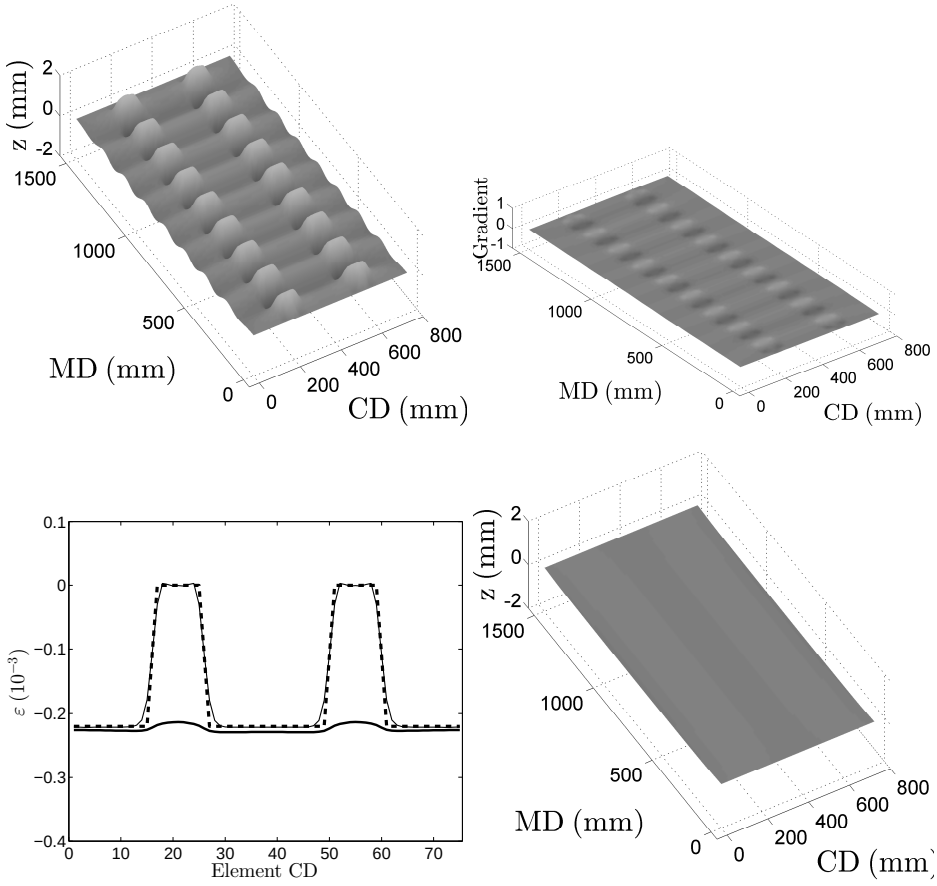

Figure 4.6: Simulated out-of-plane deformations when in the first step the surrounding of the streaks was dried from dry solids content R_{sc} = 0.90 to R_{sc} = 0.91 under MD constraint and then released (upper figures). In the second step the drying is performed to streaks (right below). CD profiles of MD strain after first step are presented in bottom left figure: the in-plane deformation of the simulated sample in MD (solid thick line), the MD strain determined using integrated MD length of the simulated sample (solid narrow line), and the shrinkage strain determined using the analytical one-dimensional model (dashed line). Homogeneous MD oriented structure with anisotropy $\xi = 2$. (Publication **V**)

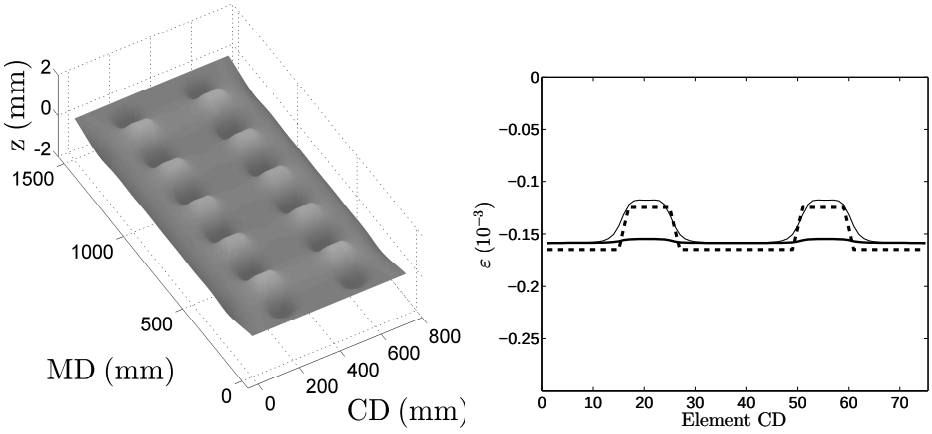

Figure 4.7: Out-of-plane deformations (left) and the CD profile of MD strain (right) after the whole sample was dried from dry solids content R_{sc} = 0.60 to R_{sc} = 0.65. In the streaks the fiber orientation anisotropy $\xi = 2.2$ and in the surrounding regions ξ = 1.8. In the figure on the right: the in-plane deformation of the simulated sample in MD (solid thick line), the MD strain determined using integrated MD length of the simulated sample (solid narrow line), and the shrinkage strain determined using the analytical one-dimensional model (dashed line). (Publication **V**)

Also, anisotropy affects hygroexpansivity, which influence can be illustrated by the following simulation example: a sheet with anisotropy streaks (the setup according to Fig. 3.5) was dried from 60% to 65% dry solids content without any constraints in MD or CD. The out-of-plane deformation and CD profile of the MD shrinkage strains are presented in Fig. 4.7. The higher orientation streaks shrunk less than other areas in the MD, but the strain difference is very small, only 0.0041%. To study the behavior of hygroscopic model without the interference of plasticity, the studied moisture changes were kept low, and all simulated results corresponded well with the result of the one-dimensional hygroexpansivity-shrinkage model.

CHAPTER V

Hygro-elasto-plastic model

The finite element simulation examples, presented in previous chapters, demonstrates the behavior of the material model and the hygroexpansivity-shrinkage model separately, although the finite element simulations of hygroscopic deformations are nevertheless not independent from the material model. To study the combined and interactive phenomena including both the hygroexpansivity and elasto-plasticity, factors of drying and draw, a few examples are presented in this chapter.

Starting with a baseline anisotropy streak case as presented in Chapter III (having dry solids content 60 % and stretched with 1% strain), the different drying conditions was applied in a second step. In the first drying case, the 1% draw was released and the sheet was dried freely from solids content 60% to 65%. This second step was fundamentally equivalent to the anisotropy streak case in Chapter IV, except there are initial plastic strain differences and minor internal stresses at the

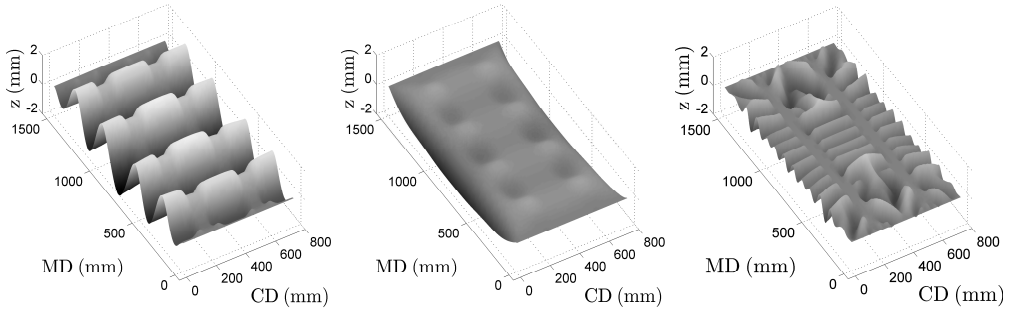

Figure 5.1: Simulated out-of-plane deformation. In the first step the sample was stretched to 0.01 strain in the MD. The strain was released and in the second step sample was freely dried from dry solids content R_{sc} = 0.60 to R_{sc} = 0.65 (left) or from dry solids content R_{sc} = 0.60 to R_{sc} = 0.75 (middle). In the figure on the right, in the second step the sample was dried under MD restraint (0.01 strain) from dry solids content R_{sc} = 0.60 to R_{sc} = 0.65, and then released. In the streaks the fiber orientation anisotropy $\xi = 2.2$; in the surrounding areas ξ = 1.8. (Publication **V**)

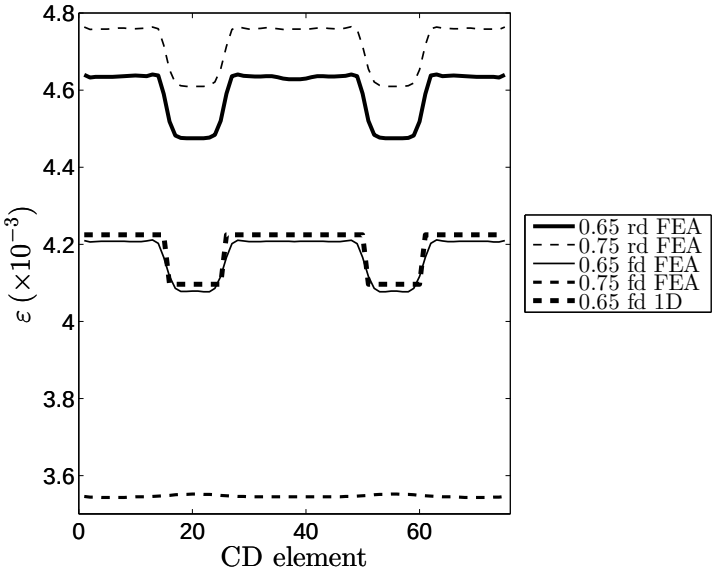

Figure 5.2: CD profiles of MD strains for cases depicted in Fig. 5.1 and in Publication **V** (FEA). Analytical one-dimensional result corresponding of Fig. 5.1 (left) presented by thick dashed line (1D).

streak boundaries. The deformation occurring after this second step is presented in Fig. 5.1 (left). By adding up the CD profile of MD strain solved by one-dimensional approach of the first step (Fig. 3.6, right) and the second step (Fig. 4.7), an equivalent profile is achieved when compared to the finite element solution, as can be seen from Fig. 5.2 (0.65 fd 1D vs. 0.65 fd FEA). When the drying in the second step was continued to a solids content of 75%, almost all deformations arising from streaks disappear (Fig. 5.1 middle), since the MD shrinkage is lower in the streaks having higher anisotropy. A significant change of deformations can be detected if the 1% draw is not released before second step drying. The drying shrinkage increases the MD tension further, resulting in an increase in the plastic strain level, as well as in the difference between the streaks and surrounding in the MD (Fig. 5.2, Fig. 5.1 and Table 5.1). According to a laboratory study by (Land et al. (2008),

Table 5.1: The strains in the streaks and surrounding region from Fig. 5.2. (Publication **V**)

	Streak (%)	Surrounding (%)	Difference (%)
65 fd	0.4075	0.4213	0.0138
75 fd	0.3543	0.3551	0.0008
65 rd	0.4475	0.4647	0.0173
75 rd	0.4609	0.4771	0.0161
One-dimensional	0.4097	0.4225	0.0128

the permanent strain differences arising from moisture streaks are also significantly dependent on the stage of drying in which the tension is released.

In the second example, the homogeneous sample (ξ = 2) was dried freely from a solids content of 80% to 90% or 95%, so that in the first step solids content profiles in the thickness direction were applied through the sample as is presented in Fig. 5.3. The profiles used are roughly based on Östlund's simulations for symmetric convective drying, for details see Östlund (2006). Only the high solids content profile (mean $R_{sc} \approx 0.85$) was used. In the second step, the whole paper achieved a uniform solids content of 90% or 95%. According to the simulations of this study (Fig. 5.3) every tested solids content profile generated the plastic strain differences between layers. The simulated stresses (Fig. 5.3) are same order of magnitude as measured results in Östlund et al. (2004) despite of the different material parameters etc. between the studies. The plastic strains of the layers in the MD and in the CD are presented in Table 5.2. The higher plastic strain in the CD than in the MD resulted from the higher shrinkage tendency and from the different plasticity properties in the CD than in the MD in the anisotropic sheet.

Both examples presented in this chapter were capable of qualitatively estimating the behaviors ob-

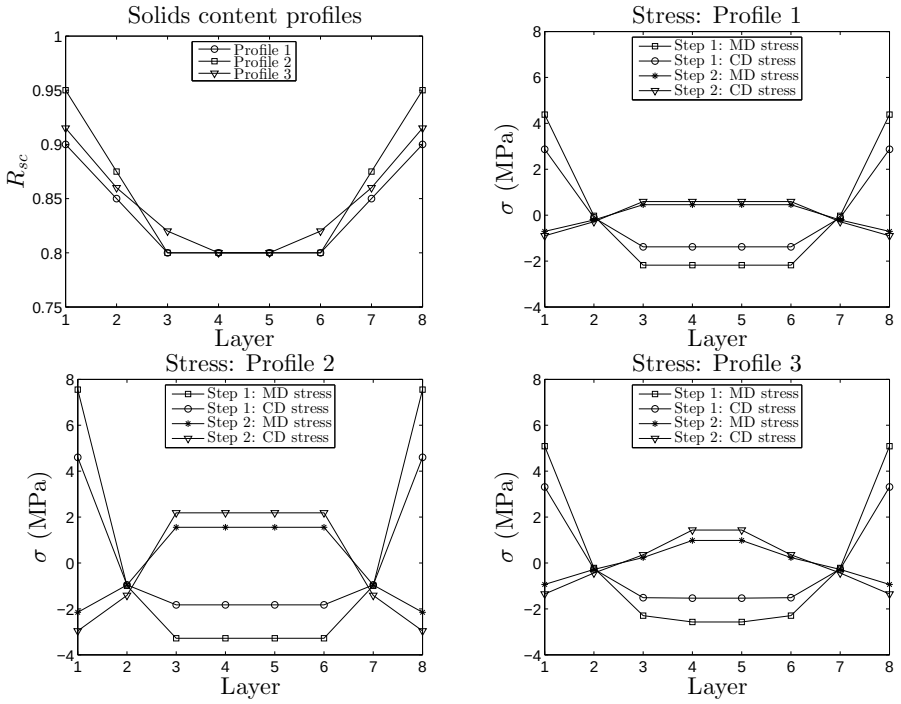

Figure 5.3: The MD and CD stress of different layers, when in the first step different through-thickness solids content profiles (top-left) are applied. In the initial situation solids content trough the sample is R_{sc} = 0.80 and in the second step every layer is dried either to R_{sc} = 0.90 (solids content profile 1) or R_{sc} = 0.95 (solids content profiles 2 and 3). (Publication **V**)

Table 5.2: The plastic strains in the layers from Fig. 5.3. (Publication **V**)

	Profile 1		Profile 2		Profile 3	
Layer	MD (%)	CD (%)	MD (%)	CD (%)	MD (%)	CD (%)
1 and 8	0.0068	0.0418	0.0160	0.0838	0.0084	0.0497
2 and 7	0	0	0	0	0	0
3 and 6	-0.0084	-0.0607	-0.0313	-0.1966	-0.0061	-0.0437
4 and 5	-0.0084	-0.0607	-0.0313	-0.1966	-0.0152	-0.1028

served in experimental studies (Land (2008) and Östlund et al. (2004)). The complexity of the simultaneous effects of the plastic and hygroscopic deformations is clearly demonstrated by these simple examples.

CHAPTER VI

Discussion and future prospects

There are several undesired phenomena that are connected to the hygroscopic and stress-strain behavior of paper or board material during production, converting and printing processes, and in end-use. Under these conditions the paper or board may be treated as a moving web under MD tension, roll, single or bound sheets, boxes, bags, cups, trays, etc. Several defective events concerning these conditions have been studied widely by different experimental and modeling approaches, but still include features that are not known.

The objective of this work was to construct a model capable of capturing the characteristic behavior of hygroscopic orthotropic planar material under moisture content change during different external in-plane stretch or stress conditions. Two independent empirical models were first constructed: the elasto-plastic material model and the hygroexpansivity-shrinkage model. Both models describe the structural properties of the paper or board sheet in terms of fiber orientation probability distribution, and both are functions of the dry solids content and fiber orientation anisotropy index. The anisotropy index, introduced in this work, simplifies the procedure of determining the constitutive parameters of the material model and hygroexpansion coefficients in different in-plane directions of the orthotropic planar material. The mathematically consistent elasto-plastic material model was achieved for a wide range of anisotropies and dry solids contents, even though the bonding mechanisms and rheological behavior in wet and dry paper is different. Usually, the hygroexpansion coefficient has been considered to characterize the deformation of a dry paper subject in a moisture change, independently from the moisture content level, although some stress relaxation and moisture history dependence may have been involved (Uesaka et al. (1992)). In this study, the dry solids content dependent hygroexpansivity, over the entire range from wet to dry, has been proposed. A few different parameters depending on the pulp type of the sample and on the free or restrained drying conditions can be selected for the hygroexpansivity-shrinkage model.

The presented elasto-plastic and hygroexpansivity-shrinkage models, can be used in an analytical approach to estimate the plastic strain and shrinkage in simple one-dimensional cases. For studies of the combined and more complicated effects of hygro-elasto-plastic behavior these two models are implemented in a finite element program for numerical solution of the web or sheet. The finite element approach also included possibilities to study different structural variations of the orthotropic sheet as well as buckling behavior and internal stress situations of a planar sample caused by local or layered strain differences.

A few simulated examples of the effect of anisotropy and moisture streaks on strain differences and

local buckling were presented. In addition, the internal stresses caused by the drying process with different layers drying at different stages, was demonstrated. Very small plastic strain differences may cause local buckling, but how visually disturbing these out-of-plane deformation defects are, depends on the paper or board grade and their usage. The buckling streakiness is considered a defect often called bagginess of the paper web. The baggy paper web may cause the risk of wrinkling, which is reported to increase if the strain difference is higher than 0.1%, although for some thin papers a strain difference of only 0.01% was enough to cause problems (Roisum (1996)). In the examples of this work the strain differences were more in the order of 0.01% than 0.1%. The simulation cases were kept simple and the stretching and dry solids content changes were selected to be small compared to the real total drying process of a paper machine. This enabled to observe the hygroexpansion and plastic strains separately, to compare the analytical and numerical in-plane deformations and to understand the phenomena comprehensively.

The complexity of the interactive and simultaneous behavior of hygroexpansivity and plasticity was revealed even with the simple simulation examples of this study. For example, the streaks having higher anisotropy than their surrounding appear as tight streaks after stretching in MD because of the lower plastic strain in that direction. The free drying performed subsequently to the stretching-releasing procedure may compensate the differences in the plastic strains, because the MD shrinkage tendency of high anisotropy streaks is lower than the surrounding areas. However, if the sample is dried under restraint the lower shrinkage tendency of the streaks may even further increases the plastic strain difference between the streaks and surrounding region. Land's (Land et al. (2008)) experimental study on the effect of the moisture streaks on permanent strain differences also showed that releasing of tension in different stages of drying is a significant factor.

According to the simulation results of this study, both the anisotropy and moisture streaks are capable of making the buckling of the sample visible, and may cause baggy webs and wrinkling. The more challenging task is to determine in which cases the generated strain differences remain as permanent plastic strain differences, perhaps even over the subsequent converting processes; and even further, in which cases they will cause problems during paper making, during the converting processes, or in end-use. Permanency of these defects is highly dependent on several process stages and tension conditions affecting the plastic deformations and their variations in the sheet or web. Some problems related to moisture streaks arising from the drying section may well vanish in the coating or calendaring processes, where moisture or heat is brought to the paper web. Structural streaks, such as anisotropy or basis weight streaks, stay in the paper once formed, and may cause problems at any stage of the paper life cycle.

The application targets of the model can be considered to include several different phenomena in paper or board production processes and in end-use. In the drying section and converting processes, where the paper or board is treated as a moving web, the development of shrinkage profiles, loose edges of web, baggy paper web causing possible wrinkling, and misregistration in printing are examples of factors affecting runnability and end product quality. The structural properties and internal stresses or plastic strain differences which build up during production also cause end-product defects related to distortion of the shape of the product such as sheet or box. Applying the hygro-elasto-plastic model to studies of several of these phenomena can be seen as a natural continuation of research. Some possible simulation cases of the presented model could (and should) be also subjected to the experimental evaluation.

It is challenging to properly define and measure plasticity and viscosity and their interaction as well as their history dependency in paper or a similar material. It is well known that when the loading of

paper is released, both immediate elastic and delayed strain recovery will take place (Rance (1956), Gates and Kenworthy (1963), Skowronski and Robertson (1986)). Nevertheless, the division of total strain into elastic and plastic components is considered to be time-dependent (Skowronski and Robertson (1986), Alava and Niskanen (2006)). The remaining plastic strain depends on the degree of stress, strain rate and time under loading. If all these components are taken into account the amount of parameters and variables which should be determined for a mechanical model is excessive. Moreover, if hygroscopic deformations occur, for example, in a simple moisture change cycle, the definitions of the plastic strain and model will become even more complicated. When complex material such as paper or a similar is studied, the choice of test conditions often determines which interpretations are available in terms of a simple model.

Without the time-dependent behaviors implemented on this hygro-elasto-plastic model either the creep or stress relaxation was not included and in some cases the tensions may increase too high if several process steps are linked consecutively. A part of this problem can be indirectly eliminated by using the hygroexpansivity function for the restraint-dried sheets, which will decrease the stress level because of the lower shrinkage tendency during drying. The objective of a further work could be the expansion of the application possibilities of the model for storage and multi-chained processes by implementing viscoelastic properties and improving history-dependency.

The use of the anisotropy index might bring new possibilities to expand the model for new materials in simple way by using the geometric mean of elastic modulus as a scaling factor for orientation distribution. The application potential of hygro-elasto-plastic model introduced in this study is versatile and includes several phenomena and defects appearing in drying, converting and end-use conditions of paper or board webs or products, or in other corresponding complex plates.

Abe, Y., Sakamoto, A., 1991. Measurement of the z-direction profile of fiber orientation in paper by laser diffraction. Japan Tappi Journal 45 (6), 694–701.

Abe, Y., Todoroki, H., Takeuchi, N., Sakamoto, A., 1995. Method for measuring fiber orientation on paper surface. Japan Tappi Journal 49 (5), 849–860.

Alava, M., Niskanen, K., 2006. The physics of paper. Reports on Progress in Physics 69, 669–723.

Alftan, J., 2004. The effect of humidity cycle amplitude on accelerated tensile creep of paper. Mechanics of Time-Dependent Materials 8 (4), 289–302.

Andersson, O., Berkyto, E., 1951. Some factors affecting the stress-strain characteristic of paper. Svensk Papperstidning 54 (13), 437–444.

Bauer, W., Stark, H., 1988. Über die messung der faserorientierung in einem papierblatt mittels laserstrahlung. Wochenblatt für Papierfabrikation 116 (11), 461–468.

Bloom, F., Coffin, D., 2000. Modelling the hygroscopic buckling of layered paper sheets. Mathematical and Computer Modelling 31 (8–9), 43–60.

Boulay, R., Drouin, B., Gagnon, R., 1986. Measurement of local fibre orientation variations. Journal of Pulp and Paper Science 12 (6), 177–181.

Brezinski, J., 1956. The creep properties of paper. Tappi 39 (2), 116–128.

Carlsson, L., Fellers, C., Htun, M., 1980. Curl and two-sidedness of paper. Svensk Papperstidning 83 (7), 194–197.

Castro, J., Ostoja-Starzewski, M., 2003. Elasto-plasticity of paper. International Journal of Plasticity 19, 2083–2098.

Constantino, R., I'Anson, S., Sampson, W., 2005. The effect of machine conditions and furnish properties on paper CD shrinkage profile. In: Proceedings of 13th Pulp and Paper Fundamental Research Symposium. Cambridge, England, pp. 283–306.

Cowan, W. F., Cowdrey, E. J. K., 1974. Evaluation of paper strength components by short-span tensile analysis. Tappi 57 (2), 90–93.

Craver, J., Taylor, D., 1965. Nondestructive sonic measurement of paper elasticity. Tappi 48 (3), 142–147.

Crosby, C., Eusufzai, A., Mark, R., Perkins, R., Chang, J., Uplekar, N., 1981. A digitizing system for quantitative measurement of structural parameters in paper. Tappi 64 (3), 103–106.

Danielson, R., Steenberg, B., 1947. Quantitative determination of fibre orientation in paper. Svensk Papperstidning 50 (13), 301–305.

de Ruvo, A., Lundberg, S., Martin-Löf, S., Södermark, C., 1976. Influence of temperature and humidity on the elastic and expansional properties of paper and the constituent fibre. In: The Fundamental Properties of Paper Related to Its Uses, Transactions of the Symposium. London, England, pp. 785–806.

Drouin, B., Gagnon, R., 1993. Optical measurement of paper fiber orientation. Optical Engineering 32 (9), 2138–2142.

Enomae, T., Han, Y.-H., Isogai, A., 2004. Fiber orientation distribution of paper surface calculated by image analysis. Journal of Tianjin University of Light Industry 19 (2), 51–57.

Enomae, T., Han, Y.-H., Isogai, A., 2008. Z-Directional distribution of fiber orientation of Japanese and western papers determined by confocal laser scanning microscopy. Journal of Wood Science 54 (4), 300–307.

Erkkilä, A.-L., 1995. Mechanism and measurements of the layered orientation structure of paper sheets, Licentiate Thesis. University of Jyväskylä, Jyväskylä.

Erkkilä, A.-L., Pakarinen, P., Odell, M., 1999. The effect of forming mechanisms on layered fiber structure in roll and blade gap forming. In: Proceedings of Tappi Papermakers Conference. Atlanta, USA, pp. 389–400.

Fahey, D., Chilson, W., 1963. Mechanical treatments for improving dimensional stability of paper. Tappi 46 (7), 393–399.

Fellers, C., Westerlind, B., de Ruvo, A., 1983. An investigation of the biaxial failure envelope of paper – experimental study and theoretical analysis. In: Proceedings of Fundamental Research Symposium. Cambridge, England, pp. 527–559.

Fiadeiro, P., Pereira, M., Jesus, M., Silvy, J., 2002. The surface measurement of fibre orientation anisotropy and misalignment angle by laser diffraction. Journal of Pulp and Paper Science 28 (10), 341–346.

Fleischman, E., Baum, G., Habeger, C., 1982. A study of the elastic and dielectric anisotropy of paper. Tappi Journal 65 (10), 115–118.

Forgacs, O., Strelis, I., 1963. The measurement of the quantity and orientation of chemical pulp fibres in the surfaces of newsprint. Pulp and Paper Magazine of Canada 64 (1), 3–13.

Gates, E., Kenworthy, I., 1963. Effects of drying shrinkage and fibre orientation on some physical properties of paper. Paper Technology 4 (5), 485–493.

Glynn, P., Jones, H., Gallay, W., 1961. Drying stresses and curl in paper. Pulp and Paper Magazine of Canada 62 (1), 39–48.

Habeger, C., Baum, G., 1987. The use of microwave attenuation as a measure of fiber orientation anisotropy. Tappi Journal 70 (2), 109–113.

Haslach, H., 1994. Relaxation of moisture accelerated creep and hygroexpansion. In: Proceedings of the Moisture-Induced Creep Behavior of Paper and Board Conference. Stockholm, Sweden, pp. 121–138.

Hill, H., 1944. Determination of stress-strain relations from "offset" yield strength values. In: Technical Notes National Advisory Committee for Aeronautics, Technical Note No. 927. Washington, USA.

Hill, R., 1948. A theory of the yielding and plastic flow of anisotropic metals. In: Proceedings of the Royal Society of London. Series A, Mathematical and Physical Sciences 191. London, England, pp. 281–297.

Hirn, U., Bauer, W., 2007. Evaluating an improved method to determine layered fibre orientation by sheet splitting. In: Proceedings of the 61st Annual APPITA Conference & 2007 Paper Physics Conference, Vol. 2. Gold Coast, Australia, pp. 71–80.

Hoole, S., I'Anson, S., Ora, M., Ashworth, T., Briggs, D., Phillips, B., Hoyland, R., 1999. CD Shrinkage Profiles of Paper – Experiments on a Commercial Paper Machine. Paper Technology 40 (10), 63–70.

Ivarsson, B., 1954. Introduction of Stress into a Paper Sheet During Drying. Tappi 37 (12), 634–639.

Johnson, M., Urbanik, T., 1984. A nonlinear theory for elastic plates with application to characterizing paper properties. Journal of Applied Mechanics 51, 146–152.

Johnson, M., Urbanik, T., 1987. Buckling of axially loaded, long rectangular paperboard plates. Wood and Fiber Science 19 (2), 135–146.

Johnson, M., Urbanik, T., Denniston, W., 1979. Optimum fiber distribution in singlewall corrugated fiberboard. In: USDA, Forest Service, Research paper FPL No. 348. Madison, USA.

Kallmes, O., 1969. Technique for determining the fiber orientation distribution throughout the thickness of a sheet. Tappi 52 (3), 482–485.

Kärkkäinen, S., Penttinen, A., Ushakov, N., Ushakova, A., 2001. Estimation of orientation characteristic of fibrous material. Advances in Applied Probability 33 (3), 559–575.

Kijima, T., Yamakawa, I., 1978. Effect of shrinkage during drying on dimensional stability of paper. Japan Tappi Journal 32 (10), 584–592.

Kiviranta, A., Pakarinen, P., 2001. New insight into fiber orientation streaks. In: Proceedings of Tappi Papermakers Conference. Cincinnati, USA, p. 7.

Kiyoaki, I., 1987. The computer simulation on a web shrinkage in a paper machine dryer section. Part 1. Elastic modulus and drying force as a function of a web moisture. Japan Tappi Journal 41 (12), 1229–1234.

Kondo, Y., Aidun, C., 2007. Development of method for analyzing internal properties of coated paper : image analysis using x-ray microtomography. Japan Tappi Journal 61 (5), 593–601.

Koskimies, J., 1986. Leaning behaviour of form paper stack. In: Preprints CPPA-TS 72nd Annual Meeting. Montreal, Canada, pp. 123–129.

Kouko, J., Salminen, K., Kurki, M., 2007. Laboratory scale measurement procedure for the runnability of a wet web on a paper machine, part 2. Paper and Timber 89 (7–8), 424–430.

Kulachenko, A., Gradin, P., Uesaka, T., 2005. Tension wrinkling and fluting in heatset web offset printing process – post-buckling analysis. In: Proceedings of 13th Pulp and Paper Fundamental Research Symposium. Cambridge, England, pp. 1075–1099.

Land, C., Wahlström, T., Stolpe, L., 2008. Moisture streaks and their relation to baggy paper webs. Journal of Pulp and Paper Science 34 (4), 234–239.

Larson, P., Wågberg, L., 2008. Influence of fibre-fibre joint properties on the dimensional stability of paper. Cellulose 15 (4), 515–525.

Lavrykov, S., Ramarao, B., Lyne, Å., 2004. The planar transient hygroexpansion of copy paper: experiments and analysis. Nordic Pulp and Paper Research Journal 19 (2), 183–190.

Leppänen, T., Erkkilä, A.-L., Hämäläinen, J., 2008. Effect of fiber orientation structure on simulated cockling of paper. Pulp and Paper Canada 109 (2), 31–38.

Leppänen, T., Erkkilä, A.-L., Jetsu, P., Hämäläinen, J., 2006. Mathematical modelling of moisture induced cockling of a paper sheet. In: Proceedings of PAPTAC 92nd Annual Meeting. Montreal, Canada, pp. 315–320.

Leppänen, T., Sorvari, J., Erkkilä, A.-L., Hämäläinen, J., 2005. Mathematical modelling of moisture induced out-of-plane deformation of a paper sheet. Modelling and Simulation in Materials Science and Engineering 13, 841–850.

Li, Z., Li, K., Camm, C., Chen, Z., 2009. Dimensional stability of paper made from mixtures of BCTMP and kraft fibres. Journal of Pulp and Paper Science 35 (3–4), 123–129.

Lif, J., 2006. Hygro-viscoelastic stress analysis in paper web offset printing. Finite Elements in Analysis and Design 42 (5), 341–366.

Lif, J., Fellers, C., Söremark, C., Sjödahl, M., 1995. Characterizing the in-plane hygroexpansivity of paper by electronic speckle photography. Journal of Pulp and Paper Science 21 (9), 302–309.

Lif, J., Östlund, S., Fellers, C., 1999. Applicability of anisotropic viscoelasticity of paper at small deformations. Mechanics of Time-Dependent Materials 2 (3), 245–267.

Lif, J., Östlund, S., Fellers, C., 2005. In-plane hygro-viscoelasticity of paper at small deformations. Nordic Pulp and Paper Research Journal 20 (1), 139–149.

Lindström, S., Uesaka, T., Hirn, U., 2009. Evolution of the paper structure along the length of a twin-wire former. In: Proceedings of 14th Pulp and Paper Fundamental Research Symposium. Oxford, England, pp. 207–245.

Lipponen, P., Leppänen, T., Kouko, J., Hämäläinen, J., 2008. Elasto-plastic approach for paper cockling phenomenon: on the importance of moisture gradient. International Journal of Solids and Structures 45, 3596–3609.

Lloyd, M., Chalmers, I., 2001. Use of fibre orientation analysis to investigate sheet structural problems during forming. Appita Journal 54 (1), 15–21.

Lu, W., Carlsson, L., 2001. Influence of viscoelastic behavior on curl of paper. Mechanics of Time-Dependent Materials 5, 79–100.

Ludwik, P. (Ed.), 1909. Elemente der Technologischen Mechanic. Springer-Verlag, Berlin.

Lyne, Å., Fellers, C., Kolseth, P., 1996. The effect of filler on hygroexpansivity. Nordic Pulp and Paper Research Journal 11 (3), 152–163.

Lyne, L., Gallay, W., 1954. Fiber properties and fiber water relationships in relation to the strength and rheology of wet webs. Tappi 37 (12), 581–596.

Mäkelä, P., 2009. Effect of drying conditions on the tensile properties of paper. In: Proceedings of 14th Pulp and Paper Fundamental Research Symposium. Oxford, England, pp. 1079–1094.

Mäkelä, P., Östlund, S., 2003. Orthotropic elastic-plastic material model for paper materials. International Journal of Solids and Structures 40, 5599–5620.

Mann, R., Baum, G., Habeger, C., 1980. Determination of all nine orthotropic elastic constants for machine-made paper. Tappi 63 (2), 163–166.

Manninen, M., Kajanto, I., Happonen, J., Paltakari, J., 2011. The effect of microfibrillated cellulose addition on drying shrinkage and dimensional stability of wood-free paper. Nordic Pulp and Paper Research Journal 26 (3), 297–305.

Mendes, A., Park, S., Ferreira, P., Almeida, F., 2011. Hygroexpansivity profiles on a commercial paper machine. Nordic Pulp and Paper Research Journal 26 (3), 312–318.

Meyer, H., 1971. Hydrodynamics of the sheet-forming process. Tappi 54 (9), 1426–1450.

Nanko, H., Wu, J., 1995. Mechanisms of paper shrinkage during drying. In: Proceedings of International Paper Physics Conference (CPPA and Tappi). Atlanta, USA, pp. 103–113.

Nanri, Y., Uesaka, T., 1993. Dimensional stability of mechanical pulps – drying shrinkage and hygroexpansivity. Tappi Journal 76 (6), 62–66.

Neagu, R., Gamstedt, E., Lindström, M., 2005. Influence of wood-fibre hygroexpansion on the dimensional instability of fibre mats and composites. Composites Part A: Applied Science and Manufacturing 36 (6), 772–788.

Niskanen, K., 1993. Anisotropy of laser paper. Paper and Timber 75 (5), 321–328.

Niskanen, K., Sadowski, J., 1989. Evaluation of some fibre orientation measurements. Journal of Pulp and Paper Science 15 (6), 220–224.

Nordman, L., 1958. Laboratory investigations into the dimensional stability of paper. Tappi 41 (1), 23–50.

Osaki, S., 1987. Microwaves quickly determine the fiber orientation of paper. Tappi journal 70 (2), 105–108.

Östlund, M., 2006. Modeling the influence of drying conditions on the stress buildup during drying of paperboard. Journal of Engineering Materials and Technology 128 (4), 495–502.

Östlund, M., Östlund, S., Carlsson, L., Fellers, C., 2004. The influence of drying restraints and beating degree on residual stress build-up in paperboard. Journal of Pulp and Paper Science 30 (11), 289–293.

Page, D., Tydeman, P., 1962. A new theory of the shrinkage, structure and properties of paper. In: Transactions of the Symposium on Formation and Structure of Paper, British Paper and Board Makers' Association. London, England, pp. 397–413.

Parker, J., 1972. The sheet-forming process. In: Tappi stap no.9. Technical Association of the Pulp and Paper Industry. Atlanta, USA.

Parker, J., Mih, W., 1964. A new method for sectioning and analyzing paper in the transverse direction. Tappi 47 (5), 254–263.

Pecht, M., Johnson, M., 1985. The strain response of paper under various constant regain states. Tappi Journal 68 (1), 90–93.

Pecht, M., Johnson, M., Rowlands, R., 1984. Constitutive equations for the creep of paper. Tappi Journal 67 (5), 106–108.

Prager, W., 1942. Fundamental theorems of a new mathematical of plasticity. Duke Mathematical Journal 9, 228–233.

Prud'homme, R., Hien, N., Noah, J., Marchessault, R., 1975. Determination of fiber orientation of cellulosic samples by x-ray diffraction. Journal of Applied Polymer Science 19 (9), 2609–2620.

Radvan, B., Dodson, C., Skold, C., 1965. Detection and cause of the layered structure of paper. In: Consolidation of the Paper Web: Transactions of 3rd Fundamental Research Symposium. Cambridge, England, pp. 189–215.

Ramberg, W., Osgood, W., 1943. Description of stress-strain curves by three parameters. In: Technical Notes National Advisory Committee for Aeronautics, Technical Note No. 902. Washington, USA.

Rance, H., 1954. Effect of water removal on sheet properties. Tappi 37 (12), 640–648.

Rance, H., 1956. The formulation of methods and objectives appropriate to the rheological study of paper. Tappi 39 (2), 104–115.

Rand, J., 1995. A nonlinear viscoelastic creep model. Tappi Journal 78 (7), 178–182.

Roisum, D., 1996. The mechanics of wrinkling. Tappi Journal 79 (10), 217–226.

Ruck, H., Krässig, H., 1958. The determination of fiber orientation in paper. Pulp and Paper Magazine of Canada 59 (6), 183–190.

Rudström, L., Sjölin, U., 1970. A method for determining fibre orientation in paper using laser light. Svensk Papperstidning 73 (5), 117–121.

Sadowsky, J., 1979. Measurement of fiber orientation in paper by optical Fourier transform. Paper and Timber 61 (9), 588–595.

Salmen, L., Fellers, C., Htun, M., 1987. The development and release of dried-in stresses in paper. Nordic Pulp and Paper Research Journal 2 (2), 44–48.

Sampo, J., Takalo, J., Siltanen, S., Miettinen, A., Lassas, M., Timonen, J., 2014. Curvelet-based method for orientation estimation of particles from optical images. Optical Engineering 53 (3), 1–10.

Scharcanski, J., Dodson, C., 1996. Texture analysis for estimating spatial variability and anisotropy in planar stochastic structures. Optical Engineering 35 (8), 2302–2309.

Scharcanski, J., Dodson, C., 2000. Stochastic texture image estimators for local spatial anisotropy and its variability. IEEE Transactions on Instrumentation and Measurement 49 (5), 971–979.

Setterholm, V., Kuenzi, E., 1970. Fiber orientation and degree of restraint during drying – effect of tensile anisotropy of paper handsheet. Tappi 53 (10), 1915–1920.

Silvy, J., 1971. Effects of drying on web characteristics. Paper Technology 12 (5), 377–387.

Skowronski, J., Robertson, A., 1986. The deformation properties of paper: tensile strain and recovery. Journal of Pulp and Paper Science 12 (1), 20–25.

Stamm, A., Beasley, J., 1961. Dimensional stabilization of paper by acetylation. Tappi 44 (4), 271–275.

Steenberg, B., 1947. Paper as a visco-elastic body. Svensk Papperstidning 50 (6), 127–140.

Stenberg, N., Fellers, C., Östlund, S., 2001. Plasticity in the thickness direction of paperboard under combined shear and normal loading. Journal of Engineering Materials and Technology 123, 184–190.

Strömbro, J., Gudmundson, P., 2008. Mechano-sorptive creep under compressive loading – a micromechanical model. International Journal of Solids and Structures 45 (9), 2420–2450.

Suhling, J., Rowlands, R., Johnson, M., Gunderson, D., 1985. Tensorial strength analysis of paperboard. Experimental Mechanics 25 (1), 75–84.

Swift, H., 1952. Plastic instability under plane stress. Journal of the Mechanics and Physics of Solids 1 (1), 1–18.

Takalo, J., Timonen, J., Sampo, J., Marjanen, K., Siltanen, S., Lassas, M., 2014. Evaluation of the orientation distribution of fibers from reflection images of fibrous samples. European Physical Journal: Applied Physics 65 (1), 1–10.

Tausif, M., Duffy, B., Grishanov, S., Carr, H., Russell, S., 2014. Three-dimensional fiber segment orientation distribution using x-ray microtomography. Microscopy and Microanalysis 20 (4), 1294–1303.

Thorpe, J., 1999. Exploring fibre orientation within copy paper. In: Proceedings of the 1999 TAPPI International Paper Physics Conference. San Diego, USA, pp. 447–458.

Tydeman, P., Wembridge, D., Page, D., 1966. Transverse shrinkage of individual fibers by microradiography. In: Consolidation of the Paper Web: Transactions of the Symposium. Cambridge, England, pp. 119–144.

Uesaka, T., 1991. Dimensional stability of paper – upgrading paper performance in end use. Journal of Pulp and Paper Science 17 (2), 39–46.

Uesaka, T., 1994. General formula for hygroexpansion of paper. Journal of Material Science 29 (9), 2373–2377.

Uesaka, T., Kodaka, I., Okushima, S., Fukuchi, R., 1989. History-dependent dimensional stability of paper. Rheologica Acta 28, 238–245.

Uesaka, T., Moss, C., Nanri, Y., 1992. The characterisation of hygroexpansivity of paper. Journal of Pulp and Paper Science 18 (1), 11–16.

Uesaka, T., Murakami, K., Imamura, R., 1980. Two-dimensional linear viscoelasticity of paper. Wood Science and Technology 14, 131–142.

Uesaka, T., Qi, D., 1994. Hygroexpansivity of paper: effects of fibre-to-fibre bonding. Journal of Pulp and Paper Science 20 (6), 175–179.

Urbanik, T., 1982. Method analyzes analogue plots of paperboard stress-strain data. Tappi 65 (4), 104–108.

Urbanik, T., 1995. Hygroexpansion-creep model for corrugated fiberboard. Wood and Fiber Science 27 (2), 134–140.

Voce, E., 1948. The relationship between stress and strain for homogeneous deformation. Journal Institute of Metals 74, 537–562.

Wahlström, T., Adolfsson, K., Östlund, S., Fellers, C., 1999. Numerical modelling of the cross direction shrinkage profile in a drying section: a first approach. In: Proceedings of the 1999 TAPPI International Paper Physics Conference. San Diego, USA, pp. 517–531.

Wahlström, T., 2004. Development of paper properties during drying. In: Ek, M., Gellerstedt, G., Henriksson, G. (Eds.), Paper Products Physics and Technology. Berlin : Walter de Gruyter, pp. 69 – 107.

Wahlström, T., Fellers, C., 2000. Biaxial straining of handsheets during drying – effects on in-plane mechanical properties. Tappi Journal 83 (8), 1–8.

Wahlström, T., Lif, J., 2003. Dryer section simulator for laboratory investigations of shrinkage profile. In: Proceedings of International Paper Physics Conference (PAPTAC). Victoria, Canada, pp. 169–173.

Waterhouse, J., Stera, S., Brennan, D., 1987. Z-direction variation of internal stress and properties in paper. Journal of Pulp and Paper Science 13 (1), 33–37.

Xia, Q., Boyce, M., Parks, D., 2002. A constitutive model for the anisotropic elastic-plastic deformation of paper and paperboard. International Journal of Solids and Structures 39, 4053–4071.

Xu, L., Parker, I., Filonenko, Y., 1999. A new technique for determining fibre orientation distribution through paper. In: Proceedings of the 1999 TAPPI International Paper Physics Conference. San Diego, USA, pp. 421–427.

Yeh, K., Considine, J., Suhling, J., 1991. The influence of moisture content on the nonlinear constitutive behavior of cellulosic materials. In: Tappi Proceedings: 1991 International Paper Physics Conference. Havaii, USA, pp. 695–711.

Yuhara, T., Hasuike, M., Murakami, K., 1991. Fibre orientation measurement with the two-dimensional power spectrum of a high-resolution soft x-ray image. Journal of Pulp and Paper Science 17 (4), 110–114.

PART II: PUBLICATIONS

PUBL. I

A.-L. Erkkilä, P. Pakarinen and M. Odell, Sheet forming studies using layered orientation analysis, *Pulp & Paper Canada*, 99(1), 81-85, 1998.

Sheet forming studies using layered orientation analysis

Can lead to a better understanding of the drainage process

By A.-L. Erikkilä, P. Pakarinen and M. Odell

THE DRAINAGE in the dewatering zone of a paper machine is the main factor in controlling the paper structure. Depending on the state of fibre mobility in suspension, drainage may proceed by thickening or filtration [1,2]. In practice both of these mechanisms occur, however, filtration is normally the dominant process. During filtration each individual fibre layer is formed separately. The exact nature of how each layer was formed is governed by the conditions of the flow field that were prevailing as that layer was drained.

During drainage, orientated shear occurs between the unformed suspension and the wire/fibre mat which produces paper with an orientated structure. This elementary mechanism can be described by a simple theory of inclined filtration [2,3,4]. By means of this theory, the degree of fibre orientation (anisotropy), as well as the misalignment angle (deviation) for each individual layer, can be calculated by varying both the shear and dewatering velocity of the suspension.

Because of the importance of the drainage process, much experimental [5-7] and theoretical [4,8,9] research work has been applied to this field worldwide. From a theoretical standpoint, the flow dynamics of fibre suspensions during drainage is known to be very complex since it involves varying pressure pulses [10] influencing water removal through a compressible porous fibre mat [11,12]. If mathematical models are used, cumbersome boundary conditions will cause convergence difficulties in the calculation procedure. Moreover, these models often only deal with a single dewatering element, such as a forming roll, and therefore do not describe the whole drainage process. Also, some of these models include empirical factors which must be fixed by experimental measurements. In any event, experimental measurements are needed in this type of work, also, to measure the performance of any kind of mathematical model.

The nature of fibre suspensions is such that complete experimental measurements are impossible to make. The present state of the art in fibre suspension measurement is such that there are various techniques (often experimental) that permit the previously inaccessible flow patterns in a twin-wire nip to be investigated to a limited extent.

In order to avoid some of these difficulties this paper introduces an alternative method to study the sheet forming process. The idea is based on the fact that the paper sheet carries information about the drainage process in the form of the orientation characteristic of each layer. For these studies an optical method to determine the layered orientation distribution of a paper sheet has been developed [13]. Layered orientation measurements of paper have also been reported by Eguchi *et al.* [14].

The method introduced in this paper has turned out to be rather useful in analysing the layered structure from different types of formers under varying process conditions. When the layered anisotropy and misalignment angle parameters are included in a simple theory of inclined filtration, the suspension flow dynamics for the drainage of each layer can be determined. By means of this technique it is possible to gain some further insight into the forming process. However, complete analysis would still require measurements of dewatering flow velocity, consistency and turbulence during the drainage process.

INCLINED FILTRATION

Orientated shear causes an orientated fibre distribution in each layer of paper. Conversely, the result of turbulence during drainage is to increase randomness and so reduces the effects of orientated shear. Total randomness is an idealized condition; in real flows some degree of preferred orientation always exists.

$$\tan\theta = \frac{v}{u - u_w} \qquad (1)$$

The basic relationship between orientated shear and fibre orientation of paper was stated by Lund as early as 1934 [2]. As drainage occurs, one end of an individual fibre or fibre floc becomes anchored in the thickening fibre mat. The other relatively mobile end, one that projects into the shear field, is dragged in the direction of shear flow immediately before it becomes immobilized in the fibre mat. As a result, the fibres acquire a preferred orientation in this direction [3]. This process is known as the theory of inclined filtration — schematically illustrated in Fig. 1. It can be represented as a pair of coupled equations for each fibre layer as follows

$$e = k_1\cos\varnothing = k_1 \frac{\sqrt{w^2 + (u - u_w)^2 + v^2}}{w} \qquad (2)$$

where θ is the orientation deviation angle from the machine direction and e defines the anisotropy of fibre orientation as the ratio of major to minor axes of the orientation distribu-

A.-L. ERKKILÄ,
VTT, Technical Research Centre of Finland, Jyväskylä, Finland

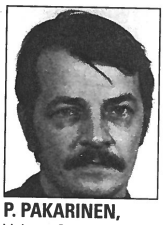

P. PAKARINEN,
Valmet Corp., Jyväskylä, Finland

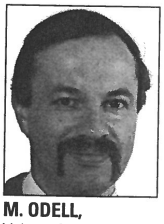

M. ODELL,
Valmet Corp., Jyväskylä, Finland

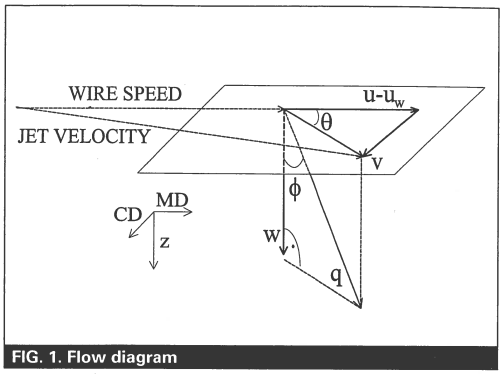

FIG. 1. Flow diagram

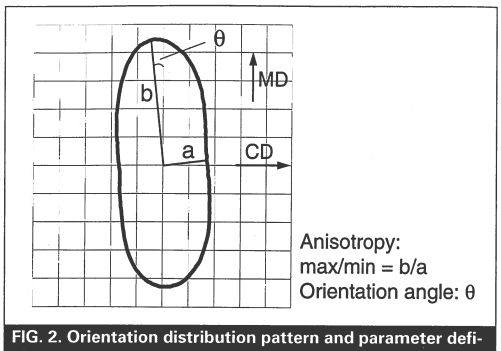

FIG. 2. Orientation distribution pattern and parameter definition.

tion ellipse. The velocity of suspension flow during filtration is denoted by q having components (u, v, w) in the machine, cross and z directions, respectively, and the wire velocity u_w. Equation 2 also includes an adjustable parameter k_1 that characterises the linear relationship between the measured axis ratio of the distribution pattern and the velocity ratio w/q = cos ø, where ø is the projecting angle of fibres into the shear field.

For $(u - u_w) \neq 0$, equation (1) and (2) can be combined to give

$$e = k_1 \sqrt{1 + \left(\frac{u - u_w}{w \cos\theta}\right)^2} \qquad (3)$$

Equation (3) connects the measured anisotropy of each layer to the unknown ratio of velocity components $(u - u_w)/w$. By means of equation (3) it can be clearly seen that the anisotropy e decreases with increasing dewatering velocity w and with decreasing velocity difference $(u - u_w)$. In order to separate these two, further information about the filtration process is needed. Dewatering flowrate measurements along the drainage zone gives one possibility. In continuum form this relationship can be stated simply as

$$Q'(x) = w(x) \qquad (4)$$

where Q'(x) denotes a change in flowrate (derivative) at the point x, which is defined as a co-ordinate along drainage line. If twin-wire filtration is considered, each wire side has to be treated separately. The relationship between the co-ordinate x along the drainage line and the layer of the paper can be fixed by the formula, which gives an accumulated basis weight G(x) during filtration. In continuum form this can be presented as follows

$$G(x) = \frac{c_p}{u_w} \int_x R(x) w(x) dx \qquad (5)$$

where c_p denotes a consistency of suspension in the headbox and R(x) denotes a local value of retention.

MEASURING METHOD

To experimentally determine orientation angle q and anisotropy for each layer, the original sheet must be reduced to its individual layers. This is done by the tape-stripping technique. The size of each strip is 50 mm by 200 mm. The sheet is first split in two parts by double-sided tape and then the individual layers are split from both of these halves by one-sided inextensible lucid tape. The grammage of each layer is measured in splitting. Typically an 80-gsm printing paper of 100 microns thickness can be stripped to 10 to 12 individual layers between five and 15 gsm. Each layer is placed against dark background and illuminated by an annular fluorescent tube. Two images (30 mm by 30 mm in size) are obtained from each layer by high resolution video camera and the result is digitized and calculations performed by a PC. The fibres and fibre bundles are distinguished lighter against the dark background. In image analysis, intensity variations are sharpest at fibre boundaries. This result is used in the form of gradients to establish the magnitude and direction of fibres in every image element (640 by 640 elements).

By plotting the result for each layer using polar co-ordinates, an ellipse-type fibre orientation distribution pattern is obtained. Parameters such as anisotropy and orientation angle can be determined from the shape of the distribution pattern, as presented in Fig. 2. Anisotropy is defined as the ratio of major to minor axes of the distribution pattern ellipse. Orientation angle is defined as the deviation angle of the main orientation of pattern from the machine direction (MD). The sign rules for orientation angles are as follows: positive angles are defined to be left of MD, negative to the right of MD, when looking onto the paper's top side.

LAYERED ORIENTATION

Layered anisotropy of commercial paper samples, manufactured by three different former types all operating in rush, are compared in Fig. 3. The values of anisotropy are plotted as a function of grammage percentage from bottom to top side of paper.

In the Fourdrinier case, the shape of the anisotropy profile decreases in magnitude from bottom to top side. This kind of behavior is well-known for Fourdrinier machines which show strong orientation two-sidedness. The measured layered anisotropy indicates a decreasing oriented shear during drainage.

Under rush conditions the fibre suspension velocity is progressively decreasing to match that of the wire as the suspension is carried along the wire. This occurs because of energy losses caused by dewatering impulse, viscous and air drag forces. In spite of this the anisotropy for the extreme bottom surface shows a lowered tendency. This is caused by the high initial dewatering rate over the forming board and first foils. Also the level of initial turbulence from the jet has an effect on orientation in the initial drainage stage.

In gap forming, the anisotropy profile is found to be symmetric between bottom and top side. This behavior can be explained by the fact that dewatering through both wires is symmetric enough to produce paper with minimum orientation two-sidedness.

In the gap forming example considered here, the jet impinges into a curved gap created by the convergence of two wires around a roll. The static pressure which is created in the gap by wire tension, is responsible for the outwards dewatering (bottom side in this example). Dewatering toward the roll (top side) is influenced also by vacuum. Drainage after the roll is mostly toward the bottom side over a series of blades, under the influence of vacuum. As the jet impinges in the gap the velocity of suspension slows down in the pressure field of the gap [15]. This explains the shape of the anisotropy profile with a local minimum in the centre of the sheet since this area is formed last

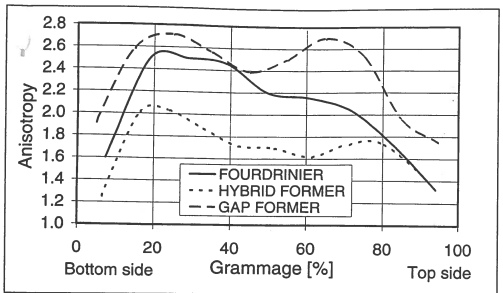

FIG. 3. Former comparison in rush.

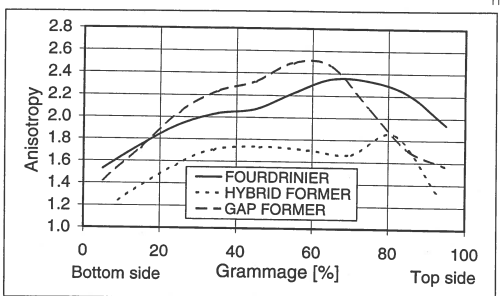

FIG. 4. Former comparison in drag.

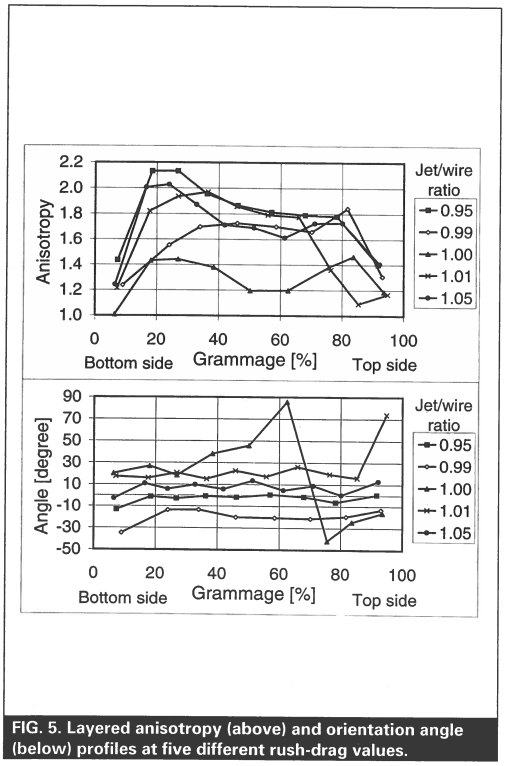

FIG. 5. Layered anisotropy (above) and orientation angle (below) profiles at five different rush-drag values.

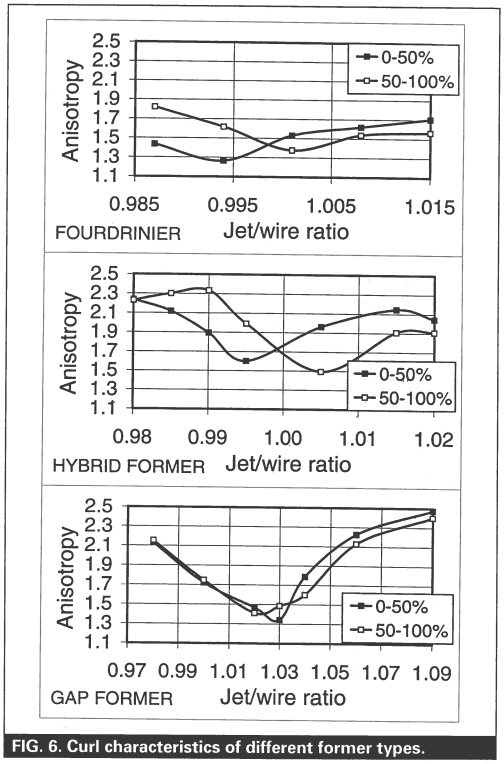

FIG. 6. Curl characteristics of different former types.

under conditions of minimum suspension velocity (or orientated shear). Also both surfaces show a lowered level of anisotropy. This is due to the high initial dewatering velocity and can also be influenced by the jet's initial turbulence level.

In hybrid forming the initial dewatering is similar to that of the Fourdrinier case. Thus, the bottom two-thirds of the anisotropy profiles are also similar. The hybrid unit drains the top (approximately one-third) of the sheet with a high dewatering rate, low turbulence level and some degree of orientated shear depending which type of hybrid former. The net result is an anisotropy profile, which has in the bottom two thirds, characteristics of a Fourdrinier but the top third shows characteristics of a gap former.

The drag side case has also been studied. The shapes of the layered anisotropy profiles are presented in Fig. 4 and have quite a different nature compared to the rush situation in Fig. 3.

In the Fourdrinier case the anisotropy profile has an increasing tendency toward the top side. This indicates that the velocity of the pulp suspension is decreasing while travelling down the wire. However, near the top surface, the level of anisotropy has a slight decreasing tendency which indicates that in the final phase of drainage the pulp suspension is accelerated toward the wire velocity possibly due to an increase in top surface viscosity. In general terms, the drag side anisotropy profile shows an inverse tendency compared to the rush situation.

In gap forming there is a very signifi-

cant difference in the layered anisotropy profiles between the rush and drag cases. In drag the centre of the sheet has the maximum anisotropy, whereas in rush there is a local minimum. This indicates that in drag the suspension velocity continually decreases during dewatering. There is no evidence of any acceleration effect caused by the wires, as might be expected. It is possible that the boundary layers necessary to transmit shear are not formed in the rapid initial dewatering phase so the energy transfer from wire to suspension is minimal. It is significant to note that only in the gap former case is the anisotropy profile symmetric around the sheet centre line in both rush and drag situations — i.e., exhibits minimal orientation two-sidedness regardless of the jet-to-wire ratio.

In hybrid forming the shape of the anisotropy profile is again a combination of the Fourdrinier and gap former drag side cases.

RESPONSE TO CHANGE

The speed difference between the headbox jet and the wire is one of the most important papermaking process control factors. Paper structure and many paper properties are very sensitive to adjustments in the jet-to-wire ratio. The following discussion focuses only on the response of the layered orientation structure to jet-to-wire ratio for the hybrid former case.

The layered anisotropy and corresponding orientation angle profiles are shown in Fig. 5. Five different jet-to-wire ratio values have been used in this case. In rush side forming the absolute level of anisotropy decreases as the jet-to-wire ratio decreases from 1.05 to 1.01 as predicted from equation 2. In particular the anisotropy shows very low values near the top surface which indicates that quite rapid drainage has taken place under conditions of low speed difference between pulp suspension and top fabric. Correspondingly, the values of the layered orientation angles tend to increase as predicted by equation 1. The orientation angle for the outermost top layer reaches the rather extreme value of +70 degrees.

In the case of the jet-to-wire ratio equal to 1.0 the lowest average level of anisotropy is obtained. However on the top surface the values start to increase compared to the situation at ratio 1.01. Also the signs of the orientation angles are reversed in the top layers. Both of these factors indicate that at the unity point (ratio 1.0) the bottom surface was formed in rush but the top surface in drag. Behavior close to the unity point is rather unstable with high absolute orientation angles and reversed signs through the sheet thickness. According to equation 1, when operating near the unity point (i.e., $(u - u_w) \approx 0$), the values of orientation angles can in theory reach 90°. These experimental results indicate that this extreme behavior does occur in practice.

When decreasing the jet-to-wire ratio down to 0.99, the whole sheet exhibits drag side behaviour. The level of anisotropy is increased and the orientation angles reverse in sign. Finally, at a jet-to-wire ratio of 0.95, which is extreme drag side forming, the absolute values of the orientation angles approach zero while the values of anisotropy indicate a high level of orientation as predicted by theory (equations 1 and 2).

ANALYSIS OF TWO-SIDEDNESS

In printing and converting processes, a high level of orientation two-sidedness is an undesirable property that adversely effects the functional behavior of paper — mostly resulting in curl. A practical way to study the two-sidedness of orientation is to present the results of layered orientation analysis (anisotropy and angles) as average values for each half of the sheet. In averaging, the weighted mean by basis weight of each layer is used.

In Fig. 6 the averaged anisotropy for the top and bottom halves of the sheet are presented as a function of the jet-to-wire ratio for three different formers. It should be noted that the jet-to-wire ratio scale is different for each former type (Fourdrinier, hybrid and gap) according to their normal range of operating conditions. The orientation two-sidedness as a function of jet-to-wire ratio is effectively a structural curl tendency characteristic. There are significant differences in the structural curl characteristic of these three former types.

The difference between top and bottom side orientation changes significantly as a function of jet-to-wire ratio in both the Fourdrinier and hybrid former cases. The minimum anisotropy for each of the top and bottom sides occur at different jet-to-wire ratios. The minimum for the bottom half occurs in drag and for the top half in rush. Consequently, there are only rather narrow bands of jet-to-wire ratio where it is possible to achieve minimal orientation two-sidedness (i.e., minimum structural curl tendency). Considering that many other paper properties in addition to orientation two-sidedness are influenced by the jet-to-wire ratio, this type of curl characteristic restricts the possibility to optimise paper quality.

In gap forming, however, the orientation difference between top and bottom sides remains relatively small over the full operating range of jet-to-wire ratio. This is because in this former configuration both sides of the sheet experience the same amount of shear and have similar dewatering rates and initial turbulence levels. This characteristic has a significant advantage in that the structural curl tendency does not depend on the jet-to-wire ratio and so other important paper properties can be better optimized than in the Fourdrinier or hybrid former cases. In any event the final curl tendency remains the net result of the structural curl tendency and other curl control factors such as after-dryer steam pressure ratio, size application and press configuration.

Another point of interest in these curves is that the level of anisotropy does not continue to increase to its theoretical limit as the level of applied shear (jet-to-wire ratio) increases, as would be predicated by equation 3. The anisotropy function eventually levels off to some asymptotic value. It is possible that this behavior is due to the formation of a turbulent boundary layer at the interface between the unformed suspension and fibre mat under conditions of high shear. This turbulence then interferes with the simple drainage mechanism by which the degree of anisotropy should increase continuously with increasing shear.

CONCLUSIONS

The optical orientation measuring method described in this paper allows the magnitude and direction of orientation for each layer to be determined. These results together with a simple theory of inclined filtration have been a useful means to gain further insight into the sheet forming mechanism. By means of this theory the orientated filtration of fibres are explained solely by velocity components in machine, cross and z-directions. The main shortcoming with this theory is that it does not explicitly take account of turbulence, which can in practice play an important role in determining orientation behavior. However, the effect of turbulence is included in the measured orientation parameters that have been used to describe the sheet forming mechanisms. Another drawback of the simple theory of inclined filtration is its failure to predict the levelling off of anisotropy level as shear is increased.

To consider curl tendency, a symmetric structure of orientation with respect to the centreline of sheet thickness, is desirable. As pointed out in this work, such symmetry can be achieved by gap forming over a wide range of jet-to-wire ratios. However, it should be noted that a symmetric structural curl tendency alone does not guarantee paper will not curl. The z-direction distributions of fillers, fines, density and the like, together with considerations of the dried-in stresses caused by the drying process, all influence the curl tendency. Therefore, a symmetric curl structure is a necessary but not sufficient condition to avoid paper curl.

The layered orientation measuring technique results have more uses than just for verification of mathematical models of dewatering. The study of layered orientation and the mechanisms behind it have proven to be useful tools to troubleshoot and control the orientation in the sheet

thickness in production machines. These results have also been influential in considerations of forming section design.

ACKNOWLEDGEMENT

For the purpose of this work, an optical method to measure layered orientation of a paper has been developed by joint cooperation between VTT and Valmet. Thereby one of authors, Ms. A.-L. Erkkilä, wishes to thank her colleagues at VTT and Valmet RTD for valuable discussions during her Lic. Thesis work.

REFERENCES

1. RADVAN, B., DODSON, C. and SKOLD, C. G. Consolidation of the Paper Web. Ed F. Bolam. Tech. Sec., British Paper and Board Makers' Assoc. London, 189-214 (1966).
2. PARKER, J. D. The Sheet-Forming Process. TAPPI Stap no.9. Tech. Assoc. of the Pulp and Paper Industry. Atlanta, GA, 99 (1972).
3. RYTI, N., AALTONEN, P., PERTTILÄ, T. and TALJA, M. Device for the Production of Fibre-Oriented Laboratory Handsheets. *Paperi ja puu* 51(3): 207-212 (1969).
4. MEYER, H. Hydrodynamics of the Sheet-Forming Process. *Tappi J.* 54(9): 1426-1450 (1971).
5. HERGERT, R. E. and SANFORD, C. L. Pressure Measurements In The Forming Zone of a Twin Wire Machine. *Pulp Paper Can.* 85(6): T134-T137 (June 1984).
6. KEREKES, R. J. and McDONALD, J. D. A Decreasing Permeability Model of Wet pressing. 76th Annual Meeting, CPPA, Tech Section, Montreal, B173-B179 (1990).
7. INGMANSON, W. L. and WHITNEY, R. P. The Filtration Resistance of Pulp Slurries. *Tappi J.* 37(11): 523-534 (1954).
8. KOSKIMIES, J. PERKINEN, J., PUOLAKKA, H. and SCHULTZ, E., WAHLSTRÖM, B. A Drainage Model for the Forming Zone of a Two-Wire Former. *Paperi ja Puu* 57(4a): 137-146 (1972).
9. EMMONS, H. W. The Continuum Properties of Fiber Suspensions. *Tappi J.* 48(12): 679-687 (1965).
10. NORDSTRÖM, B. and NORMAN, B. Development of STFI-former. *Nordic Pulp and Paper Research J.* (3):176-181 (1994).
11. SAYEGH, N. N. and GONZALEZ, T. O. Compressibility of Fibre Mats During Drainage. *JPPS* 21(7): J255-J261 (1995).
12. MANTAR, E., CO, A. and GENCO, J. M. Drainage Characteristics of Pulp Slurries under Dynamic Conditions. Proc. TAAPI Engineering Conf., Orlando, September 1993, 477-483.
13. ERKKILÄ, A.-L. Mechanisms and Measurements of the Layered Orientation Structure of Paper Sheets. Lic. Thesis. University of Jyväskylä, Department of Physics, Jyväskylä 1995 (in Finnish).
14. EGUCHI, A., TAJIMA, T., FUJITA, N. and MAKINO, T. Flow Characteristics in a Headbox and Fiber Orientation of Paper. *Japan Tappi J.* 47(11): 79-89 (1993).
15. NORMAN, B. Principle of Twin-Wire Forming. *Svensk Papperstidning* 82(11): 330-336 (1979).

Résumé: La structure stratifiée d'une feuille de papier contient des données sur la dynamique de l'écoulement des suspensions fibreuses durant le processus de formation de la feuille. Notre article examine de quelle façon le procédé d'égouttage peut être étudié au moyen de l'analyse de l'orientation des couches de la feuille de papier. À cette fin, nous avons développé une méthode fondée sur l'analyse des images des bandes de papier stratifiées afin de mesurer l'anisotropie et les angles d'orientation dans chaque couche. En nous servant de la simple théorie de la filtration inclinée et des mesures du taux d'essorage, nous évaluons, durant la formation de la feuille, les mécanismes hydrodynamiques comme le cisaillement orienté. Il résulte que nous pouvons étudier la réponse des différentes sections de formation et les paramètres ajustables du procédé qui influencent la structure d'orientation des couches. Nous faisons état par ailleurs de comparaisons entre les résultats de différentes études de vraie grandeur dans des conditions normales d'exploitation et de certains essais réalisés en usine pilote.

Abstract: The layered structure of a paper sheet contains information about the flow dynamics of the fibre suspension during the sheet forming process. This work discusses how the drainage process can be studied using analysis of the layered orientation of the paper sheet. For this purpose a method based on image analysis of layered paper strips, has been developed to measure the anisotropy and orientation angles in each layer. By using a simple theory of inclined filtration together with dewatering rate measurements, the hydrodynamic mechanisms like orientated shear can be estimated during the sheet forming. As a result, the response of different forming sections, as well as the adjustable process parameters influencing layered orientation structure, can be studied. This review includes comparisons of results between different mill scale studies in normal running conditions together with some pilot plant trials.

Reference: ERKKILÄ, A.-L., PAKARINEN, P., ODELL, M. Sheet forming studies using layered orientation analysis. *Pulp Paper Can* 99 (1): T39-43 (January 1998). Paper presented at the 82nd Annual Meeting, Technical Section, CPPA, in Montreal, QC, on January 30 to February 2, 1996. Not to be reproduced without permission. Manuscript received January 17, 1996. Revised manuscript approved for publication by the Review Panel on May 14, 1997.

Keywords: SHEET FORMING, DRAINAGE, IMAGE ANALYSIS, ANISOTROPY, ORIENTATION, LAYERS.

PUBL. II

P. Lipponen, A.-L. Erkkilä, T. Leppänen and J. Hämäläinen, On the importance of in-plane shrinkage and through-thickness moisture gradient during drying on cockling and curling phenomena, *Transactions of the 14th Fundamental Research Symposium*, 389-436, 2009.

ON THE IMPORTANCE OF IN-PLANE SHRINKAGE AND THROUGH-THICKNESS MOISTURE GRADIENT DURING DRYING ON COCKLING AND CURLING PHENOMENA

P. Lipponen[1], A.-L. Erkkilä[2], T. Leppänen[1] and J. Hämäläinen[1]

[1]University of Kuopio, Department of Physics, P.O.Box 1627 FI-70211 Kuopio, Finland
[2]Metso Paper, Inc., P.O. Box 587 FI-40101 Jyväskylä, Finland

ABSTRACT

Cockling and curling are unwanted phenomena that occur already in the manufacturing process and continue through the end use of paper due to moisture content changes. This paper compares the effects of different in-plane tensions and through-thickness drying profiles during the drying process on cockling and curling by means of finite element simulations. In this study, paper is treated as a heterogeneous orthotropic elasto-plastic material. The results predict that finding the optimal way to dry paper is not straightforward; it also depends on fiber orientation structure. On the other hand, defects in the fiber orientation structure of paper can be redressed at some level by drying the paper appropriately.

Keywords: Cockling; Curling; Drying; Paper; Layered fiber orientation; Finite element analysis; Elasto-plasticity

1 INTRODUCTION

Paper goes through a significant metamorphosis between the headbox and reel, changing its state from a wet dilute suspension to a dry end product. The total magnitude of change in the dry solids content of paper approaches one hundred percentage points on a paper-making line, and the change occurring at the dryer section may exceed fifty percent. Due to its heterogeneous nature, paper exhibits non-uniform local moisture expansion behaviour, and therefore also significant cockling and curling tendencies during and after drying.

Drying-related out-of-plane deformations of paper, especially cockling and curling phenomena, have been studied for decades; see e.g. [1, 2, 3, 4]. Although a great amount of research has concentrated on studying the relationship between drying and out-of-plane deformations, the direct effect of through-thickness drying conditions on cockling and curling phenomena has remained unknown. The method presented by Lipponen *et al.* in [5, 6, 7] provides a basis for analyzing how drying and out-of-plane behaviour relate to each other.

Other factors affecting the paper cockling phenomenon have also been widely studied, and especially local inhomogeneity [8], fiber orientation [8, 9], formation [10, 11], bending stiffness [2] and temperature [2, 12] have been noted to affect cockling. However, this study concentrates purely on modelling the shared effects of in-plane tensions during drying, through-thickness drying profile (based on profiles simulated at VTT (Technical Research Centre of Finland)), and sheet fiber orientation structure (measured by Metso Paper, Inc., see Section 2). Besides these issues, the remoisturizing phenomenon (to study how harmful curling can be straightened out after the dryer section) and sensitivity analysis of some parameters are also considered.

The fiber orientation measurements underlying the modelling are described in Section 2. Section 3 presents the modelling approach. This section also includes the drying profiles and CD tensions used in simulations. The numerical implementation of the modelling approach, as well as the boundary conditions used, is discussed in Section 4. Numerical simulations performed are presented in Section 5. A sensitivity analysis on a few primary parameters is also briefly discussed in Section 5. Discussion and concluding remarks concerning the model, and the findings are provided in Section 6.

2 LAYERED FIBER ORIENTATION MEASUREMENTS

The layered fiber orientation measuring method used has been proved to be valuable tool both for the study of paper forming conditions at the wet end of a paper machine [13, 14] and for estimating the structure based cockling tendency of paper sheet [15]. Since the measuring technique is introduced only briefly in references [13, 14], in this paper the layered orientation measuring method is presented in more detail, including the latest improvements in digitizing and sheet splitting techniques.

The method employed is based on sheet splitting and image analysis of the resulting layers. Good tape stripping requires uniform and appropriate tape adhesion. Splitting quality is also affected by the pressure applied during bonding and ambient air conditions. Furthermore, the tape applied should be non-stretching. The cockling simulation approach used benefits the analysis of at least almost size A4 sheet. The equipment used for measurement in this case consists of Brother LC-9L2R 23 cm × 20 m cold laminating tape and a GBC 3500 Pro Series laminating machine, although some other tape and laminator combination might has satisfied the above requirements as well.

Samples are conditioned and the whole splitting procedure is carried out under standard atmospheric conditions (RH = 50% ± 2%, T = 23°C ± 1°C). The tape splitting process starts with cutting and weighing the sheet (in this case 210 mm × 210 mm in size). The tape is always bonded to the sample with the help of the laminating machine. The laminating tape is first attached to the bottom side of sample and trimmed to match the cut sample sheet, at which point a scale is tared (set to zero) with the combined weight of the tape and sample resting on it. Another piece of tape is placed on the top side of the sample, and the sample is stripped in half. The bottom side, together with the tape, is weighed to determine the mass of the removed top side. The scale is now tared again using the bottom side half. Then the tape is attached to the middle layers side of the bottom half. The bottom half is split in two, whereby the new layer from the middle of the sheet is typically directly suitable (suitable basis weight) for orientation analysis. The remaining bottom half is weighed again and then used to tare the scale. Stripping continues from the middle to the bottom side until there is only one layer left (basis weight < 20 g/m^2). The same procedure is carried out on the top-side half. The resulting layers can be split further if they are too heavy, but this is needed only rarely (mainly with multilayer board samples). The splitting procedure is also illustrated in Table 1.

Samples can be digitized using either a camera or a scanner, but when the areas analyzed are as large as in this case, scanning is the easier alternative. For this research paper, digitizing was done using an UltraScan 5000 flatbed

Table 1. Paper sheet tape splitting procedure.

<table>
<tr><th></th><th>1st splitting</th><th>2nd splitting</th><th>3rd splitting</th><th></th><th>7th splitting final layers</th></tr>
<tr><td rowspan="9">Whole sheet, 70.5 g/m^2</td><td rowspan="7">Bottom side
37 g/m^2</td><td rowspan="5">Bottom side
29.8 g/m^2</td><td rowspan="4">Bottom side
23.3 g/m^2</td><td rowspan="9">. . .</td><td>BS, Layer 1, 6.7 g/m^2</td></tr>
<tr><td>Layer 2, 2.5 g/m^2</td></tr>
<tr><td>Layer 3, 3.5 g/m^2</td></tr>
<tr><td>Layer 4, 4.7 g/m^2</td></tr>
<tr><td>Layer 5, 5.9 g/m^2</td></tr>
<tr><td>Layer 6, 6.5 g/m^2</td><td>Layer 6, 6.5 g/m^2</td></tr>
<tr><td>Layer 7, 7.2 g/m^2</td><td>Layer 7, 7.2 g/m^2</td><td>Layer 7, 7.2 g/m^2</td></tr>
<tr><td rowspan="2">Top side
33.5 g/m^2</td><td rowspan="2">. . .</td></tr>
</table>

scanner. The sample layers were placed against a black background, and a 192 mm × 192 mm area was scanned from the fiber side (in contrast to the tape side) with 30 μm/pix resolution using reflective illumination. The exact alignment of layers is important.

In analyzing scanned layer images, the aim is to detect the edges of fibers or fiber bundles and to determine their orientations. Fibers are distinguishable against a dark background as high intensity values. It is also assumed that there are no other edges than those belonging to fibers. The detection of edges is based on the computation of image gradients in every image element. The gradient of the image intensity function $f(x,y)$ at position (x,y) is represented by the vector

$$\nabla f(x,y) = \begin{bmatrix} \frac{\partial f}{\partial x} \\ \frac{\partial f}{\partial y} \end{bmatrix}. \quad (1)$$

At each image point the gradient vector points in the direction of the largest possible intensity increase, and the length of the gradient vector indicates the rate of change in that direction. Thus the magnitude (length) of gradient vector is directly related to the probability that the part of the image examined represents the edge of fiber. At the fiber edge the direction of the gradient corresponds with the direction normal to the fiber edge segment in question. For a discrete digital image, the derivatives $\frac{\partial f}{\partial x}$ and $\frac{\partial f}{\partial y}$ can be

approximated through a discrete differentiation operator. The operator uses two kernels $k_x(i,j)$ and $k_y(i,j)$ that are convolved with the original image $f(x,y)$ to calculate approximations of the horizontal and vertical derivatives:

$$\frac{\partial f(x,y)}{\partial x} \approx D_x(x,y) = (f * k_x)(x,y), \tag{2}$$

$$\frac{\partial f(x,y)}{\partial y} \approx D_y(x,y) = (f * k_y)(x,y), \tag{3}$$

where * denotes a 2-dimensional convolution operation. The coefficients of the kernels used are based on the principle of binomial filter design. This ensures that no pass-band ripples are present in the Fourier transformation [16, 17]. The separable kernels designed use layer image intensity values within a 5 pixel × 5 pixel region around each image point to approximate the corresponding image gradient

$$k_x = \begin{bmatrix} 1 & 4 & 0 & -4 & -1 \\ 4 & 16 & 0 & -16 & -4 \\ 6 & 24 & 0 & -24 & -6 \\ 4 & 16 & 0 & -16 & -4 \\ 1 & 4 & 0 & -4 & -1 \end{bmatrix}, \tag{4}$$

$$k_y = \begin{bmatrix} 1 & 4 & 6 & 4 & 1 \\ 4 & 16 & 24 & 16 & 4 \\ 0 & 0 & 0 & 0 & 0 \\ -4 & -16 & -24 & -16 & -4 \\ -1 & -4 & -6 & -4 & -1 \end{bmatrix}. \tag{5}$$

With the digitizing resolution used this means a 150 μm × 150 μm region, within which 90 μm × 90 μm is pronouncedly weighted.

The magnitude $|\nabla f(x,y)|$ and direction $\theta_f(x,y)$ of gradient vectors at each local image point are calculated applying equations (6) and (7)

$$|\nabla f(x,y)| = \sqrt{D_x^2 + D_y^2}, \tag{6}$$

$$\theta_f(x,y) = \tan^{-1}\frac{D_y}{D_x}. \tag{7}$$

An orientation distribution is then computed as a weighted probability

density function of local orientations $H(\theta_H)$, where the weighting factor is gradient magnitude $|\nabla f(x,y)|$. The direction histogram is

$$H(\theta_H) = \frac{\Sigma_{x,y}\left(|\nabla f(x,y)|\,\delta_{\theta_f(x,y),\theta_H}\right)}{\Sigma_{x,y}|\nabla f(x,y)|}, \tag{8}$$

where $\delta_{\theta_f(x,y),\theta_H}$ is Kronecker's delta function ($\delta_{\theta_f(x,y),\theta_H} = 1$ if $\theta_f = \theta_H$ and 0 otherwise) and, $\{\theta_H, \theta_f \in X : 0 \le \theta_H, \theta_f < 360\}$, where X is a discrete space (a space of isolated angles) and θ_H and θ_f are in degrees (rather than radians).

An example of a small layer image region together with an illustration of its local gradient magnitude is presented in Fig. 1. The image analysis algorithm presented does not try to recognize individual fibers but is based on the premise that all edges showing in a layer image are the edges of fibers or fiber bundles. These fiber edges are detected from point to point with the degree of resolution used in image acquisition. This means that long fibers give several inputs to the fiber orientation distribution while short fibers only give a few. There is thus no need for any more sophisticated weighting of fiber lengths. The influence of fiber curvature on the distribution is directly included through the point by point calculations.

Discrete fiber orientation distribution examples with one degree bins are presented in Figs. 1 and 2. The main direction of orientation (orientation angle) θ is defined as the deviation of the longer symmetry axis from machine direction. Anisotropy ξ is defined as the ratio of the distribution value of the main direction and its normal: $\xi = H(\theta)/H(\theta + 90)$. This ratio can also be calculated using a mean of distribution values around the main and the normal directions within certain interval (in this study the mean values are calculated from 10° ($\theta \pm 5°$) interval). Mean values are used to reduce the effect of roughness of distribution occurring in small subareas. For out-of-plane simulations layer images are sectioned to 2 mm × 2 mm squares, and orientation distributions and parameters are calculated for all of these small regions (Fig. 3).

3 MODELLING

Two different through-thickness dry solids content profiles and several other drying parameters were applied to measured fiber orientation structures in order to study the effect of drying on the initial cockling and curling of paper after the paper machine dryer section. For out-of-plane simulations the dryer section was subdivided into seven sections. After that there was one extra step

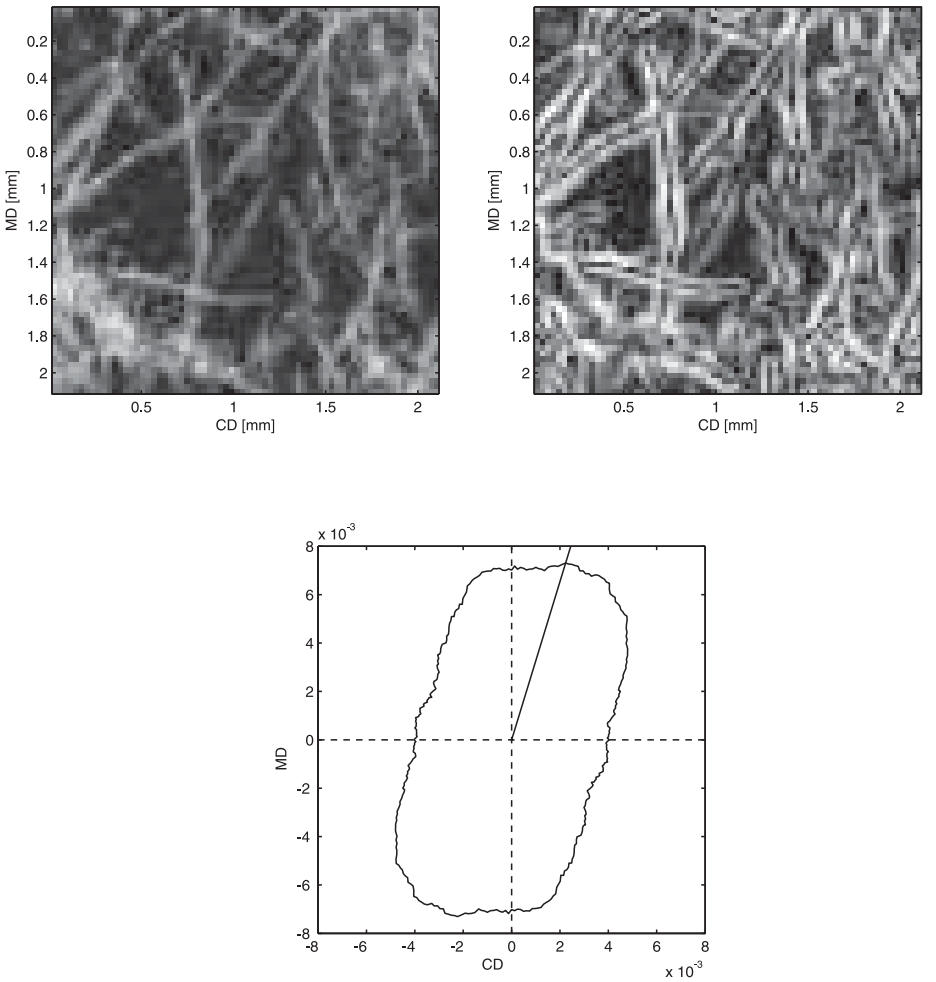

Figure 1. A small region of newsprint layer image (top left); corresponding magnitude of gradient (top right) and orientation distribution (bottom).

where external MD and CD tensions were removed (in the following this step is called drying phase 8). Fixed dry solids contents were given for different layers at each step of drying as direct inputs. Inputs were estimated using simulations of the drying model described in [18, 19]. The drying model uses such input parameters as cylinder diameter, dryer geometry, steam temperature, air humidity and temperature, etc. to calculate the sheet moisture content and drying rate along the length of the dryer section. The two through-thickness drying profiles selected for single-tier (st) and double-tier (dt) configurations are presented in Fig. 4. The simplified drying profiles used

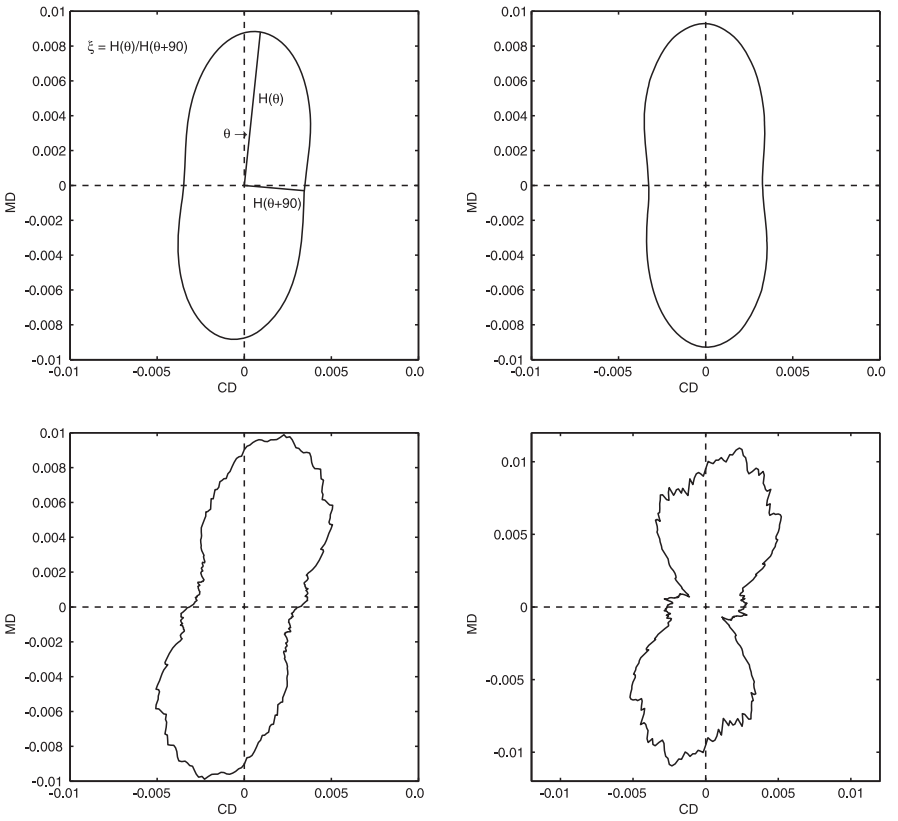

Figure 2. Examples of fiber orientation distributions calculated for areas measuring 368.64 cm^2 (above left), 9 cm^2 (above right), 0.04 cm^2 (below left), and 0.01 cm^2 (below right).

in modelling are presented in Fig. 5. These simplified profiles were obtained by first averaging layers 1, 2 and 3, which form surface 2 (st and dt), and layers 3, 4 and 5, which form surface 1 (st and dt), and then fitting a 5th degree polynomial to the averaged drying profiles. The polynomials yield the dry solids content of the paper surfaces at 7 locations along the dryer section.

To examine the effect of CD tension (together with the through-thickness drying profile), four different tension levels were studied. From the initial dry solids content to 63.9% dry solids content, CD tensions remained low due the fact that the paper web is very weak at high moisture contents and will therefore not allow high tensions at that stage [20]. After that CD shrinkage was adjusted by applying CD tensions that grew linearly to 0 N/m, 130 N/m or 260 N/m. The development of CD tension as a function of dry solids content is presented in Fig. 6. In all simulations (except the totally free drying

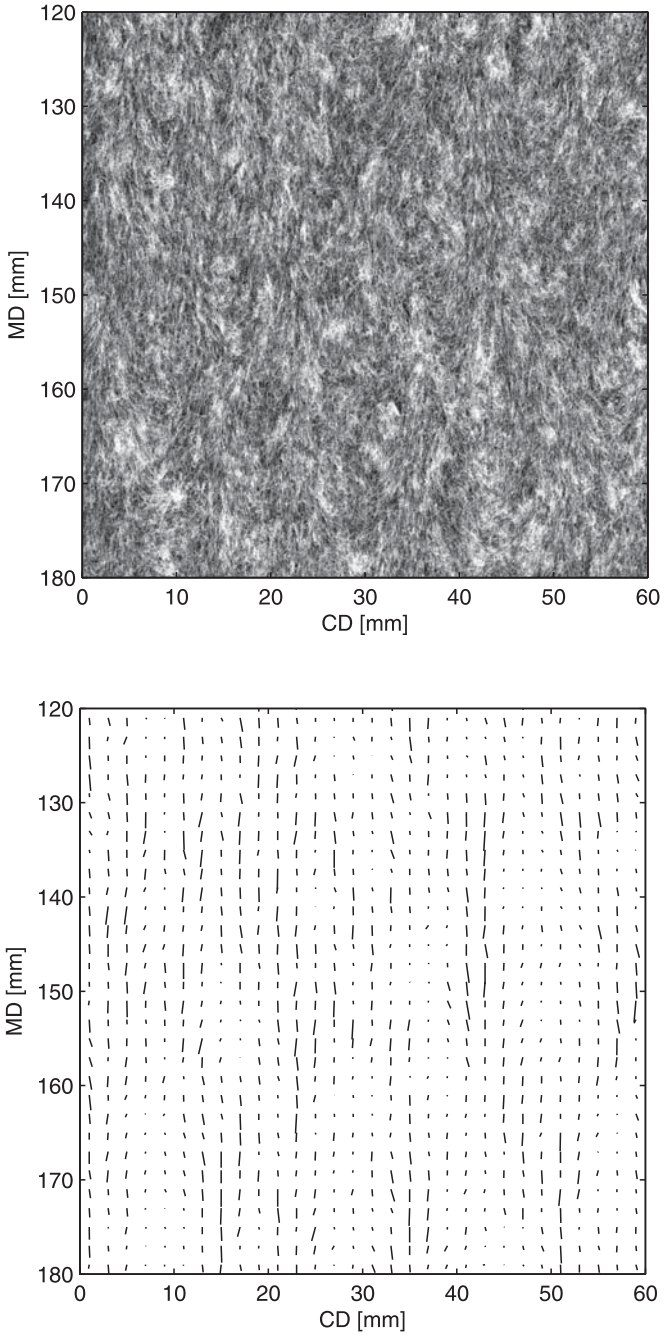

Figure 3. Example region of one layer image (top) and corresponding orientation lines (bottom) calculated for a 2 mm × 2 mm subarea. The length and direction of orientation lines describe anisotropy values and orientation angles, respectively.

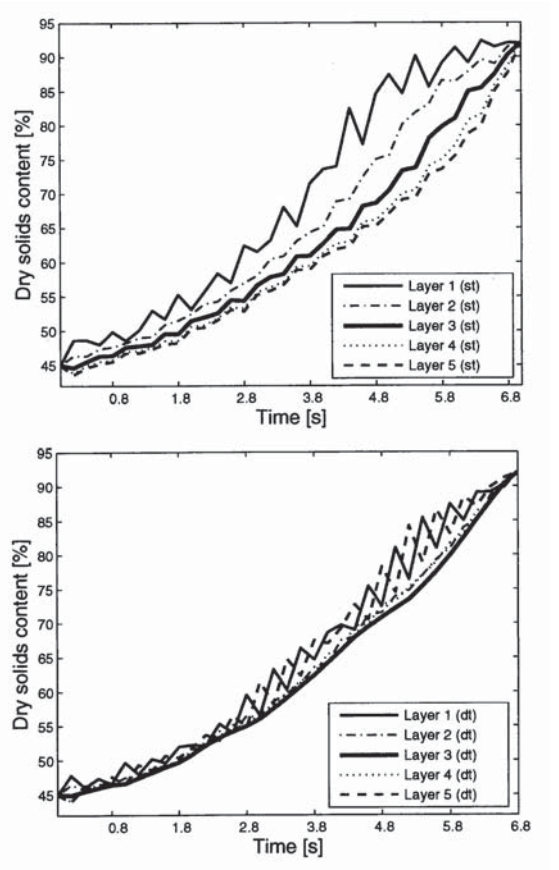

Figure 4. Simulated through-thickness drying profiles for two drying configurations. Asymmetric drying profile for a single-tier (st) drying configuration (top) and almost symmetric drying profile for a double-tier (dt) drying configuration (bottom).

case) MD tension follows CD tension, which grows to 260 N/m. The comparison of different tension levels is essential due to the fact that the paper web tends to demonstrate fairly high middle-to-edge shrinkage differences even while the total amount of shrinkage may be quite low, see e.g. [21, 22].

Although paper can be considered an elasto-visco-plastic material, the viscous nature of paper is ignored in our modelling approach. Had the viscous nature (i.e. the relaxation phenomenon in the stress-strain behaviour of paper) been included, the uncertainty of the input parameters would have increased greatly. Hence, the orthotropic elasto-plastic material model was used to investigate the effects of different drying configurations on the cockling of paper. At high enough tension levels paper crosses the border between the elastic and plastic domains and plastic (irreversible) deformation occurs.

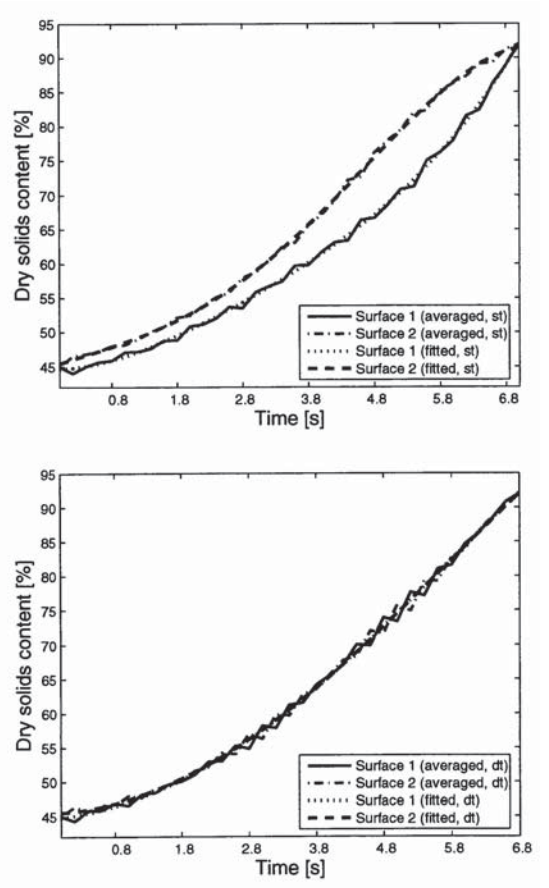

Figure 5. Simplified through-thickness drying profiles (used in modelling) for single-tier (top) and double-tier (bottom) configurations based on simulated drying profiles.

The model (which is detailed in [6]) taking into account the plastic aspects is essential when trying to capture the response from the dryer section of a paper machine. However, ignoring the viscous nature of paper affects dryer section tension levels, for example, meaning that the values obtained for the internal tension difference between the top and bottom layers of paper may increase above realistic levels. In the elasto-plastic approach used in this study, stress-strain behaviour of material is divided into elastic and plastic parts (see Fig. 7) where the yield point defines the border between the elastic and the plastic domain. The dependence used for yield stress and yield strain on dry solids content and anisotropy is based on measurements [6] and can be seen in Fig. 8 for direction 1. Direction 1 is the direction of the local fiber orientation, direction 2 runs perpendicular to that direction, and direction

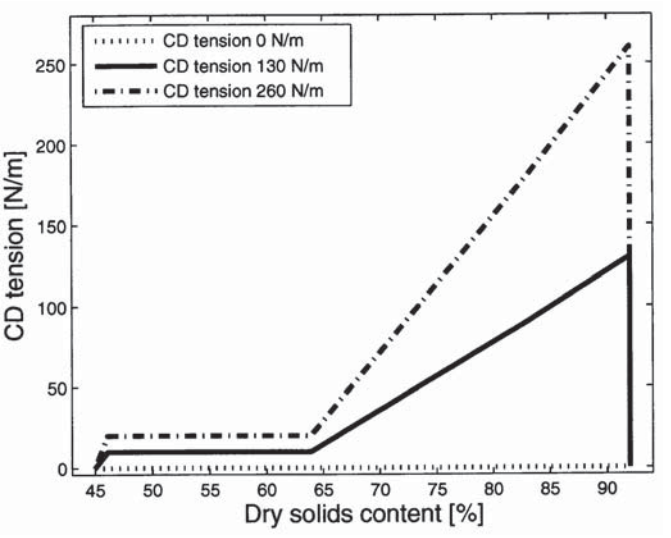

Figure 6. CD tension development to final values of 0 N/m, 130 N/m and 260 N/m for single-tier and double-tier drying configurations.

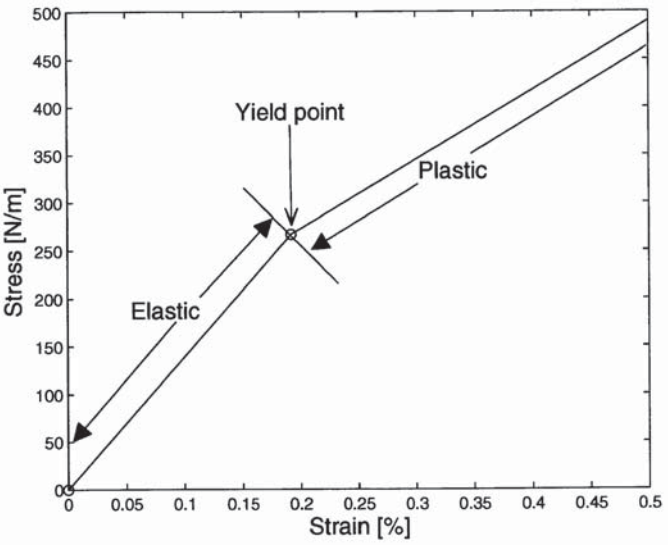

Figure 7. The yield point separates the elastic and plastic parts of materials. The yield point presented here is based on the material model used in direction 1, with anisotropy of 2 and 80% dry solids content.

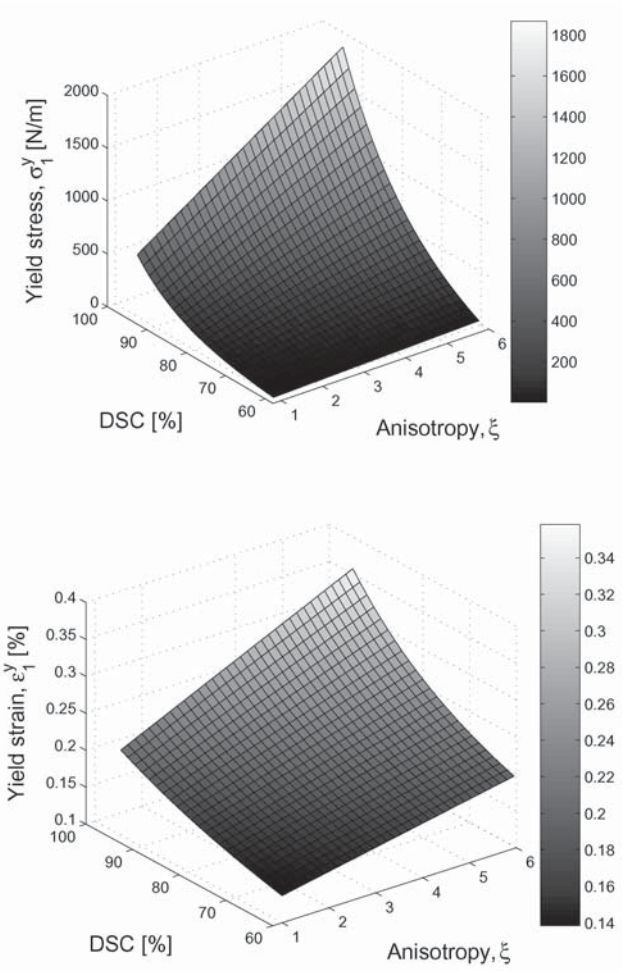

Figure 8. Example of dependence of yield stress σ^y (top) and yield strain ε^y (bottom) on anisotropy ξ and dry solids content (DSC) of paper in the elasto-plastic modelling approach in direction 1.

45° is in the middle between these directions. For more information on how local fiber orientation is treated in the model, see Section 4. The dependences of yield stress σ^y and yield strain ε^y on dry solids content β and anisotropy ξ was obtained by fitting the non-linear functions

$$\sigma^y = A_1\xi + A_2 e^{A_3\beta} + A_4 + A_5\xi e^{A_6\beta}, \tag{9}$$

$$\varepsilon^y = B_1\xi + B_2 e^{B_3\beta} + B_4 + B_5\xi e^{B_6\beta}, \tag{10}$$

to the measurement-based yield points. The values of coefficients A_i and B_i for all directions can be found in reference [6].

The yield surface, which determines whether yield is occurring, is defined by Hill's yield function

$$f(\sigma) = \sqrt{F\sigma_2^2 + G\sigma_1^2 + H(\sigma_1 - \sigma_2)^2 + 2N\sigma_{12}^2}, \tag{11}$$

where parameters F, G, H and N depend on yield stresses as follows

$$H = \frac{1}{2}, \tag{12}$$

$$F = \left(\frac{\sigma_1^y}{\sigma_2^y}\right)^2 - \frac{1}{2}, \tag{13}$$

$$N = 2\left(\frac{\sigma_1^y}{\sigma_{45^\circ}^y}\right)^2 - \frac{1}{2}\left(\frac{\sigma_1^y}{\sigma_2^y}\right)^2, \tag{14}$$

when parameter H for the biaxial stress state is approximated by Hoffman's approximation ($G = H$), the suitability of which for paper is tested in [23]. Strain hardening determines the stress-strain behaviour of materials when yield occurs. The strain hardening used is defined as in reference [6].

The construction of the elastic domain used in the model is based on the determination of yield points. The elastic moduli of paper in directions 1, 2 and 45° are defined as

$$E_1 = \frac{\sigma_1^y}{\varepsilon_1^y}, \tag{15}$$

$$E_2 = \frac{\sigma_2^y}{\varepsilon_2^y}, \tag{16}$$

$$E_{45^\circ} = \frac{\sigma_{45^\circ}^y}{\varepsilon_{45^\circ}^y}. \tag{17}$$

According to [24], shear modulus G_{12} can be approximated as

$$G_{12} = \frac{1}{\left(\frac{4}{E_{45^\circ}} - \frac{1}{E_1} - \frac{1}{E_2} + \frac{2\nu_{12}}{E_1}\right)}, \tag{18}$$

where ν_{12} is Poisson's ratio. Poisson's ratios are computed as follows

$$\nu_{12} = (1.65 - 0.015\beta)\sqrt{\xi}, \tag{19}$$

$$\nu_{21} = \frac{E_2}{E_1}\nu_{12}. \tag{20}$$

The behaviour of ν_{12} is based on experimental data presented in reference [25], and ν_{21} is simply obtained by applying a Maxwell relation. The dependence of moisture expansion coefficients on anisotropy is taken into account by quoting the work of Uesaka, see [26]. Therefore, the local moisture expansion coefficients and can be written as

$$\alpha_1 = 6 \cdot 10^{-4} - 1.5 \cdot 10^{-4}\sqrt{\xi - 1}\%^{-1}, \tag{21}$$

$$\alpha_2 = \sqrt{7 \cdot 10^{-8}(\xi - 1)} + 6 \cdot 10^{-4}\%^{-1}. \tag{22}$$

4 BOUNDARY CONDITIONS AND NUMERICAL SOLUTION

In finite element analysis paper samples are divided into 2 mm × 2 mm elements. Each element is divided into several layers in the thickness direction. Every layer of each element has its individual material parameters defined by the measured fiber orientation parameters (θ_i, ξ_i), see Fig. 9. In the

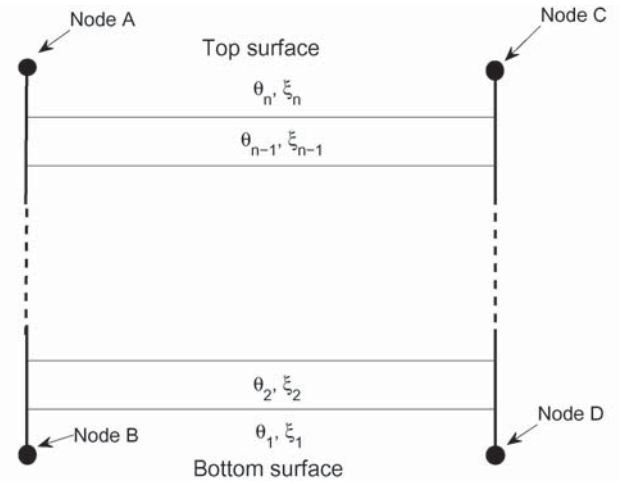

Figure 9. Cross-section of the element used in the numerical simulation. Nodes A and B form a pair, as do nodes C and D.

simulations, the tensions presented in the previous section affect the edges of the paper sheet at the dryer section. One more simulation step is carried out after the dryer section. During this step, all external tensions affecting the paper sheet are removed and displacement results are gathered.

The model is solved using ABAQUS/Standard software and element type SC8R. Element SC8R is based on first-order shear deformation theory in which the hypotheses of the classical laminated plate theory are relaxed by removing the requirement that the normal of the reference surface should remain perpendicular to the deformed reference surface. Element SC8R uses linear interpolation and reduced integration. Reduced integration means that an integration scheme one order below the full scheme is used to integrate the element's internal forces and stiffness. Reduced integration has been proven to have many advantages. For example, it could be used to avoid numerical problems and for decreasing computing time. The element used accounts for finite membrane strains and arbitrary large rotations, and it also includes the effect of thickness changes. These features make the element suitable for large-strain analysis. Unlike more commonly used shell elements, SC8R discretizes an entire 3D body. Its eight nodes are located at the corners of the top and bottom surfaces (see Fig. 9), and it has degrees of freedom only for displacements. Full details can be found in [27, 28].

Two different displacement constraints were used in the simulations depending on the phenomenon considered. The rigid body motions of the paper sheet were removed by constraining the displacements of three nodes to study curling. These nodes belong to the bottom node layer and are located in the middle of the sheet. This location allows curling fully, i.e. curling is not constrained in any direction. In one of these constrained nodes displacement is set to zero for all directions (MD, CD, z), in the second node MD and z displacement are set to zero, and in the third node only z displacement is set to zero. MD and CD displacement constraints are placed so that in-plane shrinkage between nodes is not constrained. When cockling is considered, more displacements are constrained. In addition to the nodes constrained in curling simulations, the z displacement of the bottom node layer at the sheet edges is set to zero. The displacement u_i of nodes in every pair of nodes (see Fig. 9) is also connected at the edges of the sample through the equation constraint

$$u_i^A = u_i^B, \tag{23}$$

$$u_i^C = u_i^D, \tag{24}$$

$$\vdots$$

where direction i is MD or CD depending on the sheet edge in question. If a

pair of nodes is located at the edge perpendicular to the MD, the MD displacements of the node pair are identical. The CD displacements of a pair of nodes are equal if the nodes are located at the edge perpendicular to the CD. This connection between node pair displacements removes the oscillation of stresses that appears near the edges of the sheet. This enables the use of the whole simulated area when cockling results are analyzed. Together with the z displacement constraints at the sheet edges this connection also efficiently prevents large scale out-of-plane deformations.

When the model is solved, the shear deformation capability of the element is ignored by using huge values for parameters that affect shear deformation. The effect of this approach on the solution of the model has been tested extensively. This testing has affirmed that shear deformation can be ignored when the model is solved. Numerical aspects related to the solution have in general been considered extensively *inter alia* due to the following facts:

- Automatic addition of volume-proportional damping [27, 28] is used at the final step of the simulation (when external tensions do not affect the sheet). Volume-proportional damping is accomplished by adding small viscous forces to the equilibrium equations. This stabilization helps to avoid numerical problems that may arise from local instabilities.
- Cockling is a small-scale phenomenon and full certainty of the correctness of the solution has to be obtained, i.e. the possibility of numerical error has to be eliminated.
- In the case of curling, out-of-plane deformations are large and geometrical nonlinearity plays a large role in the solution.

Fig. 10 presents the effects of the automatic addition of volume-proportional damping on the simulated cockling. The strength of damping is controlled through damping factor c which defines how strong viscous forces are used in stabilization. Smaller coefficient c values signify weaker stabilization. Image (a) shows a whole CD cross-section (from the middle of the sheet) for one cockling simulation, while (b) provides a more detailed view of the same cross-section. As can be seen, the effect of damping on the solution is minor when the damping factor is 10^{-7} or smaller. When damping factors 10^{-9} and 10^{-12} are used, the simulated cross-sections are identical. Fig. 11 shows the effect of damping on the standard deviation of the simulated cockling. Standard deviation (SD) is used to estimate the intensity of cockling. Results presented in Fig. 11 show that the SD of the simulated cockling is not affected by damping when damping factor 10^{-9} or smaller is used. In this study, the Taylor microscale [29] is used to describe the average in-plane size of cockles. It is one of the three standard turbulence length scales. It is usually calculated from an autocorrelation function of the fluctuating

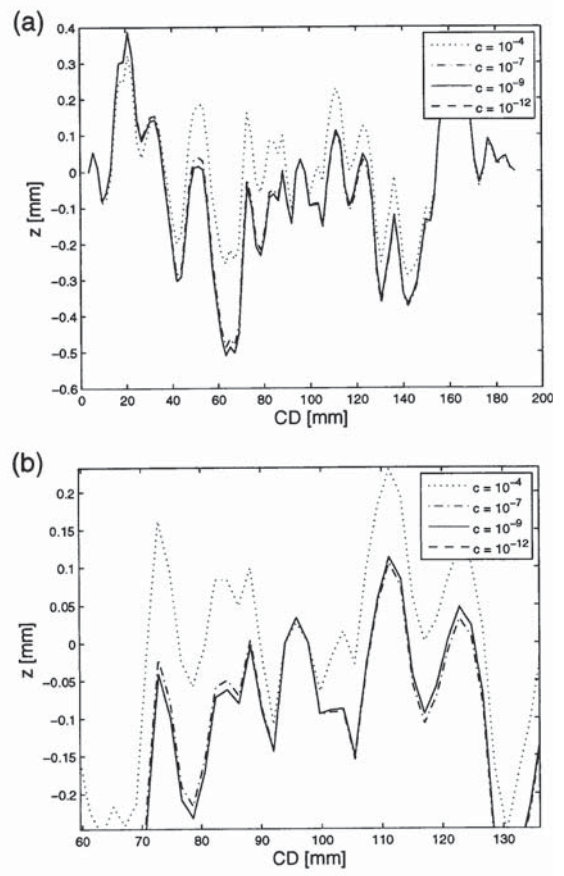

Figure 10. Effect of damping factor c on the simulated cockling. In (a), whole CD cross-section from the middle of the sheet and in (b), detail from the same cross-section.

velocity by fitting parabola (paraboloid in two-dimensional cases) around the zero-shift point at the origin and by solving the radius of the parabola. In the case of cockling, instead of fluctuating velocity, the autocorrelation is applied to the height map of cockling in spatial coordinates. The Taylor microscale is also used to characterize paper formation [29]. Fig. 12 presents how the damping factor affects MD and CD microscales. As in the case of SD, Taylor microscales are not affected by stabilization when damping factor 10^{-9} or smaller is used. Due to these observations and other numerical testing, damping factor 10^{-9} is used when cockling is considered.

Unlike cockling, curling is large-scale out-of-plane deformation. Due to this, geometrical nonlinearity plays a large role in the solution, and

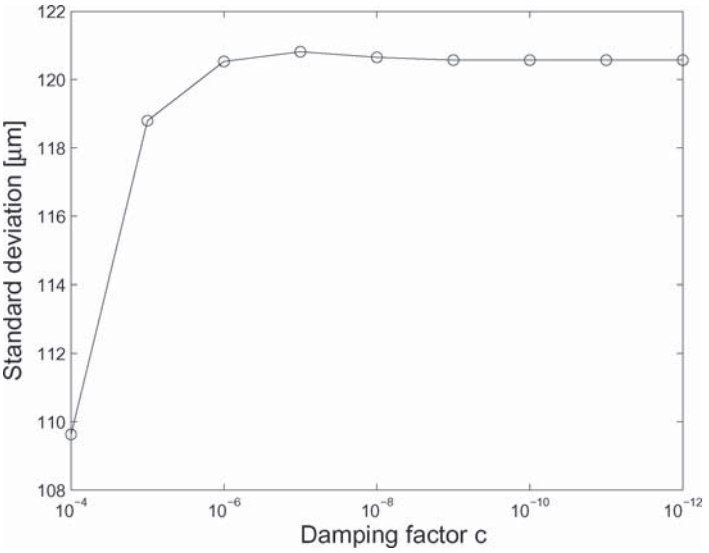

Figure 11. Standard deviation of the simulated cockling as a function of the damping factor *c*.

stabilization has a greater effect on the solution, see Fig. 13. Chart (a) shows a CD cross-section (from the middle of the sheet) for the simulated curling affected by non-symmetric drying. The results in (a) suggest that the damping factor does not affect the simulated curling when factor c is 10^{-11} or smaller. However, when small detail of the simulated curling presented in (a) is examined in (b), it can be seen that stabilization has a much stronger effect on the simulated curling than cockling. By comparing cases where damping factors are 10^{-14} and 10^{-15}, it can be seen that the difference between the cases is minor. Due to this and other testing, damping factor 10^{-15} is used when curling is considered.

5 RESULTS

The fiber orientation structures of ten different paper samples from ten different production machines were measured (see Section 2) to provide distinct base paper structures for drying simulations. A few examples of fiber orientation anisotropy structures through the thickness of paper from the bottom side to the top side are shown in Fig. 14. The effect of drying conditions on simulated out-of-plane deformations was studied through several simulations. The primary parameters studied were in-plane tensions during drying and the through-thickness drying profile. In the following, where cockling

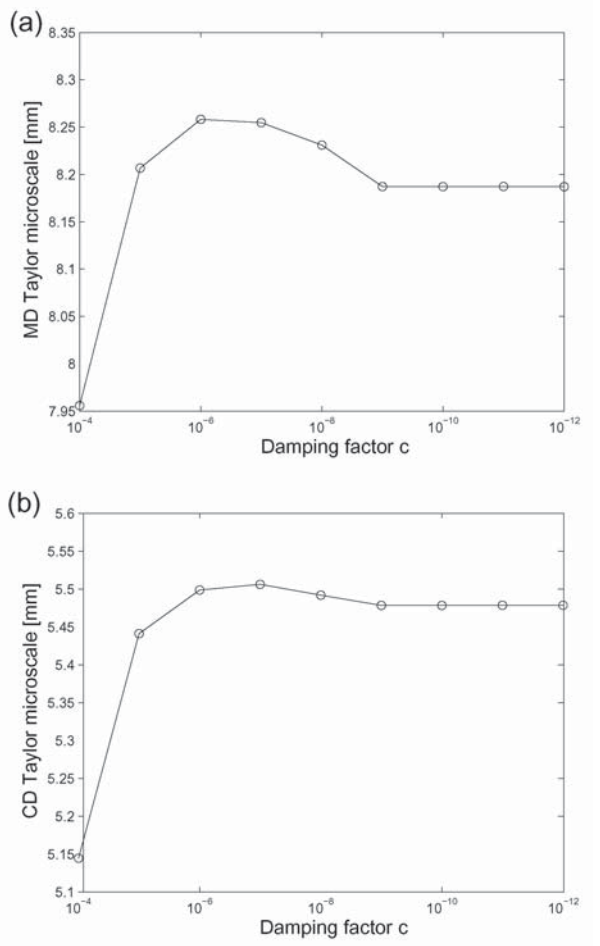

Figure 12. MD (a) and CD (b) Taylor microscales for the simulated cockling as a function of the damping factor *c*.

results are considered, the height map is filtered using a second-order classical IIR Butterworth filter with 50 mm cutoff wavelength. Further, where surface tensions are discussed, simulated stress is converted into N/m using the thickness of the layers employed in the simulations.

The results presented were simulated through the model introduced in the previous sections. As mentioned earlier, some of the model's inputs are measured and some are simulated by means of another model. It has to be kept in mind that the elasto-plastic approach used in the simulations requires the determination of a yield point (and whole yield surface). The quantification of the yield point and its dependence on anisotropy and the dry solids content of paper is based on the measurements presented in reference [6].

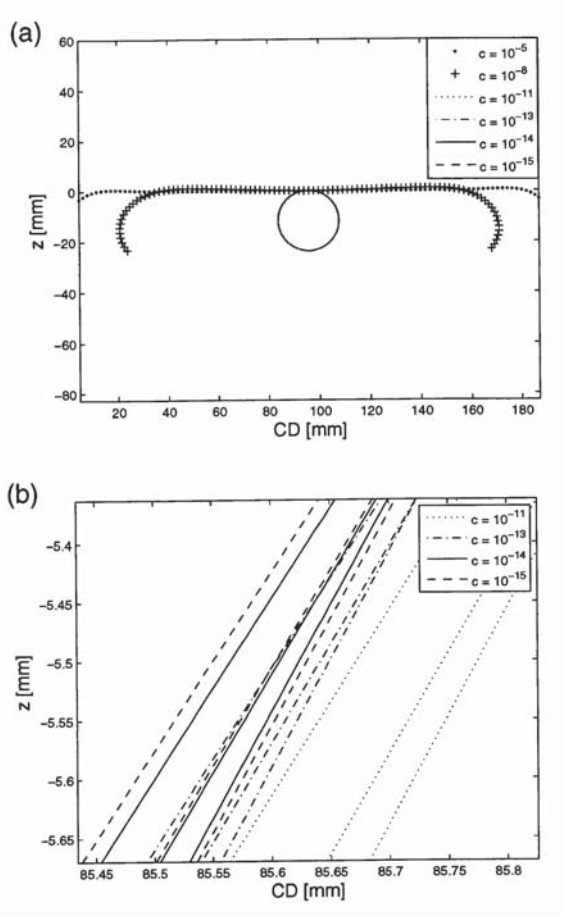

Figure 13. Effect of damping factor c on simulated curling. In (a) whole CD cross-section from the middle of the sheet and in (b) detail from the same cross-section.

However, because it is commonly known that determining the yield point is a difficult task in the case of many materials, and especially for such anisotropic materials as paper (see e.g. [30, 31, 32]), a parametric study concerning the effect of the yield point location on results is reasonable. Moreover, the effect of temperature on yield point is ignored in the model although it probably also carries its own significance as in the case of Young's modulus [33]. Fig. 15 shows two potential yield point variations. Fig. 15 shows only direction 1 yield point variation but all directions (the whole yield surface) have received similar treatment. In Fig. 15 (a) Young's modulus remains unchanged while the yield point varies, whereas in (b) Young's modulus varies while yield strain remains constant. Fig. 16 shows the effect of the variation presented in Fig. 15 (a) on simulated cockling. As can be seen in Fig. 16,

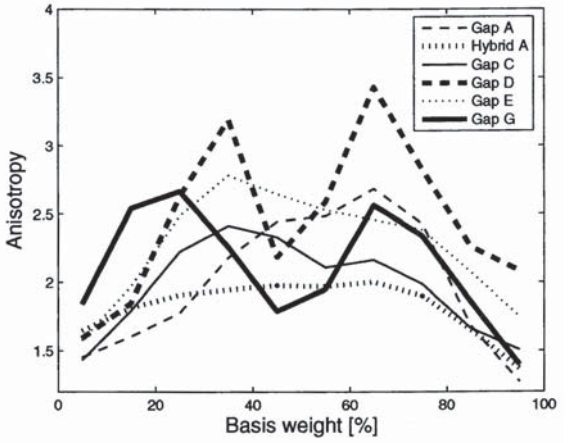

Figure 14. Fiber orientation anisotropy as a function of basis weight from bottom side to top side for different paper machine samples.

the location of the yield point has a great effect on the SD of the simulated cockling. This is quite natural, because the decrease in yield strain means that the paper enters the plastic domain earlier and more plastic deformation occurs before the release of external tensions. However, the effect seems to be very linear in nature. Meaning that the results are quite sensitive to the quantification of the yield points, but SDs still change very systematically. Therefore, when comparing the SDs of the simulated cockling of different samples, the difference between the SDs of the samples could be assumed to remain at the same level if the yield point of different samples is changed equally in the way presented in Fig. 15 (a). At the same time, the effect of a decrease in yield point on MD and CD Taylor microscales, see Fig. 16 (in the right) is not as notable as in the case of SD of cockling.

The effect of a decrease in Young's modulus, see Fig. 15 (b), can be seen in Fig. 17. As Young's modulus decreases, so does the SD of cockling. The same effect was also noticed in the case of a decreasing yield point (with constant Young's modulus, in Fig. 16), but now the effect is less significant. That is due to the fact that now only the yield stress decreases while the yield strain remains the same. As the behaviour of the SD is very linear when moving from a decrease of 15% towards a decrease of 60%, SD suddenly drops quite considerably when a 75% decrease in Young's modulus is introduced. The steepest change in MD and CD Taylor microscales (Fig. 17) also occurs between 60% and 75%.

In conclusion, it can be said that although determining the yield surface of paper is challenging, and it also seems to have a notable effect on the results,

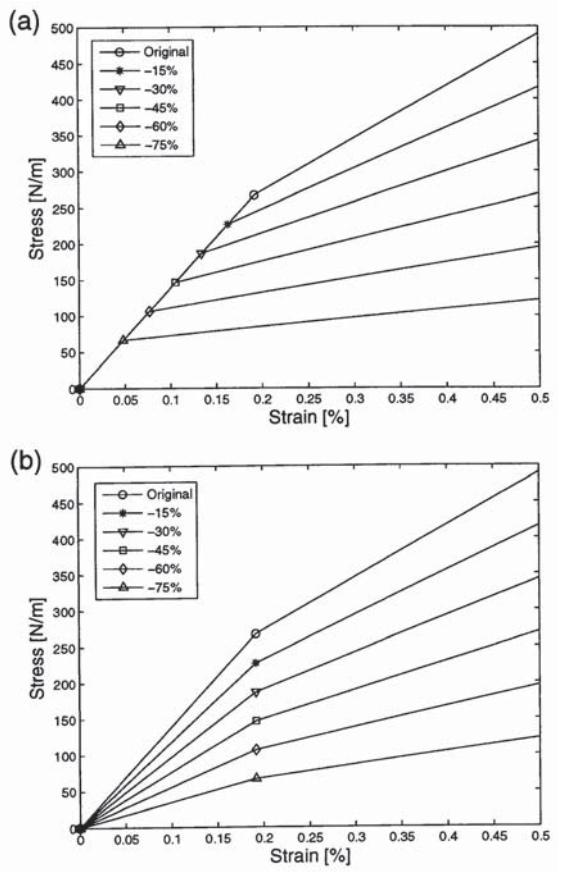

Figure 15. Example of yield point alteration (in direction 1, anisotropy 2, dry solids content 80%): in (a) decreasing yield strain and yield stress while Young's modulus remains the same, and in (b) decreasing Young's modulus while yield strain remains constant.

the effect of yield surface variations on the results is quite systematic and linear. A drop in the yield point increases plastic deformation in relation to elastic deformation. This type of a change reduces the SD of cockling, as can be observed in both of these cases.

It is widely known that through-thickness moisture gradients during the drying process represent an important factor in the curling phenomenon. Fig. 18 presents the simulated internal tension development of surfaces 1 and 2 during dt (double-tier) and st (single-tier) drying process for sample Hybrid A. As can be seen, an asymmetric drying process generates a large internal tension difference between the surfaces. In the case of a symmetric drying

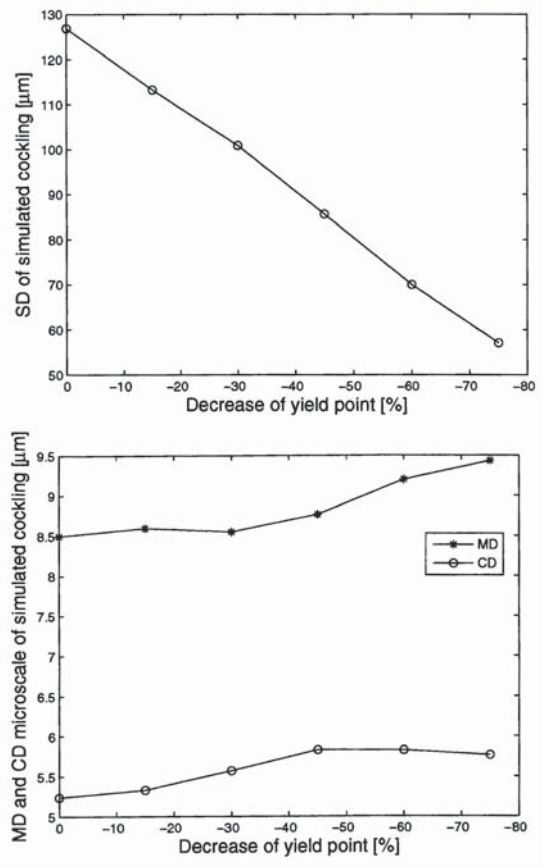

Figure 16. Effect of decreasing yield strain and yield stress on the SD of cockling and MD and CD Taylor microscales. Dt drying with tensions 260 N/m and 130 N/m in the MD and CD, respectively, is used in the simulations.

process, the small internal tension difference between the surfaces comes from the two-sided structure of the sample.

The internal tension difference between the surfaces strongly determines the magnitude and also the axis of curling. This can be seen in Figs. 19 and 20, where the internal tension difference between the surfaces and corresponding simulated curling in remoisturizing are presented for an almost homogeneous simplified sample. Remoisturizing is applied to a surface first dried in inverted st drying (surface 1 in Fig. 5) keeping the external tensions at drying phase 7 constant during remoisturizing. After moisture is applied to the sheet, dry solids content balance is restored at the sheet surfaces and external tensions affecting the sheet are subsequently removed. As can be seen in Fig. 19, minor remoisturizing reduces the tension difference between

the surfaces. When a certain limit is reached in remoisturizing, the tension difference between the surfaces changes its sign and the absolute value of difference starts to increase again.

Although the internal tension difference between the surfaces strongly affects the curling tendency of the sample, see Fig. 20, it alone does not define the axis of curling. When the internal tension difference between the surfaces is sufficiently low, the structure of the sample also has an effect on curling. This can be seen in Figs. 19 and 20, where 6% remoisturizing is applied to the sheet. Although the tension difference between the surfaces is higher in the MD, curling occurs around the MD axis. This stems from the fact that the sample has higher bending stiffness in the MD than CD.

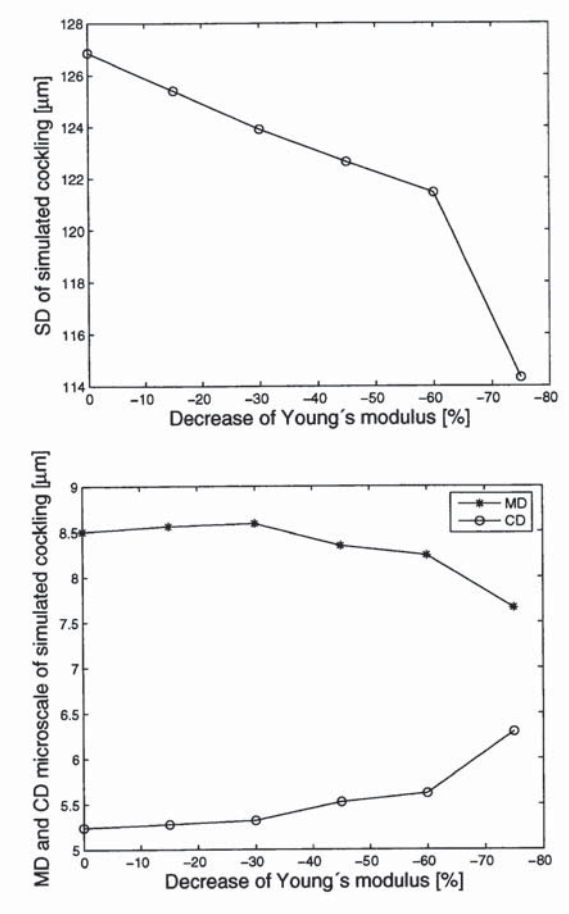

Figure 17. Effect of decreasing Young's modulus on the SD of cockling and MD and CD Taylor microscales. Dt drying with tensions 260 N/m and 130 N/m in MD and CD, respectively, is used in the simulations.

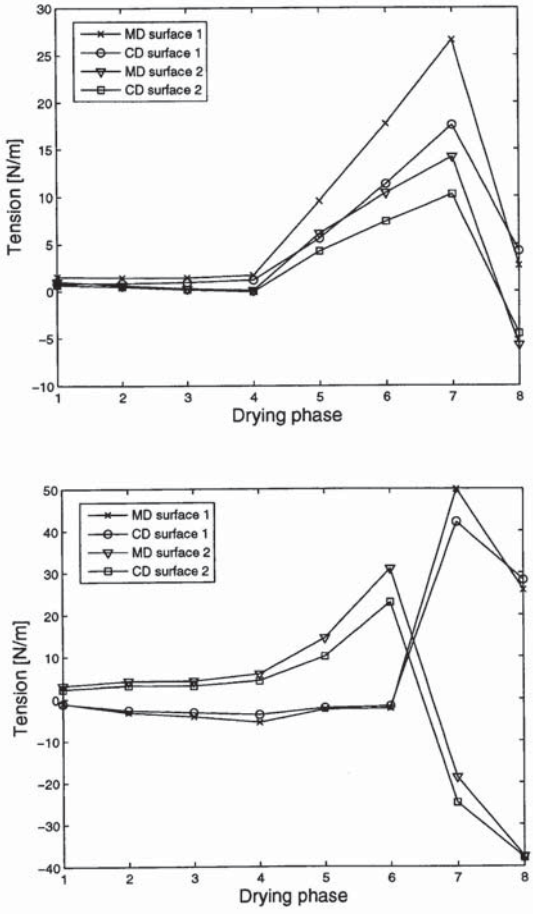

Figure 18. Internal tension (mean of surfaces) development during dt (top) and st drying (bottom) with 130 N/m CD tension for sample Hybrid A. The boundary conditions for cockling simulations are used, i.e. the sheet is not allowed to curl at drying phase 8.

Remoisturizing also affects simulated cockling. The direction of the effect of remoisturizing on cockling depends strongly on the external tensions used during the remoisturizing process. As an example, the standard deviation of simulated cockling of one sample without remoisturing when external tensions of 260 N/m in MD and 130 N/m in CD are used is 119.0 μm. If 5% remoisturizing is applied using the same external tensions during remoisturizing as at drying phase 7, the standard deviation of simulated cockling decreases to 113.2 μm. However, if external tensions in the MD and CD are released before the remoisturizing process, the SD of cockling increases to value 126.2 μm.

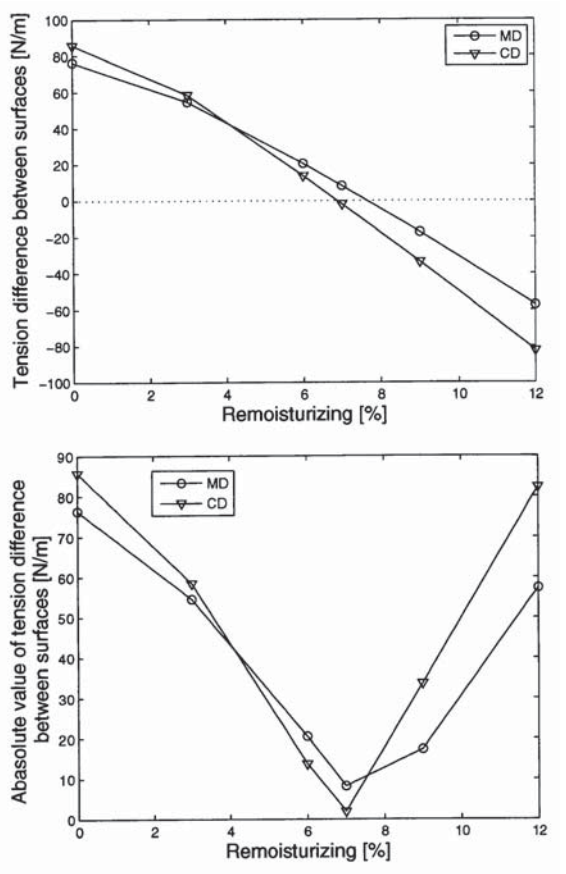

Figure 19. Internal tension difference between the surfaces before removing external tensions (top) and absolute internal tension difference between the surfaces before removing external tensions (bottom) as a function of remoisturizing for an almost homogeneous sample. The maximum values of the external tensions used are 260 N/m in the MD and 130 N/m in the CD, see Section 3. Corresponding simulated curling is presented in Fig. 20.

The local internal tension variation of the bottom and top layers for dt, st and inverted st (ID) drying with zero CD and MD external tensions during drying is presented in Fig. 21. The local tension maps simulated with boundary conditions used in the cockling studies are from drying phase 8. In inverted st drying, the drying order of the two sides of paper is changed, i.e. the surface of paper that is dried last changes. With symmetric dt drying the mean levels of internal tension are almost equal, so that the difference of mean tensions between the top and bottom layers is –6.6 N/m in the cross direction and –5.8 N/m in the machine direction. If curl were not restricted

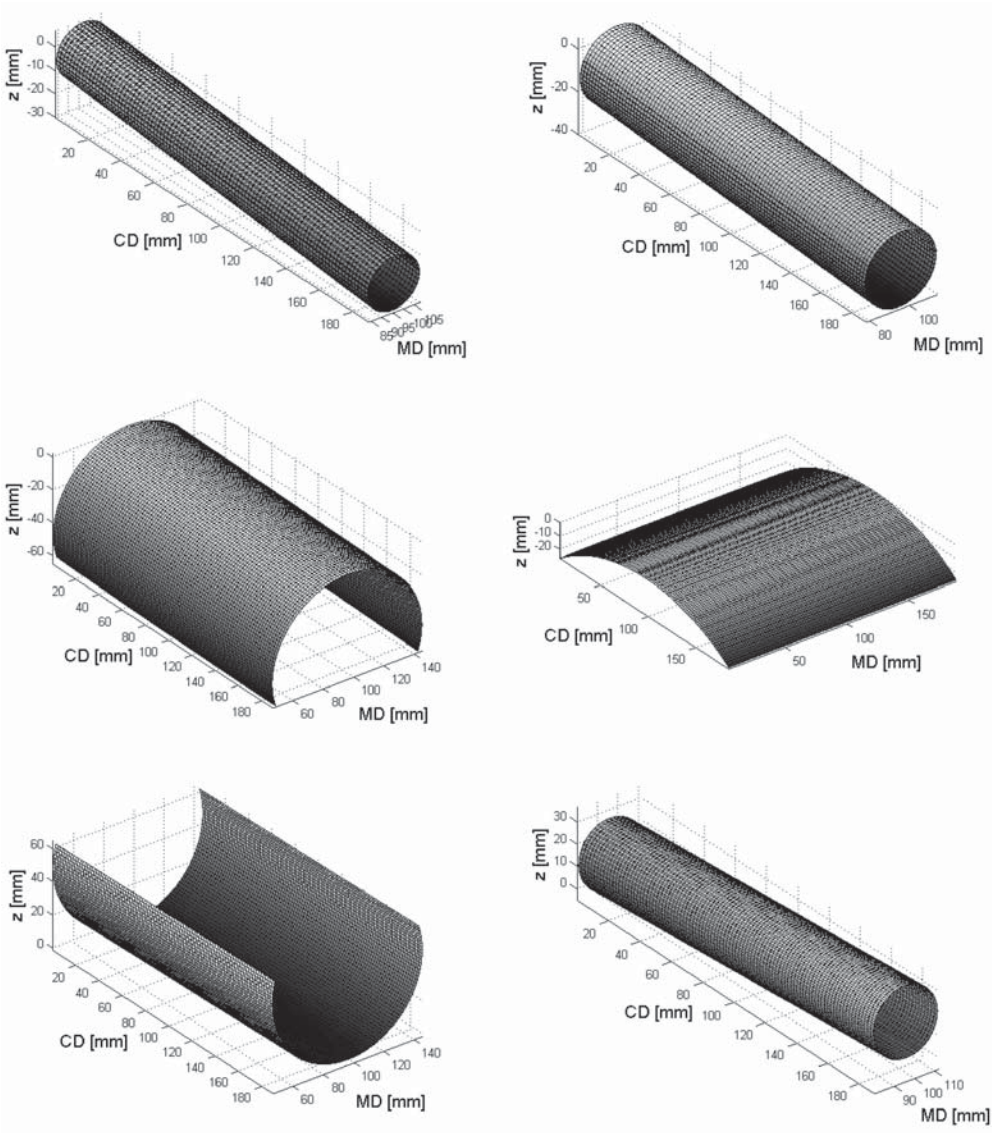

Figure 20. Simulated curling when remoisturizing 0% (top left), 3% (top right), 6% (middle left), 7% (middle right), 9% (bottom left) and 12% (bottom right) is applied to the sheet.

by means of boundary conditions, this tension difference would curl the sample so that the CD edges would rise upwards when the sample is viewed from the bottom side, i.e. the curl tendency is toward bottom side. In a non-constrained situation this curling would minimize the internal tension two-sidedness of the sample.

The tension difference between the two sides of the sheet in symmetric drying arises directly from the anisotropy two-sidedness and elasto-plastic behaviour of its inhomogenous structure. The bottom side of the sample tends to shrink more than the top side in the CD due to the higher anisotropy of the bottom than top side layers (Fig. 14 sample Hybrid A). The anisotropy difference between the top and bottom sides is $\xi_{top30\%} - \xi_{bottom30\%} = -0.15$ (the subscript means that average values for the bottom and top sides are calculated from 30% z-direction portions of the basis weight). However, curling is prevented by the boundary conditions, which leads to a situation where the bottom side is constrained to a stretched state and top side to a compressed state in the CD. When a sample is dried in asymmetric drying (st), the tension levels of the bottom and top sides change violently (Fig. 21). In the st drying case the tension difference between the top and bottom sides increases as high as –74.3 N/m in the CD and –71.1 N/m in the MD. In this st drying the top layer (surface 2 in Fig. 5) is dried first and the bottom layer second. The result is a high curling tendency toward the bottom side. If the drying order is inverted (bottom layer is dried first), the tension differences are 66.8 N/m and 63.1 N/m in the CD and MD respectively, indicating a curling tendency toward the top side. The opposite-signed high tensions generated by two-sided dryings suppress most of the structural curling tendency arising from anisotropy two-sidedness.

The variation of bottom and top layer tensions changes only slightly when the two-sidedness of drying is inverted. Changes in the simulated cockling height maps (Fig. 21) are also minor. Only few local area alterations can be detected in out-of-plane deviations. The spectra of the cockling simulations shown in Fig. 21 are presented in Fig. 22. For this sample Hybrid A, a variance of small-scale cockling increases slightly for asymmetric drying cases and total variance is higher for the inverted st drying case than for dt and st drying. The deformation of cockling for all 10 samples measured due to different drying two-sidedness is presented in Figs. 23 and 24. The standard deviation of cockling generally increases but it can also decrease when drying two-sidedness is altered from symmetric to asymmetric. The scale of cockling oftentimes changes toward smaller cockles as the two-sidedness of drying increases. If the standard deviations of two cockling maps are equal, the visual appearance of the sample containing smaller cockles is worse. Overall, these results indicate that changes in both the nature and amplitude of cockles are minor and the directions of local curling (cockles) are mainly defined by fiber orientation two-sidedness irrespective of the drying gradient. However, small differences exist between the cockling maps, which can originate only from different ratios of elastic and plastic stresses and strains in local areas on the two sides of the sheet arising from different surface stress

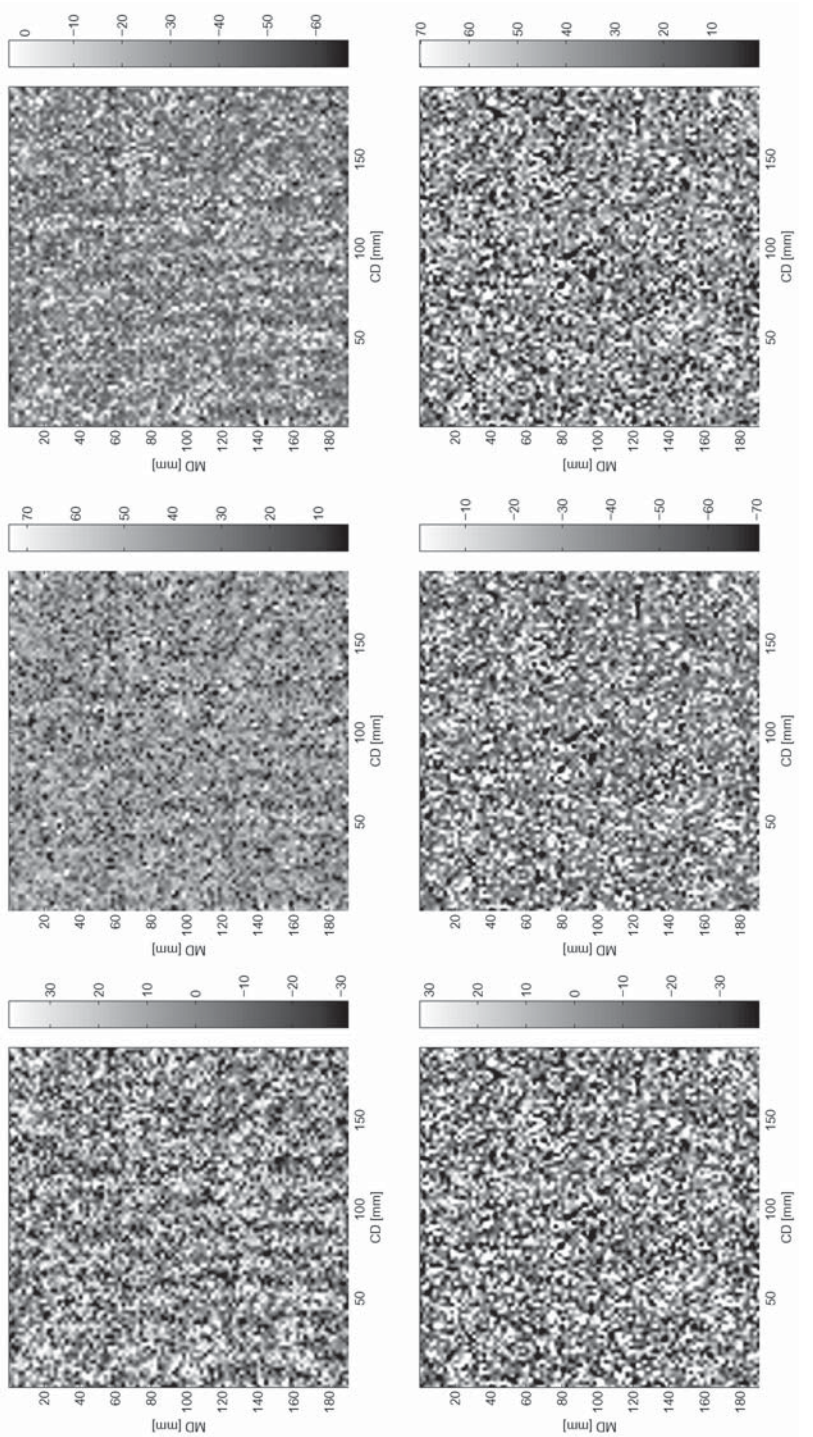
0 −10 −20 −30 −40 −50 −60
70 60 50 40 30 20 10
−70 −60 −50 −40 −30 −20 −10
70 60 50 40 30 20 10
30 20 10 0 −10 −20 −30
CD [mm]
MD [mm]
20 40 60 80 100 120 140 160 180
50 100 150

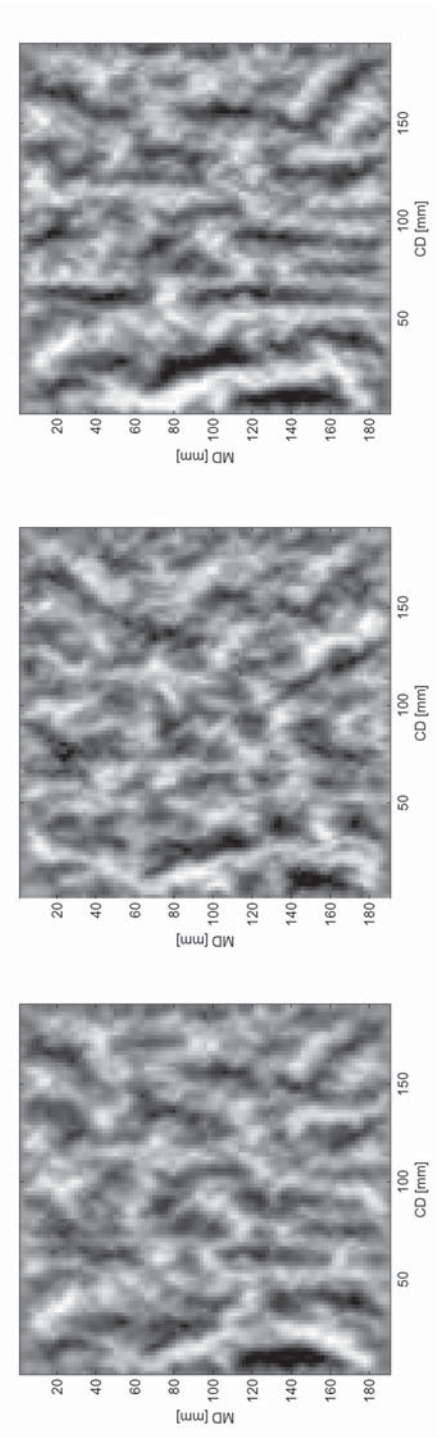

Figure 21. Local CD tensions (N/m) of bottom (top row) and top (middle row) surfaces, and corresponding cockling (bottom row) in the case of dt drying (left column), st drying (middle column) and inverted st drying (right column). The vertical distance between black and white is 1 mm for all cockling figures. The sample is Hybrid A (see Fig. 14).

levels between drying arrangements (dt, st or inverted st). When these simulated cockling results are considered, suitably arranged asymmetric drying may be beneficial with certain layered orientation structures.

A small region from the bottom side CD tension map (Fig. 21) and corresponding local orientation lines for the bottom side layer and cockling of symmetric drying are presented in Fig. 25. The texture of local variations in bottom side local tension clearly correlates with corresponding height variations in the cockling image. Since local anisotropy differences constitute the only input that brings local variations to simulations, there must be some correspondence between local orientation lines and the tension map. Some correspondences can obviously be detected, but the interdependence is not straightforward. Streak-like MD structures are also seen in the tension map. High anisotropy streaks indicate negative tensions, while low anisotropy streaks correspond with positive tensions. However, in the high orientation area it would be expected that the area would tend to shrink more than the surrounding and corresponding area on the other side of the sample. If that is true, the CD tension of high orientation streaks should be positive. Simultaneously there is also a band of high anisotropy values going in the CD direction around y-axis position 130 mm. For this high orientation area tension is positive, agreeing with the presumption discussed above. High orientation streaks tend to curl locally toward the bottom side while low orientation streaks begin to curl toward the top side. A high orientation CD band tends to concurrently compress the structure not only at positions of high orientation streaks but also at positions with low orientation streaks. This means that the CD band forces the MD streaks to bend with higher amplitude waves than would be their natural tendency. In this case the CD bands can therefore explain the reversed tensions at these streak positions.

The simulation cases studied so far were dried without any constraints in the machine and cross directions. The remarkable effect of external MD and CD tensions on paper cockling is presented for sample Hybrid A in Fig. 26. The spectra in Fig. 27 show the frequency response of cockling. In the CD, the change of MD tension from free to 260 N/m during drying decreases mostly large scale variation. In the MD, a decrease in variation influences all cockling scales. If the CD tension, along with MD, is also included (0 N/m $\rightarrow$ 130 N/m), the variations of small and middle scale cockles also decrease in the CD. No clear changes are detected in the MD. Figs. 28, 29 and 30 show how the cockling parameters of all of the samples studied depend on the CD tension used.

If drying two-sidedness is changed in a situation of restricted drying (drying tensions 260 N/m in the MD and 130 N/m in the CD), the response to this change is even lower than in the free drying case described earlier. The

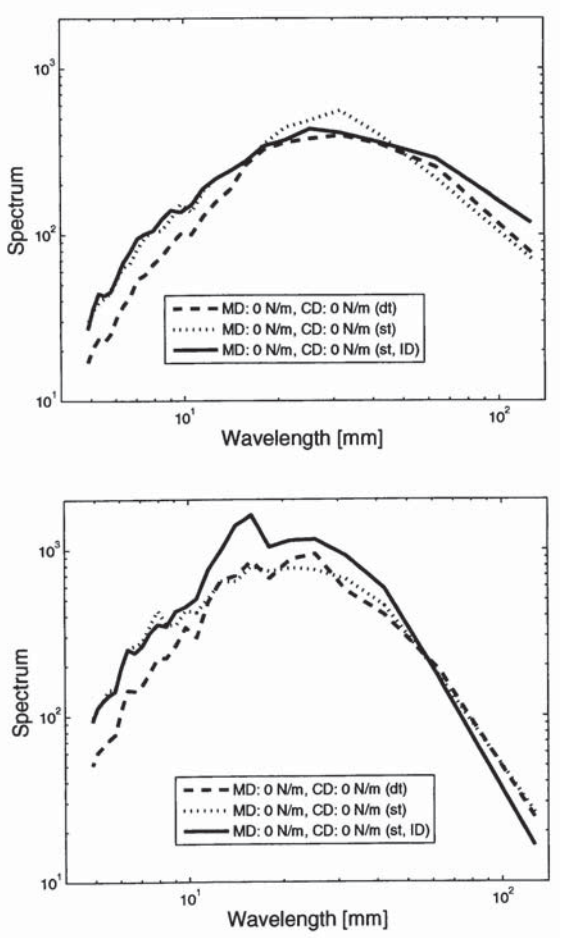

Figure 22. MD (top) and CD (bottom) spectra (from the cockling simulations shown in Fig. 21) for completely free single-tier and double-tier drying for sample Hybrid A.

cockling maps in Fig. 31 and spectra in Fig. 32 and Fig. 33 show no significant change in cockling tendency. Fig. 34 illustrates that this behaviour can be applied to all 10 production machine samples. Now, in contrast to free drying (see Fig. 23), the asymmetry of drying decreases (although only slightly) the SD of cockling in almost all cases when 260 N/m MD tension is applied. Although in st and dt drying cases the external tension introduced is equal for the same average dry solids content values (average between the top and bottom surfaces), the internal stress generated when paper dries is different in these two cases; in st drying the drier side of the paper develops higher internal stress values than either of the sides in dt drying.

With the boundary conditions used, the curl tendency of paper can be

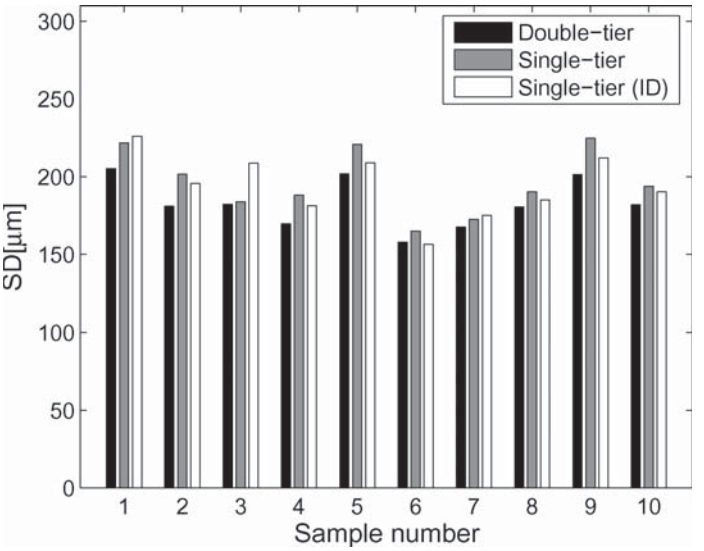

Figure 23. Standard deviation of simulated cockling in the case of completely free drying. Sample numbers 1, 2, 4, 5, 6, 8 and 9 corresponds formers gap A – G, respectively, sample number 7 correspond Fourdrinier, and sample numbers 3 and 10 corresponds hybrid A and B, respectively.

estimated on the basis of the tension difference between the two sides of the paper sheet as discussed earlier. The CD and MD tension differences of the top and bottom sides caused by different external drying tension and drying symmetry simulations are presented in Fig. 35. Symmetric dt drying shows a small negative difference in free drying and absolute value of this difference increases only slightly when drying is restricted. In symmetric drying this negative CD internal tension correlates with a negative anisotropy difference between the top and bottom sides. Both anisotropy and internal tension two-sidedness show rather low structural curl tendency for sample Hybrid A. Two-sided drying (st and inverted st) shows notably higher tension two-sidedness and thus higher curl tendency. In st drying external restrictions in the MD increases only slightly the absolute values of tension differences (CD and MD tension differences are –75.9 N/m and –73.6 N/m, respectively), and adding CD restrictions to drying lower the absolute values of internal tensions, but only slightly (CD: –66.3 N/m, MD: –63.6 N/m). In inverted st drying the internal tension difference behaves almost symmetrically when compared to st drying. Based on these simulations drying restrictions cannot reduce the extreme curl arising from two-sided drying to an acceptable level.

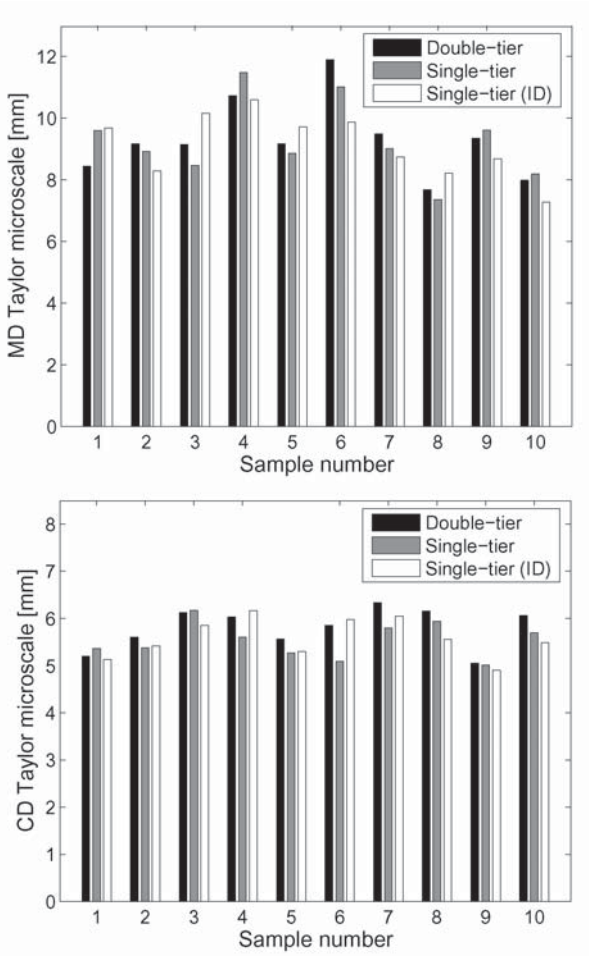

Figure 24. Taylor microscale in MD (top) and CD (bottom) in the case of completely free drying. Sample numbers 1, 2, 4, 5, 6, 8 and 9 corresponds formers gap A – G, respectively, sample number 7 correspond Fourdrinier, and sample numbers 3 and 10 corresponds hybrid A and B, respectively.

6 DISCUSSION AND CONCLUSIONS

Two different out-of-plane phenomena, the cockling and curling of paper, were examined in this study through simulations. In order to take into account the effects of the whole drying process and fiber orientation variations, an elasto-plastic material model was used despite the customary view that paper is an elasto-visco-plastic material. The viscous nature of paper means that the relaxation phenomenon in the stress-strain behaviour of the

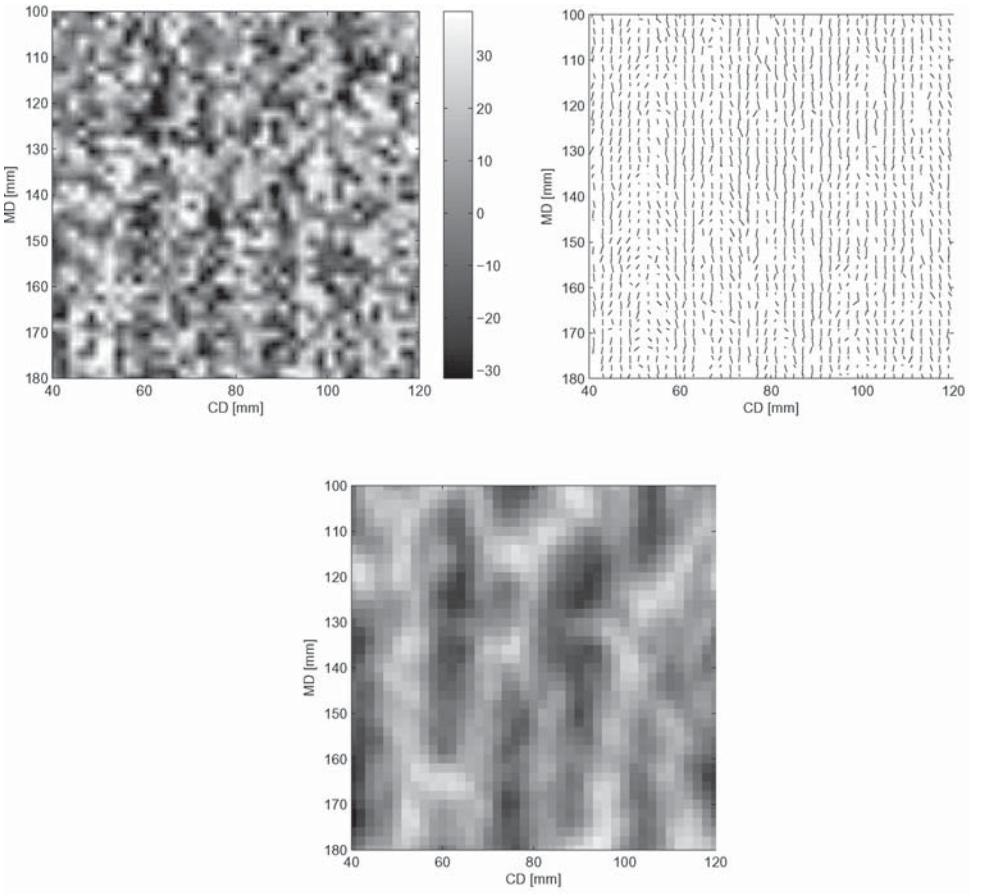

Figure 25. Small part (from sample Hybrid A) of bottom side CD tension map (top left), corresponding local orientation lines of bottom side layer (top right), and simulated cockling (bottom) when completely free dt drying is used. The vertical distance between black and white in the cockling figure is 1 mm.

sheet might also play a role in out-of-plane deformations arising at the dryer section, or at least the tensions during drying are strongly affected by relaxation. However, there is huge lack of measurement results and detailed data on the viscous phenomena taking place during the drying process. This has forced the exclusion of this viscous component from the model presented as the number of undetermined inputs would have increased to an uncontrollable level. More detailed measurement data would be needed, not only to facilitate viscous modelling but also to take full advantage of the elasto-plastic model. It should also be remembered that only one structural variation, i.e. the variation of fiber orientation, is taken into account in

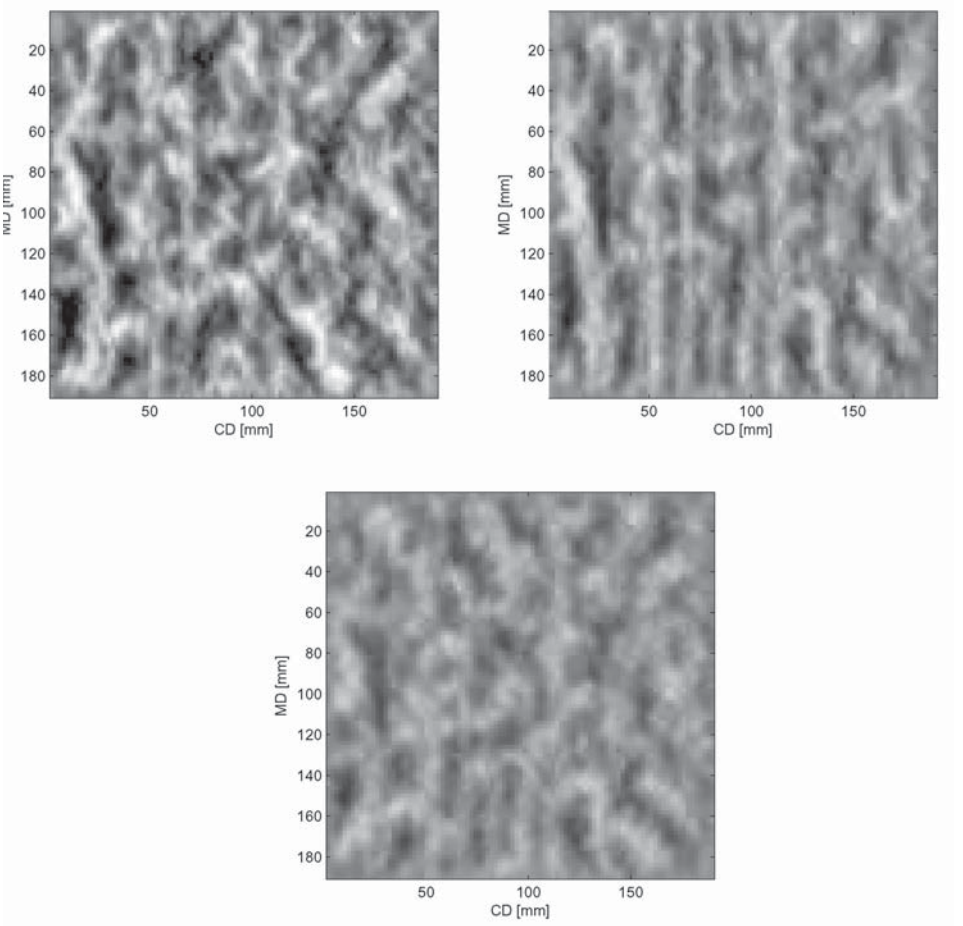

Figure 26. Simulated cockling (st drying) of sample Hybrid A in the case of completely free drying (top left), with 260 N/m MD and 0 N/m CD drying tensions (top right), and with 260 N/m MD and 130 N/m CD drying tensions (bottom). The vertical distance between black and white in the cockling figures is 1 mm.

modelling. Many other structural variations, for example in basis weight and filler content, certainly play their own important part in out-of-plane deformations. Regardless of the absence of viscous phenomena and some other detailed information of processes for inputs, the elasto-plastic model was able to produce reasonable simulation results to reveal the interactive effects of sheet structure and drying parameters on the cockling and curling of paper.

The simulation results presented in this paper indicate that the in-plane internal tensions occurring at different positions and layers of paper vary in a

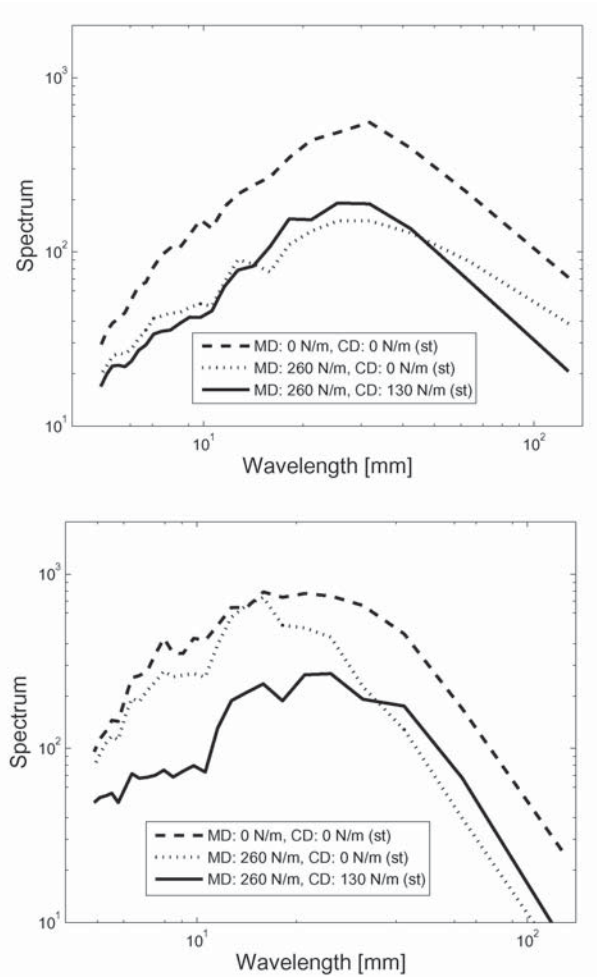

Figure 27. MD (top) and CD (bottom) spectra for single-tier drying for sample Hybrid A.

pronounced manner depending on the two-sidedness and tension conditions of drying together with the sheet's fiber orientation structure. Drying two-sidedness is a principal factor with respect to the average internal tension levels of different paper sides, but only a minor factor in terms of tension variations within paper layers. This means that drying two-sidedness defines mainly the curling tendency of paper but has only a limited effect on cockling observed immediately after the drying process. Independently of the external MD and CD tensions used in simulation, highly asymmetric drying always leads to high two-sidedness of internal tension and thus to high curl tendency. Curling can be controlled during and after drying by adjusting this

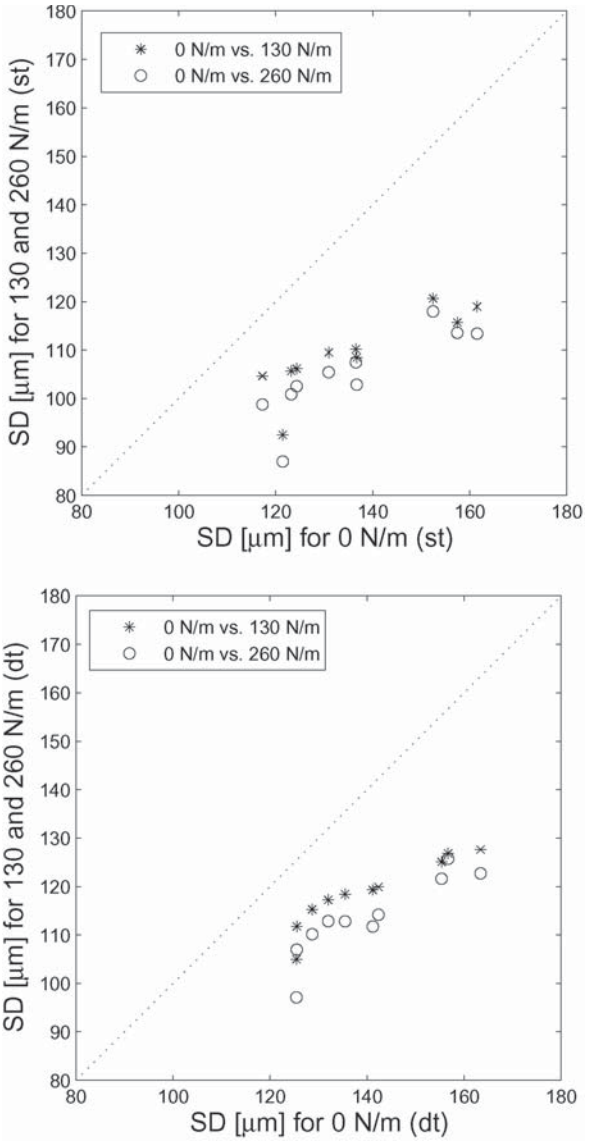

Figure 28. SD of cockling for single-tier (top) and double-tier (bottom) drying configuration in case of 0 N/m, 130 N/m and 260 N/m cross-machine tensions for ten paper samples. MD tension applied at 260 N/m. The dotted (diagonal) line is only used to facilitate comparison of the results.

internal tension two-sidedness of paper arising from drying conditions. The simulations presented in this paper show how remoisturizing and drying cycle can decrease the two-sidedness of internal tensions (and curl as well) to zero, or even force it to reverse its sign both in the MD and CD directions. This is

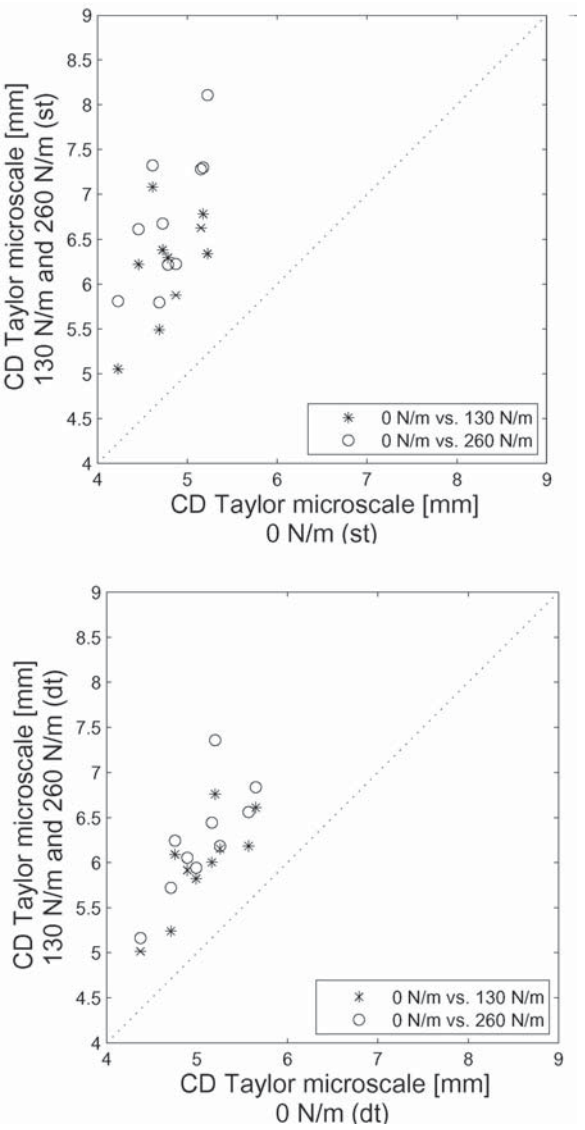

Figure 29. CD Taylor microscale of cockling for single-tier (st) and double-tier (dt) drying configurations in the case of 0 N/m, 130 N/m and 260 N/m cross-machine tensions for ten paper samples. MD tension applied at 260 N/m. The dotted (diagonal) line is only used to facilitate comparison of the results.

also true in real life: the curl tendency of asymmetric single-tier drying is always adjusted in subsequent processing of the paper web including some remoisturizing and subsequent drying or heating (e.g. remoisturizing, coating or calendering processes).

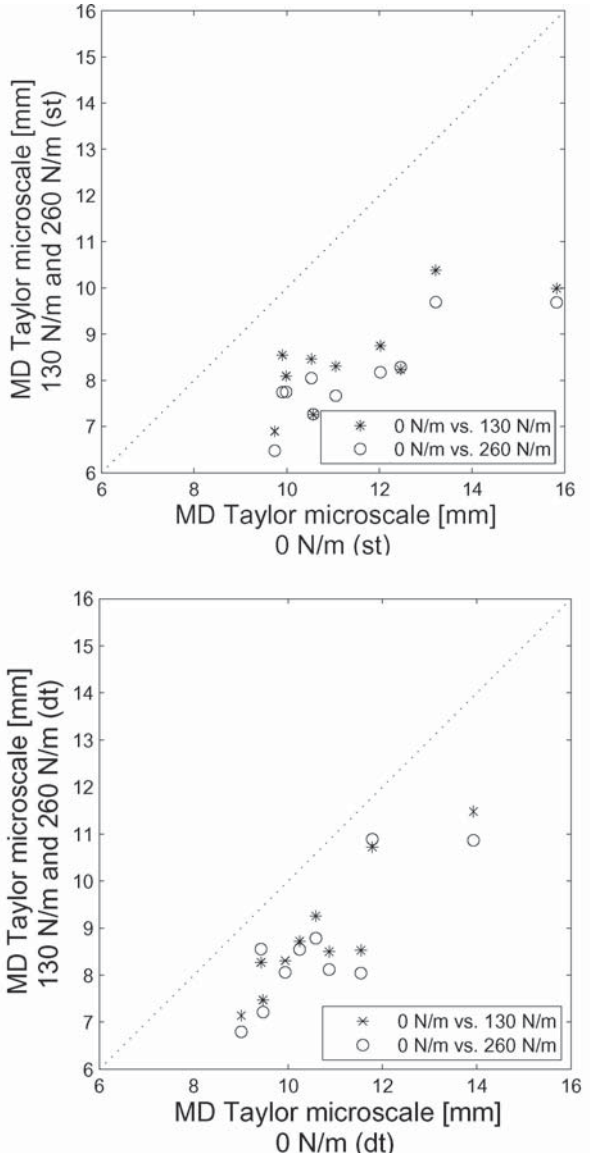

Figure 30. MD Taylor microscale of cockling for single-tier (st) and double-tier (dt) drying configurations in the case of 0 N/m, 130 N/m and 260 N/m cross-machine tensions for ten paper samples. MD tension applied at 260 N/m. The dotted (diagonal) line is only used to facilitate comparison of the results.

Based on the simulation results obtained, the asymmetry of drying has only limited ability to alter cockling tendency. Only a paper sheet with extreme two-sided variation in its fiber orientation structure can benefit from a change in the drying order of the paper surfaces. Additionally, the direction

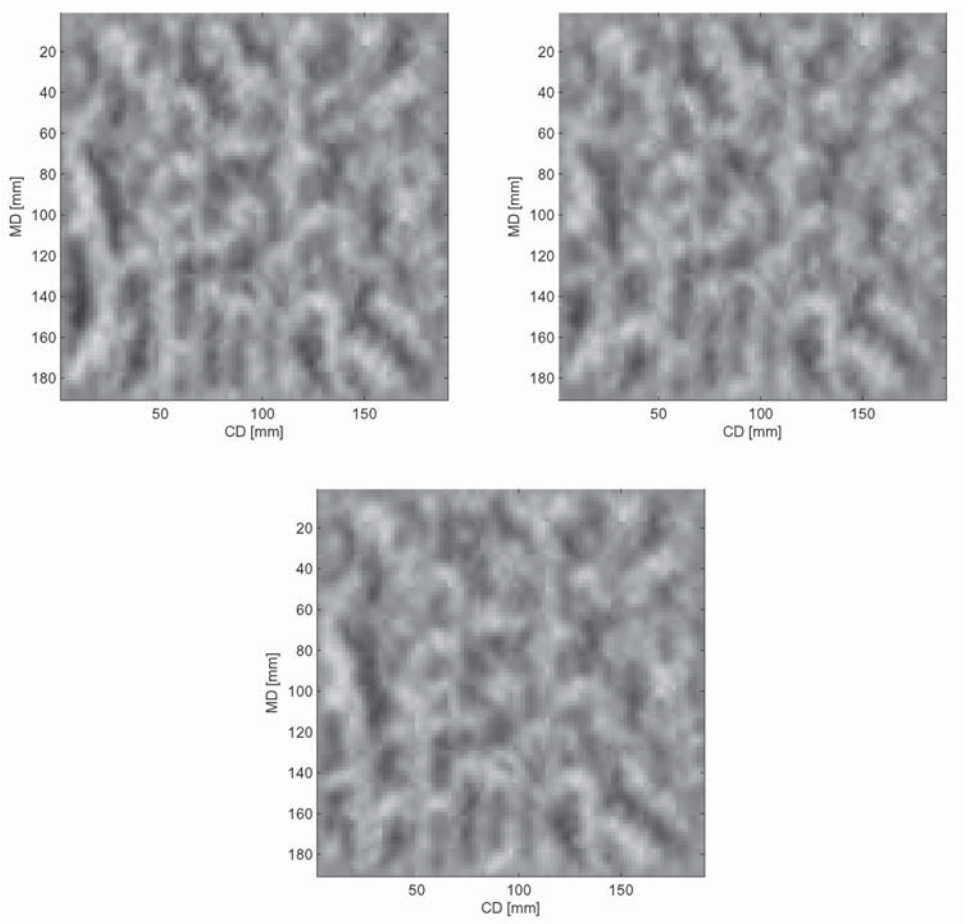

Figure 31. Cockling maps (tensions 260 N/m in the MD and 130 N/m in the CD used during drying) simulated with dt (top left), st (top right) and inverted st drying (bottom) for sample Hybrid A. Vertical distance between black and white is 1 mm for all cockling figures.

of local curls (cockles) appears to be quite stable. However, the amplitude of cockling decreases significantly if external tensions (during drying) are applied to simulated samples. The nature of cockling (such as waviness or the roundish shape of cockles) is highly influenced by the relative magnitude of MD and CD external tensions during drying, while local orientation structure defines the difference between samples taken from different production machines. The importance of drying restraints on cockling can be understood by comparing two parallel sheets, one of which is dried freely and the other totally constrained. Drying tension has to be taken into account not

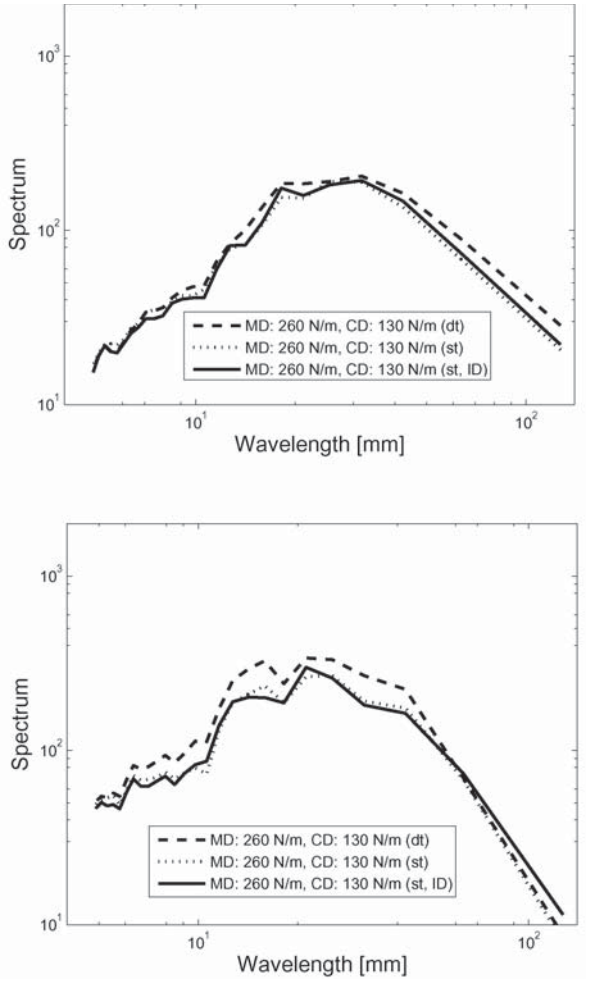

Figure 32. MD (top) and CD (bottom) spectra for dt, st and inverted st drying for sample Hybrid A with drying tensions 260 N/m and 130 N/m in the MD and CD, respectively.

only at the dryer section of a paper machine but also in the finishing, converting and conditioning of paper. If high tensions are maintained at each process stage, the risk of wasting the valuable strain potential and runnability of the paper web increases. A tension strain controlled processes might facilitate the optimization of restraints, in contrast to the straight strain (velocity) controlled drying processes typically used nowadays.

The controlling possibilities of paper machine processes concerning tensions and fiber orientation, the factors important for paper cockling, are currently inadequate. Although the profile and large-scale variations of fiber

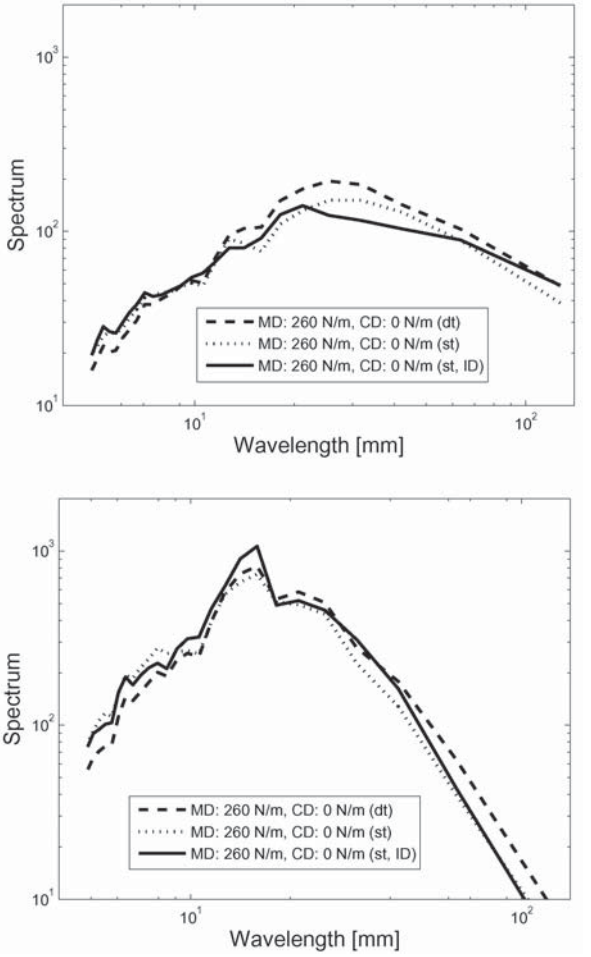

Figure 33. MD (left) and CD (right) spectra for dt, st and inverted st drying for sample Hybrid A when the CD is completely free during drying.

orientation are reasonably well controllable, controlling variations and the structure of local fiber orientation is not well understood. Precise tension levels, both MD and CD, are also impossible to adjust and control at every stage where the sheet undergoes some drying during its journey from the paper making to end use. The model presented in this paper provides a new tool for increasing general understanding of the importance of the various factors behind cockling and curl, and the simulations presented and future work with the model introduced will hopefully lead to improved process control possibilities and novel paper machine construction solutions.

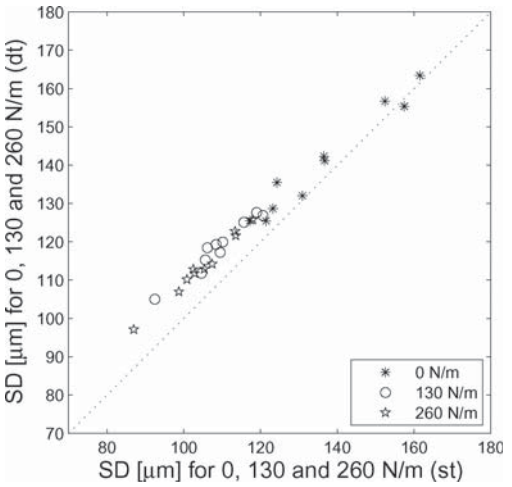

Figure 34. Comparison of the SD of cockling for single-tier (st) and double-tier (dt) drying configuration in case of 0 N/m, 130 N/m and 260 N/m cross-machine tensions for ten paper samples. MD tension applied at 260 N/m. The dotted (diagonal) line is only used to facilitate comparison of the results.

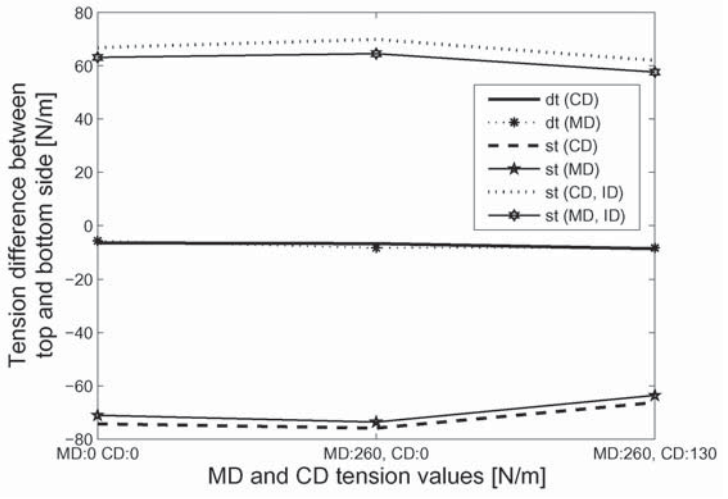

Figure 35. Internal tension difference between top and bottom sides of paper in the case of dt, st and inverted (ID) st drying for sample Hybrid A.

ACKNOWLEDGEMENTS

Special acknowledgements are due to Oleg Timofeev and Harri Kiiskinen of VTT for the through-thickness drying profiles used in this study. Special

thanks also go to Seppo Virtanen from UPM for analyzing the results and providing constructive criticism on the model, and to Heimo Ihalainen of the Tampere University of Technology for providing the signal analysis tools needed to analyze the enormous amount of data produced. The authors are grateful to UPM-Kymmene Corp. and Metso Paper, Inc. for their financial support of this research project, and for providing the experimental data used. ABAQUS/Standard, a commercial software package licensed to CSC (the Finnish IT center for science), was used to solve the model.

REFERENCES

1. Carlsson, L., Fellers, C. and Htun, M. Curl and two-sidedness of paper. Svensk Papperstidning, 83, 194–197, 1980.
2. Paik, K.H. and Nam, W.S. Cockle depending on drying conditions and local basis weight distribution. J. Pulp Pap Sci. 27, 177–181, 2001.
3. Pietikäinen, R. A mathematical model of paper sheet curling problem. Licentiate Thesis, Jyväskylä: University of Jyväskylä, 1993.
4. Smith, S.F. Dried-in strains in paper sheets and their relation to curling, cockling and other phenomena. The Paper-Maker and British Paper Trade Journal 119, 185–192, 1950.
5. Lipponen, P., Leppänen, T., Erkkilä, A.-L. and Hämäläinen, J. Effect of drying on simulated cockling of paper. J. Pulp Pap Sci. 34, 226–233, 2008.
6. Lipponen, P., Leppänen T., Kouko, J. and Hämäläinen, J. Elasto-plastic approach for paper cockling phenomenon: On the importance of moisture gradient. Int. J. Solids Struct. 45, 3596–3609, 2008.
7. Lipponen, P., Leppänen, T. and Hämäläinen, J. On the role of drying induced cross-machine shrinkage on paper cockling phenomenon. Nordic Pulp Paper Res. J. 24, 60–65, 2009.
8. Kajanto, I. Finite element analysis of paper cockling. Products of Papermaking, Oxford, England, 237–262, 1993.
9. Leppänen, T., Sorvari, J., Erkkilä, A.-L. and Hämäläinen, J. Mathematical modelling of moisture induced out-of-plane deformation of a paper sheet. Modelling Simul. Mater. Sci. Eng. 13, 841–850, 2005.
10. Hojjatie, B. and Ahrens, F. Effects of formation and heat transfer non-uniformities on development of cockle during drying of paper. Progress in Paper Physics Seminar, Trondheim, Norway, 2004.
11. Ostoja-Starzewski, M. and Castro, J. Random formation, inelastic response and scale effects in paper. Philosophical Transactions of Royal Society London A 361, 965–986, 2003.
12. Ahrens, F., Patterson, T., Mueller, S. and Hojjatie, B. Investigation of paper dryer picking, web transfer and quality issues using a new web adhesion and drying simulator. Brazilian J. Chem. Eng. 22, 217–225, 2005.

13. Erkkilä, A-L., Pakarinen, P. and Odell, M. Sheet forming studies using layered orientation analysis. Pulp Pap. Can. 99(1):81–85, 1998.
14. Erkkilä, A-L., Pakarinen, P. and Odell, M. The effect of forming mechanisms on layered fiber structure in roll and blade gap forming. TAPPI 99 – preparing for the next millennium, TAPPI Press, Atlanta, USA, 389–400, 1999.
15. Leppänen, T., Erkkilä, A.-L., Jetsu, P. and Hämäläinen, J. Mathematical modelling of moisture induced cockling of a paper sheet. PAPTAC 92nd Annual Meeting Preprints – Book A, Montreal, Canada, 315–320, 2006.
16. Jähne, B. Digital Image Processing: concepts, Algorithms and Scientific Applications. Springer-Verlag Berlin, Heidelberg, Germany, 1991.
17. Aubury, M. and Luk, W. Binomial filters. VLSI Signal Processing 12(1):35–50, 1996.
18. Karlsson, M. and Timofeev, O. Computer simulation of a multicylinder dryer with single-tier configuration. Proceedings of 5th International Symposium on Process Systems Engineering, PSE' 04, Kyongju, 363–368, 1994.
19. Karlsson, M., Timofeev, O., Paavola, P., Malshenko, A. and Taskinen, P. Analysis of performance of multicylinder dryer, using computer simulation and experimental data. Proceedings of the 48th Appita Annual General Conference, Melbourne, 291–296, 1994.
20. Wedel, G.L. Restraint dryer for the drying end of a papermaking machine and a method thereof. US Patent 5933979, 1999.
21. I'Anson, S.J., Constantino, R.P.A., Hoole, S.M. and Sampson, W.W. Estimation of the Profile of Cross-Machine Shrinkage of Paper. Measurement Sci. Technol., 19(1):015701, 2008.
22. Hoole, S.M., I'Anson, S.J., Ora, M., Ashworth, T.N., Briggs, D., Phillips, B. and Hoyland, R.W. CD shrinkage profiles of paper – Experiments on a commercial paper machine. Paper Technology 40, 63–70, 1999.
23. Suhling, J.C., Rowlands, R.E., Johnson, M.W. and Gunderson, D.E. Tensorial strength analysis of paperboard. Experimental Mechanics 25, 75–84, 1985.
24. Gibson, R. F. Principles of Composite Material Mechanics. McGraw-Hill Inc., 1994.
25. Yeh, K.C., Considine, J.M. and Suhling, J.C. The influence of moisture content on the nonlinear constitutive behavior of cellulosic materials. Proceedings of 1991 International Paper Physics Conference, Havaii, USA, 695–711, 1991.
26. Uesaka, T. General formula for hygroexpansion of paper. J. Mater. Sci. 29, 2373–2377, 1994.
27. Hibbitt, Karlsson and Sorensen Inc., 2006. ABAQUS Analysis User's Manual, Version 6.6.
28. Hibbitt, Karlsson and Sorensen Inc., 2004. ABAQUS Theory Manual, Version 6.6.
29. Avikainen, M., Markkanen, M. and Erkkilä, A.-L. Comparison of different average floc size and scale parameters of paper formation. Tappi Paper Physics Seminar, Trondheim, 169–171, 2004.
30. Christensen, R. M. Observations on the definition of yield stress. Acta Mech 196, 239–244, 2008.

31. Htun, M. and de Ruvo, M. Correlation between the drying stresses and the internal stresses of paper. Tappi J. 61, 75–77, 1978.
32. Niskanen, K., 1998. Papermaking Science and Technology, Part 16: Paper Physics, Fapet Oy.
33. Caulfield, D. Effect of moisture and temperature on the mechanical properties of paper. Solid mechanics advances in paper related industries: Proceedings of National Science Foundation workshop, Syracuse, NY, 50–62, 1990

PUBL. III

A.-L. Erkkilä, T. Leppänen and J. Hämäläinen, Empirical plasticity models applied for paper sheets having different anisotropy and dry solids content levels, *International Journal of Solids and Structures*, 50(14–15), 2151-2179, 2013.

International Journal of Solids and Structures 50 (2013) 2151–2179

Contents lists available at SciVerse ScienceDirect

International Journal of Solids and Structures

journal homepage: www.elsevier.com/locate/ijsolstr

Empirical plasticity models applied for paper sheets having different anisotropy and dry solids content levels

Anna-Leena Erkkilä [a,*], Teemu Leppänen [b,1], Jari Hämäläinen [c]

[a] Metso Paper, Inc., P.O. Box 587, FI-40101 Jyväskylä, Finland
[b] Magister Solutions Ltd., Hannikaisenkatu 41, FI-40100 Jyväskylä, Finland
[c] Lappeenranta University of Technology, P.O. Box 20, FI-53851 Lappeenranta, Finland

ARTICLE INFO

Article history:
Received 31 August 2012
Received in revised form 5 December 2012
Available online 21 March 2013

Keywords:
Paper
Elasto-plasticity
Anisotropy
Dry solids content

ABSTRACT

The rheological nature of paper or board is usually treated either as elasto-plastic or as viscoelastic depending on the studied paper making process or behavior in converting and end use. In this paper we study several stress–strain curve models and the determination of material parameters from an elasto-plastic point of view. Finally, a suitable approach for all stress–strain curves measured from 180 strips is constructed using a linear function for an elastic region and a nonlinear function for a strain hardening region. This model determines a proportional limit (elastic limit) and gives fairly elegant dependencies between material/fitting parameters and two important factors of mechanical properties of paper: dry solids content and anisotropy. In this paper the dependency of a plastic strain on dry solids content and anisotropy is estimated using the introduced stress–strain curve model. Correspondingly, the model can be used to estimate many other mechanical behaviors, for example, the tension differences arising from non-uniform moisture content of the paper web profile. However, the main target of this study is to produce competent parameters based on modeled stress–strain curves for further construction of a material model. This elasto-plastic material model will be utilized in out-of-plane deformation and fracture models.

1. Introduction

Mechanical properties of paper and board are important factors affecting the whole life-cycle of a product, including paper/board quality, production, converting and material and energy savings. Paper and board are mainly composed of natural fibers and their fragments, natural starch and mineral fillers and coatings. These components form an anisotropic and heterogeneous network, which mechanical properties are complicated result of the mechanical properties of raw materials, the bonds between fibers and network properties on the microscopic level (Niskanen, 1998). On the macroscopic level, paper can be described as elasto-visco-plastic nonlinear continuum material (Skowronski and Robertson, 1986). The mechanical properties of paper depend on several factors, which are common for most materials, such as temperature (Caulfield, 1990), production history (Silvy, 1971; Wahlström and Fellers, 2000) and anisotropy (Xia et al., 2002), but also factors that are typical for natural materials such as dry solids content (Kouko et al., 2007; Uesaka et al., 1989; Yeh et al., 1991) and the variation of raw material properties (Alava and Niskanen, 2006).

In paper manufacturing or the web-fed printing process, the continuous, moving paper web has to be transported from one paper/printing machine component to another. Tension is needed in the web velocity direction (machine direction, MD) when the paper web is moved from one roll surface to another. Within transportation from press section to drying section the dry solids content (DSC) of the paper web may be as low as 35%, while in other production stages it may increase up to 98%. The needed web tension is generated by straining the web in MD and controlled by velocity difference between supporting surfaces. When the generation and maintenance of suitable tension is considered, the time-dependent stress–strain behavior of both the wet and dry web is an essential factor. This strain controlled web transporting also generates plastic deformations on paper. Plastic deformations may vary locally and in different directions, because of irregularity in paper structure, anisotropy and processing conditions. These variations may contribute to several functionality or quality problems from roll defects to out-of-plane deformations like curl or cockling (see Fig. 1). Depending on application, mechanical behavior of paper is modeled as elastic (Johnson and Urbanik, 1984; Leppänen et al., 2005; Mann et al., 1979; Ostoja-Starzewski and Stahl,

* Corresponding author. Tel.: +358 20 482 150; fax: +358 20 482 6665.
E-mail address: anna-leena.erkkila@metso.com (A.-L. Erkkilä).
[1] Current location: JAMK University of Applied Science, P.O. Box 207, FI-40101 Jyväskylä, Finland.

0020-7683/$ - see front matter © 2013 Elsevier Ltd. All rights reserved.
http://dx.doi.org/10.1016/j.ijsolstr.2013.03.004

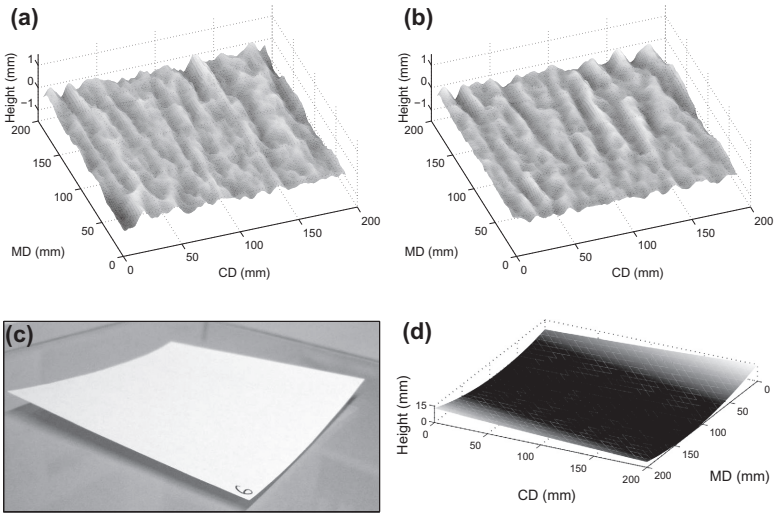

Fig. 1. Examples of out-of-plane deformations of paper: (a) measured cockling of newspaper sample, (b) simulated cockling, (c) picture of fine paper curl and (d) simulated curl. Simulations performed using model presented in Ref. Lipponen et al. (2008b).

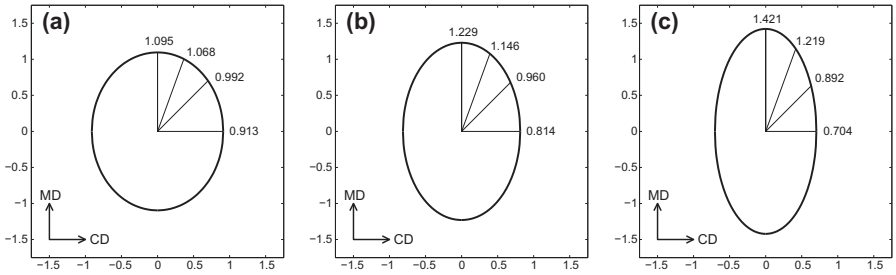

Fig. 2. Orientation distributions for anisotropy values (a) 1.20, (b) 1.51 and (c) 2.02. Twelve different ϕ values are shown in the distributions.

2000; Uesaka et al., 1979; Yeh et al., 1991), elasto-plastic (Castro and Ostoja-Starzewski, 2003; Lipponen et al., 2008b; Mäkelä and Östlund, 2003; Ostoja-Starzewski and Castro, 2003; Stenberg et al., 2001; Xia et al., 2002), viscoelastic (Brezinski, 1956; Lif et al., 2005; Lu and Carlsson, 2001; Steenberg, 1947; Uesaka et al., 1980, 1989) or sometimes even as viscoplastic (Coffin, 2008).

The ductile (or brittle) nature as well as material parameters of paper depends highly on fiber properties and their treatments, the paper making process (Setterholm and Chilson, 1964), paper structure anisotropy and ambient conditions such as humidity and temperature. Different paper grades, such as magazine, tissue, greaseproof or sac paper, are designed to fulfill the purpose of use. The testing of wet (DSC below about 65%) paper is challenging and only a few empirical studies of machine made papers with anisotropic structure are reported (Kouko et al., 2007). The "semi-wet" (DSC about from 70% to 85%) is an even more rarely studied area although many important mechanical and shrinkage phenomena are at their most intense phase at those dry solid contents (Land et al., 2010; Nanko and Wu, 1995). The stress–strain

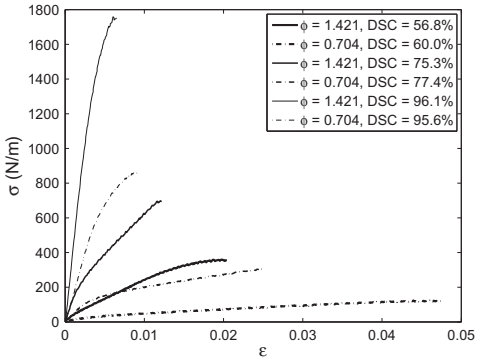

Fig. 3. Examples of different stress–strain curves of paper. Corresponding curves with fitted results for every fitting approach are presented in appendixes.

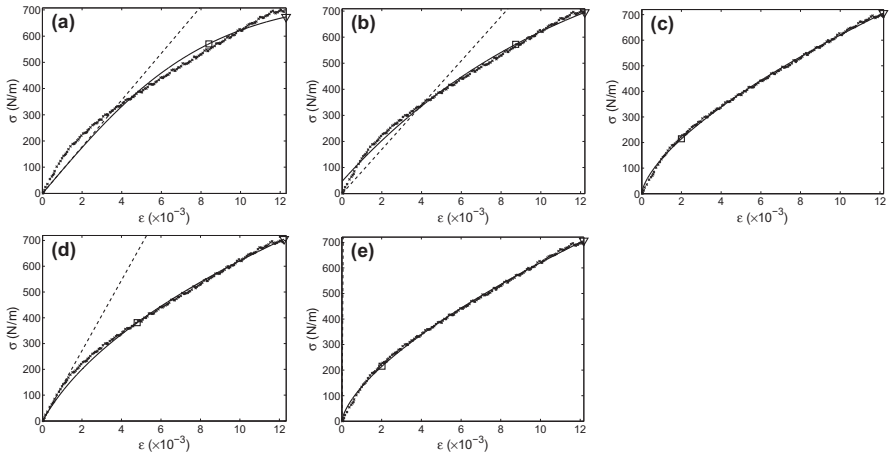

Fig. 4. Measured (marked by crosses) and fitted stress–strain curves (solid line) when different one region models are used. The offset point is marked with a square and the failure point with a triangle. If the model in question estimates the elastic modulus or finite slope at zero strain, it is drawn as a dashed line starting from the origin of the stress–strain diagram. Dry solids contents is 75.3% and anisotropy index $\phi = 1.421$. The models considered are (a) hyperbolic ($r^2 = 0.9807$), (b) exponential ($r^2 = 0.9952$), (c) power law ($r^2 = 0.9988$), (d) Ramberg–Osgood with fixed E ($r^2 = 0.9967$) and (e) Ramberg–Osgood with three free parameters ($r^2 = 0.9988$).

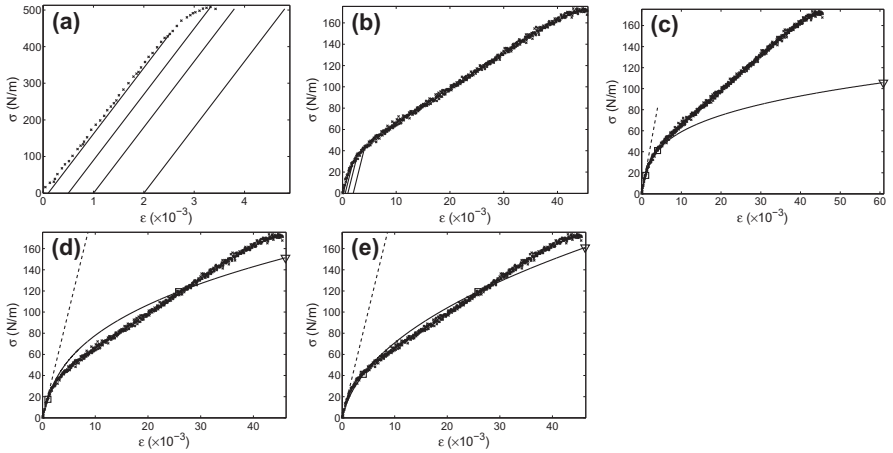

Fig. 5. The 0.01%, 0.05%, 0.1% and 0.2% offset lines have been drawn to different stress–strain diagrams. In (a) DSC = 96.4% and $\phi = 0.814$ while in (b) DSC = 66.3% and $\phi = 0.704$. The fitting using Hill's expression (Eq. (6)) is applied to the sample presented in (b) with different offset strains. Offset strains in (c) are 0.01% and 0.2%, in (d) 0.01% and 2% and in (e) 0.2% and 2%. Measured data points are marked with crosses, offset points with squares and failure points with triangles.

curve of paper contains a smooth transition from linear to non-linear behavior so that the well-defined yield point (elastic limit) does not exist. The difficulty of determining the paper's yield point is emphasized by such a rheological property of paper that, in addition to a time-independent component, the deformation has a time-dependent component, which may be observed as a delayed strain recovery at zero stress (Skowronski and Robertson, 1986).

The structural anisotropy arises from the paper making process, which usually orients fibers to align more along the machine direction than the transverse direction (cross direction, CD), so that fiber orientation distribution is virtually always anisotropic. In addition to fiber orientation anisotropy the level of mechanical anisotropy is affected by the paper making process in such a way that in the velocity direction of the web (MD) the tension needed for stable transfer increases the elastic modulus and decreases the breaking strain in that direction. In the transverse direction (CD) no external tension is applied and the web can deform more freely at the edges, although in the middle of the web the most shrinkage is prevented by internal forces.

In this study the main objective is to find a procedure to process experimental data of load-elongation tests into such a data set of material parameters, which can be utilized in construction of elasto-plastic material model and in structure and process based simulations of out-of-plane deformations (Lipponen et al., 2008a,b, 2009a) and fracture. The following requirements were set as targets for the approach:

1. The same fitting procedure (model) is capable of describing all measured cases from low DSC to high DSC as well as from low anisotropy to high anisotropy.
2. The yield point equal with the proportional limit can be defined and the elastic part ($\varepsilon < \varepsilon_y$) has to behave linearly. (The yield point, elastic limit and proportional limit are considered to be equal in this study.)
3. Modeled material parameters should behave as monotonic functions of DSC and anisotropy.

The determination of the plastic behavior is essential when the process induced phenomena are studied. An orthotropic elasto-plastic continuum mechanical model requires definition of yield point for the construction of suitable yield function. Such models

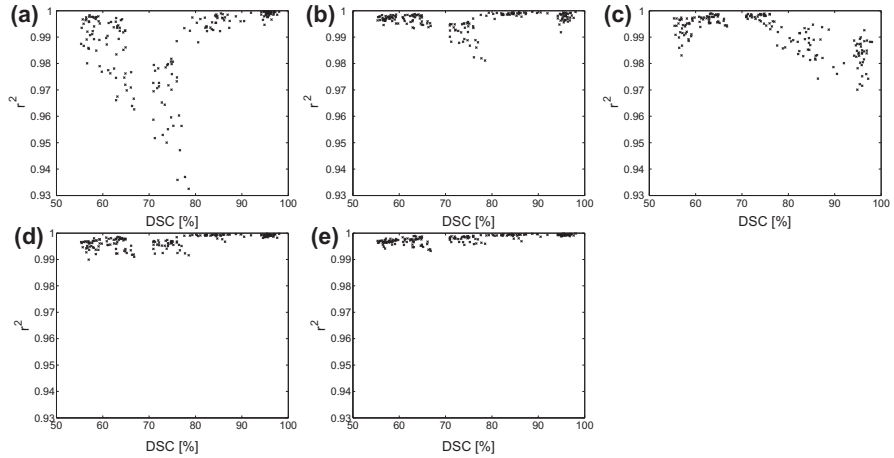

Fig. 6. Coefficient of determination r^2 in different DSC levels between measured and fitted curves when (a) hyperbolic, (b) exponential, (c) power law, (d) Ramberg–Osgood with fixed elastic modulus and (e) Ramberg–Osgood with three free fitting parameters is used.

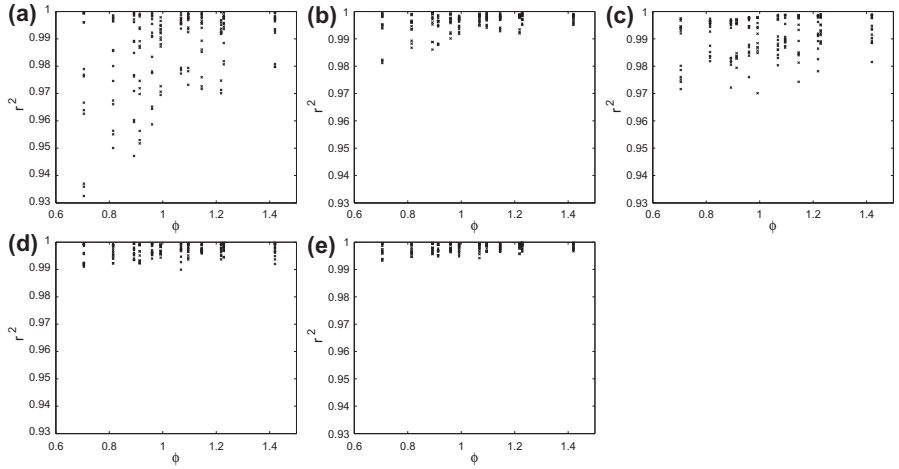

Fig. 7. Coefficient of determination r^2 in different anisotropy index levels between measured and fitted curves when (a) hyperbolic, (b) exponential, (c) power law, (d) Ramberg–Osgood with fixed elastic modulus and (e) Ramberg–Osgood with three free fitting parameters is used.

usually require linearity of the elastic region. The first and the third requirement arise from studied phenomena (for example cockling) where the local variation of the material properties and the conditions has to be covered simultaneously by the material model. The

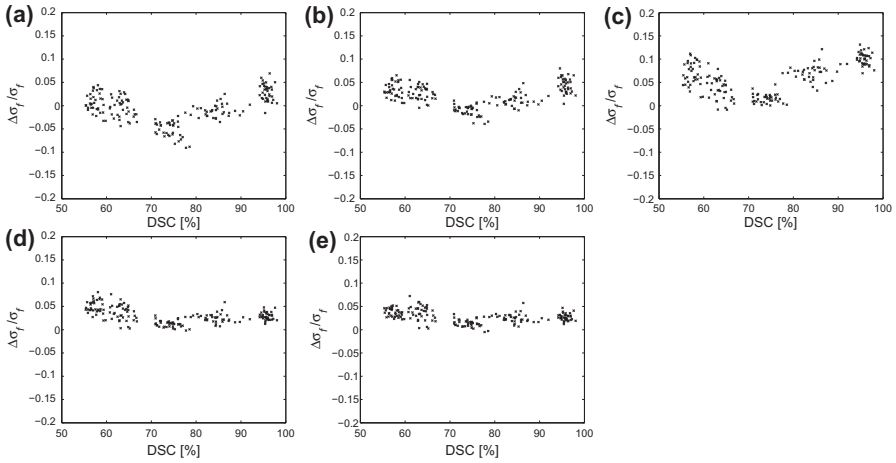

Fig. 8. Error in stress at failure between measured and fitted curves when (a) hyperbolic, (b) exponential, (c) power law, (d) Ramberg–Osgood with fixed elastic modulus and (e) Ramberg–Osgood with three free fitting parameters is used.

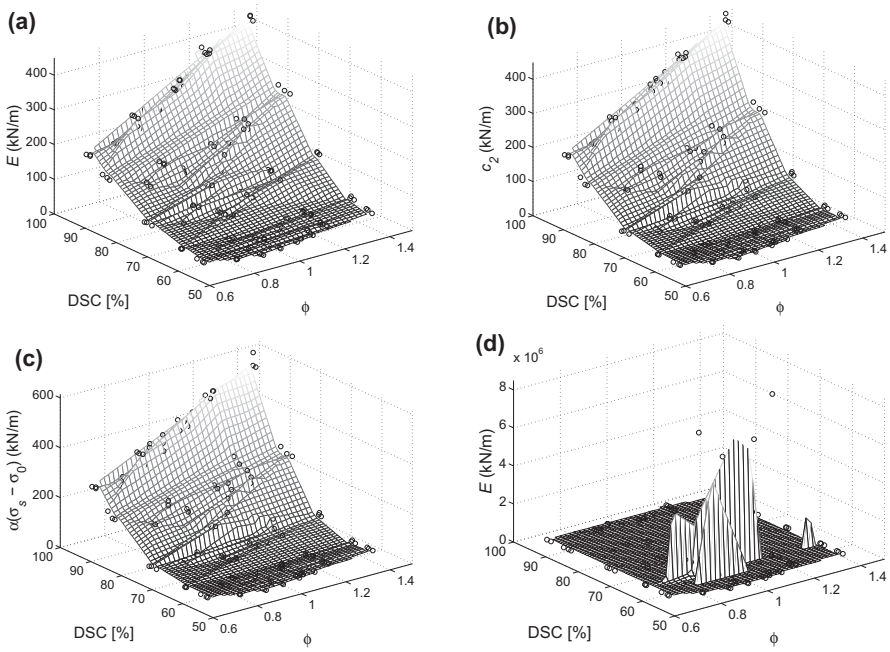

Fig. 9. Elastic modulus or derivative at zero strain as a function of DSC and anisotropy index (a) according Eq. (10), (b) hyperbolic, (c) exponential and (d) Ramberg–Osgood with three free parameters is used.

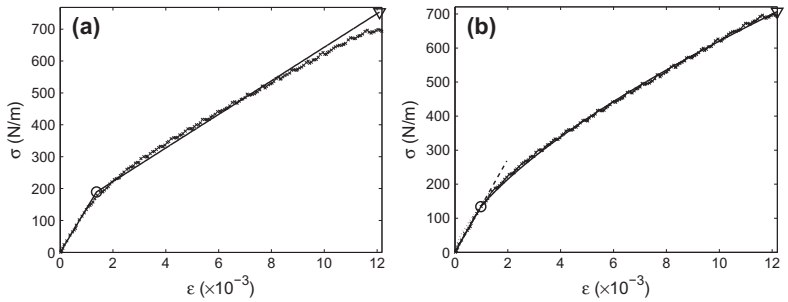

Fig. 10. Examples of measured (marked by crosses) and fitted stress–strain curves (solid line) when (a) bilinear ($r^2 = 0.9907$) and (b) linear-power law models (0.9992) are used. The yield point is marked with a circle and the failure point with a triangle. Dry solids content is 75.3% and anisotropy index $\phi = 1.421$.

third requirement is demanding or even impossible to satisfy if the true physical behavior of paper as a function of studied properties is not monotonic but still highly desirable, since the material model should be well-behaving also when it is subjected to extrapolation in deformation or fracture models. For example a high degree polynomial fitting is excluded as a possibility, since it usually goes wild at the edges and outside of region of the original data.

The empirical data consists of a large amount of uniaxial, load-elongation tests executed at different in-plane directions and applied to papers having a large variety of dry solids content and fiber orientation anisotropy. The tensile test material used in this study has been presented earlier and partly used in Ref. Lipponen et al. (2008b). In this current work the whole testing material of 180 tensile tests are used without any rejection or averaging processes. Several different single curve or two-segment stress–strain models are fitted to every load-elongation test separately. The goodness of fit as well as dependency of fitted material parameters on DSC and anisotropy is presented. Finally, a proposal of yield point determination is introduced and the chosen stress–strain model formulated in two regions is evaluated.

2. Nonlinear empirical stress–strain curve models

Several different approaches to characterize mechanical properties of sheet materials from stress–strain curves have been introduced in references (Hill, 1944; Ludwik, 1909; Prager, 1942; Ramberg and Osgood, 1943; Swift, 1952; Voce, 1948) and are applied to paper or cellulosic materials, for example, in references (Andersson and Berkyto, 1951; Castro and Ostoja-Starzewski, 2003; Johnson et al., 1979; Mäkelä and Östlund, 2003; Stenberg

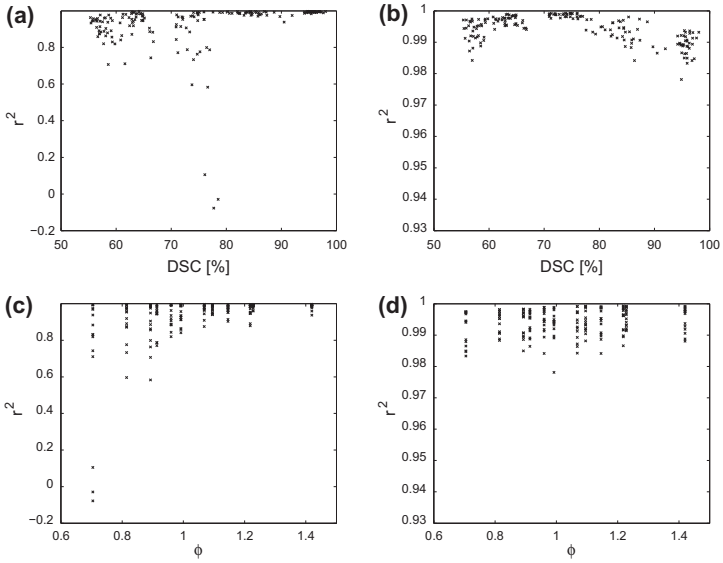

Fig. 11. Coefficient of determination r^2 in different DSC and anisotropy index levels between measured and fitted curves when bilinear ((a) and (c)) and linear-power law ((b) and (d)) models are used.

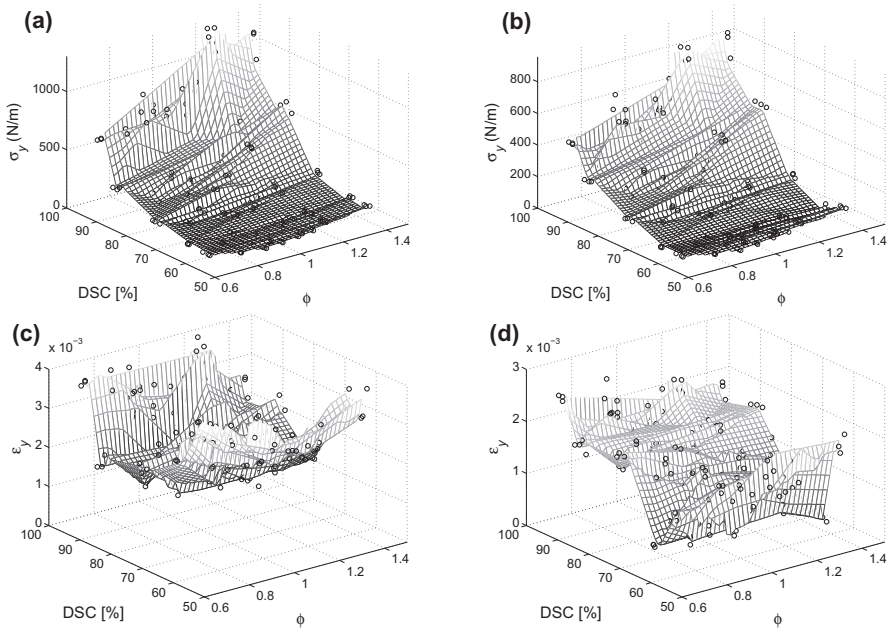

Fig. 12. Yield stress and strain as a function of DSC and anisotropy index when bilinear ((a) and (c)) and linear-power law ((b) and (d)) models are used.

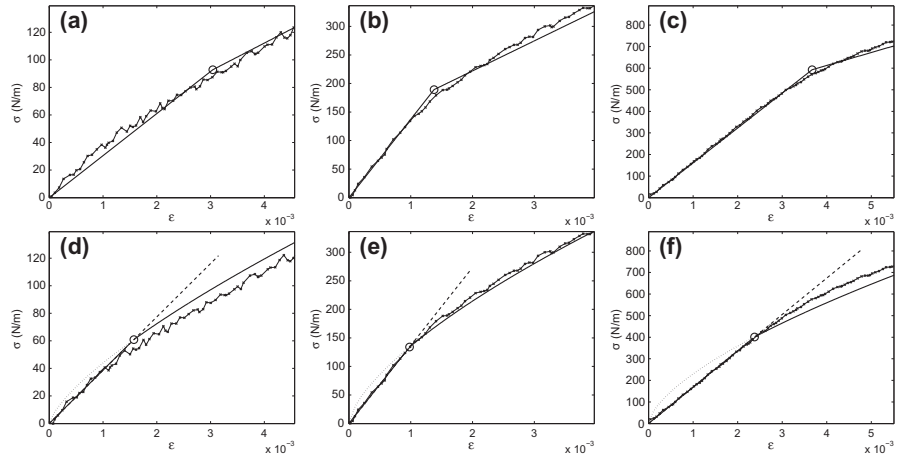

Fig. 13. Yield stress and strain determined by model. In (a)–(c) bilinear model and in (d)–(f) linear-power law model is used. In (a) and (d) DSC = 56.8%, $\phi = 1.421$, in (b) and (e) DSC = 75.3%, $\phi = 1.421$ and in (c) and (f) DSC = 95.6%, $\phi = 0.704$.

et al., 2001; Suhling et al., 1985; Urbanik, 1982). These methods have been developed to model either the overall curve shape or the material parameters, such as elastic modulus, yield point, yield offset, proportional limit, and tensile strength. If a material is considered as elasto-plastic, special interest is focused on yield point and hardening behavior.

The whole stress–strain curve and the transition from the elastic to plastic can be approximated by single continuous functions

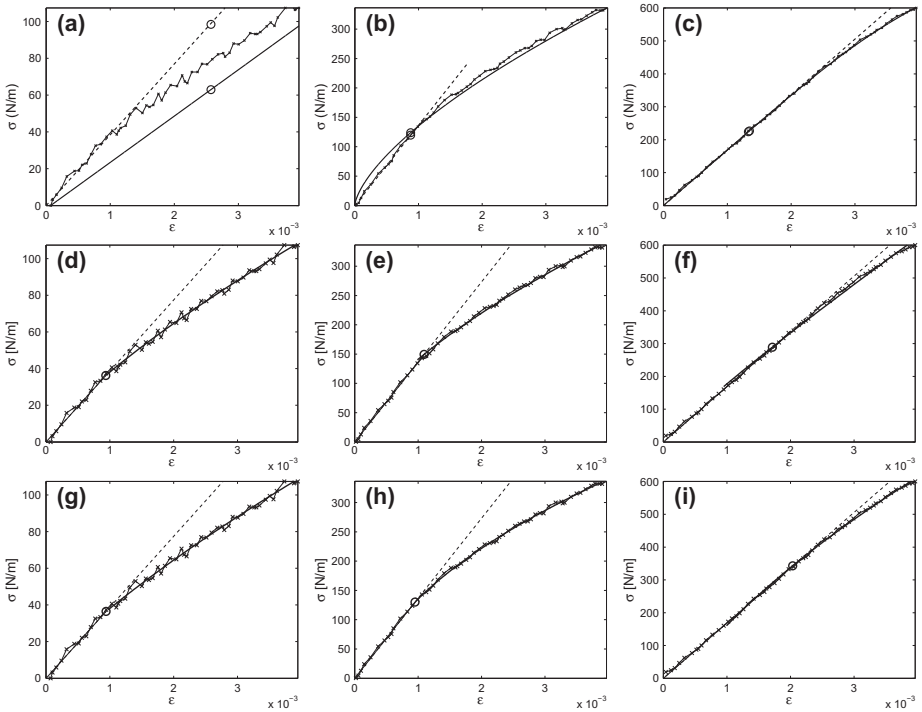

Fig. 14. Yield point determination using Ramberg–Osgood ((a)–(c)), power law ((d)–(f)) and parabolic ((g)–(i)) approach. Yield point marked by circle, measured data by crosses and f_e by dashed line. Dry solids contents and anisotropy indexes are in (a), (d) and (g) DSC = 56.8%, $\phi = 1.421$, in (b), (e) and (h) DSC = 75.3%, $\phi = 1.421$ and in (c), (f) and (i) DSC = 95.6%, $\phi = 0.704$.

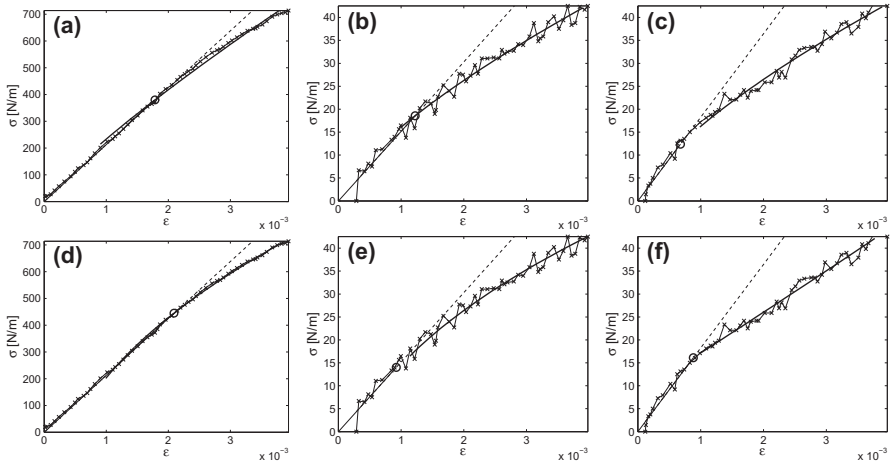

Fig. 15. Yield point determination using power law ((a)–(c)) and parabolic ((d)–(f)) approach. Yield point marked by circle, measured data by crosses and f_e by dashed line. Dry solids contents and anisotropy indexes are in (a) and (d) DSC = 95.8%, $\phi = 0.913$, in (b) and (e) DSC = 57.7%, $\phi = 0.960$ and in (c) and (f) DSC = 56.7%, $\phi = 0.992$.

such as hyperbolic, exponential or power law models. For nearly ideally plastic material the hyperbolic dependency between stress σ and strain ε in the form

$$\sigma = c_1 \tanh\left(\frac{c_2}{c_1}\varepsilon\right) \tag{1}$$

was introduced by Prager (1942) and also used directly or in modified form for the modeling of tension tests and edge-wise compression of paper or board (Andersson and Berkyto, 1951; Johnson et al., 1979; Urbanik, 1982). In Eq. (1) c_1 and c_2 are parameters to be determined from the data, c_2 is the initial slope of curve agreeing with elastic modulus and c_1 is the stress level which the curve approaches in an asymptotic manner.

The exponential function introduced by Voce (1948)

$$\sigma = \sigma_s + (\sigma_0 - \sigma_s)e^{-\alpha\varepsilon} \tag{2}$$

where σ_s, σ_0 and α are empirical parameters, is often applied for strain hardening, but in some cases also for total strain.

In its simplest form the power law proposed by Ludwik (1909) can be written as

$$\sigma = K\varepsilon^n \tag{3}$$

where K and n are parameters depending on the material. Eq. (3) predicts an infinite initial slope, but it can be used if the contribution of the elastic strain to the total strain is negligible. To accommodate the elastic range in the model the fitting of the power law may be applied only to strain hardening or some modified forms are used. The more generalized form of the power law is (Swift, 1952)

$$\sigma = K(C + \varepsilon)^n \tag{4}$$

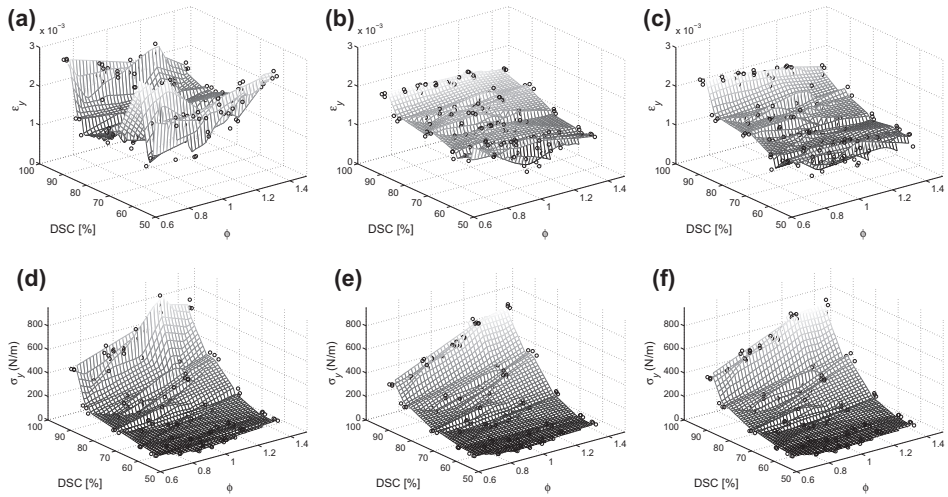

Fig. 16. Yield strain ((a)–(c)) and yield stress ((d)–(f)) as a function of DSC and anisotropy index. (a) and (d) estimated using Ramberg–Osgood, (b) and (e) by power law and (c) and (f) by parabolic approach.

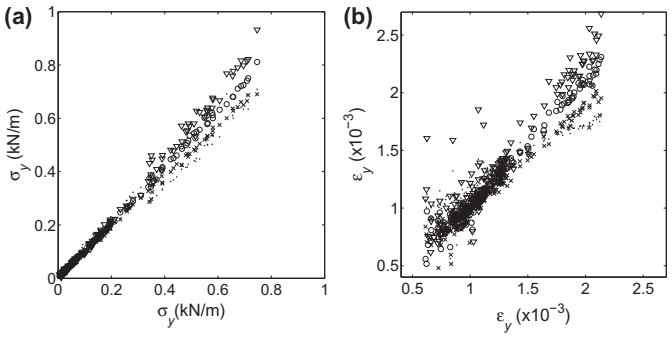

Fig. 17. Yield stress (a) and yield strain (b) determined by parabolic method (values given in horizontal axes) compared to power law method (dots) and parabolic method with specific fitting intervals (cross: 0.1–0.35, circle: 0.1–0.45, triangle: 0–0.45) (values given in vertical axes).

where C is an additional material dependent parameter. The Ramberg–Osgood relation (Ramberg and Osgood, 1943), which is a frequently used modification of the power law for ductile materials and sometimes also applied to paper (Mäkelä and Östlund, 2003), can be given in the form

$$\varepsilon = \frac{\sigma}{E} + \left(\frac{\sigma}{E_0}\right)^n \tag{5}$$

where E_0 and n are the hardening modulus and the hardening exponent. The fitting of the Ramberg–Osgood model is regularly applied using Hill's (1944) expression

$$\varepsilon = \frac{\sigma}{E} + \varepsilon_2\left(\frac{\sigma}{\sigma_2}\right)^n \tag{6}$$

where

$$n = \frac{\ln(\varepsilon_2/\varepsilon_1)}{\ln(\sigma_2/\sigma_1)}. \tag{7}$$

In Eq. (6) the modulus parameter E is determined a priori and only two offset points at offset strains ε_1 and ε_2 are needed for fitting. The corresponding offset stresses σ_1 and σ_2 are determined by the stress corresponding to the intersection of the stress–strain curve and a line parallel to the elastic part of the curve offset by a specified strain. This approach enables to estimate stress–strain relationship even in cases where only E and two offset points are available instead of whole stress–strain curve.

Even a good fit of a single continuous function on stress–strain data does not usually facilitate the determination of a yield point, if a yield point is not easily definable based on the shape of the stress–strain curve. The yield strength arbitrarily approximated by an offset method is commonly used for design and specification purposes because it avoids the practical difficulties of measuring

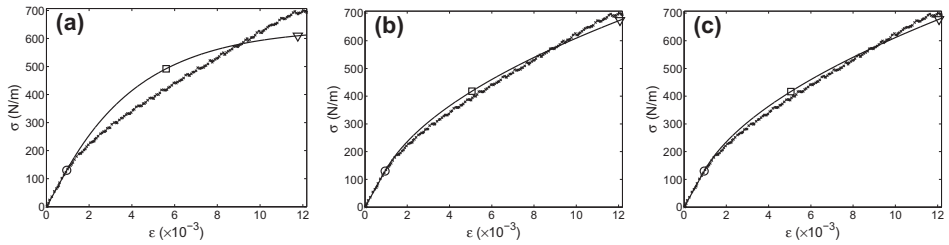

Fig. 18. Examples of measured (marked by crosses) and fitted stress–strain curves (solid line) when (a) exponential ($r^2 = 0.9205$), (b) parabolic ($r^2 = 0.9906$) and (c) power law ($r^2 = 0.9917$) models at the strain hardening region are used. Yield point is marked with circle, 0.2% offset point with square and failure point with triangle. Dry solids content is 75.3% and anisotropy index $\phi = 1.421$.

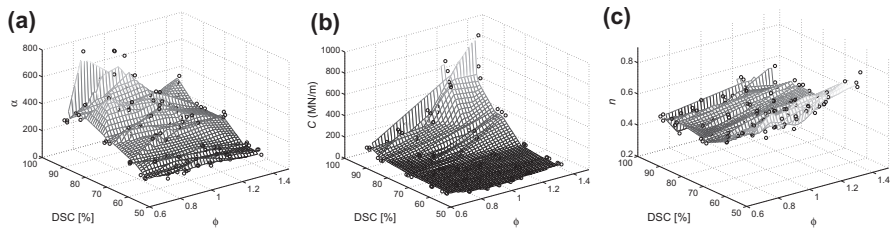

Fig. 19. Fitted strain hardening parameters for (a) exponential, (b) parabolic and (c) power law approach as a function of DSC and anisotropy.

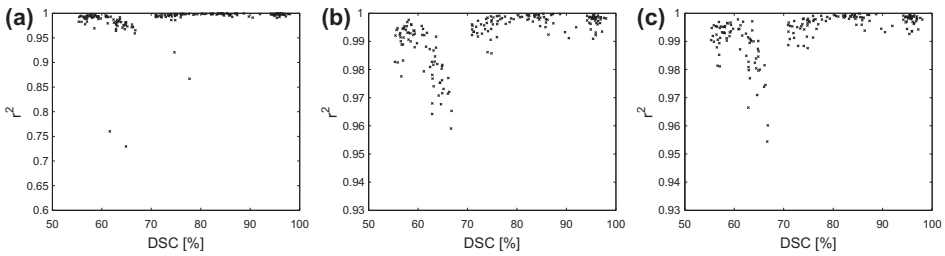

Fig. 20. Coefficient of determination as a function of DSC. Whole model with strain hardening region determined by (a) exponential, (b) parabolic, (c) power law functions. Coefficient of determination as a function of anisotropy index and errors related to failure point for (b) and (c) are presented in Fig. C.5.

the elastic limit or proportional limit. The offset strain is commonly selected to be a 0.1% or 0.2% for metals and 2% for plastics.

In some cases, the elasto-plastic analysis can be considerably simplified by using the stress–strain relation including two or more regions. The bilinear model can be used also as an approximation of the general nonlinear shapes of the stress–strain relations. In the bilinear model (Lipponen et al., 2008b; Ng et al., 2005; Saliklis et al., 2003; Stenberg et al., 2001) the two straight lines are joined at the yield point and the strain hardening is described with a linear function. The bilinear curve can be defined by the pair of equations

$$\sigma = \begin{cases} E\varepsilon & \text{if } \varepsilon \leqslant \varepsilon_y \\ \sigma_y + E_h(\varepsilon - \varepsilon_y) & \text{if } \varepsilon > \varepsilon_y \end{cases} \tag{8}$$

where σ_y and ε_y are the yield stress and the yield strain, E is the Young's modulus and E_h is the slope after the yield point.

The power law curve with its initial part replaced by a line of slope equal to E can be represented by the equation

$$\sigma = \begin{cases} E\varepsilon & \text{if } \varepsilon \leqslant \varepsilon_y \\ E\varepsilon_y(\varepsilon/\varepsilon_y)^n & \text{if } \varepsilon > \varepsilon_y \end{cases} \tag{9}$$

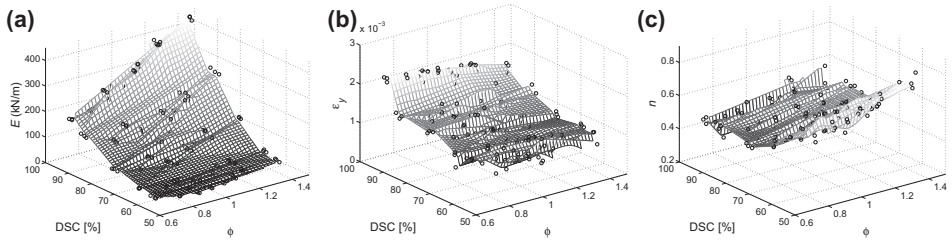

Fig. 21. Three fitting parameters of final model as a function of DSC and anisotropy index, when power law function is used in strain hardening region.

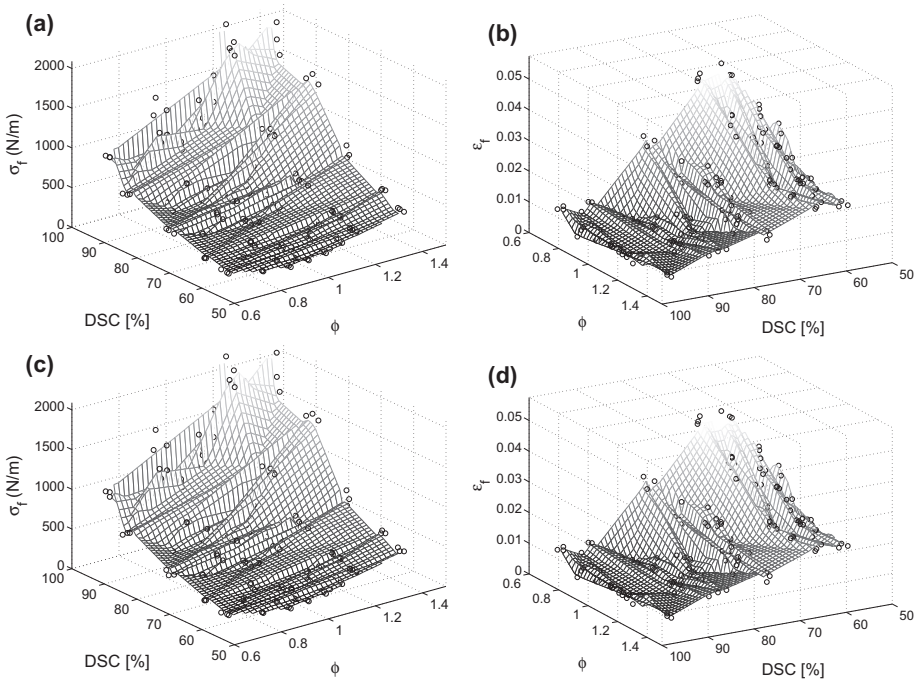

Fig. 22. Stress and strain at failure determined from measured ((a) and (b)) and modeled ((c) and (d)) stress–strain curves.

Both of these models constructed by two segments have strictly defined yield point and linear elastic behavior, but the slope at the yield point is discontinuous.

3. Samples, variables and methods

The fine paper samples with three different fiber orientation anisotropy levels were produced by Metso Paper's pilot machine 2. The dry solids contents varied from 53% to 56% at initial stage. This was the lowest achievable dry solids content level with the used pulp and minimum drying in the pilot machine process. The basis weight of samples were from 77 g/m^2 to 80 g/m^2. The stress–strain curves were measured from paper strips (width 20 mm) with a span length of 180 mm. Strips were cut from the long side along four different in-plane directions γ: 0°, 45°, 70° and 90° in relation to CD perpendicular to paper making direction (MD). The samples were dried in a tensile test machine to five target DSC levels: 55%, 65%, 75%, 85% and 95%. However, the measured DSC values during each measurement were read and used in studies instead of target DSC values. Drying shrinkage was prevented in the loading direction. The tensile stress caused by restrained shrinkage was, however, released by unloading a tensile

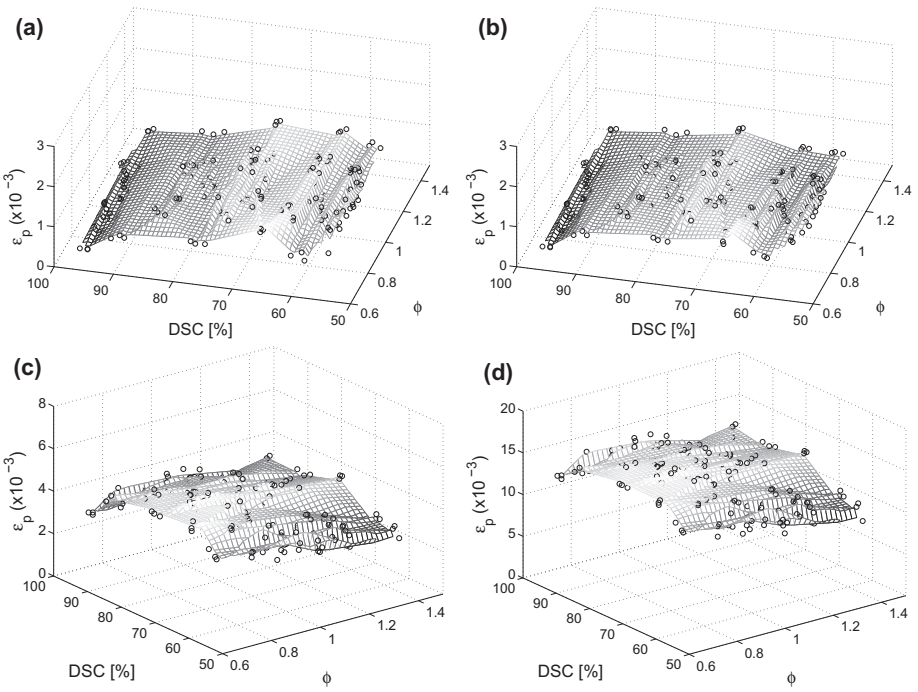

Fig. 23. The plastic strain as a function of DSC and anisotropy index (a) with elongation 0.3% determined from measured data using Eq. (22). In (b)–(d) plastic strain is estimated from modeled stress–strain curves (b) with elongation 0.3% (c) 0.8% and (d) 2%.

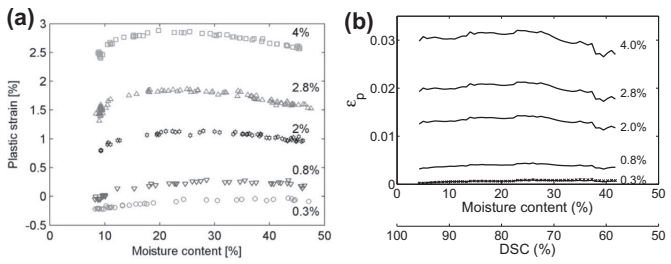

Fig. 24. In (a) plastic strain of isotropic handsheets measured using a load-unload test with different elongation levels (Land et al., 2010). In (b) plastic strain is determined from modeled stress–strain curves (solid lines) and from measured data using Eq. (22) (crosses).

test specimen before the load-elongation measurement was started. The three repetitions of measurements on each anisotropy, cutting direction and dry solids content combinations were performed. The description of the measuring method is presented in Ref. Lipponen et al. (2008b). In this study also the parallel results were used as individual test points so that the total amount of data in the fitting procedure was 180 individual stress–strain curves. At the initial stage, the apparent thickness of a paper sheet can be measured according to the standard ISO 534:2005 and the effective thickness using, for example, the methods presented in Refs. Setterholm (1984) and Schultz-Eklund et al. (1992). Still the non-uniformity, compressibility and porous structure of paper make the thickness of paper difficult to define. Hence, in the field of paper technology, it is rather common to express stress in the units that ignore the thickness of paper. For clarity this approach is also employed in this work i.e. the stress (load) is presented in units N/m instead of the load per unit cross-sectional area as reported for most materials. Obviously, the true stress during load-elongation test is practically indefinable.

For the determination of elastic modulus, E, the maximum slope of the linear function was determined by fitting lines on the data within constant elongation intervals:

$$E = \max S(\Delta\varepsilon), \quad \Delta\varepsilon = (\varepsilon - L/2, \varepsilon + L/2) \tag{10}$$

where S is the slope fitted to strain interval $\Delta\varepsilon$. The length of the strain interval used in this study is $L = 0.1\%$. With 180 mm distance of loading jaws, 10 mm/s straining speed and 0.8 kHz sampling frequency, it corresponds to about 15 measuring points.

The methods of linear and non-linear least squares are used to find solutions for fittings of stress–strain data with all different models. Because most fittings were nonlinear the goodness of fit is estimated using the general form of coefficient of determination defined by the equation

$$r^2 = 1 - \frac{\sum (\sigma_{estimated} - \sigma_{measured})^2}{\sum (\sigma_{measured} - \overline{\sigma_{measured}})^2} \tag{11}$$

When this definition is used, negative values of r^2 may also occur in cases where the mean of the measured data provides a superior fit when compared to the estimate of the model.

To estimate the failure point location on a fitted stress–strain curve, the strain energy at failure is first determined from the measured curve. The measured stress–strain curve is approximated by seventh degree polynomial and strain energy at failure, H_f, is calculated from integral

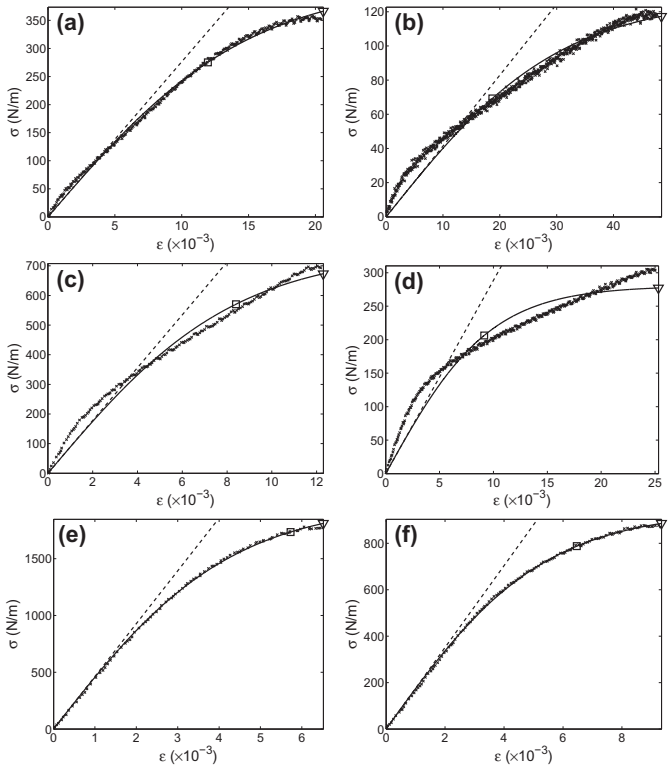

Fig. A.1. Examples of measured and fitted stress–strain curves when hyperbolic approach is used. The offset point is marked with a square, the failure point with a triangle and elastic modulus is shown with a dashed line. Dry solids contents, orientation levels and r^2 values are (a) DSC = 56.8%, $\phi = 1.421$, $r^2 = 0.9975$ (b) DSC = 60.0%, $\phi = 0.704$, $r^2 = 0.9763$ (c) DSC = 75.3%, $\phi = 1.421$, $r^2 = 0.9807$ (d) DSC = 77.4%, $\phi = 0.704$, $r^2 = 0.9370$ (e) DSC = 96.1%, $\phi = 1.421$, $r^2 = 0.9994$ (f) DSC = 95.6%, $\phi = 0.704$, $r^2 = 0.9995$.

$$H_f = \int_0^{\varepsilon_f} \sigma \mathrm{d}\varepsilon \tag{12}$$

Then the fitted failure point $(\sigma_f^{fit}, \varepsilon_f^{fit})$ is defined to be that point on the fitted curve where strain energy calculated from the fitted curve equals with the measured strain energy at failure. The accuracy of the estimated tension and strain at failure is evaluated by the relative error defined by $(fitted - measured)/measured$.

The fiber orientation distribution of paper is often approximated by elliptical distribution, the main direction of which usually coincides or deviates only a few degrees from the MD. The fiber orientation of samples were measured by the layered fiber orientation measurement method presented in Erkkilä et al. (1998) and Lipponen et al. (2009b). The anisotropy of fiber orientation distribution ξ is defined as a ratio of the maximum distribution value b and value in perpendicular direction to the maximum value a. In the layered fiber orientation method the paper is sectioned usually 8 to 15 paper layers from which the anisotropies are measured. These results of layers are averaged since, in this study, the anisotropy of whole sheet thickness is wished to be described. The measured averaged anisotropy values of the studied samples were 1.20, 1.51 and 2.02.

Now, there are three variables – DSC, anisotropy and loading direction – whose relations to material parameters are of interest. To reduce the amount of variables anisotropy index ϕ is introduced in this study. The anisotropy index is calculated for every strip depending on the mean of layered fiber orientation anisotropy $\xi = b/a$ and the direction γ of which the sample strip is cut and strained. Two assumptions are made: first the shape of orientation distribution is elliptical and secondly the area of orientation distributions of different orientation levels and samples can be normalized to the same constant value. For simplicity the area of orientation distribution is defined to be π. By these assumptions the semi-axes of the fiber orientation distribution ellipse will have values $a = 1/\sqrt{\xi}$ and $b = \sqrt{\xi}$. Then the equation for anisotropy index ϕ describing the distance of ellipse point from the origin in the direction γ can be written as

$$\phi_\gamma = \sqrt{\frac{1-\xi^2}{\xi + \tan^2\gamma/\xi} + \xi} \tag{13}$$

When four cutting/straining directions are measured from samples having three different anisotropy levels, in total 12 different anisotropy index ϕ values are obtained, see Fig. 2. Now the results of fitted material parameters can be presented as a function of only

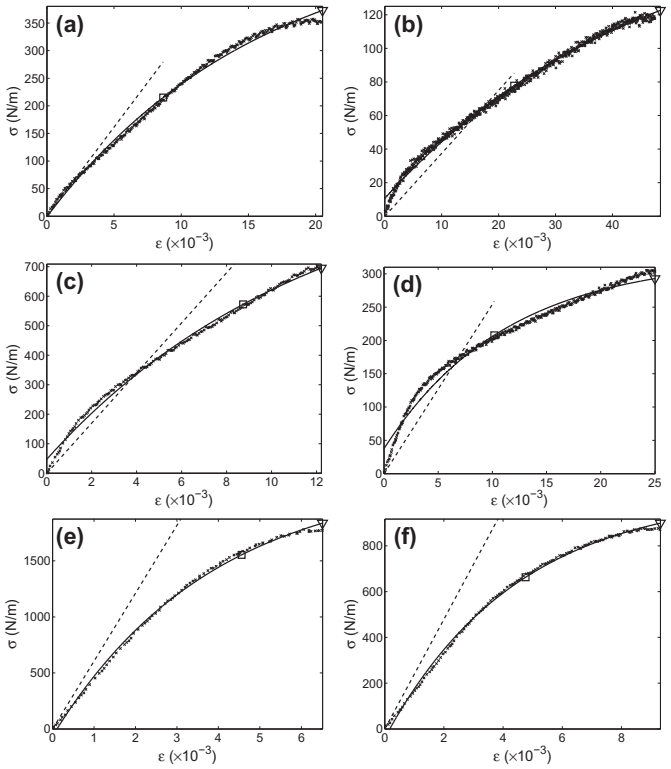

Fig. A.2. Examples of measured and fitted stress–strain curves when exponential approach is used. The offset point is market with a square, the failure point with a triangle and slope at zero strain is shown with a dashed line starting from origin. Dry solids contents, orientation levels and r^2 values are (a) DSC = 56.8%, $\phi = 1.421$, $r^2 = 0.9961$ (b) DSC = 60.0%, $\phi = 0.704$, $r^2 = 0.9951$ (c) DSC = 75.3%, $\phi = 1.421$, $r^2 = 0.9952$ (d) DSC = 77.4%, $\phi = 0.704$, $r^2 = 0.9820$ (e) DSC = 96.1%, $\phi = 1.421$, $r^2 = 0.9976$ (f) DSC = 95.6%, $\phi = 0.704$, $r^2 = 0.9980$.

two parameters, DSC and ϕ. The dependency of material parameters and fitted parameters as a function of DSC and anisotropy index is visualized as a surface formed from scattered data using linear interpolation.

4. Results and discussion

In this section several different models to describe the stress–strain behavior of paper are studied. These methods include commonly used approaches such as bilinear, hyperbolic, exponential, power law and Ramberg–Osgood approximations. By exploiting information from these approximations a modified approach to describe whole stress–strain behavior of paper is suggested. The target is to model a whole stress–strain curve and determine material parameters: elastic modulus, yield strain, yield stress and stress and strain at failure. Because with some stress–strain models the yield point as proportional limit has no expression, the yield offset 0.2% is also determined.

In Fig. 3 examples of different stress–strain curves of studied paper strips are presented to demonstrate the variety in behavior of elastic and strain hardening regions. The shape of the strain hardening region can vary from almost linear to non-linear. The drying history (restrained drying) has affected highly on the behavior of dry samples. At wet samples the nonlinear descending is in some cases observed at the end part of stress–strain curve, which may be considered as an indication of "necking", where at some location of the strip some portion of fiber–fiber bonds are already broken. This phenomenon is not accommodated to the model in this study.

4.1. Fittings using single continuous function

Examples of fitted curves and estimated material parameters of different one region models are presented in Fig. 4 and in Appendix A Figs. A.1–A.5.

In hyperbolic model (Eq. (1)) the parameter c_2 gives the slope of the curve at zero stress, and it is considered as an estimate of elastic modulus. The slope c_2 is also drawn in Figs. 4(a) and A.1 as a dashed line. The exponential relation and power law model were fitted to a whole load-elongation curve, although some samples include a significant elastic region. The exponential function has initial stress σ_0 and initial slope $-\alpha(\sigma_0 - \sigma_s)$ at zero strain. This slope of zero strain is drawn as a dashed line starting from origin of stress–strain diagrams in Figs. 4(b) and A.2. The power law model does not provide elastic modulus (slope at zero stress is infinite when $0 < n < 1$) and there is no approximation to a yield point,

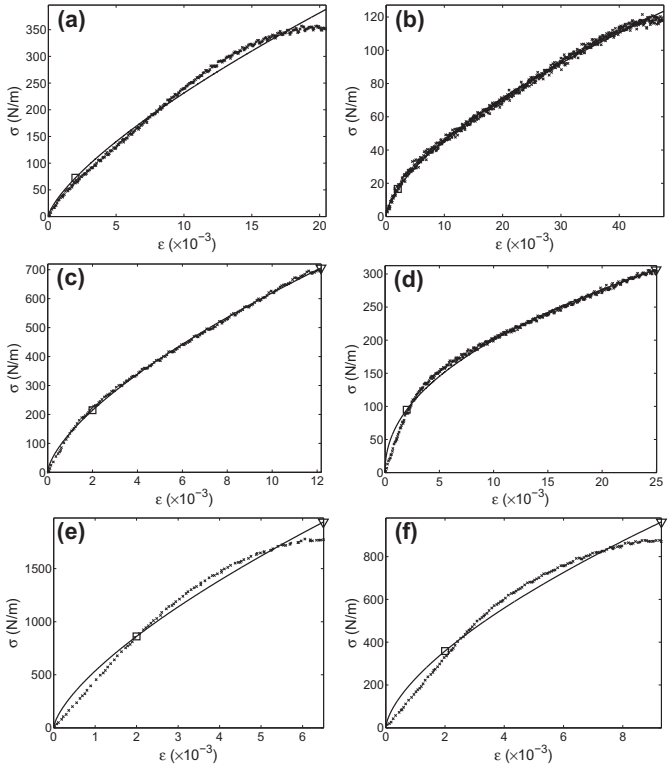

Fig. A.3. Examples of measured and fitted stress–strain curves when power law approach is used. The offset point is marked with a square and the failure point with a triangle. Dry solids contents, orientation levels and r^2 values are (a) DSC = 56.8%, $\phi = 1.421$, $r^2 = 0.9886$ (b) DSC = 60.0%, $\phi = 0.704$, $r^2 = 0.9967$ (c) DSC = 75.3%, $\phi = 1.421$, $r^2 = 0.9988$ (d) DSC = 77.4%, $\phi = 0.704$, $r^2 = 0.9919$ (e) DSC = 96.1%, $\phi = 1.421$, $r^2 = 0.9815$ (f) DSC = 95.6%, $\phi = 0.704$, $r^2 = 0.9751$.

but a stress at 0.2% strain is marked in examples presented at Figs. 4(c) and A.3.

The fitting of Ramberg–Osgood (R–O) model using Hill's expression (Eq. (6)) eliminates the possible convergence problems arising in R–O model fitting with three free parameters. By using the estimated elastic modulus (Eq. (10)) the required two offset points can be determined from the measured data. However, the usage of constant offset strains for the studied material is not straightforward, because of high diversity in stress–strain behavior between samples, which can be observed from examples presented in Fig. 5. The model fitted using Hill's expression goes exactly through the used offset stresses, which does not, however, guarantee a good fit over the whole stress–strain curve. In this study the direct least square curve fitting, using expression of Eq. (5), was preferred for fittings to find out how well the Ramberg–Osgood model approximates the whole stress–strain relationship.

Ramberg–Osgood fittings were first performed with two free parameters, n and E_0, and the elastic modulus E was determined according to Eq. (10). Good correspondences between fit and measured relationships were achieved this way, see for example Figs. 4(d) and A.4. These fitted parameters were used as initial estimates, when fittings with all three free parameters, E, n and E_0, were performed (examples in Figs. 4(e) and A.5). Now the convergence problems were confronted and with some samples the ultimate minimum was not achieved. It became evident that with some stress–strain relations the elastic modulus parameter E shows a tendency to grow to some very high value or even toward infinity. The increase of slope of elastic modulus can be observed comparing Fig. 4(d) and (e), where the slope is visualized as a dashed line. If E grows to infinity the Ramberg–Osgood equation returns to a simple power law model. This might be considered to be an indication that there is no linear elastic part existing at stress–strain curve in the consideration, or that the linear part is insignificant. By examining the measured data presented at Fig. 4 the short but distinguishable linear part at the beginning of the loading measurement can be observed.

The coefficient of determination r^2 between measured and fitted stresses are presented for all reference methods as a function of dry solids content of the sample strip during stress–strain measurement (Fig. 6) and anisotropy index (Fig. 7). For all continuous single function models all r^2 values are quite high (r^2 is always over 0.93). However the $r^2 = 0.93$ may already signify quite a consider-

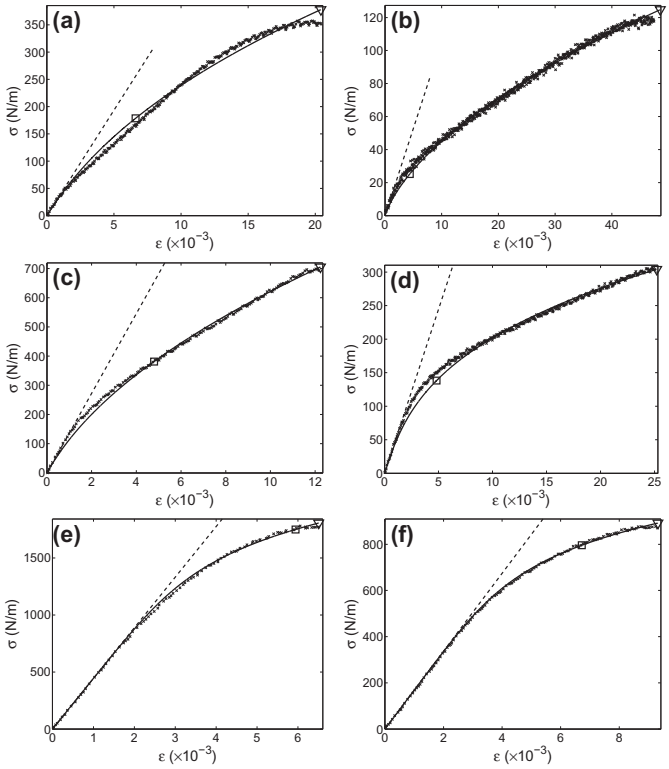

Fig. A.4. Examples of measured and fitted stress–strain curves when Ramberg–Osgood approach with fixed elastic modulus and two free parameters is used. The offset point is marked with a square, the failure point with a triangle and elastic modulus is shown with a dashed line. Dry solids contents, orientation levels and r^2 values are (a) DSC = 56.8%, $\phi = 1.421$, $r^2 = 0.9920$ (b) DSC = 60.0%, $\phi = 0.704$, $r^2 = 0.9956$ (c) DSC = 75.3%, $\phi = 1.421$, $r^2 = 0.9967$ (d) DSC = 77.4%, $\phi = 0.704$, $r^2 = 0.9923$ (e) DSC = 96.1%, $\phi = 1.421$, $r^2 = 0.9991$ (f) DSC = 95.6%, $\phi = 0.704$, $r^2 = 0.9995$.

able deviation of estimate from the measured behavior, see for example Fig. A.1(d). The DSC has more significant effect on goodness of fit than anisotropy index level in case of all studied models.

A relative error of stress at failure is presented as a function of DSC in Fig. 8. With every model the error is always between −0.1 and 0.15. The behavior of elastic modulus estimated by Eq. (10), hyperbolic, exponential and Ramberg–Osgood approaches are visualized in Fig. 9 as a function of DSC and anisotropy index. The elastic modulus has some equality in trend between hyperbolic, exponential and maximum slope (Eq. (10)) approaches. The Ramberg–Osgood model gives a few extremely high values as was demonstrated above. The behavior of other fitted parameters are presented in Fig. A.6.

The Ramberg–Osgood model gives a good fit for every measured stress–strain cases. The problems arise more from the fitting procedure itself and the tendency of the model to approach a simple power law expression if the elastic range is small compared with the strain hardening region of the stress–strain curve. The insuperable fact is that as well as hyperbolic, exponential and power law model, the Ramberg–Osgood stress–strain curves are continuously curved, i.e., no definitive linear elastic region exists followed by a well-defined yield stress. This means that none of these models is directly appropriate for our requirements. When the focus of study is on plasticity the power law and exponential models are often applied only to the strain hardening region and several approaches with two or more regions' stress–strain curve models (Nadai, 1931; Hoffman and Sachs, 1953; Jones, 2009; Lipponen et al., 2008b; Ng et al., 2005; Saliklis et al., 2003; Stenberg et al., 2001) are presented. With the groundwork presented in this subsection, two segment models, with special focus in estimation of proportional limit, are discussed in the next two subsections.

4.2. Elasto-plastic stress–strain models including two regions

In the viewpoint of further modeling the advantageous character of two segment models are that they define the exact yield point (proportional limit). The unfavorable facet is that the amount of fitting parameters of the model increases with complicity. To start with the most simple alternatives, the bilinear and linear-power law combinations, are studied in this subsection.

Although there might have been some more optimal way to progress with the bilinear method when the measured material of this study is considered, the method presented by Stenberg et al. (2001) is followed faithfully. The first linear part was fit to

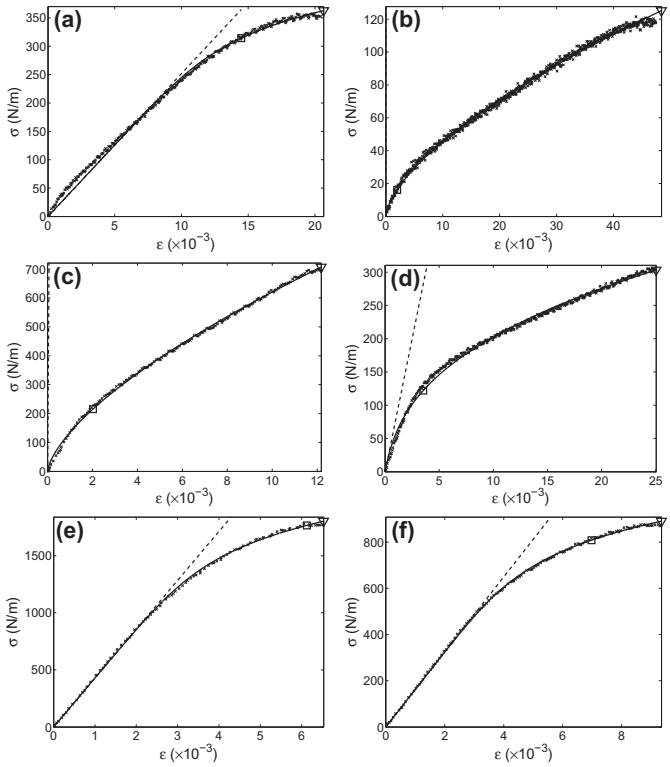

Fig. A.5. Measured and fitted stress–strain curves when Ramberg–Osgood approach is used. The offset point is marked with a square, the failure point with a triangle and elastic modulus is shown with a dashed line. Dry solids contents, orientation levels and r^2 values are (a) DSC = 56.8%, $\phi = 1.421$, $r^2 = 0.9966$ (b) DSC = 60.0%, $\phi = 0.704$, $r^2 = 0.9967$ (c) DSC = 75.3%, $\phi = 1.421$, $r^2 = 0.9988$ (d) DSC = 77.4%, $\phi = 0.704$, $r^2 = 0.9964$ (e) DSC = 96.1%, $\phi = 1.421$, $r^2 = 0.9994$ (f) DSC = 95.6%, $\phi = 0.704$, $r^2 = 0.9996$.

data between zero load and 20% of maximum load. In reference the upper limit was expected to be well below the yield point which is certainly true for the compressive tests of Ref. Stenberg et al. (2001), but this may not always be true for the in-plane tensile tests of the wet samples studied in this work. Then the fitted elastic part is removed from the data and the second line is fitted to strain interval 0 and 0.005 in this modified stress–strain curve. The estimate of the elastic limit is obviously now in the interception of these two lines, the dependence of which on DSC and anisotropy index are shown in Fig. B.1.

The linear-power law combination (Eq. (9)) is formed by substituting the beginning of the power law curve fitted in the previous subsection by line with slope E determined using Eq. (10) until the line intersects the power law curve. The strain at intersection i.e. estimated yield strain can be directly calculated by the equation

$$\varepsilon_y = \frac{E}{K} e^{(n-1)^{-1}} \tag{14}$$

The examples of fittings of models according to Eqs. (8) and (9) are presented in Figs. 10, B.2 and B.3. The coefficient of determination r^2 as function of DSC and anisotropy index are presented in Fig. 11. The bilinear model has a few negative r^2 values in semi-wet samples indicating that the mean of measured stress values would have been better estimate than fitted result (see f.ex. Fig. B.2(d)). The substitution of the beginning of the power law fitting by linear component increases the r^2 values when compared to the simple power law model (Figs. 6 and 7). The improvement is emphasized with dry samples, the linear regions of which are longer than wet samples.

The dependency of yield stress and yield strain on DSC and anisotropy index are presented in Fig. 12. The difference in yield

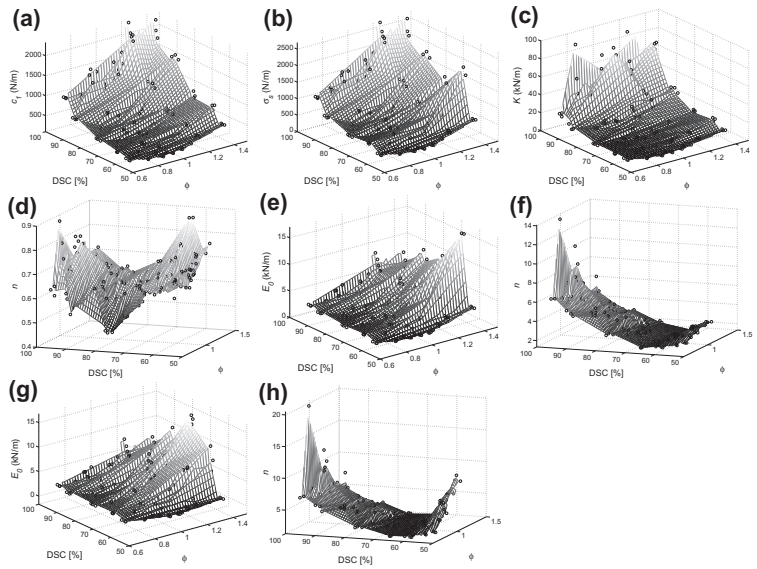

Fig. A.6. Dependences of fitted parameters on DSC and anisotropy index when one region models are used: (a) hyperbolic c_1, (b) exponential σ_s, (c) power law K, (d) power law n, (e) R–O with fixed E E_0, (f) R–O with fixed E n, (g) R–O with three free parameters E_0 and (h) R–O with three free parameters n.

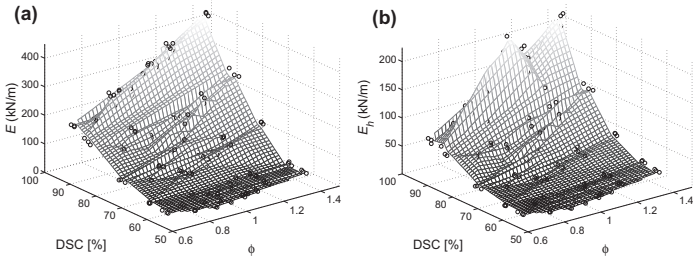

Fig. B.1. Elastic modulus (a) and slope of the yield hardening (b) as a function of DSC and anisotropy index when Stenberg's bilinear approach is used.

point behavior between models is noticeable when the yield strain surfaces are studied. Both methods estimate the yield strain to be the lowest with semi-wet samples. The increasing tendency of the yield strain when DSC decreases is against the general assumptions. For a closer investigation of the yield point determination, a few examples are presented in Fig. 13. The quality of the fits is unsatisfactory at the area of interest, which is the main reason for the unreliable yield point results. The overall goodness of fit of the bilinear model would have been improved by fitting the second line to the whole strain hardening region but this would have further decreased the fitting quality at the proportional limit region. The linear power law combination, however, shows some promising results. In the next subsection the determination of the proportional limit is studied more closely.

4.3. Yield point and model

The proportional stress is sometimes determined by using the intersection of the stress–strain curve and offset line or by line which slope is reduced from initial inclination by some percent value. With offset approaches, the goodness of fit of the initial line or elastic modulus and noisiness of the measurement data has a devastating effect on reliability; there are also opinions that for stress–strain curves such as those studied in this work the determination of the proportional limit always creates controversies because the deviation from linear dependency begins so gradually that the exact stress at which the line begins to curve cannot be determined. Obviously any offset method cannot give a true proportional limit and the high variety of load-elongation curves processed in this study makes it even more difficult to find reliable estimate of the proportional limit in every case by systematic way.

In this subsection the studies of proportional limit determination are based directly on the definition of proportional limit, that is, the proportional limit is the point at which the load-elongation curve deviates from linearity. The general idea is to determine that specific point of the stress–strain curve where the nonlinear model starts to have a better fit to the data than the linear function fitted to the beginning of the stress–strain curve. This point is then defined as the proportional limit. For nonlinear function fittings the three candidates were tested: the fittings of the Ramberg–Osgood model with three free parameters presented in the previous subsection, and power law and parabolic fittings on the proportional limit region.

The Ramberg–Osgood model proved previously to have high goodness of fitting. The sum of squared residuals between measured data and Ramberg–Osgood model, $SSR_i(f_{RO})$, and between

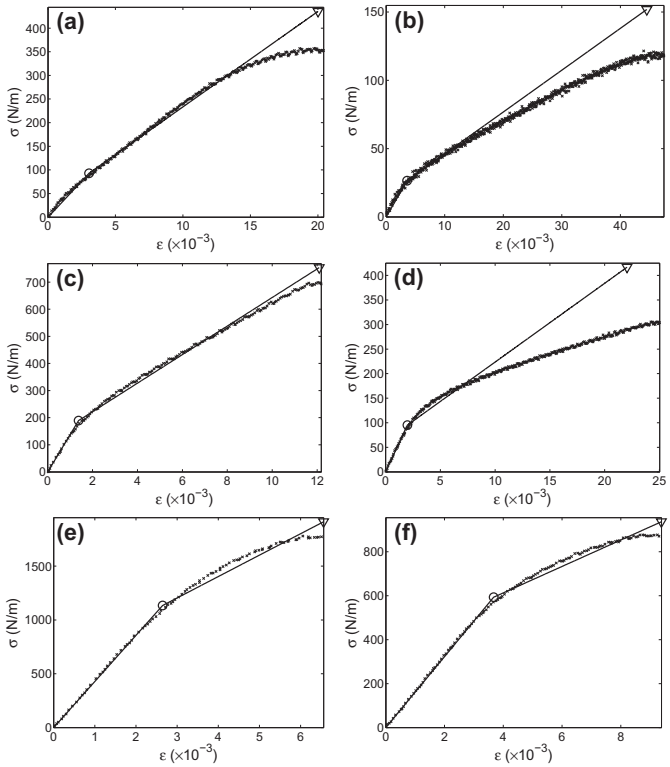

Fig. B.2. Measured and fitted stress–strain curves when Stenberg's bilinear approach is used. The yield point is marked with a circle and the failure point with a triangle. Dry solids contents, orientation levels and r^2 values are (a) DSC = 56.8%, $\phi = 1.421$, $r^2 = 0.9374$ (b) DSC = 60.0%, $\phi = 0.704$, $r^2 = 0.7108$ (c) DSC = 75.3%, $\phi = 1.421$, $r^2 = 0.9907$ (d) DSC = 77.4%, $\phi = 0.704$, $r^2 = -0.0777$ (e) DSC = 96.1%, $\phi = 1.421$, $r^2 = 0.9935$ (f) DSC = 95.6%, $\phi = 0.704$, $r^2 = 0.9954$.

measured data and linear fitting with slope E (Eq. (10)), $SSR_i(f_e)$, were calculated at all data points i using interval $(i-2, i+2)$. The maximum position i, were the $SSR_i(f_e)$ is still lower than $SSR_i(f_{RO})$ was determined as location of proportional limit in stress–strain curve.

The aim was to fit the power law and parabolic fittings only to the region where the stress–strain curve starts to deflect from linear behavior to guarantee a high goodness of fittings around the proportional limit. The power law function of the form of Eq. (3) and parabolic dependency of the form

$$\varepsilon = C_1\sigma^2 + C_2\sigma + C_3 \tag{15}$$

where C_1, C_2 and C_3 are fitted constants, were fit to strain interval from 0.1% to 0.4%. This interval may be expected to comprise proportional limit according preliminary study of previous subsection (see Fig. 12).

The goodness of fitting of two different functions fitted to same measuring data has to be equal at that infinitesimal position where those functions intersect. This intersection point can then be directly used as a proportional limit estimate when the power law or parabolic approaches are considered. The intersection of power law and linear equation can be simply calculated using Eq. (14). In a few cases of parabolic fittings no intersection between linear and parabolic fitting occurred. At these cases that point at which the tangents of linear and parabolic fittings are equal was used as a proportional limit. Hence the proportional limit using parabolic fitting was determined using the pair of equations

$$\varepsilon_y = \begin{cases} \left(-C_2 + 1/E + \sqrt{2C_2 - 2/E - 4C_1C_3}\right)/2C_1 \\ \quad \text{if } 2C_2 - 2/E - 4C_1C_3 \geqslant 0 \\ 0.5(1/E - C_2)/C_1 \\ \quad \text{otherwise} \end{cases} \tag{16}$$

where the first equation calculates the intersection point and the second equation the point of the equal tangents which is used if no intersection occurs.

Three examples of proportional limit determination of each studied method are presented in Fig. 14. Although all Ramberg–Osgood fittings have high values of coefficient of determination they do not, in most cases, guarantee adequate fitting quality in that important region where the stress–strain curve starts to deflect from linear behavior. On the other hand, in some cases of dry samples where Ramberg–Osgood fits perfectly at the beginning of the stress–strain curve, it behaves so linearly in that area that the comparison of the linear and R–O fit gives random results, which are mostly sensitive to measurement inaccuracy (see Fig. 14(c)).

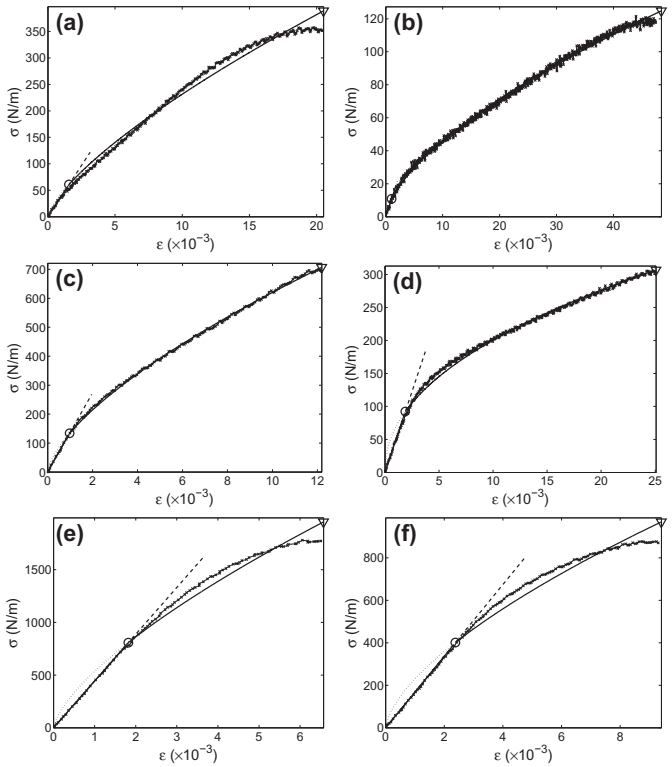

Fig. B.3. Measured and fitted stress–strain curves when power law fit for the strain hardening region is used. The yield point is marked with a circle and the failure point with a triangle. Dry solids contents, orientation levels and r^2 values are (a) DSC = 56.8%, $\phi = 1.421$, $r^2 = 0.9888$ (b) DSC = 60.0%, $\phi = 0.704$, $r^2 = 0.9967$ (c) DSC = 75.3%, $\phi = 1.421$, $r^2 = 0.9992$ (d) DSC = 77.4%, $\phi = 0.704$, $r^2 = 0.9972$ (e) DSC = 96.1%, $\phi = 1.421$, $r^2 = 0.9881$ (f) DSC = 95.6%, $\phi = 0.704$, $r^2 = 0.9849$.

The power law and parabolic methods give equivalent results for the proportional limit in several cases. Again the challenge with dry samples is the long linear part where the deviation begins so gradually from the linear behavior that the result is very sensitive to the fitting quality of both linear and nonlinear parts. The power law model, which is forced to go through the origin, does not fit perfectly on those cases and may underestimate the proportional limit (see Fig. 14(f)). The semi-wet and wet samples appear to have a more definite location where the linear part connects to the nonlinear part, but with the wet samples the challenge is arising from very short linear part and high noisiness of stress data. The apparent advance of power law and parabolic fittings is that they average smoothly the trend through noisiness.

Three more examples of two promising methods (power law and parabolic) are presented in Fig. 15. A risk of parabolic fitting is that the trend bends too fast and the intersection of parabolic and linear functions occurs at too low a stress level. This depends also on the interval of which set of data points the parabolic fitting is performed. Interestingly, if the slope of the measured curve starts to increase again after the proportional limit, the parabola may turn to open down (left) (see Fig. 15(f)).

The yield stress and yield strain as a function of DSC and anisotropy index is presented in Fig. 16. The surface of the yield strain estimated using the Ramberg–Osgood method has some similar irregularity as was studied in the previous subsection (Fig. 12). However, the estimates of the yield stress using the power law and parabolic methods form fairly smooth surfaces. The power law method estimates lower yield strains of dry samples than the parabolic method, because the quality of the power law fit is not excellent for those samples as was discussed earlier. This is the main reason why in the next fittings the yield point estimated by the parabolic method (see Fig. C.1) is used. To test the robustness of the parabolic method, the fitting intervals were varied. The results are presented in Fig. 17, showing that the determination of the proportional limit is quite insensitive to small variations of fitting interval and suggesting that it may be utilized with a high variety of samples.

The model function f_h fitted to the strain hardening section has to go through the proportional limit. Here an additional condition is set for the model: the slope f_h' (first degree derivative) has to be continuous at the connection point (proportional limit) of the functions. If the strain hardening model has three unknown

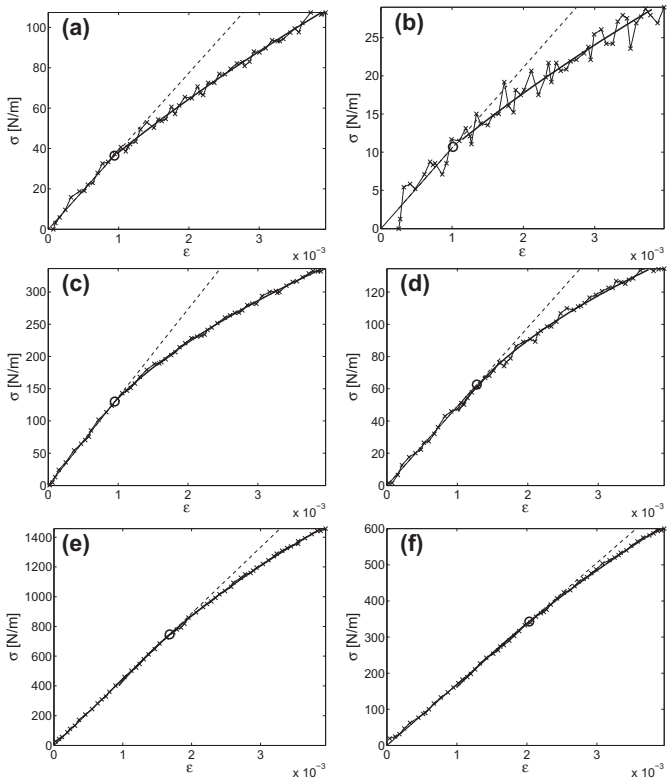

Fig. C.1. Focusing into yield point determination when linear part and parable are fitted. The yield point is marked with a circle. Whole curves utilizing this determination are shown in Figs. C.2, C.3 and C.4. Dry solids contents and orientation levels are (a) DSC = 56.8%, $\phi = 1.421$ (b) DSC = 60.0%, $\phi = 0.704$ (c) DSC = 75.3%, $\phi = 1.421$ (d) DSC = 77.4%, $\phi = 0.704$ (e) DSC = 96.1%, $\phi = 1.421$ (f) DSC = 95.6%, $\phi = 0.704$.

parameters, the two of them can be fixed using a pair of equations based on conditions

$$\begin{cases} f_h(\varepsilon_y) = E\varepsilon_y \\ f_h'(\varepsilon_y) = E \end{cases} \tag{17}$$

By starting with exponential function (2) and inserting it to Eq. (17) the form

$$\sigma = E\varepsilon_y + \frac{E}{\alpha}\left(1 - e^{-\alpha(\varepsilon-\varepsilon_y)}\right) \tag{18}$$

can be solved. Equivalently for parabolic Eq. (15) the form

$$\sigma = E\varepsilon_y - \frac{C}{2E} + \sqrt{C\left(\frac{C}{4E^2} + \varepsilon - \varepsilon_y\right)} \tag{19}$$

and for power law Eq. (4) the form

$$\sigma = E\varepsilon_y\left(\frac{n-1}{n} + \frac{\varepsilon}{n\varepsilon_y}\right)^n \tag{20}$$

can be solved. All these equations include only one additional fitting parameter, constant α in exponential, C in parabolic and n in power law model. The examples of the fitting results are presented in Fig. 18. The one fitting parameter ensures the simplicity of fitting procedure, but does not assure that fitted parameter has monotonic dependency of DSC and anisotropy index (see Fig. 19). The goodness of fit of the whole stress–strain curve model utilizing either Eq. (18), (19) or (20) model at strain hardening is presented in Fig. 20. The exponential approach (example curves in Fig. C.2) is not acceptable either according to the fitting quality or behavior of parameter α. The power law and parabolic (example curves in Figs. C.3 and C.4) fittings are quite even in goodness of fit and the surfaces of the parameters in Fig. 19 are both moderately smooth although clearly different in character. Both models including either the power law or parabolic form for strain hardening may be good alternatives for further material modeling.

If the power law function to describe the strain hardening is chosen as is done in the next studies, the final model can be summarized to be in the form

$$\sigma = \begin{cases} E\varepsilon & \text{if } \varepsilon \leqslant \varepsilon_y \\ E\varepsilon_y\left(\frac{n-1}{n} + \frac{\varepsilon}{n\varepsilon_y}\right)^n & \text{if } \varepsilon > \varepsilon_y \end{cases} \tag{21}$$

where E, ε_y and n are three parameters, which are fitted by following procedure:

1. The elastic modulus, E, is maximum slope determined using Eq. (10).
2. The yield strain, ε_y, is determined using Eq. (16), which parameters C_1, C_2 and C_3 are determined by fitting parabolic dependency (Eq. (15)) around the yield strain region of measured stress–strain curve.
3. The strain hardening exponent n is determined by fitting the second equation of Eq. (21) to the strain interval $[\varepsilon_y, \varepsilon_f]$ of the measured data.

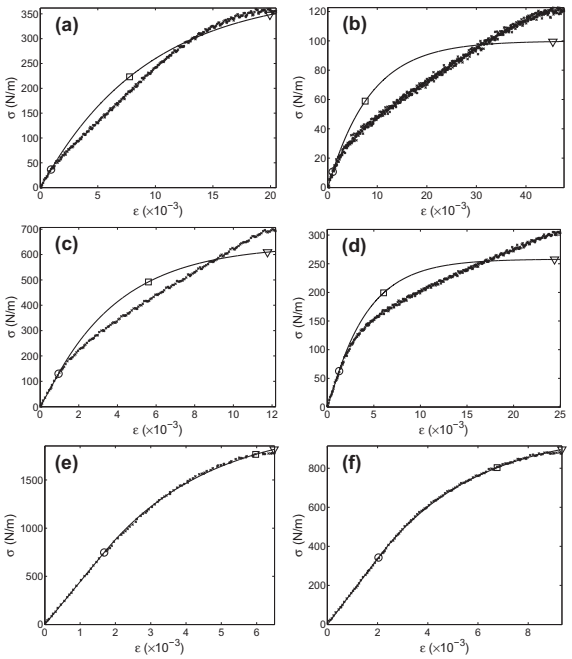

Fig. C.2. Example curves (Fig. 3) when two region approach with exponential function for strain hardening is applied. The yield point is marked with a circle, the offset point with a square and the failure point with a triangle. Dry solids contents, orientation levels and r^2 values are (a) DSC = 56.8%, $\phi = 1.421$, $r^2 = 0.9694$ (b) DSC = 60.0%, $\phi = 0.704$, $r^2 = 0.7602$ (c) DSC = 75.3%, $\phi = 1.421$, $r^2 = 0.9205$ (d) DSC = 77.4%, $\phi = 0.704$, $r^2 = 0.8670$ (e) DSC = 96.1%, $\phi = 1.421$, $r^2 = 0.9994$ (f) DSC = 95.6%, $\phi = 0.704$, $r^2 = 0.9997$.

3D surfaces of these three fitted parameters as a function of DSC and anisotropy index are collected in Fig. 21 and values are given in Tables D.1–D.3 for every single load-elongation test sample. The stress and strain at failure are determined from modeled stress–strain curves using strain energy (Eq. (12)) of measured data. The failure results determined directly from measured stress–strain curves and from modeled curves can be visually compared at Fig. 22. The measured and modeled results are fairly similar.

Land et al.'s study(2010) is one of the rare published studies where elastic and plastic strain of wet and semi-wet samples are studied empirically by load-unload tests. To test the model presented in this paper, the estimated plastic strain results are compared with Land's measurements. Land performed load-unload tests for handsheet sample strips using different strain levels 0.3%, 0.8%, 2%, 2.8% and 4%. The basis weight of handsheets were about 145 g/m^2 and the raw material consists of bleached softwood kraft pulp (flash dried). The sheet forming and pressing were performed according to ISO 5269-1 and the drying was done by leaving the samples on drying plates for specified times at 23 °C, 50%RH. There are several differences of testing materials between our study and Land's study, including pulp quality, basis weight, paper forming, pressing and drying conditions. One clear indication of different quality of pulp and pressing/drying conditions is that all of Land's samples have been strained even up to 4% strain level, while dry paper sheets in our study never hold out even 0.5% strain without failure. By using the model presented in this paper the higher strain levels can, however, be extrapolated.

At the lowest applied strain level 0.3% the plastic strain can be estimated directly from measured data by subtracting elastic strain from the applied strain using the determined elastic modulus:

$$\varepsilon_p = \varepsilon - \frac{\sigma}{E} \tag{22}$$

In higher strain levels, where the failure has already occurred in several dry samples, the determination can only be done by using a model of each stress–strain curve. The estimate of plastic strain applied by strain levels 0.3%, 0.8% and 2.0% are presented in Fig. 23 as a function of DSC and anisotropy index. Since the handsheets of Land's study are approximately isotropic, the plastic strains at specific anisotropy level 1.0 were taken from interpolated surfaces with equal loading levels for comparison presented in Fig. 24. Land's results show negative plastic strain values for 0.3% strain. The discussion section of Ref. Land et al. (2010) suggests explanations including measuring error or some physical explanation possibly related to the release of dried-in strains. If the offset

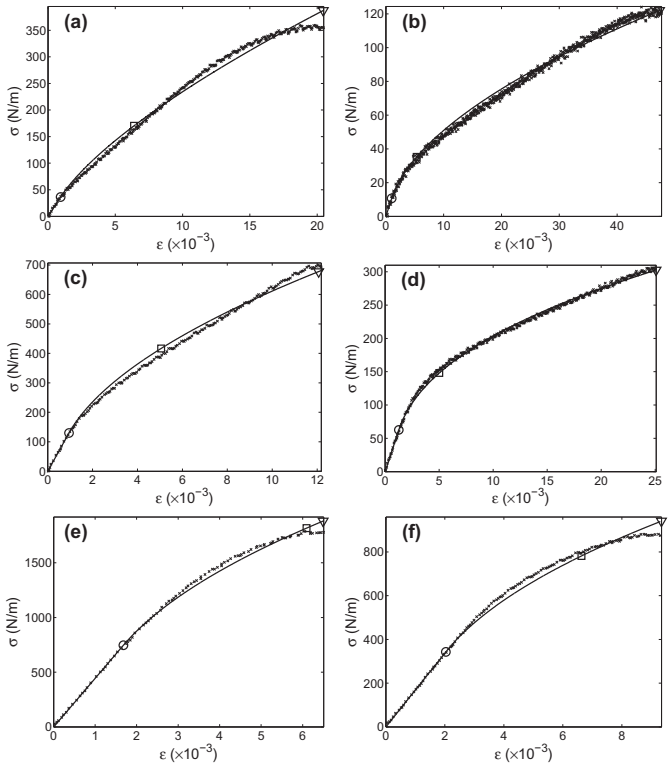

Fig. C.3. Example curves (Fig. 3) when two region approach with power law fit for strain hardening is applied. The yield point is marked with a circle, the offset point with a square and the failure point with a triangle. Dry solids contents, orientation levels and r^2 values are (a) DSC = 56.8%, $\phi = 1.421$, $r^2 = 0.9903$ (b) DSC = 60.0%, $\phi = 0.704$, $r^2 = 0.9921$ (c) DSC = 75.3%, $\phi = 1.421$, $r^2 = 0.9917$ (d) DSC = 77.4%, $\phi = 0.704$, $r^2 = 0.9978$ (e) DSC = 96.1%, $\phi = 1.421$, $r^2 = 0.9962$ (f) DSC = 95.6%, $\phi = 0.704$, $r^2 = 0.9936$.

of Land's results are taken account the plastic strain levels of these two studies would be quite similar. Although the curves of Land's work and our studies are not exactly the same by shape, it is remarkable to realize that, according to both studies, for isotropic samples the maximum plastic strain is attained for semi-wet samples around DSC 70% to 80%. The lower plastic strain of wet samples compared to semi-wet samples is against the general assumptions and should be verified further. The differences of plastic strain at different studied DSC levels are however so small that sample handling and measurement method will arise in an extremely significant role. The variation of plastic strain as a function of DSC attained by these two different studies is low in contrast to what may have been expected, when different types of curves are studied (see for example Fig. 3) or the behavior of elastic modulus, yield stress and strain, and exponent of yield hardening section (Fig. 16(f) and (21)) are considered. In fact, the plastic strain determined using Eq. (22) does not depend directly on yield point but rather on the ratio of elastic modulus and slope of strain hardening. The wet samples have low elastic modulus and, especially in the samples with high anisotropy indices, the strain hardening section has only slightly lower slope than elastic modulus (see for example Fig. C.3(a)). Furthermore, it would have been valuable to include even wetter samples (DSC below 55%) to study, but this was not possible with the used sample producing method. The problem with extrapolated results calculated from the model is confronted with dry samples, since in some cases the strain hardening region is short. Thus the amount of data points used in nonlinear function fittings is small, which suggests that the slope may be deflected from reality when high strain levels are studied by extrapolating.

5. Conclusions

The model of stress–strain curves presented in this paper is designed to be suitable for material model utilized in out-of-plane deformation and fracture models of paper. Although the mechanical behavior of wet and dry papers is different the goal was to model all samples equally to achieve a consistent fitting procedure and fitting parameter data for a mathematically consistent material model. The studied material included 180 uniaxial stress–strain curves measured from paper strips, the DSC of which varied from 55% to 98%. The pilot machine was used to produce three different anisotropy levels for wet (press dry) paper sheets from which the strips were cut at four different directions. The generated

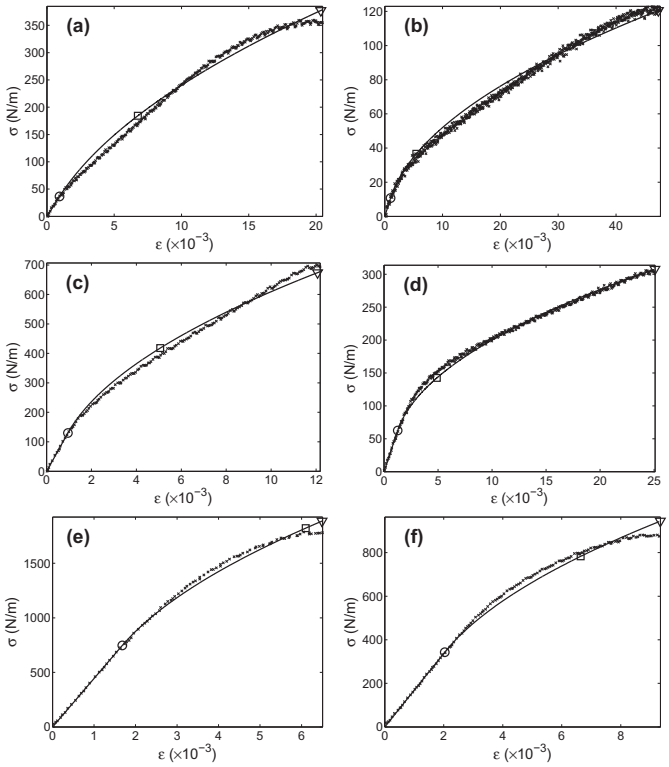

Fig. C.4. Example curves (Fig. 3) when two region approach with parable for strain hardening is applied. The yield point is marked with a circle, the offset point with a square and the failure point with a triangle. Dry solids contents, orientation levels and r^2 values are (a) DSC = 56.8%, $\phi = 1.421$, $r^2 = 0.9900$ (b) DSC = 60.0%, $\phi = 0.704$, $r^2 = 0.9881$ (c) DSC = 75.3%, $\phi = 1.421$, $r^2 = 0.9906$ (d) DSC = 77.4%, $\phi = 0.704$, $r^2 = 0.9962$ (e) DSC = 96.1%, $\phi = 1.421$, $r^2 = 0.9960$ (f) DSC = 95.6%, $\phi = 0.704$, $r^2 = 0.9931$.

three-parameter stress–strain curve model is formulated as a pair of equations. The characteristics of the model are: the elastic area behaves linearly, the yield point (elastic limit) is equal with the proportional limit and the strain hardening region is described using monotonic nonlinear function which first derivative at the yield point is equal with the elastic modulus. The three fitted parameters are elastic modulus E determined as the maximum slope of specific small interval in stress–strain curve, yield strain ε_y determined as the point where nonlinear (parabolic) function has better goodness of fit than linear function and exponent n determined by fitting of power law function on strain hardening region.

In an attempt to unify all the results of samples cut in different directions, a new anisotropy index parameter was introduced. This gave a possibility to visualize the behavior of parameters as a 3D-surface simultaneously as a function of DSC and anisotropy index. This approach also guarantees that a further material model will give equivalent results if the MD and CD parameters of the isotropic sheet are modeled. This is, of course, true only if the sample has been treated equivalently in MD and CD both during production and in measurement. In this study, in the stress–strain curve measurements the strips cut from different directions were treated equivalently by preventing shrinkage during drying, but the production of wet sheets at Metso Paper's pilot machine did not handle MD and CD equivalently. Even then the fitted parameters of the constructed stress–strain curve model were able to form fairly monotonic surfaces also as a function of the anisotropy index. Because the shrinkage of both CD and MD strips were restrained during drying the results are more suitable to describe the phenomena at the middle section of cross profile web. The result of this study is large and consistent data set of elasto-plastic material parameters of fine paper. This data set can be used directly or with simple interpolations to estimate the effect of anisotropy, DSC and loading direction on the elasto-plastic variables. However, in the future the processing of the data will continue with fittings of material parameter surfaces and by implementing that material model in out-of-plane deformation and fracture models.

The data set of elasto-plastic parameters determined by the introduced stress–strain curve model was used directly to estimate plastic strains at different anisotropy and DSC levels. As a verification, the plastic strain estimates were compared to load-unload measurements of handsheets carried out by Land et al. (2010). Although the pulp quality, sheet forming and drying conditions were different between these studies several resemblances were observed. The levels of plastic strain values were comparable between Land's study and our results. Both studies also suggest that the highest plastic strains are attained with dry solids contents

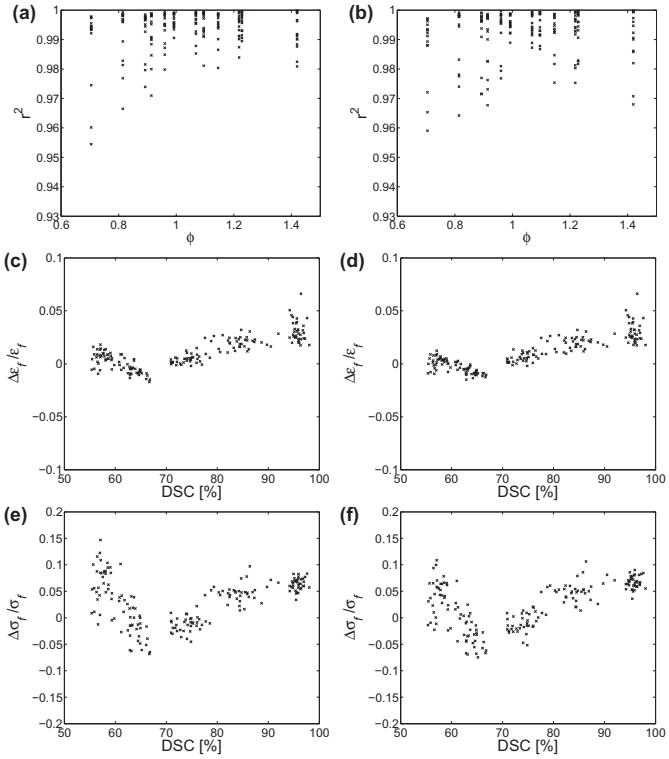

Fig. C.5. r^2 values ((a) and (b)) as a function of anisotropy index, error in strain at failure ((c) and (d)) as a function of DSC and error in stress at failure ((e) and (f)) as a function of DSC when two region models where strain hardening is described by power law ((a), (c) and (e)) and parable ((b), (d) and (f)) are used.

between 70% and 80%. This is against the general assumption that plastic strain increases if DSC decreases. Actually, the yield stress and strain, according to the results of this study, decreases with decreasing DSC, but the location of the yield point is not the most important factor of plastic strain; the elastic modulus and its relation to the slope of the strain hardening function defines the plastic strain calculated from the stress–strain curve. A great benefit from the paper maker's point of view is that the variation of plastic strain appears to be low even with such a high difference of DSC and anisotropy levels as is studied here. Unfortunately, even very small variations in strain levels can make problems during paper making and converting. The 0.1% variations in plastic strain along the paper web profile may cause problems such as wrinkling and baggy profiles (Land et al., 2010; Roisum, 1996), while a high curl appearing as a half-circle shape of paper strip with a length of 210 mm (equivalent with length of short side of A4 sheet) and a thickness of 0.1 mm (the typical thickness of copy paper sheet) is theoretically an expression of only 0.15% strain difference in the two sides of the paper strip. If such a small plastic strain differences are detected or simulated from dry paper samples or from

Table D.1
The fitting parameters for every sample having anisotropy level 1.20. Elastic modulus E, yield strain ε_y and exponent n of the final model (Eq. (21)). Corresponding yield stress σ_y and stress at failure σ_f are also included. Parameter C is constant of parabolic approach according Eq. (19).

Sample	DSC (%)	y (°)	ξ	φ_γ	E (kN/m)	ε_y (%)	σ_y (N/m)	n	σ_f (N/m)	C (MN/m)
1	57.07	90	1.199	1.095	19.73	0.062	12.3	0.760	190.9	3.63
2	57.54	90	1.199	1.095	20.47	0.117	24.0	0.655	189.5	2.84
3	56.40	90	1.199	1.095	21.16	0.102	21.7	0.65	177.2	2.58
4	56.97	70	1.199	1.068	21.24	0.075	15.9	0.623	154.1	1.67
5	56.46	70	1.199	1.068	18.83	0.102	19.1	0.642	157.4	1.94
6	55.67	70	1.199	1.068	19.39	0.063	12.3	0.68	156.8	1.87
7	55.86	45	1.199	0.992	15.61	0.096	14.9	0.633	130.4	1.19
8	55.46	45	1.199	0.992	14.70	0.083	12.2	0.618	125.3	0.86
9	56.68	45	1.199	0.992	18.23	0.088	16.1	0.547	131.3	0.83
10	56.52	0	1.199	0.913	8.58	0.112	9.6	0.635	100.7	0.45
11	55.35	0	1.199	0.913	10.29	0.092	9.4	0.606	101.2	0.43
12	55.89	0	1.199	0.913	11.08	0.085	9.4	0.588	106.9	0.41
13	63.65	90	1.199	1.095	31.58	0.066	20.9	0.668	266.2	4.75
14	63.65	90	1.199	1.095	30.15	0.088	26.6	0.63	239.5	4.05
15	63.14	90	1.199	1.095	31.09	0.107	33.1	0.595	267.2	4.04
16	62.36	70	1.199	1.068	25.51	0.103	26.2	0.621	233.2	3.17
17	61.79	70	1.199	1.068	28.21	0.086	24.3	0.678	242.8	4.90
18	61.25	70	1.199	1.068	27.12	0.106	28.9	0.648	222.2	4.26
19	60.73	45	1.199	0.992	18.93	0.111	21.1	0.608	169.5	1.70
20	60.84	45	1.199	0.992	22.80	0.102	23.2	0.555	187.9	1.58
21	61.03	45	1.199	0.992	19.42	0.074	14.3	0.646	197.2	1.75
22	64.85	0	1.199	0.913	20.03	0.069	13.7	0.573	163.6	0.99
23	64.64	0	1.199	0.913	18.38	0.109	20.1	0.524	170.8	0.88
24	65.16	0	1.199	0.913	22.53	0.073	16.5	0.554	176.8	1.13
25	75.94	90	1.199	1.095	88.73	0.088	78.3	0.498	463.2	13.56
26	73.91	90	1.199	1.095	76.69	0.076	58.3	0.550	385.2	12.64
27	71.96	90	1.199	1.095	75.48	0.092	69.8	0.500	378.4	10.49
28	71.01	70	1.199	1.068	62.03	0.100	61.9	0.537	361.5	9.80
29	73.56	70	1.199	1.068	59.73	0.100	59.7	0.528	354.6	8.58
30	71.28	70	1.199	1.068	60.63	0.083	50.4	0.548	346.6	8.53
31	70.94	45	1.199	0.992	48.30	0.117	56.7	0.484	306.8	4.89
32	70.90	45	1.199	0.992	48.48	0.114	55.2	0.495	307.3	5.15
33	71.74	45	1.199	0.992	45.67	0.114	52.3	0.504	292.7	4.89
34	71.22	0	1.199	0.913	41.92	0.098	41.1	0.459	242.8	2.53
35	72.93	0	1.199	0.913	42.49	0.110	46.9	0.437	242.9	2.51
36	76.99	0	1.199	0.913	58.91	0.101	59.3	0.424	281.9	4.06
37	81.06	90	1.199	1.095	161.49	0.117	188.4	0.478	612.3	53.58
38	84.42	90	1.199	1.095	171.69	0.115	197.2	0.497	606.9	66.72
39	85.47	90	1.199	1.095	174.96	0.112	195.9	0.496	563.0	67.21
40	80.29	70	1.199	1.068	122.29	0.138	168.3	0.460	538.6	32.46
41	82.02	70	1.199	1.068	120.50	0.151	181.3	0.418	463.4	27.39
42	79.33	70	1.199	1.068	121.63	0.120	145.5	0.479	468.8	31.50
43	80.58	45	1.199	0.992	95.42	0.126	120.0	0.453	445.3	17.12
44	78.80	45	1.199	0.992	97.24	0.132	128.4	0.446	435.4	17.99
45	77.60	45	1.199	0.992	106.25	0.136	144.5	0.440	457.3	21.43
46	82.36	0	1.199	0.913	95.38	0.127	120.8	0.431	381.3	15.22
47	82.11	0	1.199	0.913	90.61	0.128	115.9	0.425	362.3	13.32
48	83.22	0	1.199	0.913	92.88	0.127	117.5	0.425	376.7	13.78
49	95.35	90	1.199	1.095	317.87	0.155	493.3	0.473	1192.6	272.86
50	95.62	90	1.199	1.095	317.41	0.176	557.7	0.437	1105.5	257.27
51	94.20	90	1.199	1.095	305.15	0.180	549.4	0.399	1036.8	200.87
52	94.84	70	1.199	1.068	295.76	0.190	561.0	0.491	1404.7	317.24
53	95.17	70	1.199	1.068	296.38	0.189	559.7	0.411	1161.5	208.52
54	95.48	70	1.199	1.068	298.08	0.194	577.9	0.309	988.6	123.47
55	94.80	45	1.199	0.992	257.90	0.198	510.0	0.357	904.7	125.97
56	94.87	45	1.199	0.992	253.39	0.210	531.1	0.267	864.5	74.12
57	94.54	45	1.199	0.992	253.24	0.204	515.8	0.298	806.1	91.20
58	95.25	0	1.199	0.913	209.46	0.207	433.1	0.419	965.9	117.89
59	95.88	0	1.199	0.913	214.31	0.197	422.6	0.359	773.8	86.74
60	95.81	0	1.199	0.913	212.67	0.209	444.9	0.383	924.3	101.07

Table D.2
The fitting parameters for every sample having anisotropy level 1.51. Elastic modulus E, yield strain ε_y and exponent n of the final model (Eq. (21)). Corresponding yield stress σ_y and stress at failure σ_f are also included. Parameter C is constant of parabolic approach according Eq. (19).

Sample	DSC (%)	γ (°)	ξ	φ_γ	E (kN/m)	ε_y (%)	σ_y (N/m)	n	σ_f (N/m)	C (MN/m)
61	58.66	90	1.508	1.228	27.37	0.108	29.7	0.704	262.4	6.63
62	57.86	90	1.508	1.228	24.68	0.107	26.5	0.704	255.9	5.48
63	58.07	90	1.508	1.228	28.16	0.087	24.5	0.677	255.7	4.98
64	58.14	70	1.508	1.146	29.04	0.081	23.4	0.598	223.9	2.82
65	56.31	70	1.508	1.146	22.85	0.090	20.6	0.652	203.6	2.80
66	57.07	70	1.508	1.146	23.61	0.083	19.5	0.656	209.1	2.91
67	57.25	45	1.508	0.960	15.40	0.078	12.0	0.638	147.8	1.07
68	57.72	45	1.508	0.960	15.16	0.092	14.0	0.612	146.5	0.99
69	57.83	45	1.508	0.960	13.10	0.085	11.1	0.675	146.8	1.12
70	56.98	0	1.508	0.814	9.86	0.100	9.8	0.576	104.9	0.35
71	56.63	0	1.508	0.814	10.60	0.113	11.9	0.538	99.2	0.33
72	56.90	0	1.508	0.814	8.46	0.063	5.3	0.692	109.2	0.45
73	63.11	90	1.508	1.228	40.23	0.097	39.0	0.638	337.5	8.21
74	63.35	90	1.508	1.228	36.59	0.097	35.4	0.650	309.3	7.38
75	62.80	90	1.508	1.228	41.26	0.073	29.9	0.657	327.1	7.82
76	63.43	70	1.508	1.146	34.73	0.094	32.8	0.581	291.4	4.11
77	64.45	70	1.508	1.146	35.37	0.097	34.3	0.554	263.2	3.55
78	64.91	70	1.508	1.146	35.86	0.096	34.5	0.562	263.7	3.83
79	61.17	45	1.508	0.960	23.21	0.072	16.7	0.576	187.6	1.40
80	62.95	45	1.508	0.960	22.20	0.107	23.8	0.528	192.3	1.30
81	62.45	45	1.508	0.960	22.72	0.092	20.9	0.539	182.8	1.27
82	62.88	0	1.508	0.814	19.87	0.072	14.3	0.538	157.0	0.77
83	62.85	0	1.508	0.814	17.71	0.089	15.7	0.515	142.0	0.62
84	63.15	0	1.508	0.814	17.94	0.084	15.0	0.522	136.2	0.63
85	75.95	90	1.508	1.228	112.50	0.112	125.5	0.509	514.5	29.81
86	75.11	90	1.508	1.228	93.38	0.097	90.2	0.545	494.0	22.53
87	74.80	90	1.508	1.228	91.73	0.113	103.8	0.538	546.4	24.36
88	74.89	70	1.508	1.146	85.00	0.074	63.1	0.524	370.8	12.64
89	74.18	70	1.508	1.146	82.31	0.078	64.5	0.513	400.2	11.57
90	72.12	70	1.508	1.146	76.92	0.075	57.7	0.496	319.0	8.62
91	72.73	45	1.508	0.960	52.94	0.108	57.1	0.475	301.6	5.06
92	73.37	45	1.508	0.960	54.60	0.105	57.6	0.476	317.5	5.29
93	70.93	45	1.508	0.960	54.58	0.097	52.7	0.450	287.9	3.96
94	75.24	0	1.508	0.814	46.64	0.106	49.3	0.405	217.5	2.32
95	73.78	0	1.508	0.814	43.73	0.106	46.5	0.440	249.5	2.62
96	74.05	0	1.508	0.814	41.65	0.087	36.1	0.459	203.8	2.23
97	84.34	90	1.508	1.228	227.89	0.123	280.9	0.534	1049.6	156.73
98	88.69	90	1.508	1.228	243.18	0.128	310.4	0.522	1008.7	170.96
99	86.92	90	1.508	1.228	218.11	0.164	357.2	0.479	1025.4	138.49
100	86.38	70	1.508	1.146	164.69	0.129	211.8	0.419	618.5	43.37
101	84.70	70	1.508	1.146	173.86	0.110	190.7	0.459	595.9	52.53
102	83.59	70	1.508	1.146	175.45	0.108	190.1	0.487	666.4	61.82
103	84.42	45	1.508	0.960	123.66	0.150	185.4	0.406	503.3	26.43
104	84.73	45	1.508	0.960	131.71	0.121	159.7	0.469	503.1	35.11
105	84.22	45	1.508	0.960	118.09	0.126	148.9	0.452	420.9	26.82
106	84.50	0	1.508	0.814	105.72	0.121	128.4	0.417	342.3	16.87
107	85.76	0	1.508	0.814	111.87	0.108	120.3	0.430	381.6	17.66
108	86.17	0	1.508	0.814	107.95	0.131	141.5	0.428	420.9	19.92
109	96.96	90	1.508	1.228	367.32	0.178	654.8	0.541	1924.0	602.82
110	98.05	90	1.508	1.228	378.36	0.182	686.8	0.549	2200.6	686.73
111	97.63	90	1.508	1.228	354.10	0.186	657.5	0.490	1488.7	444.84
112	95.89	70	1.508	1.146	310.67	0.195	606.2	0.467	1633.8	314.48
113	95.91	70	1.508	1.146	314.37	0.195	580.5	0.434	1286.7	258.73
114	96.30	70	1.508	1.146	323.13	0.180	580.1	0.394	1160.6	214.71
115	96.92	45	1.508	0.960	250.75	0.185	464.9	0.482	1313.0	211.90
116	96.88	45	1.508	0.960	243.96	0.199	484.6	0.400	995.4	139.97
117	96.79	45	1.508	0.960	241.59	0.198	479.3	0.378	1000.4	119.74
118	95.61	0	1.508	0.814	185.15	0.211	391.5	0.446	766.6	111.33
119	96.40	0	1.508	0.814	179.77	0.206	370.4	0.312	532.2	53.21
120	95.14	0	1.508	0.814	191.92	0.203	390.5	0.426	822.5	102.48

a dry paper web, the relevance of variation might be directly detected. In the wet sample, the corresponding variation brings up several questions, such as how this difference affects subsequent paper making processes and is the difference still observable from dried paper which has undergone different tension conditions and shrinkage tendencies until it is finally dry. In any case, the small differences required for the estimation of runnability and the quality of the paper web or sheet makes the measurement and simulation of these properties demanding. The simulation of, for example, the correct amplitude of curl may be an elusive goal, but the correct tendencies and importance of the different phenomena can possibly still be studied.

Appendix A

See Figs. A.1–A.6.

Appendix B

See Figs. B.1–B.3.

Table D.3
The fitting parameters for every sample having anisotropy level 2.02. Elastic modulus E, yield strain ε_y and exponent n of the final model (Eq. (21)). Corresponding yield stress σ_y and stress at failure σ_f are also included. Parameter C is constant of parabolic approach according Eq. (19).

Sample	DSC (%)	γ (°)	ξ	φ_γ	E (kN/m)	ε_y (%)	σ_y (N/m)	n	σ_f (N/m)	C (MN/m)
121	58.50	90	2.016	1.420	38.71	0.094	36.4	0.687	387.2	10.94
122	59.03	90	2.016	1.420	39.60	0.092	36.4	0.711	393.3	13.22
123	57.14	90	2.016	1.420	34.38	0.066	22.8	0.790	384.8	15.26
124	59.34	70	2.016	1.218	34.18	0.090	30.9	0.627	282.8	5.24
125	58.46	70	2.016	1.218	31.61	0.088	27.9	0.646	284.3	5.16
126	59.10	70	2.016	1.218	34.51	0.086	29.6	0.629	285.7	5.22
127	58.59	45	2.016	0.892	18.08	0.083	15.0	0.571	156.2	0.94
128	58.10	45	2.016	0.892	14.75	0.061	9.0	0.681	166.4	1.19
129	59.26	45	2.016	0.892	14.47	0.112	16.3	0.602	161.5	1.01
130	61.62	0	2.016	0.704	10.56	0.101	10.7	0.549	122.0	0.34
131	59.31	0	2.016	0.704	8.87	0.107	9.5	0.580	110.0	0.32
132	59.78	0	2.016	0.704	9.36	0.103	9.6	0.578	114.0	0.34
133	63.91	90	2.016	1.420	55.85	0.096	53.8	0.662	516.4	18.96
134	62.88	90	2.016	1.420	49.46	0.094	46.6	0.687	500.9	17.74
135	64.18	90	2.016	1.420	48.97	0.100	48.9	0.687	475.4	17.88
136	64.85	70	2.016	1.218	42.51	0.088	37.2	0.636	382.4	8.59
137	64.43	70	2.016	1.218	43.71	0.090	39.4	0.604	362.9	7.28
138	64.77	70	2.016	1.218	45.20	0.094	42.5	0.601	376.5	7.95
139	64.90	45	2.016	0.892	22.29	0.079	17.7	0.560	203.7	1.26
140	66.12	45	2.016	0.892	25.01	0.093	23.3	0.537	233.0	1.55
141	66.05	45	2.016	0.892	24.22	0.100	24.2	0.518	212.3	1.34
142	66.67	0	2.016	0.704	18.05	0.102	18.5	0.478	156.5	0.55
143	66.78	0	2.016	0.704	18.65	0.097	18.0	0.474	153.2	0.54
144	66.30	0	2.016	0.704	20.34	0.066	13.4	0.515	164.9	0.61
145	74.68	90	2.016	1.420	136.52	0.095	130.0	0.525	677.6	41.53
146	74.86	90	2.016	1.420	138.29	0.103	141.8	0.530	804.8	47.74
147	74.05	90	2.016	1.420	134.07	0.090	120.4	0.537	709.2	41.20
148	76.01	70	2.016	1.218	117.90	0.079	92.9	0.532	626.4	27.44
149	74.82	70	2.016	1.218	120.38	0.087	104.5	0.481	564.3	21.92
150	72.10	70	2.016	1.218	104.02	0.095	98.7	0.492	540.3	19.31
151	76.44	45	2.016	0.892	70.42	0.125	88.1	0.415	372.6	6.90
152	76.62	45	2.016	0.892	67.50	0.121	81.6	0.412	386.9	5.81
153	74.73	45	2.016	0.892	72.11	0.105	75.6	0.422	347.1	6.28
154	77.74	0	2.016	0.704	49.02	0.128	62.6	0.411	302.7	3.19
155	78.52	0	2.016	0.704	46.84	0.120	56.2	0.422	305.0	2.93
156	76.11	0	2.016	0.704	46.14	0.129	59.7	0.409	291.6	2.80
157	85.31	90	2.016	1.420	272.15	0.143	389.2	0.528	1567.3	250.83
158	87.27	90	2.016	1.420	280.46	0.124	348.4	0.546	1505.0	259.37
159	83.48	90	2.016	1.420	270.11	0.125	338.3	0.540	1518.1	235.41
160	82.39	70	2.016	1.218	223.69	0.120	268.4	0.498	1019.8	119.12
161	82.49	70	2.016	1.218	207.59	0.125	258.5	0.501	1039.9	108.33
162	83.82	70	2.016	1.218	202.57	0.126	255.7	0.498	980.9	102.73
163	85.89	45	2.016	0.892	148.90	0.131	195.7	0.439	610.0	40.62
164	85.85	45	2.016	0.892	152.69	0.153	233.7	0.413	613.9	43.51
165	87.36	45	2.016	0.892	152.23	0.128	195.6	0.446	636.3	43.07
166	90.50	0	2.016	0.704	125.09	0.125	156.2	0.432	543.0	25.67
167	91.97	0	2.016	0.704	128.75	0.135	174.3	0.464	527.8	36.69
168	89.73	0	2.016	0.704	121.54	0.132	160.8	0.454	558.4	29.73
169	96.32	90	2.016	1.420	443.93	0.168	746.6	0.474	1881.6	579.29
170	95.43	90	2.016	1.420	431.87	0.164	709.3	0.452	1641.1	474.72
171	96.38	90	2.016	1.420	441.44	0.143	633.0	0.579	2126.8	870.13
172	94.95	70	2.016	1.218	374.71	0.190	713.1	0.485	2084.1	493.87
173	95.66	70	2.016	1.218	369.72	0.188	695.6	0.500	1918.7	517.74
174	94.68	70	2.016	1.218	386.10	0.175	674.3	0.483	1880.3	476.16
175	95.41	45	2.016	0.892	249.83	0.208	519.4	0.436	1584.4	178.48
176	96.06	45	2.016	0.892	249.47	0.196	488.3	0.456	1327.5	191.50
177	94.19	45	2.016	0.892	248.03	0.187	463.1	0.450	1126.2	176.51
178	95.93	0	2.016	0.704	168.58	0.203	342.8	0.467	941.1	96.89
179	95.93	0	2.016	0.704	165.55	0.214	353.6	0.427	949.7	77.80
180	97.21	0	2.016	0.704	164.77	0.212	349.9	0.446	938.5	85.76

Appendix C

See Figs. C.1–C.5.

Appendix D

See Tables D.1–D.3.

References

Alava, M., Niskanen, K., 2006. The physics of paper. Reports on Progress in Physics 69, 669–723.
Andersson, O., Berkyto, E., 1951. Some factors affecting the stress–strain characteristic of paper. Svensk Papperstidning 54 (13), 437–444.
Brezinski, J.P., 1956. The creep properties of paper. Tappi 39 (2), 116–128.
Castro, J., Ostoja-Starzewski, M., 2003. Elasto-plasticity of paper. International Journal of Plasticity 19, 2083–2098.

Caulfield, D., 1990. Effect of moisture and temperature on the mechanical properties of paper. In: Solids Mechanics Advances in Paper Related Industries: Proceedings of National Science Foundation Workshop, New York, pp. 50–62.
Coffin, D., 2008. Developing constitutive equations for paper that are valid for multi-time scales and large stresses. In: Proceedings of Progress in Paper Physics Seminar, Otaniemi, pp. 17–20.
Erkkilä, A.-L., Pakarinen, P., Odell, M., 1998. Sheet forming studies using layered orientation analysis. Pulp and Paper Canada 99 (1), 81–85.
Hill, H.N., 1944. Determination of stress–strain relations from "offset" yield strength values. Technical Notes National Advisory Committee for Aeronautics, Technical Note No. 927, Washington.
Hoffman, O., Sachs, G., 1953. Introduction to the Theory of Plasticity for Engineers. McGraw-Hill, New York.
Johnson, M.W., Urbanik, T.J., 1984. A nonlinear theory for elastic plates with application to characterizing paper properties. Journal of Applied Mechanics 51, 146–152.
Johnson, M.W., Urbanik, T.J., Denniston, W.E., 1979. Optimum fiber distribution in singlewall corrugated fiberboard. USDA, Forest Service, Research paper FPL No. 348. Madison, WI.
Jones, R.M., 2009. Deformation Theory of Plasticity. Bull Ridge Publishing, Blacksburg.
Kouko, J., Salminen, K., Kurki, M., 2007. Laboratory scale measurement procedure for the runnability of a wet web on a paper machine, part 2. Paper and Timber 89 (7-8), 424–430.
Land, C., Wahlström, T., Stolpe, L., Beghello, L., 2010. Plastic strain of moisture streaks at different moisture contents. Nordic Pulp and Paper Research Journal 25 (4), 481–487.
Leppänen, T., Sorvari, J., Erkkilä, A.-L., Hämäläinen, J., 2005. Mathematical modelling of moisture induced out-of-plane deformation of a paper sheet. Modelling and Simulation in Materials Science and Engineering 13, 841–850.
Lif, J., Östlund, S., Fellers, C., 2005. In-plane hygro-viscoelasticity of paper at small deformations. Nordic Pulp and Paper Research Journal 20 (1), 139–149.
Lipponen, P., Leppänen, T., Erkkilä, A.-L., Hämäläinen, J., 2008a. Effect of drying on simulated cockling of paper. Journal of Pulp and Paper Science 34 (4), 226–233.
Lipponen, P., Leppänen, T., Kouko, J., Hämäläinen, J., 2008b. Elasto-plastic approach for paper cockling phenomenon: on the importance of moisture gradient. International Journal of Solids and Structures 45, 3596–3609.
Lipponen, P., Leppänen, T., Hämäläinen, J., 2009a. On the role of drying induced cross-machine shrinkage on paper cockling phenomenon. Nordic Pulp and Paper Research Journal 24 (1), 60–65.
Lipponen, P., Erkkilä, A.-L., Leppänen, T., Hämäläinen, J., 2009b. On the importance of in-plane shrinkage and through-thickness moisture gradient during drying on cockling and curling phenomena. In: Proceedings of 14th Pulp and Paper Fundamental Research Symposium, Oxford, pp. 389–436.
Lu, W., Carlsson, L.A., 2001. Influence of viscoelastic behavior on curl of paper. Mechanics of Time-Dependent Materials 5, 79–100.
Ludwik, P., 1909. Elemente der Technologischen Mechanic. Springer-Verlag, Berlin.
Mann, R.W., Baum, G.A., Habeger, C.C., 1979. Elastic wave propagation in paper. Tappi 62 (8), 115–118.
Mäkelä, P., Östlund, S., 2003. Orthotropic elastic-plastic material model for paper materials. International Journal of Solids and Structures 40, 5599–5620.
Nadai, A., 1931. Plasticity. McGraw-Hill, New York and London.
Nanko, H., Wu, J., 1995. Mechanisms of paper shrinkage during drying. In: Proceedings of International Paper Physics Conference (CPPA and Tappi), pp. 103–113.
Ng, S., Ng, R., Yu, W., 2005. Bilinear approximation of anisotropic stress-strain properties of woven fabrics. Research Journal of Textile and Apparel 9 (4), 50–56.
Niskanen, K. (Ed), 1998. Papermaking Science and Technology. Part 16: Paper Physics, Fapet Oy, Helsinki.
Ostoja-Starzewski, M., Stahl, D.C., 2000. Random fiber networks and special elastic orthotropy of paper. Journal of Elasticity 60, 131–149.
Ostoja-Starzewski, M., Castro, J., 2003. Random formation, inelastic response and scale effects in paper. Philosophical Transactions of the Royal Society of London A 361, 965–985.
Prager, W., 1942. Fundamental theorems of a new mathematical of plasticity. Duke Mathematical Journal 9, 228–233.
Ramberg, W., Osgood, W.R, 1943. Description of stress-strain curves by three parameters. Technical Note No. 902, National Advisory Committee for Aeronautics, Washington.
Roisum, D.R., 1996. The mechanics of wrinkling. Tappi Journal 79 (10), 217–226.
Saliklis, E.P., Urbanik, T.J., Tokyay, B., 2003. Bilinear modelling of cellulosic orthotropic nonlinear materials. Journal of Pulp and Paper Science 29 (12), 407–411.
Schultz-Eklund, O., Fellers, C., Johansson, P.-Å., 1992. Method for the local determination of the thickness and density of paper. Nordic Pulp and Paper Research Journal 7 (3), 133–139,154.
Setterholm, V., 1984. Dimensional Property Measurements. Handbook of Physical and Mechanical Testing of Paper and Paperboard. vol. 2. Marcel Dekker, New York.
Setterholm, V., Chilson, W., 1964. Effect of restraint during drying on the tensile properties of handsheets. Research paper, Forest Products Laboratory, Madison Wis.
Silvy, J., 1971. Effects of drying on web characteristics. Paper Technology 12 (5), 377–387.
Skowronski, J., Robertson, A.A., 1986. The deformation properties of paper: tensile strain and recovery. Journal of Pulp and Paper Science 12 (1), 20–25.
Steenberg, B., 1947. Paper as a visco-elastic body. Svensk Papperstidning 50 (6), 127–140.
Stenberg, N., Fellers, C., Östlund, S., 2001. Plasticity in the thickness direction of paperboard under combined shear and normal loading. Journal of Engineering Materials and Technology 123, 184–190.
Suhling, J.C., Rowlands, R.E., Johnson, M.W., Gunderson, D.E., 1985. Tensorial strength analysis of paperboard. Experimental Mechanics 25 (1), 75–84.
Swift, H.W., 1952. Plastic instability under plane stress. Journal of the Mechanics and Physics of Solids 1 (1), 1–18.
Uesaka, T., Murakami, K., Imamura, R., 1979. Biaxial tensile behavior of paper. Tappi 62 (8), 111–114.
Uesaka, T., Murakami, K., Imamura, R., 1980. Two-dimensional linear viscoelasticity of paper. Wood Science and Technology 14, 131–142.
Uesaka, T., Kodaka, I., Okushima, S., Fukuchi, R., 1989. History-dependent dimensional stability of paper. vol. 28, 1989, pp. 238–245.
Urbanik, T.J., 1982. Method analyzes analogue plots of paperboard stress-strain data. Tappi 65 (4), 104–108.
Voce, E., 1948. The relationship between stress and strain for homogeneous deformation. Journal Institute of Metals 74, 537–562.
Wahlström, T., Fellers, C., 2000. Biaxial straining of handsheets during drying – effects on in-plane mechanical properties. Tappi Journal 83 (8), 1–8.
Xia, Q.S., Boyce, M.C., Parks, D.M., 2002. A constitutive model for the anisotropic elastic-plastic deformation of paper and paperboard. International Journal of Solids and Structures 39, 4053–4071.
Yeh, K.C., Considine, J.M., Suhling, J.C., 1991. The influence of moisture content on the nonlinear constitutive behavior of cellulosic materials. In: Tappi Proceedings: 1991 International Paper Physics Conference, Tappi, pp. 695–711.

PUBL. IV

A.-L. Erkkilä, T. Leppänen, M. Ora, T. Tuovinen and A. Puurtinen, Hygroexpansivity of anisotropic sheets, *Nordic Pulp and Paper Research Journal*, In Press, 2015.

Hygroexpansivity of anisotropic sheets

Anna-Leena Erkkilä, Teemu Leppänen, Markku Ora, Tero Tuovinen and Ari Puurtinen

KEYWORDS: Hygroexpansivity, Dimensional instability, Drying shrinkage, Anisotropy, Fiber orientation

SUMMARY: Dimensional instability and more particularly its component hygroexpansivity are factors that may cause problems in any process or end-use situation in which paper or board is in contact with water or subject to changes in ambient relative humidity. Misregistration in printing, curl during copying and calender wrinkles are examples of such defects. In this paper, the in-plane hygroexpansivity of oriented laboratory sheets involving three set of samples with different pulps is studied. In each case they were dried both freely and under restraint. The relation of hygroexpansion coefficient on the elastic modulus, elastic modulus anisotropy, drying shrinkage, fiber orientation anisotropy and anisotropy index is considered. A linear relationship between the drying shrinkage and hygroexpansion coefficient of freely dried laboratory sheets having different fiber orientation anisotropies, was observed. Regardless of both the measurement direction (MD or CD) and the drying options (freely or restraint) all hygroexpansion coefficient values of each pulp type fell quite well on one single power curve as a function of the elastic modulus. Fiber orientation is considered via two different approaches: using fiber orientation anisotropy and using directional variable named as anisotropy index. When the anisotropy index is used, the MD and CD hygroexpansivity or the MD and CD drying shrinkage can be fit on a single curve, while the freely dried and restraint-dried sheets evidently need two different fitting curves. Between the hygroexpansion coefficient and the anisotropy index, a simple power law relationship, with two fitting parameters depending on pulp and drying restraints, is introduced.

ADDRESSES OF THE AUTHORS:
Anna-Leena Erkkilä (anlejoer@gmail.com)
Lappeenranta University of Technology,
P.O. Box 20, FI-53851 Lappeenranta, Finland
Teemu Leppänen (teemu.leppanen@lut.fi) and
Ari Puurtinen (ari.puurtinen@lut.fi)
LUT Savo Sustainable Technologies,
Lappeenranta University of Technology, Varkaus unit,
Osmajoentie 75, FI-78210 Varkaus, Finland
Markku Ora (markku.ora@upm.com)
UPM Research Centre, FI-53200 Lappeenranta, Finland
Tero Tuovinen (tero.tuovinen@jyu.fi)
University of Jyväskylä, P.O. Box 35,
FI-40014 Jyväskylä, Finland
Corresponding author: Anna-Leena Erkkilä

The term 'dimensional instability' of paper or board refers to dimensional changes resulting from a change in the conditions of ambient air or from moisture exchange in converting processes. Dimensional instability manifests itself as length, width and thickness changes and as out-of-plane deformations. The latter is induced by inhomogeneity in dimensional changes arising from variations in the structure and composition of the paper or board. Dimensional instability causes problems in the paper or board during drying, converting, printing, copying, storage and end-use, referring to such phenomena as curl, cockling, wrinkles, creasing, wavy edges, misregistration, stack lean, shrinkage, surface roughening, grainy edges, deformation of boxes and mechano-sorptive creep.

Depending on changes in the temperature and on the relative humidity of the air, fibers of lignocellulosic materials absorb, adsorb or desorb water. Most of the hygroexpansivity of fibers takes place diametrically; the changes in the length and cross sections are on the order of 1% to 2% and 20% to 50%, respectively, over the range of relative humidity (RH%) (Page, Tydeman 1962). The lateral hygroexpansivity of the fibers is transferred to the macroscopic dimensional changes of the paper sheet via inter-fiber bonding (Rance 1954; Page, Tydeman 1962; Uesaka 1994; Nanko, Wu 1995). The fiber composition, degree of refining and chemical modifications influence the dimensional stability of paper, while anisotropic fiber orientation generates the anisotropic in-plane hygroexpansivity of the sheet (Stamm, Beasley 1961; Page, Tydeman 1962; Fahey, Chilson 1963; Uesaka 1994; Lyne et al. 1996; Li et al. 2009). Hygroexpansivity and its anisotropy are also highly dependent on the hygroscopic, thermal and mechanical history of the sheet (Nordman 1958; Fahey, Chilson 1963; Salmén et al. 1987a; Uesaka et al. 1992; Uesaka, Qi 1994).

In this paper, the in-plane hygroexpansivity of oriented laboratory sheets made from two different pulps and their mixture is studied. The oriented laboratory samples are formed by using a dynamic sheet former and dried either freely or under restraint. Samples from a production machine are used for comparison purposes. The relation of the hygroexpansion coefficient on the elastic modulus, elastic modulus anisotropy, drying shrinkage, fiber orientation anisotropy and anisotropy index is considered. Some of the observed dependencies, together with the experimental stress-strain curve parameters presented in Erkkilä et al. (2013), have been incorporated as a part of the continuum mechanical modeling approach presented in Lipponen et al. (2009) and Erkkilä et al. (2015).

Samples and measurements

The two pulps used in this study were bleached softwood kraft pulp made from pine (SW) and thermomechanical pulp (TMP). The mixture (MIX) of these contained 71% TMP and 29% SW. Drainability (Canadian Standard Freeness (CSF)) determined according to ISO 5267-2:2001 standard was 592 ml for SW, 57 ml for TMP and 112 ml for MIX pulp. The average fiber lengths were measured on a Kajaani FS300 fiber analyzer. The length-weighted values were 2.41 mm for SW, 1.46 mm for TMP and 1.82 mm for MIX pulp. The production machine (PM) samples taken from middle and edge areas of the cross

profile had a fiber composition corresponding to the MIX pulp samples.

The oriented laboratory sheets were formed using a dynamic sheet former. The target basis weight was 65 g/m^2. At the dynamic sheet former, the stock is sprayed against a wire of the rotating drum by the traversing nozzle. The water of the fiber suspension is drained away by centrifugal dewatering pressure, forming a wet sheet on the fabric (for a detailed description of the process, see e.g. Norman (1989)). The adjustable velocity difference between the jet and the drum wall allowed for varying degrees of fiber orientation in the sheet. The jet speed varied from 800 m/min to 1020 m/min, and the wire speed from 700 m/min to 1200 m/min resulting in speed differences of the jet and wire from -400 m/min to 320 m/min. The sheets were wet-pressed according to ISO5269-1:2005, and then were either air-dried freely on a flat teflon covered plate or under restraint in standard atmosphere conditions (23°C; 50% RH). The elastic modulus (or tensile stiffness) and thickness of single sheet were measured following ISO 1924-2:1994 and ISO 534:2005 standards, respectively.

The procedure for the hygroexpansivity measurements followed the general guidelines stated in ISO 8226-1:1994 for maximum relative humidity up to 68%. The samples were conditioned under zero load at least 8 hours in RUMED Climatic Test Cabinets Type 4201, with the constant atmosphere in accordance with the DIN 50015. The changes in the MD and CD lengths of the sample were measured using the image analysis-based determination. The round sample with constant diameter was marked with crosshairs at center lines and scanned. During scanning a round metal weight was used to hold the sample in plane with constant pressure. The coordinates of the sample's peripheral were determined via image analysis to obtain the machine direction (MD) and cross machine direction (CD) lengths of round paper samples at 33% RH and 66% RH. According to ISO 8226-1:1994, the hygroexpansive strain X is

$$X = \frac{l_{66} - l_{33}}{l_{50}} \times 100 \qquad [1]$$

where l is the length in the specific RH% indicated by the subscript. However, the hygroexpansion coefficient β (%/%), defined as

$$\beta = \frac{X}{\Delta M} \qquad [2]$$

where ΔM (%) is the moisture content change, was used in this study. At least seven parallel samples were measured in each anisotropy level. The same image analysis-based method was also applied in determining the drying shrinkage S of freely dried samples as a percent relative in-plane dimensional change (%) during drying. Sheet forming and measurements of hygroexpansivity as well as drying shrinkage are described in detail in Hii (2008).

The fiber orientation anisotropy was measured using the method presented in Erkkilä et al. (1998) and Lipponen et al. (2009). The measurement is based on layering the sample by tape ripping and image gradient analysis of the layers. Mass-weighted averages of the MD/CD ratios of the layers are used to describe the fiber orientation anisotropy of the entire thickness. The anisotropy index ϕ introduced by Erkkilä et.al. (2013) is defined by

$$\phi_\gamma = \sqrt{\frac{1-\xi^2}{\xi + \tan^2\gamma/\xi} + \xi} \qquad [3]$$

where ξ is the fiber orientation anisotropy and γ is the direction in which the anisotropy index is determined. For the semi-axes of the orientation distribution, the anisotropy indices can be solved from *Eq 3* to be $\phi_{90^\circ} = \sqrt{\xi}$ and $\phi_{0^\circ} = 1/\sqrt{\xi}$. If the orientation angle coincides with the machine direction, ϕ_{90° corresponds to the machine and ϕ_{0° to the cross direction anisotropy index values.

The goodness of fit is estimated using the general form of the coefficient of determination defined by the equation

$$r^2 = 1 - \frac{\sum(\sigma_{estimated} - \sigma_{measured})^2}{\sum(\sigma_{estimated} - \overline{\sigma_{measured}})^2}. \qquad [4]$$

Negative results of the coefficient of determination r^2 are also possible, indicating that the mean of the measured results would have provided an estimate preferable when compared to the fitting under consideration.

Results and discussion

The relationship between elastic modulus and fiber orientation

Wahlström et al. (2005) suggest that for restraint-dried (rd) and freely dried samples (fd) the following relationships between elastic modulus anisotropy (or tensile stiffness) and fiber orientation anisotropy hold:

$$\frac{E_{rd,1}}{E_{rd,2}} = \xi \quad \text{and} \quad \frac{E_{fd,1}}{E_{fd,2}} = 2\xi - 1 \qquad [5]$$

where E is the elastic modulus (or tensile stiffness) and subscript indices 1 and 2 refer to MD and CD, respectively. These equations are used for comparing the elastic modulus anisotropy and the fiber orientation anisotropy results of this study (see *Fig 1*). As can be expected, the PM samples, which are outside the scope of *Eq 5*, deviate clearly from the diagonal in *Fig 1*. Otherwise, the sheets produced by the dynamic laboratory sheet former and dried either freely or under restraint follow the diagonal line reasonably well, although some nonlinearity may be observed.

Earlier observations indicate that under equal drying conditions, the geometric mean of MD and CD tensile stiffness remains constant with varying anisotropy levels (Schrier, Verseput 1967; de Ruvo et al. (1976); Htun, Fellers 1982). The relation between the tensile stiffness of the isotropic sheet and the geometric mean value may be written separately for the restraint and the free drying as

$$E_{iso} = E_{geom} = \sqrt{E_1 E_2} \qquad [6]$$

where subscripts *iso* refers to the isotropic, and subscript *geom* refers to the geometric mean.

The geometric mean of the elastic modulus of the samples studies is presented in *Fig 2* as a function of the anisotropy of the elastic modulus (E_1/E_2). The geometric mean of the elastic modulus of freely dried samples is roughly equal for all the suspensions studied (SW, TMP and MIX). For the SW samples, restraint during drying increases the elastic modulus by four times, while for the TMP samples, the level is doubled. The geometric means of the front-side and middle samples taken from the cross profile of the production machine differ from each other because of the different CD restraints prevailing during drying.

In different studies, the parameter E found in *Eqs 5* and *6* refers to the tensile stiffness, tensile stiffness index or elastic modulus. If the basis weight and the thickness of comparable samples are equal, these equations are equally accurate, independent of which of the three parameter referents is used. If *Eqs 5* and *6* are valid, then the geometric mean of the elastic modulus (or the elastic modulus of the isotropic sheet) and the fiber orientation anisotropy can be used to predict the MD and CD values of the elastic modulus of an anisotropic sheet, both for free and restraint drying conditions:

$$E_{fd} = E_{geom}(2\xi - 1)^s \quad [7]$$

$$E_{rd} = E_{geom}\xi^s \quad [8]$$

where s is 0.5 for the direction 1 (MD) and -0.5 for the direction 2 (CD). Fairly good predictability can be observed from *Fig 3* (colored lines). The geometric mean values (averaged over different anisotropies) and coefficients of determination (r^2) can be seen from *Table 1*.

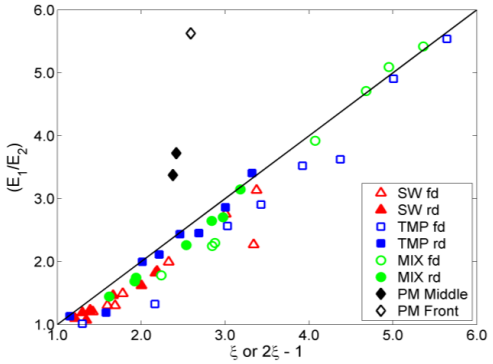

Fig 1. The elastic modulus anisotropy as a function of fiber orientation anisotropy according to *Eq* 5. *Eq* 5 for restraint drying (rd) is used for production machine (PM) samples.

Table 1. Geometric mean values of the elastic modulus and coefficient of determination r^2, when *Eqs 7* and *8* are applied.

Pulp and drying	E_{geom} (GPa)	r^2 (MD)	r^2 (CD)
SW fd	1.165	0.582	0.542
SW rd	4.074	0.396	0.344
TMP fd	1.105	0.797	0.741
TMP rd	1.959	0.881	0.887
MIX fd	1.115	0.767	0.798
MIX rd	2.595	0.782	0.721

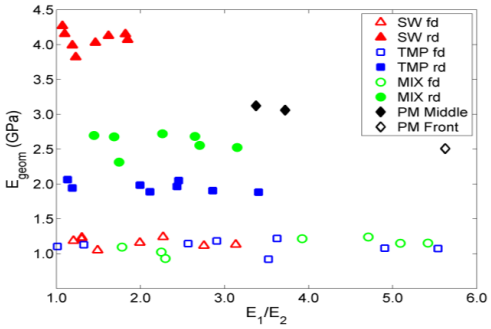

Fig 2. Geometric mean of the elastic modulus vs. the anisotropy of the elastic modulus for freely dried (fd), restraint-dried (rd) and production machine (PM) samples

If the orientation angle is zero, such as in the case of the laboratory sheets under consideration, the anisotropy index ϕ (*Eq 3*) has the value $\sqrt{\xi}$ for the machine direction and $1/\sqrt{\xi}$ for the cross direction. Then, by using the anisotropy index, *Eq 8* can be simplified to

$$E_{rd} = E_{geom}\phi. \quad [9]$$

Eq 9 is applicable to all in-plane directions. The elastic modulus of both the freely and restraint-dried samples as a function of the anisotropy index is presented in *Fig 4*. Parameters k_1 and q of the equation

$$E = k_1\phi^q \quad [10]$$

are fitted separately to the results of the freely dried and restraint-dried samples. The fitting parameters are presented in *Table 2*. The power q for the restraint-dried samples is moderately close to one which is expected because of the fairly good correlations when *Eq 8* is employed. For freely dried samples, the power q is over 1, compensating the term $(2\xi - 1)$ in *Eq 7*. The constants k_1 are virtually equal to the geometric mean values (see *Table 1*). *Eq 10* can be written as a function of anisotropy

$$E = k_1\xi^{q\times s} \approx E_{geom}\xi^{q\times s} \quad [11]$$

where s is 0.5 for MD and -0.5 for CD. The fittings of *Eq* 10, but with the change of variable according to *Eq 11*, are plotted in *Fig 3* as black lines. The power $q \times s$ and coefficient of determination r^2 are presented separately for the MD and CD relationships in *Table 3*.

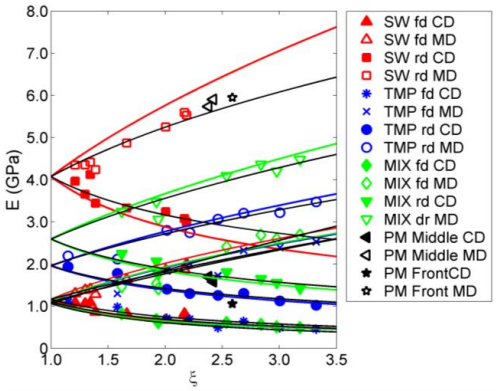

Fig 3. Measured elastic modulus *E* as a function of fiber orientation anisotropy ξ. The colored lines are relationships predicted by applying *Eqs 7* and *8*. The black lines are fittings of *Eq 10* as converted according to *Eq 11*.

Table 2. Fitted parameters (*Eq 10, Fig 4)* and the coefficient of determination.

Pulp and drying	k_1 (GPa)	q	r^2
SW fd	1.165	1.283	0.969
SW rd	4.073	0.729	0.953
TMP fd	1.103	1.362	0.968
TMP rd	1.964	0.935	0.980
MIX fd	1.062	1.603	0.964
MIX rd	2.591	0.917	0.979

Table 3. Fitted parameters (*Eq 11, Fig 3)* and the coefficient of determination (r^2).

Pulp and drying	k_1 (GPa)	MD $q \times s$	CD $q \times s$	MD r^2	CD r^2
SW fd	1.165	-0.642	0.642	0.939	0.766
SW rd	4.073	-0.365	0.365	0.905	0.750
TMP fd	1.103	-0.681	0.681	0.892	0.842
TMP rd	1.964	-0.467	0.467	0.914	0.900
MIX fd	1.062	-0.801	0.801	0.856	0.369
MIX rd	2.591	-0.458	0.458	0.866	0.797

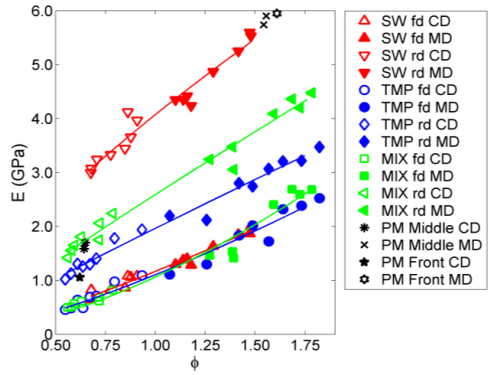

Fig 4. The elastic modulus *E* as a function of fiber orientation index ϕ. The colored lines are fittings according to *Eq 10*.

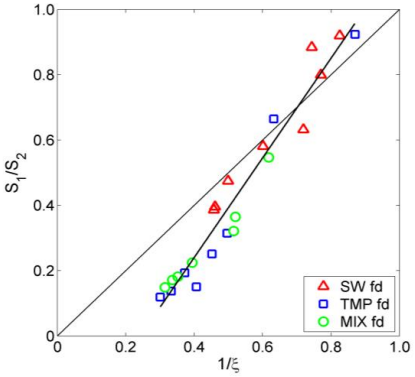

Fig 5. Drying shrinkage anisotropy vs. the inverse of fiber orientation anisotropy. The diagonal line is based on *Eq 12*.

Drying shrinkage anisotropy

Wahlström (2004) and Wahlström and Mäkelä (2005) proposed the following relationship between drying shrinkage anisotropy and fiber orientation anisotropy:

$$S_1/S_2 = 1/\xi \qquad [12]$$

where S is the drying shrinkage and subscript indices 1 and 2 refer to MD and CD, respectively. According to the results of this study, presented in *Fig 5*, $1/\xi$ is not directly suitable for predicting the drying shrinkage anisotropy. The linear fitting yields $S_1/S_2 = 1.53/\xi - 0.37$, and $r^2 = 0.948$. Certain factors, such as pressing conditions or the method for measuring fiber orientation, may have caused the deviation from earlier observations.

Relationship between drying shrinkage and hygroexpansivity

In his studies, Nordman (1958) found a linear relationship between drying shrinkage and hygroexpansivity; and that this is independent of pulp, beating or degree of restraining during drying. Similar correlations have also been found in other studies (Fahey, Chilson 1963; Manninen et al. 2011). Nordman stated, however, that in simulations of machine direction conditions by the uniaxial stretching of strips, the linear relationship no longer holds. Freely dried unbeaten pulp samples, having very low drying shrinkages ($S < 3\%$), also fell from the linear fit. Salmén et al. (1987b) found that the changes in the degree of wet pressing have an effect on the relationship. Nanri and Uesaka (1993) also showed that the correlation between the drying shrinkage and hygroexpansion coefficient is not particularly high ($r^2 = 0.618$) for freely-dried laboratory sheets of different pulps. A better correlation was achieved by comparing the drying shrinkage with the difference in hygroexpansion coefficients between freely dried and restraint-dried sheets.

A good correlation between the drying shrinkage and hygroexpansion coefficient of the freely dried samples can be observed from the results of this study in *Fig 6*. The relationship is quite linear over the range of anisotropies measured, but between the different pulps, some slight

differences in the slopes are detected. The fitting constants and coefficient of determination (r^2) values are presented in *Table 4*. The results presented in Nanri and Uesaka's (1993) study are plotted in red in *Fig 7* and labeled "Reference". Although in principle the data points of Reference follow the trend of the results of this study, the scattering of different pulp samples clearly deviates from the slope of fitted line. The correlations of the results of this study do not improve if the difference in the hygroexpansion coefficients between freely dried and restraint-dried sheets is used instead, as can be seen from *Fig 8* and from the r^2 values in *Table 4*.

These results indicate, at least for some limited cases, that both the hygroexpansion coefficient of freely dried sheets and the difference of the hygroexpansion coefficients have a linear dependence on drying shrinkage, and that this relationship is valid for samples having different fiber orientation anisotropies. If this result is combined with Nordman's (1958) observation that the linear relationship is also valid for samples having different degrees of restraining during drying, it leads to an assumption that if an appropriate degree of restraining (or stretching) during drying results in a situation where no shrinkage has occurred ($S = 0$), the hygroexpansion coefficient of all samples would be independent of the anisotropy and measuring direction (MD or CD). Then this zero shrinkage hygroexpansion coefficient should be the crossing point of the y-axis of the fittings of *Fig 6*, which is approximately $b = \beta_0 \approx 0.025$ %/% for all the pulps studied. To take the assumption even further, the fittings of *Fig 6* predict that the hygroexpansion coefficient may be zero if the permanent strain of the sheet, due to the appropriate degree of stretching during drying, is roughly $b/a \approx 1\%$ (a and b are the fitting constants from *Table 4*).

The measured hygroexpansion coefficients are used to predict the drying shrinkage (S_{est}) of restraint-dried laboratory sheets and production machine samples according to the assumption depicted above. The resulting estimates are presented in *Fig 9* as a function of fiber orientation anisotropy. The estimated MD values of MIX samples with high fiber orientation anisotropy approach zero percent shrinkage ($\beta \approx \beta_0$). For the TMP sheets, both the MD and CD values are higher, even rising to an estimated drying shrinkage of 3% in the case of the highly anisotropic CD samples. This high level of shrinkage seems unrealistic, although a certain amount of stress build-up during restraint drying (Wahlström, Fellers (1999)) might not have been relaxed before release, and thus the strain recovery may have decreased the dimensions of these sheets. Delayed strain recovery has also been detected by Skowronski and Robertson (1986). By examining the results of Nordman (1958), Nanko and Wu (1995) and Larsson and Wågberg (2008), it can be estimated that drying shrinkage of a totally restrained isotropic sheet may be on the order of 0.5%.

Table 4. The fitted constants ($\beta = aS + b$ or $\beta_{fd} - \beta_{rd} = aS + b$) related to *Figs 6-8* and the coefficient of determination.

***Fig*, samples**	***a* (1/%)**	***b* (%/%)**	r^2
6, SW	0.026	0.024	0.997
6, TMP	0.030	0.025	0.995
6, MIX	0.025	0.025	0.996
7, SW+TMP+MIX	0.026	0.028	0.979
7, Reference	0.015	0.057	0.618
8, SW+TMP+MIX	0.020	-0.006	0.947
8, Reference	0.014	-0.003	0.976

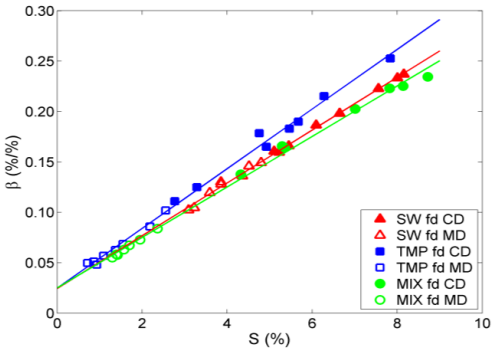

Fig 6. Relationship between the drying shrinkage S and the hygroexpansion coefficient β.

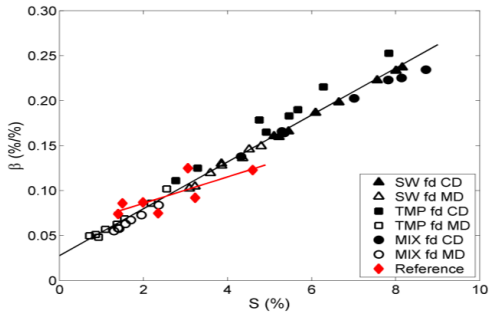

Fig 7. Results of this study from *Fig 6* are indicated by black markers. Reference results from Nanri and Uesaka's (1993) study are plotted in red.

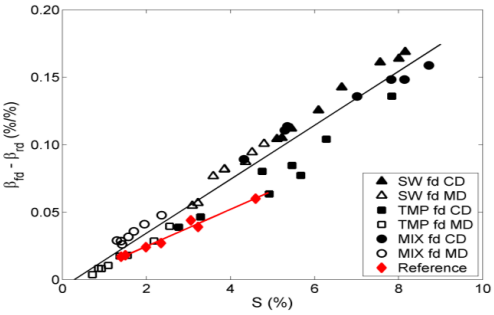

Fig 8. Difference between freely dried and restraint-dried samples in the moisture expansion coefficient β vs. the drying shrinkage S. Results of this study are in black; the reference results from Nanri and Uesaka's (1993) study are in red.

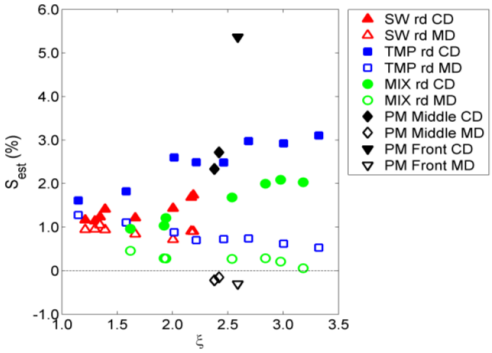

Fig 9. Estimated shrinkage S_{est} as a function of fiber orientation anisotropy.

The estimated MD shrinkage S_{est} of the production machine samples is negative for all positions (Middle: -0.15% and -0.22%, FS: -0.31%), indicating a slight elongation in the MD. The estimated CD shrinkage S_{est} of the PM samples for the middle is 2.72% and 2.33%, and for the front-side, 5.36%. Based on wire marking frequency detection, the shrinkage difference between the middle and front-side samples was about 5.5%. However, an accurate shrinkage value of the edge-position sample is difficult to determine, since the shrinkage difference between the left and right edges of the front side A4 sample was high, about 4%. The MD and CD results of the middle samples seem reasonable, but the estimated CD shrinkage of the front-side sample is probably lower than the correct value. In uniaxial stretching, the detectable shrinkage includes not only hygroscopic shrinkage but also narrowing due to the MD stretching, which may be one reason why the assumption is not valid for the production machine samples.

The relationship between the elastic modulus and hygroexpansivity

The hygroexpansivity of an anisotropic sheet has been previously presented as a function of tensile stiffness or elastic modulus anisotropy (Uesaka 1994; Lyne et al. 1996). The hygroexpansion coefficient for equally wet-pressed and dried sheets is studied herein as a function of the elastic modulus, as introduced in *Fig 10*. The simple power law fittings are applied separately for the different pulps:

$$\beta = k_2 E^p \qquad [13]$$

where k_2 and p are the fitting parameters presented in *Table 5*.

Table 5. Fitted parameters of *Eq 13*.

Pulp	k_2 ((%/%)GPa^{-p})	p	r^2
SW	0.172	-0.795	0.977
TMP	0.120	-0.854	0.956
MIX	0.117	-0.987	0.979

Table 6. Fitted parameters of *Eq 14*. $p \times s$ gets negative values for MD and positive for CD.

Pulp and drying	$k_2 E_{geom}^p$ (%/%)	$\lvert p \times s \rvert$	MD r^2	CD r^2
SW fd	0.153	0.397	0.703	0.876
SW rd	0.056	0.397	-1.405	0.150
TMP fd	0.110	0.427	0.789	0.945
TMP rd	0.067	0.427	0.895	0.752
MIX fd	0.105	0.493	0.301	0.969
MIX rd	0.046	0.493	0.190	0.827

Table 7. Fitted parameters of *Eq 15*.

Pulp, drying and direction	k_3 (%/%)	t	r^2
SW fd MD	0.155	-0.344	0.821
SW fd CD	0.152	0.408	0.877
SW rd MD	0.050	-0.153	0.385
SW rd CD	0.053	0.394	0.734
TMP fd MD	0.101	-0.452	0.969
TMP fd CD	0.107	0.464	0.959
TMP rd MD	0.063	-0.371	0.951
TMP rd CD	0.073	0.407	0.912
MIX fd MD	0.096	-0.321	0.904
MIX fd CD	0.113	0.433	0.989
MIX rd MD	0.038	-0.269	0.688
MIX rd CD	0.038	0.648	0.933

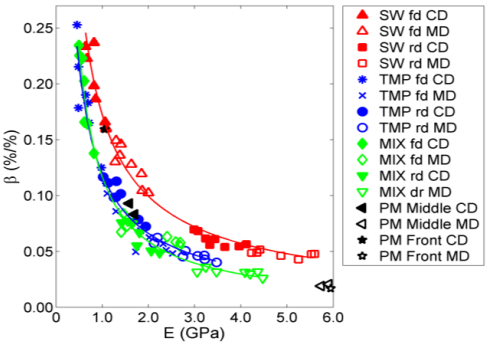

Fig 10. Moisture expansion coefficient β as a function of the elastic modulus E and fitted curves (*Eq 13*) for different pulp types.

The unique fitting can be extended to both freely and restraint-dried samples of same pulp. Even the production machine samples fit quite well in the MIX pulp curve, with the exception of CD results of the front-side sample. In that case, the elastic modulus, the hygroexpansivity or both are higher than expected, according to the laboratory sheet measurements. *Eq 13* can be used to determine individual equations for MD and CD as a function of the geometric mean and elastic modulus anisotropy

$$\beta = k_2 E_{geom}^p (E_1/E_2)^{p \times s}. \qquad [14]$$

The constant $k_2 E_{geom}^p$, power $p \times s$ and coefficient of determination (r^2) are listed in *Table 6*. The fittings of *Eq 13* with the change of variables according to *Eq 14* are

presented in *Fig 11* as colored lines. The direct fittings are made using power equation

$$\beta = k_3(E_1/E_2)^t. \qquad [15]$$

Fitting parameters k_3 and t are presented in *Table 7*, and the fitted curves are plotted as black lines in *Fig 11*. The poor r^2 of the fittings of the SW-rd-MD samples are also an indication of the almost nonexistent anisotropy dependency not being able to exceed the measuring inaccuracy. In that case, the average of the hygroexpansion values of the SW-rd-MD samples provides an equally good estimate as the power law fitting. Accordingly, Uesaka (1994) concluded that particularly for restraint-dried, low-density sheets, the MD hygroexpansivity does not show significant dependence on the elastic stiffness ratio.

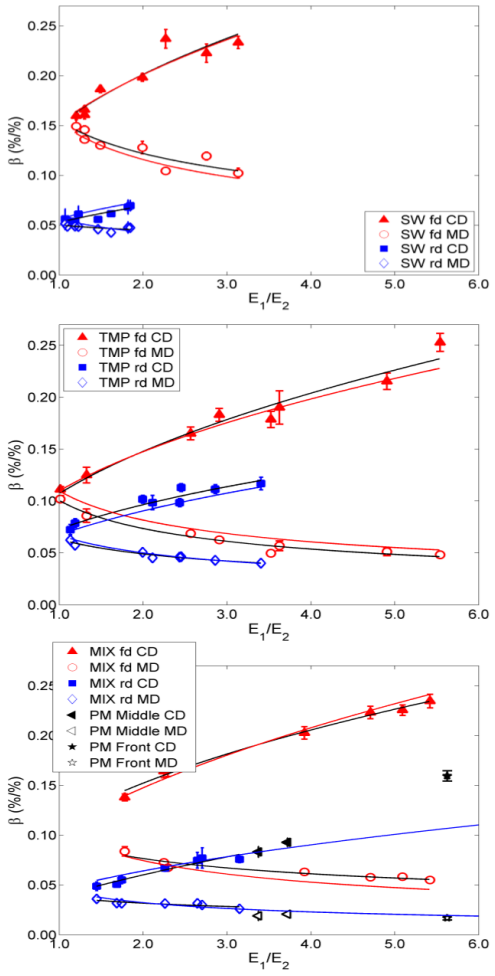

Fig 11. Hygroexpansion β as a function of the elastic modulus anisotropy E. The fittings of *Eq 13* converted according to *Eq 14* are depicted by colored lines, and the fittings of *Eq 15* by black lines. The error bars indicate the 95% confidence intervals.

The relationship of hygroexpansivity and drying shrinkage to fiber orientation

The fiber orientation anisotropy ξ can be transformed into a directional parameter by using the anisotropy index ϕ. The hygroexpansion coefficient β and drying shrinkage S as a function of ϕ, is presented in *Fig 12*. The parameters k_4 and v of the power fittings

$$\beta = k_4\phi^v \text{ or } S = k_4\phi^v \qquad [16]$$

and the coefficient of determination r^2 are presented in *Table 8*.

Both the MD and CD of one pulp treated under an equivalent degree of restraint during drying are fitted in a single power curve. The restraining decreases the absolute value of power v and factor k_4, indicating that both the hygroexpansivity level and the variability due to the anisotropy and the measuring direction decrease when drying shrinkage is prevented. If the assumption of the linear relationship would hold, the appropriate amount of stretching during drying (given zero drying shrinkage) would result in a power equal to 0, and dependency of hygroexpansivity on anisotropy would disappear. However, in every case the drying shrinkage has slightly higher powers than that of hygroexpansion coefficient of freely dried sheets, indicating that the relationship between hygroexpansivity and drying shrinkage is not strictly linear.

The change of the variable from the anisotropy index to fiber orientation anisotropy can be performed using *Eq 17*:

$$\beta = k_4\xi^{v\times s} \qquad [17]$$

The results are presented in *Fig 13*. The coefficient of determination r^2 values calculated individually for samples SW-rd-MD and MIX-rd-MD (*Table* 9) are poor, but low values for those samples are also observed when direct power law fittings (*Table 10*) are employed. This could be indication of the low dependency of hygroexpansion on anisotropy as well as an indication of poor fitting quality.

Table 8. Fitted parameters of *Eq 16*.

Pulp and drying or drying shrinkage	k_4 (%/%)	v	r^2
SW fd β	0.156	-0.981	0.961
SW rd β	0.053	-0.499	0.863
SW fd S	4.973	-1.164	0.965
TMP fd β	0.104	-1.343	0.982
TMP rd β	0.069	-0.900	0.986
TMP fd S	2.527	-1.734	0.970
MIX fd β	0.110	-1.302	0.995
MIX rd β	0.044	-0.901	0.956
MIX fd S	3.164	-1.710	0.995

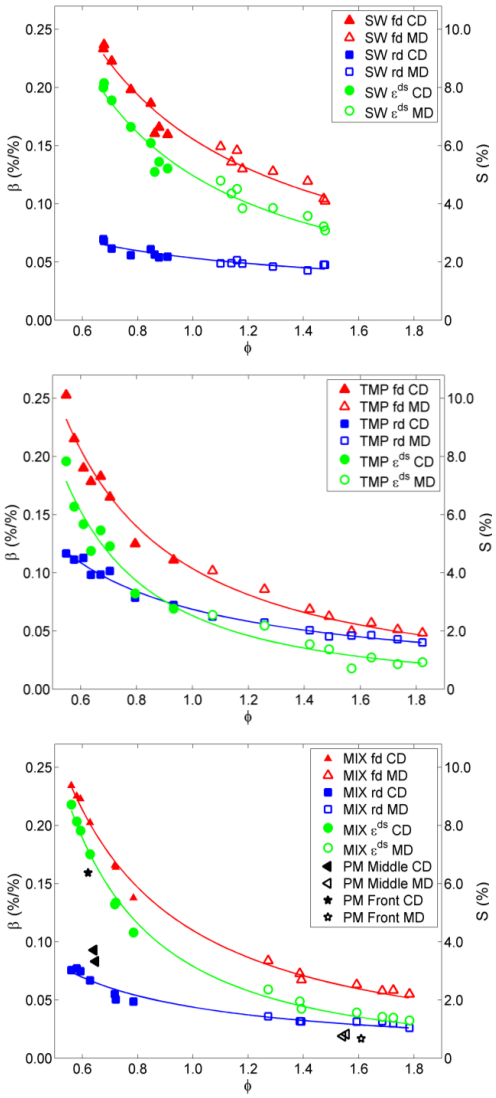

Fig 12. Fitted curves (*Eq 16*) for hygroexpansion β and drying shrinkage S as a function of the fiber orientation index ϕ.

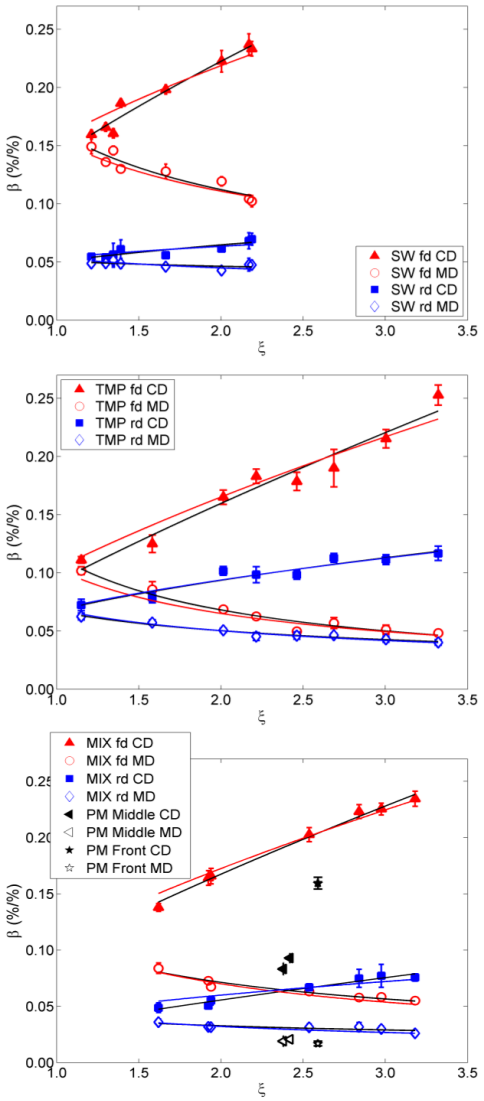

Fig 13. Hygroexpansion coefficient β as a function of fiber orientation anisotropy ξ. The fittings of *Eq 16* converted according to *Eq 17* are shown with colored lines, and the direct power law fittings with the black lines.

Table 9. Fitted parameters of *Eq 17*. $v \times s$ gets negative values for MD and positive for CD.

Pulp, drying and direction	k_4 (%/%)	$\lvert v \times s \rvert$	MD r^2	CD r^2
SW fd	0.156	0.490	0.847	0.895
SW rd	0.053	0.249	0.074	0.679
TMP fd	0.104	0.672	0.910	0.933
TMP rd	0.069	0.450	0.947	0.917
MIX fd	0.110	0.651	0.881	0.972
MIX rd	0.044	0.451	0.300	0.813

Although SW pulp has both the highest shrinkage potential and the steepest slope of anisotropy dependency of the freely dried samples, it also has the lowest hygroexpansivity when SW restraint-dried samples are compared with TMP and MIX samples. In accordance with this phenomenon, Nanri and Uesaka (1993) found indications that the effect of drying restraint on hygroexpansivity for chemical pulps is higher than that for mechanical pulps, because of the higher drying shrinkage potential of the chemical pulps. The restraint-dried SW samples show only a weak dependence on anisotropy

when compared to the TMP and MIX pulps. Restrain or stretching narrows the hygroexpansivity differences between different pulps or other treatments, as has been observed in several studies (Fahey, Chilson 1963; Nordman 1958; Stamm, Beasley 1961; Salmén et al. 1987b). Stretching during drying decreases the MD hygroexpansivity of the production machine samples under the curve of the restraint-dried laboratory samples. The CD hygroexpansivity of the production machine samples falls between the restraint-dried and freely dried laboratory sheet results.

Conclusions

A considerably linear relationship between the hygroexpansion coefficient of freely dried sheets and drying shrinkage from press-dry to equilibrium conditions was observed for laboratory sheets having different fiber orientation anisotropies. The corresponding linear relationship had earlier been observed to be valid for equally pressed samples dried freely or under different degree of restraining (Nordman 1958). In this study, some deviations were noted to arise due to the different pulp or in cross directional values of cross profile edge samples produced under uniaxial draw of the production machine. Based on the linearity of relationship, the following assumption was made: an adequate degree of restraint may remove the anisotropy dependency of the hygroexpansion coefficient. However, in reality, neither the linearity is complete nor the degree of restraint (or stretching) could be arranged in such a way that would subsequently lead to a situation in which the permanent strain is zero for all directions of an anisotropic sheet. Nevertheless, a very low dependency of the hygroexpansion coefficient on anisotropy was achieved with the restraint-dried samples, providing a way to minimize problems coming from local or two-sided variation of hygroexpansivity, for example. Condebelt drying is an excellent example of the effect of restraint drying on improving dimensional stability (Retulainen, Hämäläinen (2000)) and suppressing cockling tendency. Irreversible hygroexpansion behavior and recoverable strain due to humidification may, however, change the hygroexapnsion behavior, but those phenomena did not fall within the scope of this research.

Table 10. Direct power law fittings ($\beta = k_5 \phi^w$) presented in *Fig 13.*

Pulp, drying and direction	k_5 (%/%)	w	r^2
SW fd MD	0.163	-0.542	0.895
SW fd CD	0.141	0.663	0.965
SW rd MD	0.051	-0.132	0.353
SW rd CD	0.050	0.362	0.752
TMP fd MD	0.115	-0.755	0.959
TMP fd CD	0.092	0.795	0.952
TMP rd MD	0.067	-0.411	0.956
TMP rd CD	0.068	0.465	0.918
MIX fd MD	0.106	-0.573	0.932
MIX fd CD	0.099	0.761	0.992
MIX rd MD	0.040	-0.293	0.656
MIX rd CD	0.033	0.754	0.963

It is interesting to note that independently both the measurement direction (MD and CD) and drying option (freely and restraint) all hygroexpansion coefficient values of a particular pulp fall on a single power curve when studied as a function of elastic modulus. This relationship does not necessarily imply causation, but both properties, hygroexpansion coefficient and elastic modulus, depend on anisotropy and drying restraint. Using the anisotropy index, the fiber orientation anisotropy was converted into a directional variable. When anisotropy index is used, the MD and CD hygroexpansion coefficient may also be fitted on a single curve, while the freely and restraint-dried sheets evidently require two different fitting curves. An equivalent power law fitting can also be used when the relationship between the drying shrinkage and the anisotropy index are studied. These fittings can be restored as a function of the anisotropy of the elastic modulus or the anisotropy of fiber orientation with a simple change of the variable.

The fittings of the hygroexpansion coefficient as a function of the anisotropy index and the relationship between drying shrinkage and hygroexpansivity will be used in construction of a hygroexpansivity-shrinkage model. This hygroexpansivity-shrinkage model together with an elasto-plastic material model based on the experimental stress-strain curve parameters presented in Erkkilä et al. (2013), have been incorporated as a part of the continuum mechanical modeling approach presented in Lipponen et al. (2009) and Erkkilä et.al. (2015).

Acknowledgements

The authors are thankful to Collin Hii and Juha Happonen for their high contribution on the experimental results.

Literature

de Ruvo, A., Lundberg, S., Martin-Löf, S., Södermark, C. (1976): Influence of temperature and humidity on the elastic and expansional properties of paper and the constituent fibre, In: The Fundamental Properties of Paper Related to Its Uses, Transactions of the Symposium 1973, F. Bolan (ed.) Brittish Paper Board Industry Federation, London, 785 -806.

Erkkilä, A.-L., Pakarinen, P. and Odell, M. (1998): Sheet forming studies using layered orientation analysis, Pulp Paper Can. 99(1), 81-85.

Erkkilä A.-L., Leppänen T. and Hämäläinen J. (2013): Empirical plasticity models applied for paper sheets having different anisotropy and dry solids levels, International Journal of Solids and Structures 50(14-15), 2151-2179.

Erkkilä A.-L., Leppänen T., Hämäläinen J. and **Tuovinen, T.** (2015): Hygro-elasto-plastic model for planar orthotropic material, International Journal of Solids and Structures (Accepted 2015).

Fahey, D.J. and Chilson, W.A. (1963): Mechanical treatments for improving dimensional stability of paper, Tappi 46(7), 393-399.

Hii, C. (2008): Hygroexpansivity of paper, M.Sc. Thesis, Helsinki University of Technology, Espoo, Finland.

Htun, M. and Fellers, C. (1982): The invariant mechanical properties of oriented handsheets, Tappi 65(4), 113-117.

Larsson P.A. and Wågberg L. (2008): Influence of fibre-fibre joint properties on the dimensional stability of paper, Cellulose 15(4), 515-525.

Li, Z., Li, K., Camm, C. and Chen, Z. (2009): Dimensional stability of paper made from Mixtures of BCTMP and Kraft Fibres, J. Pulp Paper Sci. 35(3-4), 123-129.

Lipponen, P., Erkkilä, A.-L., Leppänen, T. and Hämäläinen, J. (2009): On the importance of in-plane shrinkage and through-thickness moisture gradient during drying on cockling and curling phenomena, In: I'Anson S.J. (ed.), Advances in Pulp and Paper Science and Technology, The Pulp and Paper Fundamental Research Society, Manchester, pp. 389-436.

Lyne, Å., Fellers C. and Kolseth, P. (1996): The effect of filler on hygroexpansivity, Nord. Pulp Paper Res. J. 11(3), 152-163.

Manninen, M., Kajanto, I., Happonen, J. and Paltakari, J. (2011): The effect of microfibrillated cellulose addition on drying shrinkage and dimensional stability of wood-free paper, Nord. Pulp Paper Res. J. 26(3), 297-305.

Nanko, H. and Wu, J. (1995): Mechanisms of paper shrinkage during drying, Int. Paper Physics Conf., Niagara-on-the-lake, Ontario, Canada, September 11-14, 1995, C.P.P.A and Tappi, pp. 103-113.

Nanri, Y. and Uesaka, T. (1993): Dimensional stability of mechanical pulps - drying shrinkage and hygroexpansivity, Tappi J. 76(6), 62-66.

Nordman, L.S. (1958): Laboratory investigations into the dimensional stability of paper, Tappi 41(1), 23-50.

Norman, B. (1989): Overview of the physics of forming, In: Baker, C.F. and Punton, V.W. (eds.), Fundamentals of papermaking, Vol. 3, Mechanical Engineering Publications London, pp. 674-693.

Page D.H. and Tydeman P.A. (1962): A new theory of the shrinkage, structure and properties of paper, In: Bolam, F. (ed.), The formation and structure of paper, Vol. 2, British Paper and Board Makers' Assoc. London, pp. 397-413.

Rance, H.F. (1954): Effect of water removal on sheet properties, Tappi 37(12), 640-648.

Retulainen, E. and Hämäläinen, A. (2000): Three years of Condebelt drying at Stora Enso´s Pankakoski mill, Tappi J. 83(5), 84, Tappi web site 1-8.

Salmén, L., Fellers, C. and Htun, M. (1987a): The development and release of dried-in stresses in paper, Nord. Pulp Paper Res. J. 2(2), 44-48.

Salmén, L., Boman, R., Fellers, C. and Htun, M. (1987b): The implications of fiber and sheet structure for the hygroexpansivity of paper, Nord. Pulp Paper Res. J. 2(4), 127-131.

Schrier, B.H. and Verseput, H.W. (1967): Evaluating the performance of folding cartons, Tappi 50(3), 114-117.

Skowronski, J. and Robertson, A.A. (1986): The deformation properties of paper: tensile strain and recovery, J. Pulp Paper Sci. 12(1), 20-25.

Stamm, A.J. and Beasley, J.N. (1961): Dimensional stabilization of paper by acetylation, Tappi 44(4), 271-275.

Uesaka, T., Moss, C. and Nanri, Y. (1992): The characterisation of hygroexpansivity of paper, J. Pulp Paper Sci. 18(1), 11-16.

Uesaka, T. (1994): General formula for hygroexpansion of paper, Journal of Material Science 29(9), 2373-2377.

Uesaka, T. and Qi, D. (1994): Hygroexpansivity of paper - Effects of fibre-to-fibre bonding, J. Pulp Paper Sci. 20(6), 175-179.

Wahlström, T. and Fellers, C. (1999): Biaxial straining of paper during drying, relations between stresses, strains and properties, In: Tappi Engineering Conference, Anaheim, CA, USA, September 12-16, 1999, pp. 705-720.

Wahlström, T. (2004)**:** The invariant shrinkage and stiffness of paper – modeling anisotropic behaviour based on isotropic handsheets, In: Progress in Paper Physics Seminar, Trondheim, Norway, June 21-24, 2004, pp. 105.

Wahlström, T. and Mäkelä, P. (2005): Predictions of anisotropic multiply board properties based on isotropic ply properties and drying restraints, In: I'Anson S.J. (ed.), Advances in Paper Science and Technology, The Pulp and Paper Fundamental Research Society, Manchester, pp. 241-281.

PUBL. V

A.-L. Erkkilä, T. Leppänen, J. Hämäläinen and T. Tuovinen, Hygro-elasto-plastic model for orthotropic sheet, *International Journal of Solids and Structures*, In Press, 2015.

ARTICLE IN PRESS

International Journal of Solids and Structures xxx (2015) xxx–xxx

Contents lists available at ScienceDirect

International Journal of Solids and Structures

journal homepage: www.elsevier.com/locate/ijsolstr

Hygro-elasto-plastic model for planar orthotropic material

Anna-Leena Erkkilä [a,*], Teemu Leppänen [b], Jari Hämäläinen [a], Tero Tuovinen [c]

[a] Lappeenranta University of Technology, PO Box 20, FI-53851 Lappeenranta, Finland
[b] LUT Savo Sustainable Technologies, Lappeenranta University of Technology, Varkaus unit, Osmajoentie 75, FI-78210 Varkaus, Finland
[c] University of Jyväskylä, PO Box 35, FI-40014 Jyväskylä, Finland

ARTICLE INFO

Article history:
Received 17 October 2014
Received in revised form 28 January 2015
Available online xxxx

Keywords:
Paper
Elasto-plasticity
Hygroexpansivity
Shrinkage
Anisotropy
Dry solids content
Buckling

ABSTRACT

An in-plane elasto-plastic material model and a hygroexpansivity-shrinkage model for paper and board are introduced in this paper. The input parameters for both models are fiber orientation anisotropy and dry solids content. These two models, based on experimental results, could be used in an analytical approach to estimate, for example, plastic strain and shrinkage in simple one-dimensional cases, but for studies of the combined and more complicated effects of hygro-elasto-plastic behavior, a numerical finite element model was constructed. The finite element approach also offered possibilities for studying different structural variations of an orthotropic sheet as well as buckling behavior and internal stress situations under local strain differences. A few examples are presented of the effect of the anisotropy and moisture streaks under stretching and drying conditions on strain differences and buckling. The internal stresses were studied through a case in which the drying of different layers occurred at different stages. Both the anisotropy and moisture streaks were capable of rendering the buckling of the sample visible. The permanency of these defects highly depends on several process stages and tension conditions of the sheet, as demonstrated in this paper. The application possibilities of the hygro-elasto-plastic model are diverse, including investigation into several phenomena and defects appearing in drying, converting and printing process conditions.

1. Introduction

Paper and board have elasto-visco-plastic properties, exhibiting such rheological behaviors as delayed strain recovery, stress relaxation and creep (Skowronski and Robertson, 1986; Rance, 1956; Steenberg, 1947; Gates and Kenworthy, 1963; Lyne and Gallay, 1954). The hygroscopic nature of the pulp fibers causes dimensional changes in the paper or the board when subject to influences of humidity changes or treatments which involve water intake or drying (Rance, 1954; Page and Tydeman, 1962; Uesaka, 1994; Nanko and Wu, 1995). Shrinkage during drying (Wahlström and Lif, 2003; Hoole et al., 1999; Nanri and Uesaka, 1993; Kiyoaki, 1987) and hygro- and hydroexpansivity (Uesaka, 1991; Salmen et al., 1987; Larsson and Wagberg, 2008; Lif et al., 1995; Mendes et al., 2011) are widely studied components of sorption based dimensional instabilities. Natural fibers and their treatments, bonds between fibers and their orientation in the fiber network, additives and manufacturing conditions all affect dimensional instability and mechanical properties of paper or board (Silvy, 1971; Wahlström and Fellers, 2000; Alava and Niskanen, 2006; Kouko et al., 2007; Nordman, 1958; Fahey and Chilson, 1963; Salmen et al., 1987; Uesaka et al., 1992; Uesaka and Qi, 1994; Mäkelä, 2009; Lyne et al., 1996; de Ruvo et al., 1976; Manninen et al., 2011; Setterholm and Kuenzi, 1970; Glynn et al., 1961; Leppänen et al., 2008).

Several models to predict in-plane mechanical and rheological properties, shrinkage and hygroexpansivity have been introduced in the literature. Johnson and Urbanik (1984) and Johnson and Urbanik (1987) have provided a nonlinear elastic model to study material behavior in stretching, bending and buckling of axially loaded paperboard plates. Nonlinear elastic biaxial failure criteria have been studied by Suhling et al. (1985) and Fellers et al. (1983). In-plane orthotropic elasto-plastic approaches to estimate the tensile response and deformation of paper have been presented by Castro and Ostoja-Starzewski (2003), Mäkelä and Östlund (2003) and Xia et al. (2002). Viscoelastic models have been used extensively in studying creep or relaxation behavior (Brezinski, 1956; Lif et al., 1999; Lu and Carlsson, 2001; Pecht et al., 1984; Pecht and Johnson, 1985; Rand, 1995; Uesaka et al., 1980).

A formula for the hygroexpansion of paper relating to the hygroexpansion of a single fiber and the efficiency of the stress transfer between fibers has been derived by Uesaka (1994). The traditional theory of linear thermoelasticity was applied to

* Corresponding author. Tel.: +358 40 848 8526; fax: +358 5 411 7201.
E-mail address: anlejoer@gmail.com (A.-L. Erkkilä).

http://dx.doi.org/10.1016/j.ijsolstr.2015.02.001
0020-7683/

Please cite this article in press as: Erkkilä, A.-L., et al. Hygro-elasto-plastic model for planar orthotropic material. Int. J. Solids Struct. (2015), http://dx.doi.org/10.1016/j.ijsolstr.2015.02.001

estimate hygroexpansion strains in the study of Lavrykov et al. (2004). Hygro-viscoelastic models have been applied to estimate history dependent dimensional stability and hygroexpansivity by Uesaka et al. (1989), Uesaka (1991), Lif et al. (2005) and Lif (2006). Mechano-sorptive creep has been studied, for example, by Urbanik (1995), Strömbro and Gudmundson (2008), Alfthan (2004) and Haslach (1994). Shrinkage profiles have been modeled by Wahlström et al. (1999) and Constantino et al. (2005). The measured moisture dependency of material constants has been employed within the nonlinear elastic model for an investigation of the effect of moisture on mechanical behavior by Yeh et al. (1991). Hygroscopic out-of-plane deformations, such as curling and buckling, have been studied, using elastic constitutive models, by Bloom and Coffin (2000), Leppänen et al. (2005) and Kulachenko et al. (2005); while an elasto-plastic model has been introduced in Lipponen et al. (2008, 2009). The hygroexpansion coefficients are independent of moisture content in these models.

In this paper, an in-plane elasto-plastic material model and a hygroexpansivity-shrinkage model that are functions of the dry solids content and fiber orientation anisotropy index are introduced. The elasto-plastic model is based on fittings of the uni-axial stress–strain curves presented by Lipponen et al. (2008) and Erkkilä et al. (2013). The dependency of the dry paper hygroexpansion coefficient on the anisotropy index was determined using the measurement results presented in Erkkilä et al. (submitted for publication). The drying shrinkage strain as a function of the dry solids content was constructed with an exponential formula based on the measurements provided by Ivarsson (1954), Kijima and Yamakawa (1978) and Tydeman et al. (1966) and summarized by Wahlström et al. (1999) and Wahlström (2004). The relation between the hygroexpansivity and the solids content was derived from the drying shrinkage strain function. Usually, the hygroexpansivity has been considered to be constant (i.e. independent of the moisture content level), which estimates the change in dimensions of a dry paper subject to the relative humidity change. However, in this paper, the dry solids content dependent hygroexpansivity, over the entire range from wet to dry, has been introduced. These two models, the elasto-plastic material model and the hygroexpansivity-shrinkage model, were exploited when numerical solutions were obtained with the finite element method. The use of the anisotropy index instead of that of traditional fiber orientation anisotropy simplified the handling of different in-plane directions in the case of the anisotropic sheet and, for instance, the determination of Hill's yield surface for the finite element approach is straightforward. Analytical one-dimensional solutions were used to estimate plastic and hygroscopic strains in simple cases and the results were compared with numerical simulations.

2. Models

In this section, the one-dimensional elasto-plastic material model (Section 2.1) and the hygroexpansivity-shrinkage model (Section 2.2) are presented. The continuum mechanical model is constructed in Section 2.3 and the numerical solution approach is described in Section 2.4.

2.1. Elasto-plasticity

The stress–strain measurements, used here as the basic data for constructing the material model, were presented in Lipponen et al. (2008) and Erkkilä et al. (2013). The stress–strain curve fittings for the determination of the elastic modulus, yield strain, yield stress and function for the strain hardening behavior were discussed in detail in Erkkilä et al. (2013). The following equation was considered suitable for describing all the uniaxial stress–strain relationships studied:

$$\sigma = \begin{cases} E\varepsilon & \text{if } \varepsilon \leqslant \varepsilon_y \\ E\varepsilon_y - \frac{H}{2E} + \sqrt{H\left(\frac{H}{4E^2} + \varepsilon - \varepsilon_y\right)} & \text{if } \varepsilon > \varepsilon_y \end{cases} \quad (1)$$

where σ is the stress and ε is the strain; the elastic modulus E, the yield strain ε_y and the hardening constant H are the fitting parameters. The fitting parameters were determined for different dry solids contents (R_{sc}) and anisotropy index (ϕ) levels from the materials measured in Erkkilä et al. (2013). To construct the material model, the following equation was used to fit the parameters σ_y, ε_y and H as functions of R_{sc} and ϕ:

$$P = (A_1 + A_2\phi + A_3 R_{sc})^{1/n} \quad P = \{\sigma_y, \varepsilon_y, H\} \quad (2)$$

where A_1, A_2, A_3 and n are the fitting constants listed in Table 1. In Erkkilä et al. (2013) the anisotropy index was defined as:

$$\phi = \sqrt{\frac{1-\xi^2}{\xi + \tan^2\gamma/\xi} + \xi} \quad (3)$$

where ξ is the fiber orientation anisotropy and γ is the angle from the minor axis of the fiber orientation distribution. The anisotropy index in the main direction and cross direction (direction perpendicular to the main direction) obtain values of $\sqrt{\xi}$ and $1/\sqrt{\xi}$, respectively. Table 1 also includes the coefficient of determination r^2 values between the measured parameters from Erkkilä et al. (2013) and their estimates according to Eq. (2). The elastic modulus is determined by $E = \sigma_y/\epsilon_y$, with $r^2 = 0.985$. The material model parameters as a function of ϕ and R_{sc} are presented in Fig. 1. Since the functions fitted according Eq. (2) behave monotonically a reasonable amount of extrapolation is permitted. This may be needed, for example, if the local variation of the fiber orientation is considered. The model has a lower limit for solids content; i.e., it is valid if $R_{sc} > 0.3$; the parenthetical expression of Eq. (2) reaches negative values for yield stress σ_y with low solids content if the anisotropy index is also simultaneously low. The material model can be used directly to calculate the material parameters of the orthotropic sample in any in-plane direction or at any solids content level. Examples of the determination of plastic strain as a consequence of stretching either 0.3% or 1% and releasing afterwards are presented in Fig. 2.

2.2. Hygroexpansivity and shrinkage

The hygroexpansivity-shrinkage model is based on the measured relationships between the dry paper hygroexpansivity β_d and anisotropy index ϕ

$$\beta_d = k\phi^{\nu} \quad (4)$$

and between the drying strain ε_{ds} and the dry paper hygroexpansivity

$$\varepsilon_{ds} = -\frac{1}{a}\beta_d + \frac{b}{a} \quad (5)$$

where k, ν, a and b are fitted constants for freely-dried (fd) and restraint-dried (rd) samples made of either softwood pulp (SW), thermomechanical pulp (TMP) or a mixture of those (MIX); see

Table 1
The fitting parameters of Eq. (2) and the coefficients of determination r^2 for the yield stress σ_y, the yield strain ε_y and the hardening constant H.

	A_1	A_2	A_3	n	r^2
σ_y	−5.9030 (Pa^n)	3.1959 (Pa^n)	18.3077 (Pa^n)	0.1760 (–)	0.965
ε_y	380.4181 (–)	14.3408 (-)	−269.8327 (–)	−0.7720 (–)	0.816
H	−0.6021 (Pa^{2n})	4.0423 (Pa^{2n})	11.3795 (Pa^{2n})	0.0715 (–)	0.890

Please cite this article in press as: Erkkilä, A.-L., et al. Hygro-elasto-plastic model for planar orthotropic material. Int. J. Solids Struct. (2015), http://dx.doi.org/10.1016/j.ijsolstr.2015.02.001

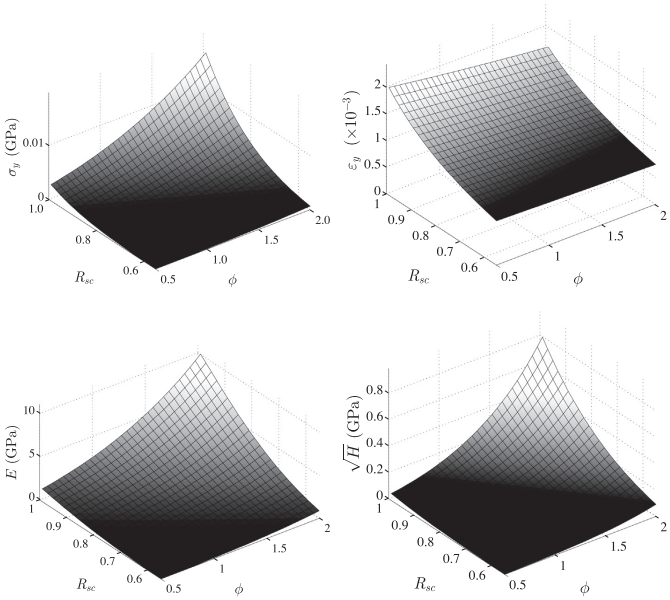

Fig. 1. Material parameters as a function of the anisotropy index ϕ and solids content R_{sc}.

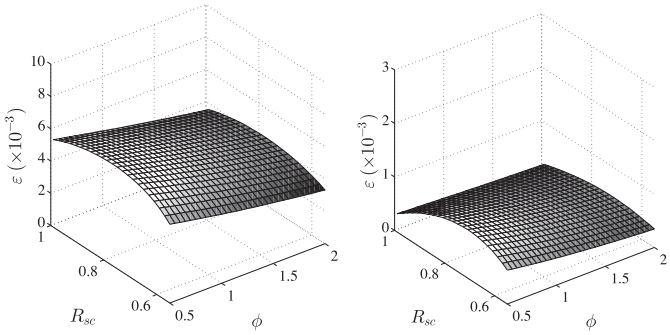

Fig. 2. Plastic strains induced by 0.01 stretching (left) and 0.003 stretching (right) as a function of the anisotropy index ϕ and solids content R_{sc}.

Table 2. The measurements and fitting procedures were presented in Erkkilä et al. (submitted for publication). In addition to the freely-dried sheets, the linear relationship between the drying shrinkage strain and hygroexpansion coefficient (Eq. (5)) can also be applied to restraint-dried sheets, but its validity does not extend to the sheets dried under additional stretch (Nordman, 1958). If $\beta_d = 0$, the ε_{ds} is estimated to have a positive strain (stretch) equal to b/a. The stretch component is subtracted from the term b/a by approximating the dry sample strain ε_d with the following equation

$$\varepsilon_d = -\frac{1}{a}\beta_d + \frac{b}{a}\left(1 - \exp\left(-100\frac{\beta_d}{a}\right)\right). \quad (6)$$

Table 2
The fitting parameters of Eq. (4)–(6) in the cases freely dried (fd) and restraint-dried (rd) samples made of SW, TMP or MIX pulp.

	k (–)	v (–)	a (–)	b (–)
SW fd	0.1557	−0.9809	2.6599	0.0244
SW rd	0.0535	−0.4987	2.6599	0.0244
TMP fd	0.1037	−1.3436	2.9596	0.0249
TMP rd	0.0687	−0.9002	2.9596	0.0249
MIX fd	0.1098	−1.3015	2.5054	0.0250
MIX rd	0.0439	−0.9015	2.5054	0.0250

Please cite this article in press as: Erkkilä, A.-L., et al. Hygro-elasto-plastic model for planar orthotropic material. Int. J. Solids Struct. (2015), http://dx.doi.org/10.1016/j.ijsolstr.2015.02.001

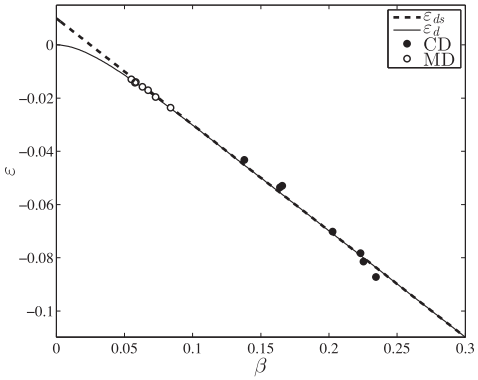

Fig. 3. The relationship between drying shrinkage strain ε and hygroexpansion coefficient β of the dry sample. Measured results of MIX samples are shown for cross direction in (CD) (with full dots), the machine direction (MD) (with open dots), the linear fitting Eq. (5) (with a dashed line) and relationship according to Eq. (6) (with a solid line).

Now if the hygroexpansion coefficient of the dry sample is $\beta_d = 0$, then the shrinkage of sample from wet to dry is $\varepsilon_d = 0$. The effect of the modification on the MIX pulp can be seen in Fig. 3. The measured data points from Erkkilä et al. (submitted for publication) are also presented.

Wahlström et al. (1999) and Wahlström (2004) introduced a function for the development of drying shrinkage strain ε_{h0} from wet to moisture ratio M:

$$\varepsilon_{h0} = \varepsilon_d \exp(B \times M) \tag{7}$$

where M is the moisture ratio and B is the fitting constant. For the freely-dried sheet, the value −2.6 was fitted for B by Wahlström (2004). As a function of solids content R_{sc}, Eq. (7) may be written in the form

$$\varepsilon_{h0} = \varepsilon_d \exp\left(B\left(\frac{1}{R_{sc}} - 1\right)\right). \tag{8}$$

Assuming that the hygroscopic strain behaves reversibly in infinitesimal solids content changes, the hygroexpansion coefficient can be approximated as a negative derivative of ε_{h0} with respect to solids content R_{sc}:

$$\beta = -\frac{\partial \varepsilon_{h0}}{\partial R_{sc}} = \frac{B}{R_{sc}^2}\varepsilon_d \exp\left(B\left(\frac{1}{R_{sc}} - 1\right)\right). \tag{9}$$

If the requirement $\beta(R_{sc} = 1) = \beta_d$ is set, the parameter B can be solved as

$$B = \frac{\beta_d}{\varepsilon_d}. \tag{10}$$

Lastly, the following equation for the hygroexpansion coefficient as a function of solids content can be derived:

$$\beta = \frac{\beta_d}{R_{sc}^2} \exp\left(\frac{\beta_d}{\varepsilon_d}\left(\frac{1}{R_{sc}} - 1\right)\right), \tag{11}$$

where β_d is defined by Eq. (4), and ε_d by Eq. (6). The hygroscopic shrinkage strain in the dry solids content interval $[R_{sc1} R_{sc2}]$ can be expressed as an integral

$$\varepsilon_h = -\int_{R_{sc1}}^{R_{sc2}} \beta dR_{sc}. \tag{12}$$

In the case of the isotropic sheet, the hygroexpansivity β as a function of R_{sc} and ε_h for interval $[0, R_{sc}]$ are presented in Fig. 4 for freely and restraint dried SW, TMP and MIX pulp samples. The dependency of β on ϕ and R_{sc} for freely and restraint dried MIX samples is presented in Fig. 5.

2.3. Continuum mechanical model

In the continuum mechanical model plane stress is assumed and the dependence between stress $\sigma = (\sigma_1, \sigma_2, \sigma_{12})^\top$ and strain $\varepsilon = (\epsilon_1, \epsilon_2, \epsilon_{12})^\top$ is defined by the generalized Hooke's law as

$$\sigma = C(\varepsilon - \varepsilon_h) \tag{13}$$

where C is the constitutive matrix and ε_h is the hygroscopic strain defined as

$$\varepsilon_h = -\begin{pmatrix} \beta_1 \\ \beta_2 \\ 0 \end{pmatrix} \Delta R_{sc} \tag{14}$$

where ΔR_{sc} is the solids content change and β_1 and β_2 are the hygroexpansion coefficients in the main direction and cross direction, respectively. Hygroexpansivities β_1 and β_2 and their dependence on ϕ and R_{sc} are defined by Eq. (11). Hill's yield function (Hill, 1948) is used to describe the yield surface. Hill's yield function is commonly used for paper and paperboard although there are known limitations related to it, for example, the origin symmetry of Hill's yield surface does not generally hold for paper or paperboard. An essential factor supporting the usage of Hill's yield function is the relatively simplicity of the parameter definition; in the case of paper the measurements needed for the determination of more exact yield

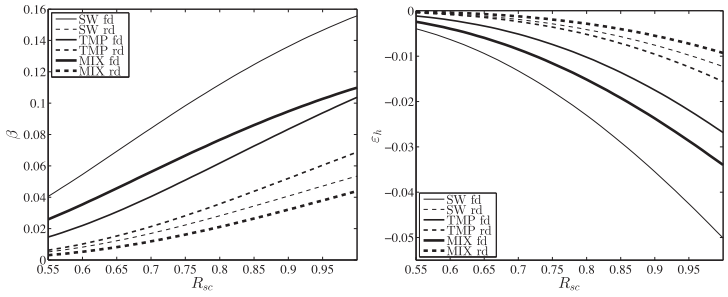

Fig. 4. Hygroexpansion coefficient β (left) and cumulative drying shrinkage strain ε_h (right) of an isotropic sheet as a function of solids content R_{sc}.

Please cite this article in press as: Erkkilä, A.-L., et al. Hygro-elasto-plastic model for planar orthotropic material. Int. J. Solids Struct. (2015), http://dx.doi.org/10.1016/j.ijsolstr.2015.02.001

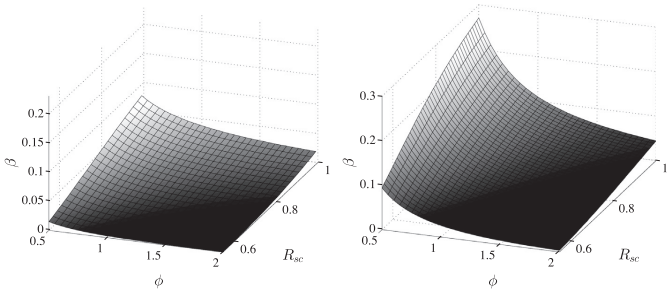

Fig. 5. The dependence of hygroexpansion coefficient β on anisotropy index ϕ and solids content R_{sc} for restraint dried (left) and freely dried (right) MIX samples.

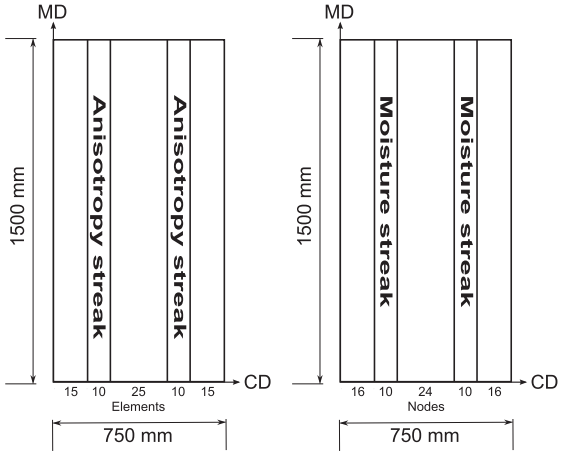

Fig. 6. The sample setup for the numerical simulations. The locations of the anisotropy (left) and moisture (right) streaks.

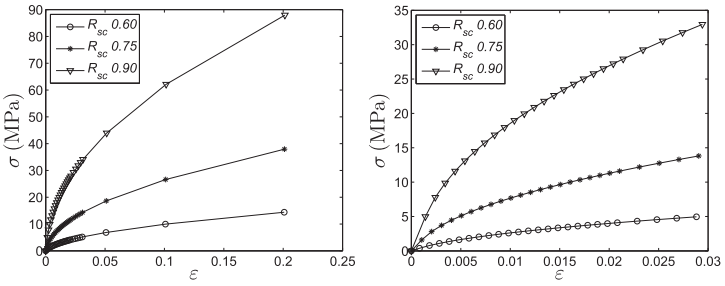

Fig. 7. Examples of discretized stress–strain relationships. The three solids content R_{sc} levels are 0.60, 0.75 and 0.90, and the anisotropy $\xi = 2.0$. Whole stress–strain curves (left), and the beginning of the curves of the left-hand figure (right).

surface are very complicated. According to Hoffman's approximation as found in Lipponen et al. (2008) the yield function has the form

$$f(\sigma) = \sqrt{\sigma_1^2 - \sigma_1\sigma_2 + \left(\frac{\sigma_{y,1}}{\sigma_{y,2}}\right)^2(\sigma_2^2 - \sigma_{12}^2) + \left(\frac{2\sigma_{y,1}}{\sigma_{y,45^\circ}}\right)^2\sigma_{12}^2} \qquad (15)$$

where σ_1, σ_2 and σ_{12} are the components of the stress tensor and $\sigma_{y,1}$, $\sigma_{y,2}$ and $\sigma_{y,45^\circ}$ are the yield stresses in the main direction, cross direction and the direction deviating 45° from the main direction, respectively. The elastic modulus is defined for directions 1, 2 and 45° as

Please cite this article in press as: Erkkilä, A.-L., et al. Hygro-elasto-plastic model for planar orthotropic material. Int. J. Solids Struct. (2015), http://dx.doi.org/10.1016/j.ijsolstr.2015.02.001

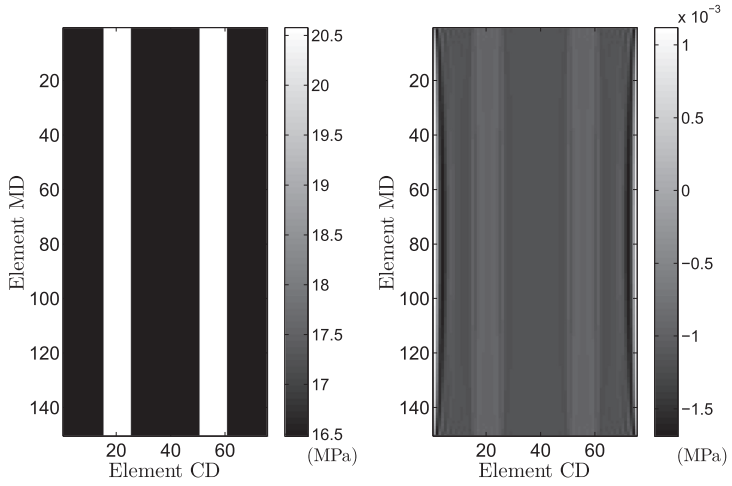

Fig. 8. MD stress (left) and CD stress (right) under 0.01 strain. Solids content $R_{sc} = 0.9$.

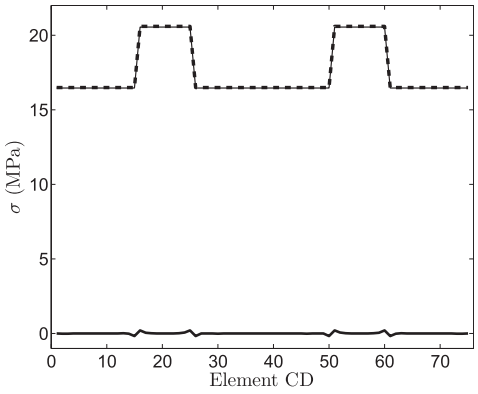

Fig. 9. CD profile of MD stress. The solids content $R_{sc} = 0.9$. Stress under 0.01 strain: the numerical result (solid narrow line), the one-dimensional analytical result (dashed line). The numerical result after release of the stretching (solid thick line).

$$E_i = \frac{\sigma_{y,i}}{\varepsilon_{y,i}}, \tag{16}$$

where $\varepsilon_{y,i}$ is the yield strain in the direction specified by the subscript i. All in-plane stress and strain parameters are defined by Eq. (2). The shear modulus is approximated as in Gibson (1994):

$$G_{12} = \frac{1}{\left(\frac{4}{E_{45^\circ}} - \frac{1}{E_1} - \frac{1}{E_2} - \frac{2\nu_{12}}{E_1}\right)}, \tag{17}$$

where ν_{12} is Poisson's ratio defined as

$$\nu_{12} = (0.015(1 - R_{sc}) + 0.15)\phi_1, \tag{18}$$

where ϕ_1 is the anisotropy index of the main direction. The dependence of ν_{12} on the anisotropy index and solids content is roughly based on the results presented in Yeh et al. (1991). By Maxwell's relation Poisson's ratio ν_{21} is defined as $\nu_{21} = \nu_{12}E_2/E_1$.

2.4. Sample setup and numerical solution

For the simulation examples, the finite element method (FEM) was used to obtain the numerical solution. Simulations were performed using ABAQUS/standard and shell element S4R with

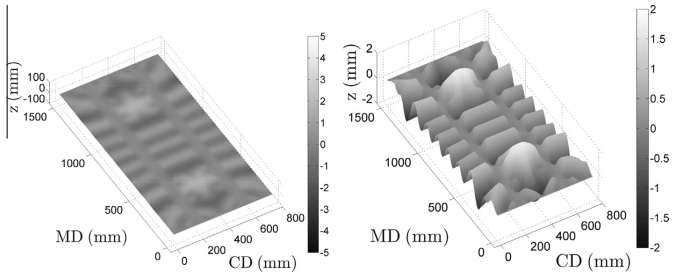

Fig. 10. Simulated out-of-plane deformations after the sample was stretched to 0.01 strain in the MD and released. In the streaks, the fiber orientation anisotropy $\xi = 2.2$ and in the surrounding areas $\xi = 1.8$. Solids content $R_{sc} = 0.9$.

Please cite this article in press as: Erkkilä, A.-L., et al. Hygro-elasto-plastic model for planar orthotropic material. Int. J. Solids Struct. (2015), http://dx.doi.org/10.1016/j.ijsolstr.2015.02.001

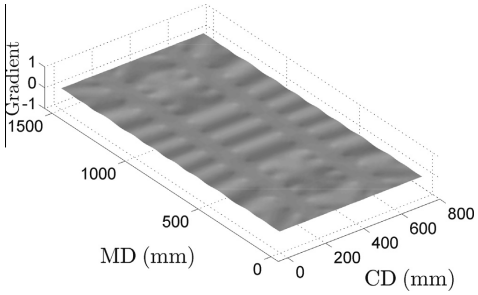

Fig. 11. Gradient representation of the out-of-plane deformation map in Fig. 10.

composite structure; see ABAQUS (2013). The sample size was 1500 mm in the machine direction (MD) and 750 mm in the cross machine direction (CD); see Fig. 6. The thickness of the sample was 0.1 mm. The element size in both MD and CD was 10 mm, and in the thickness direction, the element was divided into eight layers of equal thickness. Since there were eight material layers, the solids content was defined by nine equally spaced interfaces in the thickness direction. In all simulations, except for the case where the thickness directional solids content variation was studied, the solids content was the same in eight of the interfaces. The solids content of the top surface was 0.5% lower than in other interfaces. This approach was used to eliminate the symmetry of the sample, enabling the potential out-of-plane deformation.

In the numerical solution approach, the anisotropy, solids content, and stress–strain curve is discretized. When solids content and stress–strain space are considered, a linear behavior between defined points is assumed. In the case of anisotropy, the anisotropy is rounded to the nearest discrete value. The anisotropy was discretized with 0.1 intervals covering anisotropies between 1.0 and 6.0. The solids content dependence of the elastic properties, isotropic hardening, Hill's yield surface and moisture expansion coefficient was discretized with a resolution of 1%, covering the solids content values from 55% to 100%. The stress–strain curve was discretized into 29 unequal intervals; see Fig. 7. The first point from the origo is the yield point defining the borderline between elastic and plastic behavior. Higher resolution was used with small plastic strains, as can be seen from Fig. 7.

The sample may have one of three different anisotropy-solids content-structures (Fig. 6), contingent on the simulation case scenario:

1. The solids content is constant throughout the sample, while the anisotropy has two 100 mm through-thickness MD streaks. Within the streaks, the anisotropy ξ is 2.2, while in the surroundings, anisotropy ξ is 1.8.
2. The anisotropy is constant throughout the sample ($\xi = 2$), while the solids content has two through-thickness MD streaks.
3. The anisotropy is constant throughout the sample ($\xi = 2$), while the solids content varies in the thickness direction.

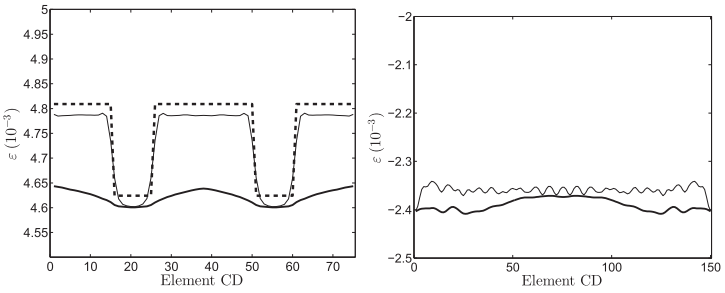

Fig. 12. The CD profile of the MD plastic strains (left), and the MD profile of the CD plastic strain (right) after the sample was stretched to 0.01 strain in the MD and released. The in-plane deformation of the simulated sample (solid thick line), the strain determined using integrated length of the simulated sample (solid narrow line) and the plastic strain using analytical one-dimensional model (dashed line). Solids content R_{sc} = 0.9.

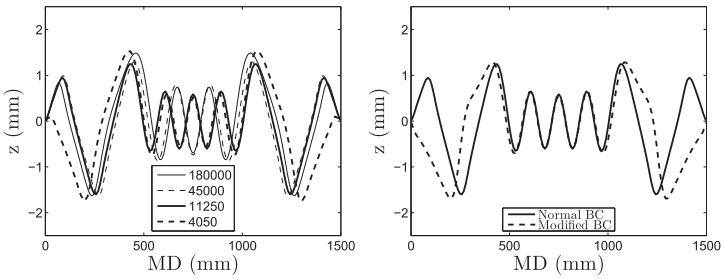

Fig. 13. MD out-of-plane profile from the middle of the sample when different number of equal sized elements are used in the numerical solution procedure (left). In the right figure, result obtained from this normal simulation setup (11250 elements) is compared with case where out-of-plane displacement and rotations are restricted in the vertical edges (CD = 0 mm and CD = 750 mm), see Fig. 6.

Please cite this article in press as: Erkkilä, A.-L., et al. Hygro-elasto-plastic model for planar orthotropic material. Int. J. Solids Struct. (2015), http://dx.doi.org/10.1016/j.ijsolstr.2015.02.001

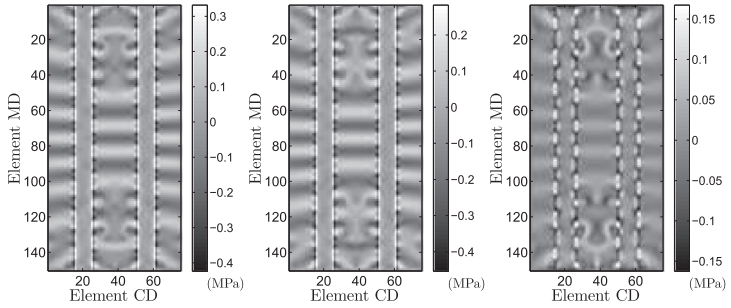

Fig. 14. Local MD and CD stresses after the sample was stretched to 0.01 strain in the MD and released. The bottom side MD stress (left), the top side MD stress (middle) and the bottom side CD stress (right). Dry solids content R_{sc} = 0.9.

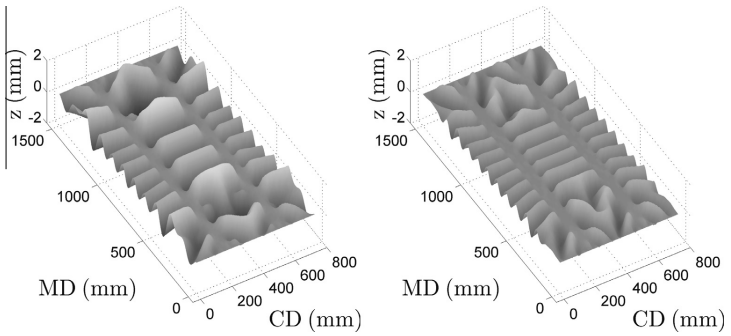

Fig. 15. Simulated out-of-plane deformations after the sample was stretched to 0.01 strain in the MD and released. The solids content R_{sc} = 0.75 (left) and solids content R_{sc} = 0.60 (right). In the streaks, the fiber orientation anisotropy $\xi = 2.2$; in the surrounding area ξ = 1.8.

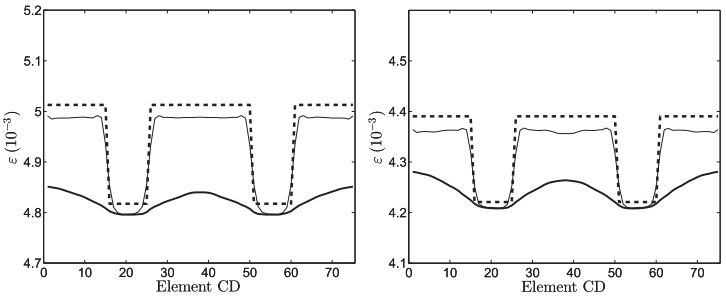

Fig. 16. CD profile of the MD plastic strains after the sample was stretched to 0.01 strain in the MD and released. The solids content R_{sc} = 0.75 (left), and the solids content R_{sc} = 0.60 (right). The in-plane deformation of the simulated sample (solid thick line), the strain determined using integrated length of the simulated sample (solid narrow line) and the plastic strain using analytical one-dimensional model (dashed line).

One or several boundary conditions were used during the simulation, depending on the case in question. However, throughout every simulation the following boundary conditions are used:

1. The MD and CD displacement of the middle node (MD = 750 mm, CD = 370 mm, see Fig. 6) of the sample was restricted.

Please cite this article in press as: Erkkilä, A.-L., et al. Hygro-elasto-plastic model for planar orthotropic material. Int. J. Solids Struct. (2015), http://dx.doi.org/10.1016/j.ijsolstr.2015.02.001

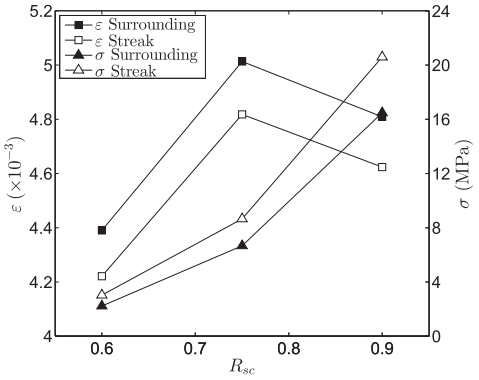

Fig. 17. Stress, σ, under 0.01 strain and the plastic strain, ε, after release.

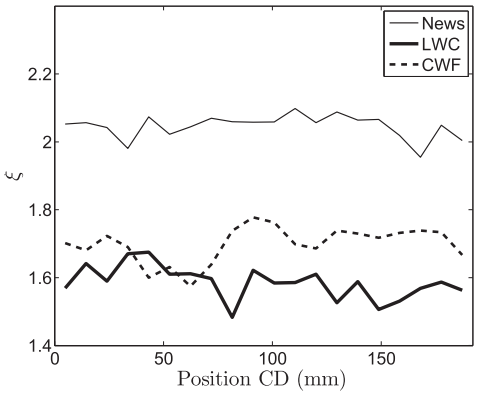

Fig. 18. Measured fiber orientation anisotropy CD profiles for News, LWC and CWF samples.

2. The out-of-plane displacement and rotations of the nodes located at the horizontal edges (MD = 0 mm and MD = 1500 mm, see Fig. 6) were restricted.

3. The numerical simulations and one-dimensional analytical results

3.1. Elasto-plastic deformation

In this section, some examples using elasto-plastic model in stretching conditions without solids content changes are presented. In the first case, the sample with the anisotropy streaks depicted in Fig. 6 had a solids content of 90%. In the simulation, 1% MD stretching was applied to the sheet, while the CD was unconstrained. The MD and CD stress prevailing during the stretching is presented in Fig. 8. The simulated MD stresses in the streaks and other positions were equivalent to MD stresses determined analytically from the one-dimensional material model, as can be seen from the CD profiles of the MD stress from Fig. 9. Through uniform stretching higher tension was created in the streaks where the anisotropy is higher. After release of the stretching, the stress dropped back to zero, and only some minor disturbance could be detected in the boundary areas of the streaks (Fig. 9). The out-of-plane deformations appeared after the stretch was released; see Fig. 10. The out-of-plane deformations were small compared to the in-plane dimensions of the simulated sample. For topography examination, the z-axis will henceforth be zoomed in on, as in Fig. 10 (right). For visual inspection, the MD gradient image is presented in Fig. 11. The gradient image simulates the inclined illuminated situation and may reveal some small-scale sharp details that are normally quelled by the higher amplitude of long wavelengths in the topography map detection. In reality, the visual appearance of an out-of-plane deformation depends highly on illumination and the detection angle, the glossiness of the surface and the ratio of the wavelength to detection distance.

The in-plane deformation and strain in MD and CD are presented in Fig. 12. The strain of the deformed sample was determined by discrete integration. The plastic MD strain determined analytically using a one-dimensional material model (Eq. (2)) is drawn as dashed line in Fig. 12. The narrowing of CD (see Fig. 12) was determined by Poisson's ratio. The plastic strain differences between the streaks and other areas caused the tight streaks and buckling in the slack surrounding areas of sheet, as is presented in Fig. 10. Buckling is highly dependent on boundary conditions, element size, disturbance, etc., so the topography result can only be considered as approximate or suggestive, see Fig. 13. Local stresses of the bottom and top sides could be detected, as could be expected, as being negative to each other: the local curl caused shrinkage in the concave surface and positive strain in the convex surface of the local buckle (see Fig. 14). The total stress, however, reached zero, leaving no global internal stresses, except some disturbances near the interfaces between regions with different anisotropies (as shown in Fig. 9).

For the 75% and 60% solids contents, simulations with 1% stretching were performed. In the case of 60% solids content, the decreased stiffness caused a higher frequency in waviness when compared to 75% or 90% solids contents; see Fig. 15. As can be expected, the stress applied by the 1% stretching did increase toward higher dry solids content (Fig. 17). The highest plastic strain at the middle solids content (75%) results from elasto-plastic material model, see Fig. 2. This is also consistent with Land's study (Land et al., 2008). However, higher plastic strain level did not increase the plastic strain difference of the streaks and surrounding areas significantly (see Figs. 16 and 17). In any case, all plastic strain differences were small, below 0.02%, but buckling behavior was estimated by the simulations.

1% stretching or even more stretching of a wet sheet is common when the web is transferred from the press section to the drying section of a paper machine. In other stages, when the dry solids content of sheet is higher, a 1% stretch is unusual, since the tension needed for web runnability rises due to the drying shrinkage. To clarify the phenomena occurring in these examples, the anisotropy difference between streaks and other areas was higher than is usually found in machine made papers. Anisotropy profiles of three production machine samples – newsprint (News), light weight coated (LWC) and coated wood free (CWF) – are presented in Fig. 18. These profiles were measured by layered fiber orientation measurement (Lipponen et al., 2009) and the anisotropy values were averaged over the layers. The samples were 192 mm × 192 mm, and the fiber orientation was determined from 20 adjacent areas each having a length of 192 mm in the MD and a width of 192/20 mm in the CD. In these three samples the deviation (max–min) of the profile was approximately 0.2, while in simulations, the used difference of anisotropies between streaks and

Please cite this article in press as: Erkkilä, A.-L., et al. Hygro-elasto-plastic model for planar orthotropic material. Int. J. Solids Struct. (2015), http://dx.doi.org/10.1016/j.ijsolstr.2015.02.001

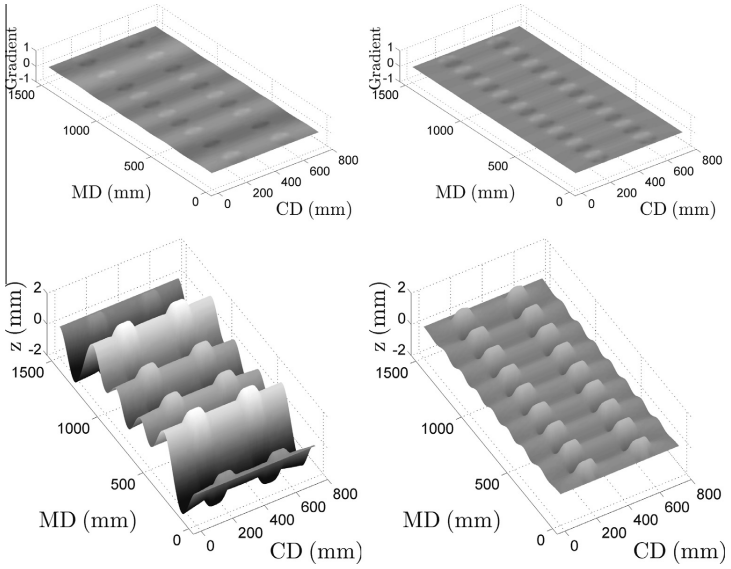

Fig. 19. Simulated out-of-plane deformations when the surroundings of the streaks are dried from solids content R_{sc} = 0.90 to R_{sc} = 0.91. In the upper row the gradient images and in lower row topography pictures. In the left column the sample has been unconstrained during drying while in right column the MD shrinkage is restricted during drying. Homogenous structure with anisotropy $\xi = 2$.

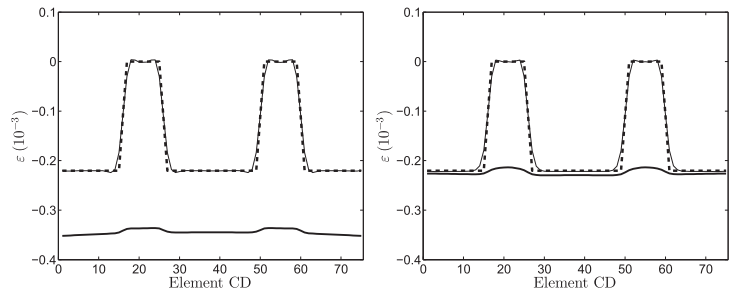

Fig. 20. CD profiles of MD shrinkage strains when the surroundings of the streaks are dried from dry solids content R_{sc} = 0.90 to R_{sc} = 0.91. The in-plane deformation of the simulated sample (solid thick line), the strain determined using integrated length of the simulated sample (solid narrow line) and the hygroscopic strain using analytical one-dimensional model (dashed line). Unconstrained drying (left) and MD shrinkage is restricted during drying (right).

surrounding areas was 0.4. However, it should be noted that anisotropy variations are often clearly higher if different layers or local deviations are studied (Erkkilä et al., 1998; Lipponen et al., 2009).

3.2. Hygroscopic deformations

In this section, simple examples of the effect of moisture changes on dimensional deformations using the hygroexpansivity-shrinkage model are presented. Obviously, even when the purpose is solely to study the effects of hygroexpansivity through finite element simulations, the results are not independent of the material model. However, using Eq. (12), the one-dimensional analytical results may indeed be solved directly without a material model. In the first example of this section, the moisture streaks of a structurally homogeneous anisotropic sheet (ξ = 2) were arranged as illustrated in Fig. 6. The sample was dried rendering a solids content change of 90% to 91%, except in the areas of the 100 mm wide streaks, in which no changes were applied; i.e. the solids content in those streaks remained at 90%. The drying was performed either under MD restraint with unconstrained CD, or under no constraint for both MD and CD, so that the sample was free to deform during the drying in all directions. The MD restraint sample was released after drying and allowed to deform freely. The fitting parameters of the restraint-dried MIX sheet were used in these simulations (see Table 2 and Eqs. (4) and (6)). The gradient and topography images are presented in Fig. 19. Freely and restraint-dried cases

Please cite this article in press as: Erkkilä, A.-L., et al. Hygro-elasto-plastic model for planar orthotropic material. Int. J. Solids Struct. (2015), http://dx.doi.org/10.1016/j.ijsolstr.2015.02.001

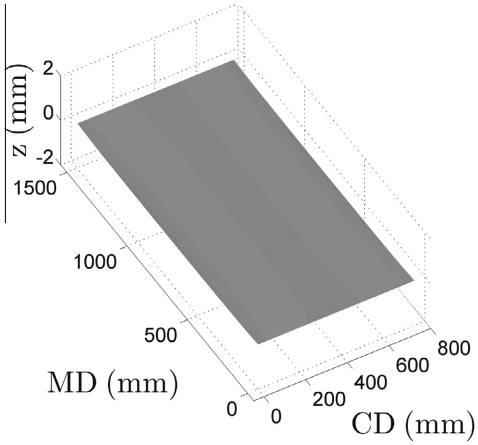

Fig. 21. Simulated out-of-plane deformations when in the first step the surrounding areas of the streaks were dried from the solids content R_{sc} = 0.90 to R_{sc} = 0.91, and in the second step equal drying was performed for the streaks. Homogenous structure with anisotropy $\xi = 2$.

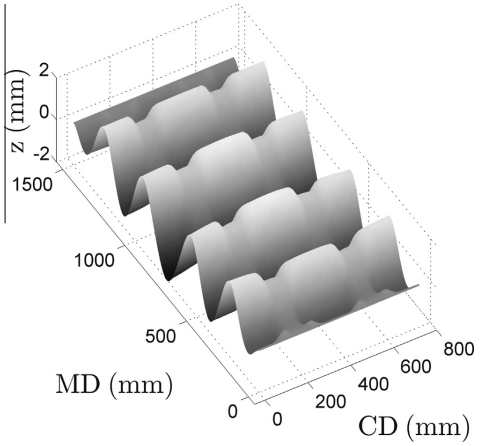

Fig. 23. Simulated out-of-plane deformation. In the first step, the sample was stretched to 0.01 strain in the MD and released, and in the second step, it was freely dried from solids content R_{sc} = 0.60 to R_{sc} = 0.65. In the streaks, the fiber orientation anisotropy $\xi = 2.2$; in the surrounding areas ξ = 1.8.

were almost identical when the average CD profiles of the MD shrinkage strain were compared and furthermore were congruent with the analytical one-dimensional results; see Fig. 20. Visually, the biggest difference could be detected in the buckling behavior. The overall low frequency bending of the freely dried sheet lowered the frequency of waviness in the streaks and smoothed the tensions slightly in the streak boundaries (the maximum-minimum difference was 232 kPa for the freely dried sample and 244 kPa for the MD restraint-dried sample). If in the following step the streak areas are dried equivalently from 90% to 91% (Fig. 21), all out-of-plane deformations disappear, the internal stresses are reduced to zero at every position, and the amount of shrinkage is equal everywhere and congruent with the one-dimensional hygroexpansivity model. No plastic deformations arose either in restraint-dried or freely dried cases under such a small stress difference (808 kPa (tension = 80.8 N/m) in the restraint sample) or due to shrinkage differences, only 0.022% between the surrounding and streak areas.

Also, anisotropy affects hygroexpansivity. A sheet with anisotropy streaks was dried from 60% to 65% solids content without any constraints in the MD nor CD. The out-of-plane deformation and CD profile of the MD shrinkage strains are presented in Fig. 22. The streaks having higher anisotropy levels shrunk less than the other areas. The strain difference is very small, only 0.0041%. In order to more purely study the behavior of the hygroscopic model without the interference of plasticity, the studied moisture changes were kept low, and all simulation results corresponded well with the results of the one-dimensional hygroexpansivity model.

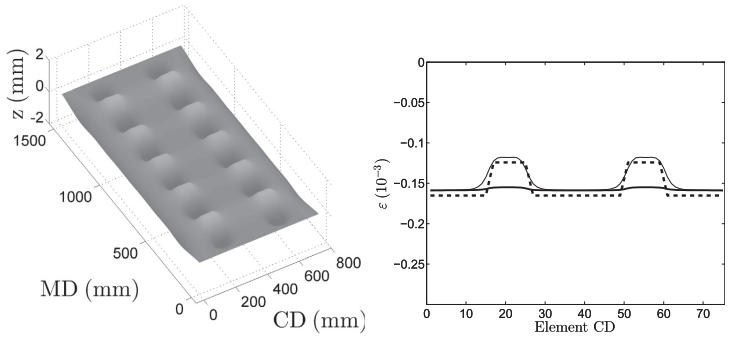

Fig. 22. The out-of-plane deformation (left), and the CD profile of MD hygroscopic strains (right) after the sample containing anisotropy streaks was dried from solids content R_{sc} = 0.60 to R_{sc} = 0.65. In the right-hand figure, the in-plane deformation of the simulated sample (solid thick line), the strain determined using integrated length of the simulated sample (solid narrow line) and the hygroscopic strain using analytical one-dimensional model (dashed line).

Please cite this article in press as: Erkkilä, A.-L., et al. Hygro-elasto-plastic model for planar orthotropic material. Int. J. Solids Struct. (2015), http://dx.doi.org/10.1016/j.ijsolstr.2015.02.001

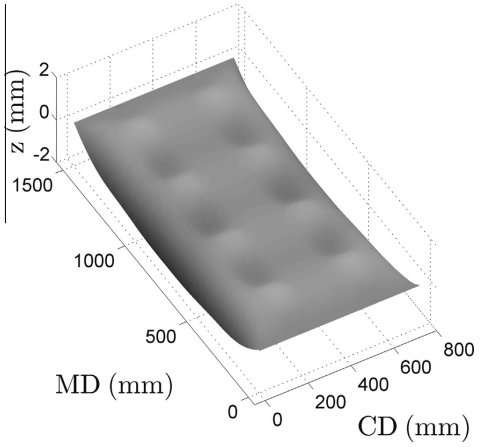

Fig. 24. Simulated out-of-plane deformation. In the first step, the sample was stretched to 0.01 strain in the MD and released, and in the second step, it was freely dried from solids content R_{sc} = 0.60 to R_{sc} = 0.75.

3.3. Brief study of interactions between moisture changes and stretching

The aim in the previous sections was to demonstrate the behavior of the material model and the hygroexpansivity model separately, although the finite element simulations of hygroexpansivity are not independent of the material model in any case. To study simultaneous and interactive phenomena, including factors of drying and draw from both the hygroexpansivity model and the material model, a few examples are presented here.

Starting with a baseline anisotropy streak case (as presented in Section 3.1) having a solids content of 60%, the different drying conditions could be applied. The first step was thus a draw of 1% in the MD. In the second step, the draw was released, and then the sheet was dried freely from a solids content of 60% to 65%. The second step was fundamentally the same as the anisotropy streak case of Section 3.2, excepting for initial plastic strain differences and minor internal stresses at the streak boundaries. The deformation occurring after this second step is presented in Fig. 23. After adding up the CD profiles of MD strain solved by the one-dimensional approach of the first step (Fig. 16, right) and the second step (Fig. 22), an equivalent profile was achieved as that of the finite element simulation; see Fig. 26. When the drying in the second step were continued to a solids content of 75%, almost all deformations arising from the streaks disappeared (Fig. 24), since the shrinkage amount is lower in the streak areas. A significant change in deformations can be detected if the 1% draw is not released before the second step drying. The drying shrinkage increases the MD tension further, resulting in an increase in the plastic strain level as well as in the difference between the streaks and surrounding areas in the MD (Figs. 25, 26 and Table 3).

Table 3
The strains in the streaks and surrounding areas from Fig. 26.

	Streak (%)	Surrounding (%)	Difference (%)
65 fd	0.4075	0.4213	0.0138
75 fd	0.3543	0.3551	0.0008
65 rd	0.4475	0.4647	0.0173
75 rd	0.4609	0.4771	0.0161
One-dimensional	0.4097	0.4225	0.0128

In the second example, the anisotropic homogeneous sample (ξ = 2) was freely dried from a solids content of 80% to 90% or 95%, so that in the first step solids content profiles in the thickness direction were applied through the sample as is presented in Fig. 27. The profiles used are roughly based on Östlund's simulations for symmetric convective drying. The sample with basis weight 300 g/m^2 was dried symmetrically from R_{sc} = 0.435 to R_{sc} = 0.997, for details see Östlund (2006). Only the high solids content profile (mean $R_{sc} \approx 0.85$) was used. In the second step, the whole paper would finally achieve a uniform solids content of 90% or 95%. According to the simulations of this study (Fig. 27) every tested solids content profile generates plastic strain differences between layers. The simulated stresses (Fig. 27) are same order of magnitude as measured results in Östlund et al. (2004) despite of the different material parameters etc. between the studies. The plastic strains of the layers in the MD and in the CD are presented in Table 4. The higher plastic strain in the CD than in the MD resulted from the higher shrinkage tendency and from the different plasticity properties in the CD than in the MD in the anisotropic sheet.

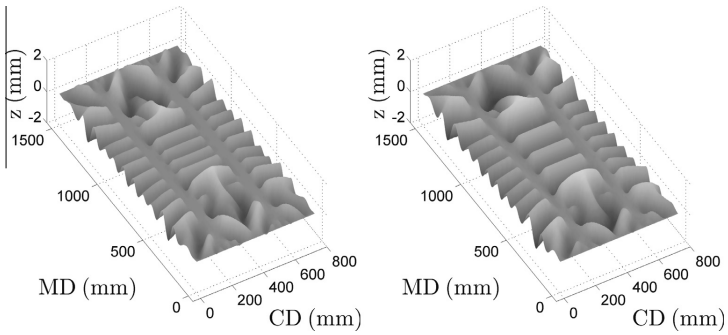

Fig. 25. Simulated out-of-plane deformation. In the first step, the sample was stretched to 0.01 strain in the MD, and in the second step, it was dried under MD restraint from solids content R_{sc} = 0.60 to R_{sc} = 0.65 (left), and from solids content R_{sc} = 0.60 to R_{sc} = 0.75 (right).

Please cite this article in press as: Erkkilä, A.-L., et al. Hygro-elasto-plastic model for planar orthotropic material. Int. J. Solids Struct. (2015), http://dx.doi.org/10.1016/j.ijsolstr.2015.02.001

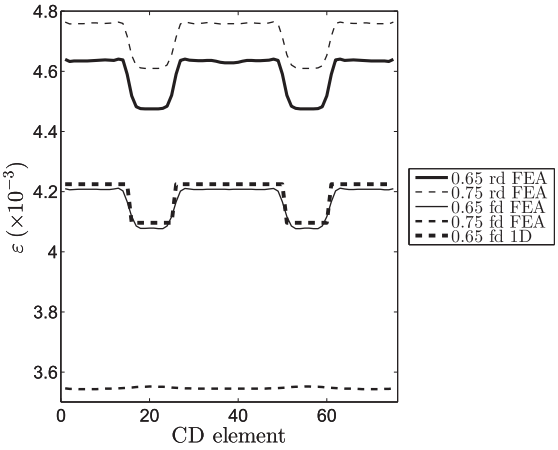

Fig. 26. CD profiles of MD deformations for the cases depicted in Figs. 23–25. The analytical one-dimensional result corresponding to the case of Fig. 23 is presented by a thick dashed line.

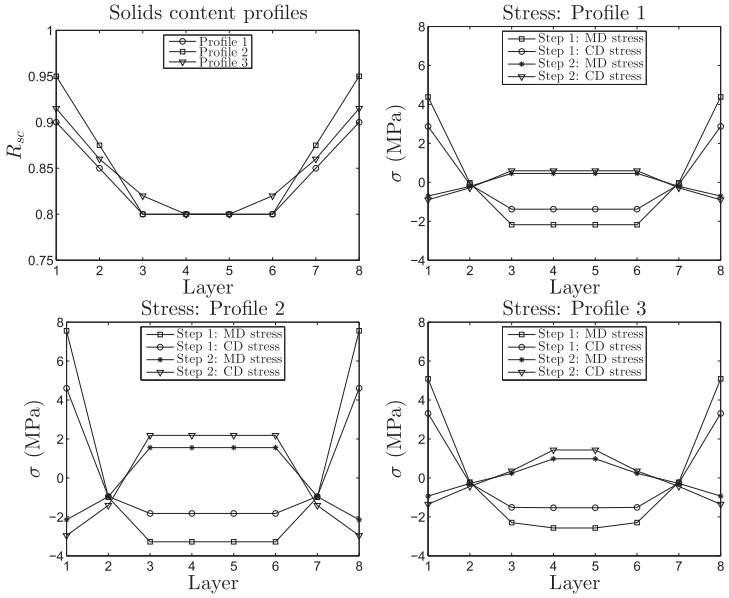

Fig. 27. The MD and CD stress of different layers, when in the first step different through-thickness solids content profiles (top-left) are applied. In the initial situation solids content trough the sample is R_{sc} = 0.80 and in the second step every layer is dried either to R_{sc} = 0.90 (solids content profile 1) or R_{sc} = 0.95 (solids content profiles 2 and 3).

Table 4
The plastic strains in the layers from Fig. 27.

	Profile 1		Profile 2		Profile 3	
Layer	MD (%)	CD (%)	MD (%)	CD (%)	MD (%)	CD (%)
1 and 8	0.0068	0.0418	0.0160	0.0838	0.0084	0.0497
2 and 7	0	0	0	0	0	0
3 and 6	−0.0084	−0.0607	−0.0313	−0.1966	−0.0061	−0.0437
4 and 5	−0.0084	−0.0607	−0.0313	−0.1966	−0.0152	−0.1028

4. Conclusions

The hygro-elasto-plastic model introduced herein offers the possibility to study several complex phenomena of such orthotropic planar materials as board or paper. The elasto-plastic model and hygroexpansivity-shrinkage model based on experimental results can be solved analytically and separately in one dimension, but the full potential of these models is achieved through the

Please cite this article in press as: Erkkilä, A.-L., et al. Hygro-elasto-plastic model for planar orthotropic material. Int. J. Solids Struct. (2015), http://dx.doi.org/10.1016/j.ijsolstr.2015.02.001

numerical solution of a continuum mechanical model. With finite element analysis, the simultaneous and interactive situations combining these two separate models as well as the effect of plastic and hygroscopic strains on the buckling behavior of a sheet or web can be simulated. The time- or history-dependent behaviors are not implemented on the introduced hygro-elasto-plastic model. Thus, the applicability of the model on studies of storage and multi-chained processes is limited. The input parameters of the model are the fiber orientation anisotropy index (Erkkilä et al., 2013), the dry solids content, the external strain or stress and the change in the dry solids content. The use of the anisotropy index instead of that of traditional fiber orientation anisotropy simplified the handling of different in-plane directions. Usually, the hygroexpansion coefficient has been considered to characterize the deformation of a dry paper subject to a moisture change, independently of the moisture content level, although some stress relaxation and moisture history dependence may have been involved (Uesaka et al., 1992). In this study, the dry solids content dependent hygroexpansivity, over the entire range from wet to dry, has been suggested. A few different parameters to model hygroexpansivity depending on the pulp type of the sample and on the free or restrained drying conditions can be selected.

With the use of the finite element method, different sheet structures and dimensions can be applied, such as sheets or webs including anisotropy, basis weight or moisture content variation in-plane and throughout the different layers. The application possibilities are versatile for studies on paper web or sheet behavior in drying, converting, printing or copying processes. The corresponding defects may include, for example, shrinkage profiles, misregistration in printing, deformation of boxes, different buckling phenomena such as cockling, curling and heatset web offset fluting, internal stresses build up due to the two sidedness of different processes and the streakiness of the web.

To demonstrate the model responses, a few examples of the effect of anisotropy and moisture streaks of otherwise homogenous anisotropic sheets on strain differences and buckling have been presented. Also, the internal stresses caused by the drying process with different layers drying at different stages have been discussed. Very small plastic strain differences may cause buckling, but how visually disturbing these out-of-plane deformation defects are depends on paper or board grade and usage. This kind of buckling streakiness is considered as a defect, and is often called the bagginess of a paper web. The baggy paper web brings up the risk of wrinkling, which is reported to increase if the strain difference is higher than 0.1%, although for some thin papers, a strain difference of only 0.01% is enough to cause noticeable problems (Roisum, 1996). In the examples of this work, the strain differences have been more on the order of 0.01% than 0.1%. The simulation cases were kept simple and the stretching and dry solids content changes were selected to be small compared to the real total drying process of a paper machine. This enables to observe the hygroexpansion and plastic strains separately, to compare the analytical and numerical in-plane deformations and to understand the phenomena comprehensively.

The complexity of the interactive and simultaneous behavior of hygroexpansivity and plasticity was revealed even with the simple examples presented in this paper. For example, the streaks having a higher anisotropy level than in the surrounding areas appeared as tight streaks after stretching in the MD because of the lower plastic strain in the MD. The free drying performed subsequently to the stretching-releasing procedure may compensate for the difference in the plastic strains, because the MD shrinkage tendency of the high anisotropy streaks is lower than that of the surrounding areas. However, if drying is done under restraint, the lower shrinkage of the streaks may even further increase the plastic strain difference between the streaks and surrounding areas. Land's experimental study (Land et al., 2008) of the effect of the moisture streaks on permanent strain differences also showed that the releasing of tension at different stage of drying is a significant factor.

According to the simulation results of this study, the buckling could be caused by both the anisotropy and the moisture streaks. The more challenging task is to determine in which cases the generated buckling and strain differences remain as permanent plastic strain differences, perhaps over subsequent converting processes; and even further, in which cases they cause problems during paper making and converting processes. Some problems of moisture streaks arising from the drying section may well vanish in the coating or calendaring processes, where moisture or heat is brought to the paper web. Structural streaks, such as anisotropy or basis weight streaks, stay in the paper once formed, and may create problems at any stage of the paper life cycle.

Acknowledgements

Simulations were performed by commercial software ABAQUS which was licensed to CSC (the Finnish IT center for science).

References

ABAQUS, 2013. ABAQUS Documentation. Dassault Systèmes, Providence, RI, USA.
Alava, M., Niskanen, K., 2006. The physics of paper. Rep. Prog. Phys. 69, 669–723.
Alfthan, J., 2004. The effect of humidity cycle amplitude on accelerated tensile creep of paper. Mech. Time Depend. Mater. 8 (4), 289–302.
Bloom, F., Coffin, D.W., 2000. Modelling the hygroscopic buckling of layered paper sheets. Math. Comput. Model. 31 (8–9), 43–60.
Brezinski, J.P., 1956. The creep properties of paper. Tappi 39 (2), 116–128.
Castro, J., Ostoja-Starzewski, M., 2003. Elasto-plasticity of paper. Int. J. Plast. 19, 2083–2098.
Constantino, R.P.A., l'Anson, S.J., Sampson, W.W., 2005. The effect of machine conditions and furnish properties on paper CD shrinkage profile. In: Proceedings of 13th Pulp and Paper Fundamental Research Symposium, Cambridge, pp. 283–306.
de Ruvo, A., Lundberg, S., Martin-Löf, S., Södermark, C., 1976. Influence of temperature and humidity on the elastic and expansional properties of paper and the constituent fibre. In: The Fundamental Properties of Paper Related to Its Uses, Transactions of the Symposium, British Paper Board Industry Federation, London, pp. 785–806.
Erkkilä, A.-L., Pakarinen, P., Odell, M., 1998. Sheet forming studies using layered orientation analysis. Pulp Pap. Canada 99 (1), 81–85.
Erkkilä, A.-L., Leppänen, T., Hämäläinen, J., 2013. Empirical plasticity models applied for paper sheets having different anisotropy and dry solids content levels. Int. J. Solids Struct. 50, 2151–2179.
Erkkilä, A.-L., Leppänen, T., Ora M., Tuovinen, T., Puurtinen, A., submitted for publication. Hygroexpansivity of anisotropic sheets. Nordic Pulp Pap. Res. J.
Fahey, D.J., Chilson, W.A., 1963. Mechanical treatments for improving dimensional stability of paper. Tappi 46 (7), 393–399.
Fellers, C., Westerlind, B., de Ruvo, A., 1983. An investigation of the biaxial failure envelope of paper – experimental study and theoretical analysis. In: Proceedings of Fundamental Research Symposium, Cambridge, pp. 527–559.
Gates, E.R., Kenworthy, I.C., 1963. Effects of drying shrinkage and fibre orientation on some physical properties of paper. Pap. Technol. 4 (5), 485–493.
Gibson, R.F., 1994. Principles of Composite Material Mechanics. McGraw-Hill Inc.
Glynn, P., Jones, H.W.H., Gallay, W., 1961. Drying stresses and curl in paper. Pulp Pap. Mag. Canada 62 (1), 39–48.
Haslach, H.W., 1994. Relaxation of moisture accelerated creep and hygroexpansion. In: Proceedings of the Moisture-Induced Creep Behavior of Paper and Board Conference, Stockholm, pp. 121–138.
Hill, R., 1948. A theory of the yielding and plastic flow of anisotropic metals. Proc. R. Soc. London Ser. A, Math. Phys. Sci. 191, 281–297.
Hoole, S.M., l'Anson, S.J., Ora, M., Ashworth, T.N., Briggs, D., Phillips, B., Hoyland, R.W., 1999. CD shrinkage profiles of paper – experiments on a commercial paper machine. Pap. Technol. 40 (10), 63–70.
Ivarsson, B.W., 1954. Introduction of stress into a paper sheet during drying. Tappi 37 (12), 634–639.
Johnson, M.W., Urbanik, T.J., 1984. A nonlinear theory for elastic plates with application to characterizing paper properties. J. Appl. Mech. 51, 146–152.
Johnson, M.W., Urbanik, T.J., 1987. Buckling of axially loaded, long rectangular paperboard plates. Wood Fiber Sci. 19 (2), 135–146.
Kijima, T., Yamakawa, I., 1978. Effect of shrinkage during drying on dimensional stability of paper. Jpn. Tappi J. 32 (10), 584–592.
Kiyoaki, I., 1987. The computer simulation on a web shrinkage in a paper machine dryer section. Part 1. Elastic modulus and drying force as a function of a web moisture. Japan. Tappi J. 41 (12), 1229–1234.

Please cite this article in press as: Erkkilä, A.-L., et al. Hygro-elasto-plastic model for planar orthotropic material. Int. J. Solids Struct. (2015), http://dx.doi.org/10.1016/j.ijsolstr.2015.02.001

Kouko, J., Salminen, K., Kurki, M., 2007. Laboratory scale measurement procedure for the runnability of a wet web on a paper machine, part 2. Pap. Timber 89 (7–8), 424–430.

Kulachenko, A., Gradin, P., Uesaka, T., 2005. Tension wrinkling and fluting in heatset web offset printing process – post-buckling analysis. In: Proceedings of 13th Pulp and Paper Fundamental Research Symposium, Cambridge, pp. 1075–1099.

Land, C., Wahlström, T., Stolpe, L., 2008. Moisture streaks and their relation to baggy paper webs. J. Pulp Pap. Sci. 34 (4), 234–239.

Larsson, P.A., Wågberg, L., 2008. Influence of fibre–fibre joint properties on the dimensional stability of paper. Cellulose 15 (4), 515–525.

Lavrykov, S., Ramarao, B.V., Lyne, A.L., 2004. The planar transient hygroexpansion of copy paper: experiments and analysis. Nordic Pulp Pap. Res. J. 19 (2), 183–190.

Leppänen, T., Sorvari, J., Erkkilä, A.-L., Hämäläinen, J., 2005. Mathematical modelling of moisture induced out-of-plane deformation of a paper sheet. Model. Simul. Mater. Sci. Eng. 13, 841–850.

Leppänen, T., Erkkilä, A.-L., Hämäläinen, J., 2008. Effect of fiber orientation structure on simulated cockling of paper. Pulp Pap. Canada 109 (2), 31–38.

Lif, J.O., Fellers, C., Söremark, C., Sjödahl, M., 1995. Characterizing the in-plane hygroexpansivity of paper by electronic speckle microscope. J. Pulp Pap. Sci. 21 (9), 302–309.

Lif, J., Östlund, S., Fellers, C., 1999. Applicability of anisotropic viscoelasticity of paper at small deformations. Mech. Time Depend. Mater. 2 (3), 245–267.

Lif, J., Östlund, S., Fellers, C., 2005. In-plane hygro-viscoelasticity of paper at small deformations. Nordic Pulp Pap. Res. J. 20 (1), 139–149.

Lif, J.O., 2006. Hygro-viscoelastic stress analysis in paper web offset printing. Finite Elem. Anal. Des. 42 (5), 341–366.

Lipponen, P., Leppänen, T., Kouko, J., Hämäläinen, J., 2008. Elasto-plastic approach for paper cockling phenomenon: on the importance of moisture gradient. Int. J. Solids Struct. 45, 3596–3609.

Lipponen, P., Erkkilä, A.-L., Leppänen, T., Hämäläinen, J., 2009. On the importance of in-plane shrinkage and through-thickness moisture gradient during drying on cockling and curling phenomena. In: Proceedings of 14th Pulp and Paper Fundamental Research Symposium, Oxford, pp. 389–436.

Lu, W., Carlsson, L.A., 2001. Influence of viscoelastic behavior on curl of paper. Mech. Time Depend. Mater. 5, 79–100.

Lyne, L.M., Gallay, W., 1954. Fiber properties and fiber water relationships in relation to the strength and rheology of wet webs. Tappi 37 (12), 581–596.

Lyne, A., Fellers, C., Kolseth, P., 1996. The effect of filler on hygroexpansivity. Nordic Pulp Pap. Res. J. 11 (3), 152–163.

Manninen, M., Kajanto, I., Happonen, J., Paltakari, J., 2011. The effect of microfibrillated cellulose addition on drying shrinkage and dimensional stability of wood-free paper. Nordic Pulp Pap. Res. J. 26 (3), 297–305.

Mendes, A.H.T., Park, S.W., Ferreira, P.J.T., Almeida, F.S., 2011. Hygroexpansivity profiles on a commercial paper machine. Nordic Pulp Pap. Res. J. 26 (3), 312–318.

Mäkelä, P., Östlund, S., 2003. Orthotropic elastic–plastic material model for paper materials. Int. J. Solids Struct. 40, 5599–5620.

Mäkelä, P. 2009. Effect of drying conditions on the tensile properties of paper. In: Proceedings of 14th Pulp and Paper Fundamental Research Symposium, Oxford, pp. 1079–1094.

Nanko, H., Wu, J., 1995. Mechanisms of paper shrinkage during drying. In: Proceedings of International Paper Physics Conference (CPPA and Tappi), pp. 103–113.

Nanri, Y., Uesaka, T., 1993. Dimensional stability of mechanical pulps – drying shrinkage and hygroexpansivity. Tappi J. 76 (6), 62–66.

Nordman, L.S., 1958. Laboratory investigations into the dimensional stability of paper. Tappi 41 (1), 23–50.

Page, D.H., Tydeman, P.A., 1962. A new theory of the shrinkage, structure and properties of paper. In: Transactions of the Symposium on Formation and Structure of Paper, British Paper and Board Makers' Association, London, pp. 397–413.

Pecht, M.G., Johnson, M.W., Rowlands, R.E., 1984. Constitutive equations for the creep of paper. Tappi 67 (5), 106–108.

Pecht, M., Johnson, M.W., 1985. The strain response of paper under various constant regain states. Tappi 68 (1), 90–93.

Rance, H.F., 1954. Effect of water removal on sheet properties. Tappi 37 (12), 640–648.

Rance, H.F., 1956. The formulation of methods and objectives appropriate to the rheological study of paper. Tappi 39 (2), 104–115.

Rand, J.L., 1995. A nonlinear viscoelastic creep model. Tappi J. 78 (7), 178–182.

Roisum, D.R., 1996. The mechanics of wrinkling. Tappi J. 79 (10), 217–226.

Salmen, L., Fellers, C., Htun, M., 1987. The development and release of dried-in stresses in paper. Nordic Pulp Pap. Res. J. 2 (2), 44–48.

Setterholm, V., Kuenzi, E.W., 1970. Fiber orientation and degree of restraint during drying – effect of tensile anisotropy of paper handsheet. Tappi 53 (10), 1915–1920.

Silvy, J., 1971. Effects of drying on web characteristics. Pap. Technol. 12 (5), 377–387.

Skowronski, J., Robertson, A.A., 1986. The deformation properties of paper: tensile strain and recovery. J. Pulp Pap. Sci. 12 (1), 20–25.

Steenberg, B., 1947. Paper as a visco-elastic body. Svensk Papperstidning 50 (6), 127–140.

Strömbro, J., Gudmundson, P., 2008. Mechano-sorptive creep under compressive loading – a micromechanical model. Int. J. Solids Struct. 45 (9), 2420–2450.

Suhling, J.C., Rowlands, R.E., Johnson, M.W., Gunderson, D.E., 1985. Tensorial strength analysis of paperboard. Exp. Mech. 25 (1), 75–84.

Tydeman, P.A., Wembridge, D.R., Page, D.H. 1966. Transverse shrinkage of individual fibers by microradiography. In: Consolidation of the Paper Web: Transactions of the Symposium, Cambridge, pp. 119–144.

Uesaka, T., Murakami, K., Imamura, R., 1980. Two-dimensional linear viscoelasticity of paper. Wood Sci. Technol. 14, 131–142.

Uesaka, T., Kodaka, I., Okushima, S., Fukuchi, R., 1989. History-dependent dimensional stability of paper. Rheol. Acta 28, 238–245.

Uesaka, T., 1991. Dimensional stability of paper – upgrading paper performance in end use. J. Pulp Pap. Sci. 17 (2), 39–46.

Uesaka, T., Moss, C., Nanri, Y., 1992. The characterisation of hygroexpansivity of paper. J. Pulp Pap. Sci. 18 (1), 11–16.

Uesaka, T., 1994. General formula for hygroexpansion of paper. J. Mater. Sci. 29 (9), 2373–2377.

Uesaka, T., Qi, D., 1994. Hygroexpansivity of paper: effects of fibre-to-fibre bonding. J. Pulp Pap. Sci. 20 (6), 175–179.

Urbanik, T.J., 1995. Hygroexpansion-creep model for corrugated fiberboard. Wood Fiber Sci. 27 (2), 134–140.

Wahlström, T., Adolfsson, K., Östlund, S., Fellers, C. 1999. Numerical modelling of the cross direction shrinkage profile in a drying section: a first approach. In: Proceedings of the 1999 TAPPI International Paper Physics Conference, San Diego, California, pp. 517–531.

Wahlström, T., Fellers, C., 2000. Biaxial straining of handsheets during drying – effects on in-plane mechanical properties. Tappi J. 83 (8), 1–8.

Wahlström, T., Lif, J.O., 2003. Dryer section simulator for laboratory investigations of shrinkage profile. In: Proceedings of International Paper Physics Conference (PAPTAC), pp. 169–173.

Wahlström, T., 2004. Development of paper properties during drying. Pap. Prod. Phys. Technol., 69–107

Xia, Q.S., Boyce, M.C., Parks, D.M., 2002. A constitutive model for the anisotropic elastic–plastic deformation of paper and paperboard. Int. J. Solids Struct. 39, 4053–4071.

Yeh, K.C., Considine, J.M., Suhling, J.C., 1991. The influence of moisture content on the nonlinear constitutive behavior of cellulosic materials. In: Tappi Proceedings: 1991 International Paper Physics Conference, Tappi, pp. 695–711.

Östlund, M., Östlund, S., Carlsson, L.A., Fellers, C., 2004. The influence of drying restraints and beating degree on residual stress build-up in paperboard. J. Pulp Pap. Sci. 30 (11), 289–292.

Östlund, M., 2006. Modeling the influence of drying conditions on the stress buildup during drying of paperboard. J. Eng. Mater. Technol. Trans. ASME 128 (4), 495–502.

Please cite this article in press as: Erkkilä, A.-L., et al. Hygro-elasto-plastic model for planar orthotropic material. Int. J. Solids Struct. (2015), http://dx.doi.org/10.1016/j.ijsolstr.2015.02.001

ACTA UNIVERSITATIS LAPPEENRANTAENSIS

593. UUSITALO, VILLE. Potential for greenhouse gas emission reductions by using biomethane as road transportation fuel. 2014. Diss.

594. HAVUKAINEN, JOUNI. Biogas production in regional biodegradable waste treatment – possibilities for improving energy performance and reducing GHG emissions. 2014. Diss.

595. HEIKKINEN, JANNE. Vibrations in rotating machinery arising from minor imperfections in component geometries. 2014. Diss.

596. GHALAMCHI, BEHNAM. Dynamic analysis model of spherical roller bearings with defects. 2014. Diss.

597. POLIKARPOVA, MARIIA.Liquid cooling solutions for rotating permanent magnet synchronous machines. 2014. Diss.

598. CHAUDHARI, ASHVINKUMAR. Large-eddy simulation of wind flows over complex terrains for wind energy applications. 2014. Diss.

599. PURHONEN, MIKKO. Minimizing circulating current in parallel-connected photovoltaic inverters. 2014. Diss.

600. SAUKKONEN, ESA. Effects of the partial removal of wood hemicelluloses on the properties of kraft pulp. 2014. Diss.

601. GUDARZI, DAVOOD. Catalytic direct synthesis of hydrogen peroxide in a novel microstructured reactor. 2014. Diss.

602. VALKEAPÄÄ, ANTTI. Development of finite elements for analysis of biomechanical structures using flexible multibody formulations. 2014. Diss.

603. SSEBUGERE, PATRICK. Persistent organic pollutants in sediments and fish from Lake Victoria, East Africa. 2014. Diss.

604. STOKLASA, JAN. Linguistic models for decision support. 2014. Diss.

605. VEPSÄLÄINEN, ARI. Heterogenous mass transfer in fluidized beds by computational fluid dynamics. 2014. Diss.

606. JUVONEN, PASI. Learning information technology business in a changing industry landscape. The case of introducing team entreneurship in renewing bachelor education in information technology in a university of applied sciences. 2014. Diss.

607. MÄKIMATTILA, MARTTI. Organizing for systemic innovations – research on knowledge, interaction and organizational interdependencies. 2014. Diss.

608. HÄMÄLÄINEN, KIMMO. Improving the usability of extruded wood-plastic composites by using modification technology. 2014. Diss.

609. PIRTTILÄ, MIIA. The cycle times of working capital: financial value chain analysis method. 2014. Diss.

610. SUIKKANEN, HEIKKI. Application and development of numerical methods for the modelling of innovative gas cooled fission reactors. 2014. Diss.

611. LI, MING. Stiffness based trajectory planning and feedforward based vibration suppression control of parallel robot machines. 2014. Diss.

612. KOKKONEN, KIRSI. From entrepreneurial opportunities to successful business networks – evidence from bioenergy. 2014. Diss.

613. MAIJANEN-KYLÄHEIKO, PÄIVI. Pursuit of change versus organizational inertia: a study on strategic renewal in the Finnish broadcasting company. 2014. Diss.

614. MBALAWATA, ISAMBI SAILON. Adaptive Markov chain Monte Carlo and Bayesian filtering for state space models. 2014. Diss.

615. UUSITALO, ANTTI. Working fluid selection and design of small-scale waste heat recovery systems based on organic rankine cycles. 2014. Diss.

616. METSO, SARI. A multimethod examination of contributors to successful on-the-job learning of vocational students. 2014. Diss.

617. SIITONEN, JANI. Advanced analysis and design methods for preparative chromatographic separation processes. 2014. Diss.

618. VIHAVAINEN, JUHANI. VVER-440 thermal hydraulics as computer code validation challenge. 2014. Diss.

619. AHONEN, PASI. Between memory and strategy: media discourse analysis of an industrial shutdown. 2014. Diss.

620. MWANGA, GASPER GODSON. Mathematical modeling and optimal control of malaria. 2014. Diss.

621. PELTOLA, PETTERI. Analysis and modelling of chemical looping combustion process with and without oxygen uncoupling. 2014. Diss.

622. NISKANEN, VILLE. Radio-frequency-based measurement methods for bearing current analysis in induction motors. 2014. Diss.

623. HYVÄRINEN, MARKO. Ultraviolet light protection and weathering properties of wood-polypropylene composites. 2014. Diss.

624. RANTANEN, NOORA. The family as a collective owner – identifying performance factors in listed companies. 2014. Diss.

625. VÄNSKÄ, MIKKO. Defining the keyhole modes – the effects on the molten pool behavior and the weld geometry in high power laser welding of stainless steels. 2014. Diss.

626. KORPELA, KARI. Value of information logistics integration in digital business ecosystem. 2014. Diss.

627. GRUDINSCHI, DANIELA. Strategic management of value networks: how to create value in cross-sector collaboration and partnerships. 2014. Diss.

628. SKLYAROVA, ANASTASIA. Hyperfine interactions in the new Fe-based superconducting structures and related magnetic phases. 2015. Diss.

629. SEMKEN, R. SCOTT. Lightweight, liquid-cooled, direct-drive generator for high–power wind turbines: motivation, concept, and performance. 2015. Diss.

630. LUOSTARINEN, LAURI. Novel virtual environment and real-time simulation based methods for improving life-cycle efficiency of non-road mobile machinery. 2015. Diss.